



DIPARTIMENTO DI INGEGNERIA AEROSPAZIALE
POLITECNICO DI MILANO

Receptivity and Control of Flow Instabilities in a Boundary Layer

Simone ZUCCHER

Tesi di Dottorato di Ricerca in Ingegneria Aerospaziale - XIV Ciclo
Dicembre 2001

Il candidato:

Simone ZUCCHER

Il tutore:

Prof. Paolo LUCHINI

Il coordinatore del
dottorato di ricerca:

Prof. Paolo MANTEGAZZA

Abstract

Fluid dynamic instabilities leading to transition from laminar to turbulent flow in an incompressible boundary layer are considered in this thesis. Both Tollmien–Schlichting instabilities, and algebraically growing instabilities are analyzed. In the former case attention is paid to the receptivity process of free–stream and wall disturbances, whereas in the latter the optimization of exciting disturbances at the leading edge and their optimal and robust control via suction/blowing at the wall are investigated.

The problem of boundary–layer receptivity to the quadratic mixing of different disturbances is solved by introducing the multiple–scale technique for the non homogeneous case and applying it to the linearized Navier–Stokes equations. Multiple scales offer the possibility to account for nonparallel effects due to boundary–layer growth. The resulting algorithm is not computationally expensive and can be efficiently included in industrial codes for transition prediction.

The optimization of initial perturbation and suction at the wall is performed for the steady three–dimensional, algebraically growing instability of an incompressible boundary layer past a flat plate in the completely nonlinear regime. An adjoint–based optimization technique is used in order to determine first sinusoidal optimal perturbations at the leading edge which provide the maximum energy growth for a given initial energy, and then the steady spanwise–uniform optimal suction to be applied at the wall in order to reduce the energy growth to a minimum for that initial perturbation. However, since the control at the wall modifies the initial optimal perturbation, robust optimal control is finally computed.

Acknowledgments

I would like to thank, first of all, Professor Paolo Luchini, who has supervised my Ph.D study with knowledge and wisdom. He has taught to me how to look at problems from more than one perspective and usually different from the common ones. His guidance and suggestions have been very helpful in order to find the answers I was looking for.

Secondly, Professor Alessandro Bottaro, who supervised the study performed during my visiting period at IMFT (Institut de Mécanique des Fluides de Toulouse). I am very grateful to him for the possibility to exchange ideas with people working on the specific topic of boundary-layer transition, and for his suggestions regarding the preliminary version of the present thesis.

I thank also CIRA (Centro Italiano Ricerche Aerospaziali - *Italian Aerospace Research Center*), and especially Raffaele Donelli, for the post-graduate grant which has made my Ph.D research possible.

Finally, I would like to thank all the friends I met at Aerospace Engineering Department in Milano, at IMFT in Toulouse and at CIRA in Capua.

Contents

| | |
|---|------------|
| Abstract | i |
| Acknowledgments | iii |
| Introduction | 1 |
| 1 Stability and transition | 5 |
| 1.1 Introduction | 5 |
| 1.1.1 Boundary–layer instabilities, receptivity and control | 5 |
| 1.1.2 Classical linear stability theory | 8 |
| 1.1.3 Algebraic instability | 11 |
| 1.2 Transition scenarios | 12 |
| 1.2.1 Receptivity | 12 |
| 1.2.2 Transition due to Tollmien–Schlichting waves | 13 |
| 1.2.3 Transition due to non–modal disturbance growth | 13 |
| 1.3 Transition prediction | 14 |
| 1.3.1 Correlation methods | 14 |
| 1.3.2 e^N method | 15 |
| 1.3.3 H – R_x method | 16 |
| 1.4 Transition control | 16 |
| 1.4.1 Suction at the wall | 17 |
| 1.4.2 Shaping | 18 |
| 1.4.3 Wave cancellation | 19 |
| 2 Receptivity using multiple scales | 21 |
| 2.1 Introduction | 21 |
| 2.1.1 Different receptivity configurations | 22 |
| 2.1.2 Possible modeling approaches | 24 |
| 2.1.3 Multiple–scale technique | 26 |
| 2.1.4 Motivations for the present work | 27 |
| 2.2 Problem formulation | 28 |
| 2.2.1 Velocity decomposition and linearization | 29 |
| 2.2.2 Order ϵ and δ | 32 |
| 2.2.3 Order $\epsilon\delta$ | 37 |
| 2.3 Multiple scales | 37 |

| | | |
|----------|--|------------|
| 2.3.1 | Non-homogeneous multiple-scale theory | 37 |
| 2.3.2 | Application to the Navier-Stokes equations | 39 |
| 2.4 | Interacting disturbances | 44 |
| 2.4.1 | Wall vibration – wall roughness interaction | 45 |
| 2.4.2 | Possible disturbance interactions | 46 |
| 2.4.3 | Receptivity function | 47 |
| 2.5 | Results | 49 |
| 2.5.1 | Acoustic wave – wall roughness interaction | 50 |
| 2.5.2 | Vorticity wave – wall roughness interaction | 52 |
| 2.5.3 | Acoustic wave – vorticity wave interaction | 54 |
| 2.6 | Conclusions | 55 |
| 3 | Optimization and control | 57 |
| 3.1 | Introduction | 57 |
| 3.1.1 | Algebraic instability | 57 |
| 3.1.2 | Previous work | 58 |
| 3.1.3 | Goal of the present work | 60 |
| 3.2 | Problem formulation | 60 |
| 3.2.1 | Choice of the objective function and initial conditions | 62 |
| 3.2.2 | Constrained optimization and linear adjoint problem | 64 |
| 3.2.3 | Iterative optimization | 67 |
| 3.2.4 | Implementation and numerical solution | 69 |
| 3.2.5 | Optimal perturbation, optimal control and robust control | 76 |
| 3.3 | Optimal perturbations: results | 79 |
| 3.3.1 | Different objective functions – linear case | 79 |
| 3.3.2 | Comparisons for varying $\beta\delta$ and E_0 | 80 |
| 3.3.3 | Comparisons at fixed $\beta\delta$ | 82 |
| 3.3.4 | Comparisons at fixed E_0 | 83 |
| 3.3.5 | Comparisons at optimal $\beta\delta$ | 85 |
| 3.4 | Optimal control: results | 85 |
| 3.4.1 | Different objective functions – linear case | 86 |
| 3.4.2 | Comparisons for varying $\beta\delta$ and E_w | 87 |
| 3.4.3 | Comparisons at fixed $\beta\delta$ | 89 |
| 3.4.4 | Comparisons at fixed E_w | 96 |
| 3.4.5 | Comparisons at optimal $\beta\delta$ | 98 |
| 3.4.6 | Controlling on a finite window | 99 |
| 3.5 | Robust control: results | 101 |
| 3.5.1 | Comparisons for varying $\beta\delta$, E_0 and E_w | 101 |
| 3.5.2 | Comparisons at fixed $\beta\delta$ | 102 |
| 3.5.3 | Comparisons at fixed E_w | 104 |
| 3.5.4 | Comparisons at optimal $\beta\delta$ | 106 |
| 3.6 | Concluding summary | 108 |
| 4 | Conclusions | 111 |

CONTENTS

vii

| | |
|--|------------|
| A Basic matrix properties | 115 |
| B Homogeneous multiple scales example | 119 |
| C Example of optimization | 123 |
| D Problem discretization | 129 |

Introduction

The present thesis concerns the study of flow instabilities in a boundary layer. In particular, two main subjects are considered. The first regards *modal* disturbances developing in a nonparallel boundary layer and generated by external exciting sources. The receptivity problem is investigated in order to understand how these external perturbations can produce unstable Tollmien–Schlichting waves inside the boundary layer. The second subject concerns *non-modal* instabilities and their algebraic growth. In this case, an optimization problem is solved to find the initial condition, for the boundary layer equations, which produces the maximal energy growth for a given initial energy. A control, in the form of a spanwise–uniform wall suction, that optimally opposes this instability’s growth is then computed but since the presence of the control at the wall makes the optimal initial perturbation different from the uncontrolled one, robust optimal control is finally applied.

The interest in the subject of boundary layer instabilities is mainly due to the drastic economic consequences of boundary layer transition from laminar to turbulent flow. It has been estimated that if laminar flow could be maintained on the wings of a large transport aircraft, a fuel savings of up to 25% would be obtained [96].

This can be done by delaying, or totally avoiding, transition to turbulence. A better understanding of the instabilities which lead to the transition process is therefore needed.

The route to transition, in boundary layer flows, can be divided into different stages. First, the external disturbances are internalized in the boundary layer through the *receptivity* process. Then a wave, due to the external perturbations, originates inside the boundary layer, growing and leading to a *linear amplification* or decay as described by the linearized Navier–Stokes equations. If the amplitude of the excited wave is greater than a certain threshold, a further instability called *secondary instability* can occur, provoking a non-linear breakdown and causing transition from laminar to turbulent flow.

It can happen that this transition scenario, related to the exponential growth of Tollmien–Schlichting waves (modal disturbances), is bypassed by another strongly amplifying mechanism due to linear phenomena but caused by other than exponential instabilities. In fact, the linear theory for the instability analysis sometimes fails predicting a stable behavior for flows which experiments show to be unstable. For example, the theory applied to a pipe flow reveals that all the eigenvalues are stable. Despite this consideration, it is well known from experiments that if the Reynolds number is greater than a certain threshold, transition is observed. Moreover, for certain flows, for example plane Poiseuille flow, transition practically occurs at a *Re* number smaller than the critical value expected from the theory. This means that there must be another instability growing mechanism which cannot be seen in the classical Orr–Sommerfeld formulation.

This is called bypass transition and basically regards algebraic instabilities and transient growth.

Since transition turns out to have a quite heavy economic impact, transition prediction criteria are usually applied in order to estimate the location of transition during the aerodynamic design of aircraft wings. The most used and apparently most reliable criterion is the e^N method. It was introduced only for the exponentially growing disturbances like Tollmien–Schlichting waves and is based on the idea that when the amplitude of the unstable wave is e^N times (where N is between 9 and 11) the amplitude of the wave at the first neutral point, transition occurs. Clearly, the external environment and its influence on the boundary layer stability is not accounted for by this technique.

On the contrary, the goal of a receptivity study is to improve transition prediction methods extending transition criteria to include the free-stream disturbance environment. In other words, receptivity allows us to relate the amplitude of the instability wave produced inside the boundary layer (Tollmien–Schlichting wave) to the physical amplitude of the external exciting disturbance. The main excitation sources are usually acoustic waves, vorticity waves and wall vibrations. However, their temporal frequency and spatial wavelength are not in the same range as those of the Tollmien–Schlichting waves, so that resonance can be reached only via an “adaptation mechanism”, for instance produced by wall roughness.

In the present work, multiple scales are introduced in a non-homogeneous form in order to investigate the interaction between different disturbances. This technique is not usually used in fluid dynamic problems, but can be preferable to other methods for the study of boundary-layer receptivity, because it offers the possibility to account for nonparallel effects due to boundary-layer growth, it does not have numerical stability problems, it is not computationally expensive, and therefore can be included in industrial codes for transition prediction. The non-homogeneous form is here introduced for the first time to treat the quadratic mixing between the single disturbances (acoustic and vorticity waves, wall vibration and wall roughness). This interaction produces a forcing term which has the right frequency and wavelength typical of Tollmien–Schlichting waves, originating a resonant problem.

Another interesting problem related to receptivity is to find the “optimal perturbation”, which represents the leading-edge excitation that provides the maximum energy growth for a given initial energy. This is done, in the present work, by considering the three-dimensional, algebraically growing instability of a Blasius boundary layer in the nonlinear regime. Adjoint-based optimization is used to determine the “optimal” steady, but spanwise-sinusoidal leading-edge excitation which represents the most dangerous initial perturbation as far as the stability of the flow is concerned.

Once the optimal perturbation has been calculated, another interesting question is how to delay transition (and therefore the instability by which it was produced) when this initial “optimal” condition is applied.

This subject is known as flow control and its importance is related to the great potential benefits achievable in drag reduction. Control strategies can be classified in different ways. One possibility is to consider the energy or power required in order to control the flow field, obtaining a first main division in *passive* or *active* control. In the former case no energy support is needed during the control (NACA 6-series airfoils for

which transition was delayed just by shaping the upper wall in a specific way), in the latter energy is required (blowing/suction at the wall, wall heating/cooling, wall motion, wave cancellation). However when active control is applied, for instance on the wing of an airplane, attention should be paid in order to obtain a gain in drag reduction at least greater than the energy necessary to apply it.

In this work the optimal control in the form of a spanwise–uniform wall suction that optimally opposes the algebraic instability growth is computed using an adjoint–based optimization technique similar to the one used for the optimal perturbation. However, when suction is applied, the boundary conditions at the wall are no longer homogeneous. This implies that the optimal initial perturbation for that suction distribution is not the same that was found without control. Robust optimal control is thus applied, which consists in finding the initial optimal perturbation and the optimal control suction at the same time while accounting for their mutual interaction.

The first chapter of this thesis is devoted to stability and transition. The aim is to briefly introduce the classical linear stability theory for Tollmien–Schlichting waves and the more recent subject of algebraic instability. Transition scenarios due to this kind of instabilities are presented together with an introduction to transition–prediction methods and transition–control techniques.

In the second chapter the receptivity problem is considered using multiple scales. The multiple–scale method is presented in the non homogeneous framework and applied to the linearized Navier–Stokes equations. The mutual interactions between acoustic wave, vorticity wave, wall vibration and wall roughness are discussed and the receptivity function, which relates the amplitude of the excited wave to the amplitude of the exciting sources, is computed. This chapter will be summarized in a paper and submitted to an international journal (Physics of Fluids)

In the third chapter the optimal perturbation, optimal control and robust optimal control are computed for the boundary layer past a flat plate. The constrained optimization is performed using the method of Lagrange multipliers, obtaining a system of adjoint equations. Since both the direct and adjoint problems are parabolic, a forward and backward iterative technique is best suited. Results are compared and discussed for different cases. This chapter will be submitted to an international journal (Journal of Fluid Mechanics) in the form of two papers, one regarding optimal control and another regarding optimal control and robust control.

The last chapter summarizes the conclusions of this thesis.

Chapter 1

Boundary layer stability and transition to turbulence

It is a common experience to see someone smoking a cigarette. If the smoker is keeping it in a vertical position, without moving too much, it is possible to realize that the smoke close to the end of the cigarette is quite regular forming almost parallel patterns. On the contrary, taking a look further from the end of the cigarette and following the smoke development, a complete different scenario is encountered: strange smoke patterns interacting with each other, forming nonsensical or magnificent figures (depending on the observer's imagination) and spreading into the environment so that, after a while, all the smoke is completely mixed to the air. If the smoker cannot keep the cigarette without moving, this process of "smoke fading" is faster and the regular behavior can be observed only for a short time.

1.1 Introduction

1.1.1 Boundary-layer instabilities, receptivity and control

The every-day experience of the smoke from a cigarette contains the concept of flow instability. The fluid is air and the smoke is just a trick in order to visualize what happens. When the fluid is regularly moving, the flow regime is called *laminar*, when it shows very complicated and strange patterns it is called *turbulent* and the passage from the former to the latter is called *transition*, for obvious reasons. The laminar flow regime is characterized by order, predictability and low mixing, like the smoke just at the end of the burning cigarette. The turbulent flow regime is exactly the opposite: it shows high disorder, random unsteadiness, apparent unpredictability and very high mixing like the "smoke visualization" far from the cigarette.

Laminar flows, however, have a poor resistance that makes them become turbulent. For this reason it is quite difficult to find examples of laminar flow in every-day life whereas it is much simpler to enumerate turbulent flows: the coffee mixed in a cup in order to make it cool or in order to dissolve the sugar inside of it, the water coming out from any tap, the smoke rising from a chimney, any river.

The boundary layer on a body interacting with a flow field can be laminar or turbulent, exactly as the flow originating from the cigarette. The explanation of why, when and where the transition from laminar to turbulent flow occurs is related to the concept of *stability*: a laminar flow is defined stable (or stable for small disturbances) if it returns to its original state after any perturbation (or a small perturbation) has been applied. The laminar flow is unstable if the disturbance generated by the perturbation does not disappear but grows changing the laminar state to the turbulent one. The concept of stability applied to the example of the cigarette thus reveals that the original state, the laminar flow just at the end of the cigarette, undergoes an instability process which leads to the turbulent flow state. That particular laminar flow is unstable.

Under which conditions does the flow become unstable? The answer to this question is still open and it is the object of fluid–dynamic–instability study. A common feature, however, seems to be the dependence on the Reynolds number¹, which represents the relative importance of the convective and inertial mechanisms to the dissipative ones. Experiments show that in very high Reynolds–number flows, turbulence eventually develops. The first experimental evidence of this dependence was demonstrated by Reynolds in his famous pipe–flow experiences (1883): he observed that transition from laminar to turbulent flow can occur if Reynolds number Re is larger than a certain characteristic value, called critical Reynolds number Re_{cr} . It is important to remark that Re_{cr} is the Reynolds–number value for which the laminar flow shows the beginning of the instability process: this does not necessarily mean that the flow will develop towards turbulence, since damping effects could avoid that. However, if the flow becomes turbulent, Re_{tr} is the transitional Reynolds number defined as the value at which the flow is fully turbulent.

How is a fluid dynamic instability excited? In general, in order to excite an instability process, an *exciting source*, which represents the external disturbance, is needed together with an *exciting mechanism*, which should introduce the exciting source into the system. Reynolds, in his experiments, had to deal with the problem of the external disturbances and how they influence the flow, finding a strong dependence of the spatial location where transition occurs on the environmental conditions. He used a tank full of water connected to a pipe and putted a needle at the beginning of the tube in order to let a dye filament visualize the flow pattern. He noticed that if attention is paid to the design of the connection between the reservoir and the pipe, transition can be delayed, whereas if the pipe–fitting is too sharp or if roughness is present inside the duct, transition is anticipated. These experiences show how much transition is related to the external environment in which exciting sources can be identified.

However, transition cannot occur if the exciting source does not have the possibility of being introduced into the flow. The way by which the external disturbances can enter inside a particular flow is nowadays called *receptivity*. Obviously, receptivity does not necessarily mean instability or transition: if the base flow is stable or if the perturbation is too weak in order to cause the onset of the instability or if damping effects arise, the flow continues behaving in a laminar regime. If the flow turns out to be unstable, the instability develops eventually leading the flow to the turbulent regime. An important feature of the receptivity mechanism is the great advantage of relating the stability

¹Reynolds number Re is defined as $Re = UL/\nu$ where U is a characteristic convective velocity, L the typical longitudinal length scale and ν is a fluid property, the kinematic viscosity

properties to the external disturbances, allowing to predict transition as a function of the environmental conditions.

A certain base flow was said to be stable if it returns to its original state after a disturbance has been applied. However, the stability concept can be *temporal* or *spatial*. In the temporal framework, a perturbation is applied at a certain initial time (at all the spatial locations) and its evolution observed as a function of time: if the disturbance decays, the flow is stable; unstable if the disturbance grows with time. By contrast, in the spatial framework, the perturbation applied at a certain location (for all the time) is followed and its spatial evolution observed.

When dealing with systems characterized by an infinite spatial extension, another classification of the instability can be related to where the perturbation is applied. For instance, it could be applied everywhere or only locally. In the second case, it is worth to ask if the introduced disturbance remains localised or moves during its evolution, leading to the definition of *absolute* and *convective* instability. The instability is defined *convective* if the disturbance grows everywhere but not where it was applied, and *absolute* if it grows also where it was applied. This basically implies that in the convective instability the disturbance moves away downstream, whereas in the absolute instability the disturbance will eventually appear at any spatial location.

When a flow becomes turbulent, like the smoke at a certain distance from the cigarette, three-dimensionality and large diffusion can be easily observed. These features imply an increase of the mixing characteristics, which can be welcome or unwelcome depending on the problem under investigation. Every time high mixing is required, turbulence is desirable: for example in dilution of polluting dispersions or in chemical reactions, where high momentum exchange allows the species to get in touch very fast and accelerate the process. Moreover, turbulence implies very high heat transfer rates and therefore it is welcome in heating or cooling processes. On the contrary, the high mixing rates of turbulent flows are usually unwelcome in aerodynamic or hydrodynamic fields such as design of turbines, low-velocity vehicles, submarines, subsonic and supersonic civil and military aircrafts, hypersonic and reentry vehicles. The main problems related to these subjects are first the increase of drag on every body moving in a fluid, implying a much greater amount of fuel or energy needed in order to move, and second significant heat loads in supersonic or hypersonic applications, introducing structural difficulties.

Transition to turbulence is therefore an important topic with heavy economic consequences. It has been estimated that if laminar flow could be maintained on the wings of a large transport aircraft, a fuel saving of up to 25% would be obtained [96]. Clearly, the laminar flow can be maintained avoiding transition to turbulence or making the turbulent flow to become laminar again (relaminarization): in any case, *control* techniques are applied. One possibility is to shape the body such that the flow is laminar as far downstream as possible, looking for the best “aerodynamic shape”. Another possibility is to delay transition acting on the base flow and changing its stability characteristics, for example applying a suction of the boundary layer at the wall. However, the power usually required in order to do so is much greater than the gain in drag reduction, making this approach often useless. Other more sophisticated techniques “feel” the flow field and change some wall quantities in order to react, stabilizing the base flow (*feedback control*).

1.1.2 Classical linear stability theory

The aim of hydrodynamic stability theory is to find an answer to the question: “What makes an initial laminar flow become turbulent?”.

Basic introductions to this field can be found in chapter 16 of Schlichting [102], chapter 5 of White [108], chapter 22 of Panton [93] and chapter 6 of Cebeci and Cousteix [21]. Whole books devoted to the subject of stability are Chandrasekhar [23], Lin [76], Drazin and Reid [40]. Special reviews on boundary layer stability and transition are those by Bayly *et al.* [8], Herbert [61], Reed and Saric [95], Huerre and Monkewits [64], Saric [99], Kachanov [67], Reed *et al.* [96] and Henningson and Alfredsson [59]. In these books and articles further detailed references can be found.

The classical approach to the boundary layer stability theory [102] [108] [93] [21] [23] [76] [40] is based on the linearization of the Navier–Stokes equations about a given base flow, obtaining the equations for the disturbance. The behavior of the disturbance is then determined: if it grows, the base flow is unstable; if it decays, the base flow is stable. Without entering in the mathematical detail (which can be found in the cited references), supposing that the base flow is two–dimensional (only the streamwise component U and wall–normal component V of the velocity are present) and parallel ($V = 0$ and U depends only on the wall–normal coordinate, $U = U(y)$ so that $U_x = 0$), and the considering a two–dimensional perturbation², the linearized Navier–Stokes equations read

$$\begin{aligned} u_x + v_y &= 0 \\ u_t + Uu_x + vU_y &= -p_x + Re^{-1}\nabla^2 u \\ v_t + Uv_x &= -p_y + Re^{-1}\nabla^2 v \end{aligned}$$

The perturbation is usually expressed as a traveling wave:

$$(u, v, p) = (u(y), v(y), p(y))e^{i\alpha x - \omega t}$$

so that, on eliminating p , the classical equation for the velocity v can be derived:

$$i[(\alpha U - \omega)(v_{yy} - \alpha^2 v) - \alpha U_{yy}v] = Re^{-1}((\cdot)_y - \alpha^2)^2 v$$

It is a fourth–order linear homogeneous ordinary differential equation, first derived independently by Orr (1907) and Sommerfeld (1908) and for this reason called Orr–Sommerfeld equation. The proper boundary conditions require the perturbation to vanish at the borders of the domain:

$$\begin{array}{ll} v(\pm h) = v_y(\pm h) = 0 & \text{Duct flows} \\ v(0) = v_y(0) = 0; \quad v(\infty) = v_y(\infty) = 0 & \text{Boundary layers} \\ v(\pm\infty) = v_y(\pm\infty) = 0 & \text{Free shear layers} \end{array}$$

Since both the equation and boundary conditions are homogeneous, an eigenvalue problem is derived which furnishes the dispersion relation:

$$D(\alpha, \omega, Re) = 0$$

²Historically two–dimensional perturbations have been considered much more than three–dimensional ones because of the Squire’s theorem, which guarantees that for two–dimensional parallel base flows the minimum critical unstable Reynolds number occurs for two–dimensional disturbances propagating along the same direction [108].

When the temporal stability is considered, α and Re are fixed and real so that ω is complex and its imaginary part gives the temporal growth rate; for the spatial stability ω and Re are fixed and real, and the imaginary part of α furnishes the spatial growth rate. The solution $v(y)$ is called eigenfunction. From this analysis, the neutral stability curve can be obtained: it represents the locus of points for which the growth rate (spatial or temporal) is zero, identifying regions of stability or instability in the α – Re or ω – Re plane (depending on the case).

Inviscid stability

Dropping the viscous terms in the Orr–Sommerfeld equation (those containing Re^{-1}), the Rayleigh equation is found³:

$$v_{yy} - \left(\frac{U_{yy}}{U - c} + \alpha^2 \right) v = 0$$

where $c = \omega/\alpha$ is the phase velocity. It has been derived in the limit $Re \rightarrow \infty$ so that the equation provides helpful informations for large Reynolds–number flows. The most important conclusions regarding inviscid stability are summarized in five theorems [108]:

Theorem 1 [Rayleigh (1880)] For the inviscid instability it is necessary for the velocity profile $U(y)$ to have an inflection point: $U_{yy}(y_{ip}) = 0$ where y_{ip} is the y location of the inflection point

Theorem 2 [Fjrtof (1950)] For the inviscid instability it is necessary for the shear $|U_y|$ to be maximum at the inflection point y_{ip}

Theorem 3 [Fjrtof (1950)] If an inflection point exists, for the inviscid instability it is further necessary $U_{yy}(U - U(y_{ip})) = 0$ somewhere on the profile

Theorem 4 [Lin (1945)] Let y_c be the position at which $U - c = 0$: if $U(y)$ has an inflection point at $y = y_c$, a neutral disturbance ($c_i = 0$) may exist whose phase velocity $c_r = U(y_c)$

Theorem 5 [Rayleigh (1880)] The phase velocity c_r of an amplified disturbance must always lie between the minimum and maximum value of $U(y)$

The most important consequence of these theorems is that velocity profiles with an inflection point are unstable in *real life* at high Reynolds number. On the other hand, for many years it was believed that viscous profiles without a point of inflection would be stable. Indeed the viscosity can be destabilizing in certain cases: Poiseuille flow is stable in the inviscid case, unstable in the viscous one.

³Since it is a second–order differential equation, only two boundary conditions are required

Viscous stability for parallel flows

If the viscous part is taken into account, the complete Orr–Sommerfeld equation reads

$$i [(\alpha U - \omega) (v_{yy} - \alpha^2 v) - \alpha U_{yy} v] = Re^{-1} ((\cdot)_y - \alpha^2)^2 v$$

The base flow can be any parallel one (Poiseuille, Couette or Blasius profile); here we consider only the Blasius boundary layer. In this case, the unstable perturbation wave is called Tollmien–Schlichting wave and from the Orr–Sommerfeld equation the neutral stability curve can be obtained. In the spatial stability framework, it represents the locus of points, in ω – R plane, for which $\alpha_i = 0$.

Some interesting characteristics regarding the Tollmien–Schlichting wave in a Blasius boundary layer past a flat plate can be derived [108]: the minimal critical Reynolds number Re_{cr} is $R = 520$ or $Re_x = 91000$ where $Re_x = U_e x / \nu$ and $R = \sqrt{Re_x}$. At Re_{cr} (first neutral point) the wave parameters are $\alpha \delta^* = 0.3012$ (δ^* is the displacement thickness), $\omega / \alpha_r = 0.3961 U_e$ and $\omega \nu / U_e^2 = 2.29 \cdot 10^{-4}$. The maximum wavenumber for the instability is $\alpha \delta^* = 0.35$ therefore the smallest wavelength is $\lambda_{min} = 2\pi \delta^* / 0.35 \approx 18 \delta^* \approx 6\delta$ ($\delta = \sqrt{x\nu/U_e}$), thus Tollmien–Schlichting waves are long compared to boundary–layer thickness. Finally, the maximum phase velocity is $\omega / \alpha_r \approx 0.4 U_e$ meaning that the Tollmien–Schlichting waves travel quite slowly and arise close to the wall. It is important to remark that the critical Reynolds number predicted by the theory is not the point of the transition to turbulence. The transitional Reynolds number is $Re_{tr} \approx 3 \cdot 10^6$, about 30 times further downstream.

Stability of more complex boundary–layer flows

The Orr–Sommerfeld equation was derived for parallel flows. However, real life is characterized by more complex boundary layers such as two–dimensional base flows varying in the streamwise direction, Falkner–Skan profiles accounting for pressure gradient effects, separated flows, three–dimensional boundary layers, curved and/or rotating boundary layers. This field is clearly very wide and it is the most interesting from the engineering point of view. Henningson and Alfredsson [59] describe this topic and provide numerous references, whereas in Reed and Saric [95] a complete and detailed review regarding the stability of three–dimensional boundary layers can be found.

As far as two–dimensional boundary layer is concerned, applying the multiple–scale technique Saric and Nayfeh [101] first computed the neutral curve in the non–parallel flow framework. More recently, the Parabolized Stability Equations (PSE) have been used accounting for non–parallel effects (see Bertolotti *et al.* [10], Herbert [62], Airiau [2] and Pralits *et al.* [94]). Unfortunately depending on the way in which these equations are implemented in a code, numerical stability problems can arise due to the x –step so that stabilization techniques are needed. The neutral stability curve for Blasius, including non–parallel flow corrections, predicts a critical Reynolds number slightly smaller than in the parallel case. As far as the Falkner–Skan profiles are concerned those accelerating are more stable in the sense that Re_{cr} is shifted downstream with respect to the Blasius case, while for those decelerating the opposite is valid.

Here, since we are interested in the boundary layer over a flat plate, the stability of Blasius profile will be considered, but accounting for non–parallel effects. This is obtained

by deriving and solving the boundary layer stability equations using the multiple-scale approach in the non homogeneous case. With respect to PSE, multiple scales do not have numerical stability problems and thus represent a fast and efficient tool to be utilized in transition prediction for the aerodynamic wing design.

1.1.3 Algebraic instability

Before the 1940s, experimental investigators were unable to identify the Tollmien–Schlichting waves. The reason is that transition was caused by other instabilities and growing mechanisms, like an unspecified “direct” nonlinear one that was believed to be driven by large values of environmental disturbances. Since the linear evolution of Tollmien–Schlichting waves was bypassed, the term *bypass transition* identified this phenomenon.

During the 1980s and 1990s, attention was paid to a physical mechanism called *lift-up*, which seemed to be at the origin of this fast growth. The name derives from the fact that low-velocity fluid is lifted up and high-velocity fluid pushed down so that a streak-like spanwise non-uniformity originates in the velocity field close to the wall. Since the boundary layer is elongated with a typical size in the streamwise direction $Re^{1/2}$ times greater than its thickness, the accumulated streamwise-velocity disturbance can be $\mathcal{O}(Re^{1/2})$ times greater than the crossflow disturbance from which it originated.

From the theoretical point of view, this mechanism could nowadays be explained by transient growth due to *algebraic instability*. Basically, the asymptotic exponential behavior, typical of Tollmien–Schlichting waves, may be overshadowed by a significant transient phase of algebraic growth, making the exponential phase unobservable in practice. Ellingsen and Palm [43] and Landahl [74] analyzed the lift-up mechanism in an inviscid-fluid context, finding that, if the flow field has no streamwise variation or contains at least a Fourier component with zero streamwise wavenumber, the streamwise velocity non-uniformity accumulates indefinitely and grows linearly. Hultgren and Gustavsson [65] observed that if viscosity is taken into account an initially inviscid growing phase is followed by a viscous decay. In more recent years, numerical simulations confirmed the nonlinear evolution subsequent to the linear lift-up phenomenon (Henningson *et al.* [60]) stressing the importance of the algebraic growth in the transition process. Trefethen *et al.* [107], using the method of pseudospectra, showed that non-modal mechanisms can originate transient growth leading to transition. In the works cited above, the temporal formulation has been adopted. On the other hand, Luchini [78] showed, in the spatial case, that in a nonparallel boundary layer the algebraic instability grows indefinitely even in the presence of viscosity, whereas in parallel flow the algebraic growth is always eventually followed by viscous decay. Other works followed, finding the optimal initial conditions that produce the maximal algebraic growth in a spatial framework (Luchini [79] and Andersson *et al.* [4])

1.2 Transition scenarios

The inviscid, viscous and algebraic instabilities introduced in the previous sections, properly excited by external disturbances and consequently amplified, can lead to transition. However, a physical mechanism involving the excitation of the instabilities, nowadays called *receptivity* (figure (1.1)), is needed. It represents the way in which external dis-

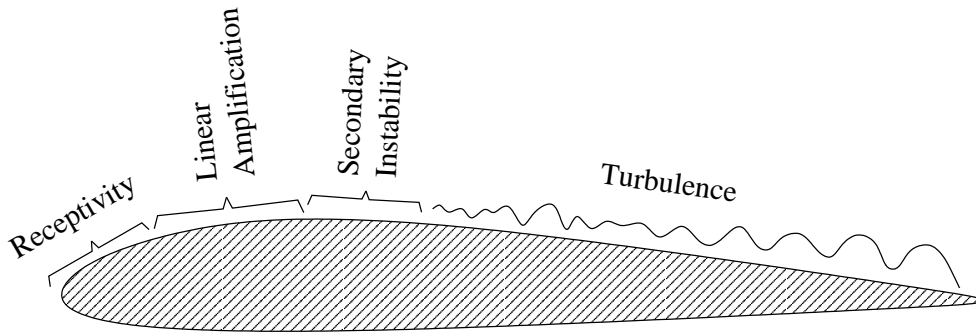


Figure 1.1: Transition scenario: receptivity, linear amplification, secondary instability and turbulence

turbances actually enter the boundary layer and produce a perturbation inside of it. In other words, receptivity states how much the boundary layer is “receptive” (i.e. sensitive) to environmental perturbations. Initially these disturbances may be too small to be observed and they can be actually measured only after a second stage of *linear amplification* (figure (1.1)). The disturbance progressively grows as described by the linear stability theories previously introduced. However, when the disturbance amplitude exceeds a certain threshold, nonlinear effects can become important leading to a saturated nonlinear state. The latter often turns out to be unstable, producing the *secondary instability* (see Herbert [61]). The final breakdown eventually leads to *turbulence*.

1.2.1 Receptivity

Numerous experimental investigators proved that the transition process and the transitional Reynolds number strongly depends on the environmental perturbations. Already Reynolds noticed that roughness or a bad design of the connection between the pipe and the reservoir in his experimental set-up shifted the transition location upstream. This process of entraining disturbances into the boundary layer is nowadays termed receptivity (Morkovin [87], Reshotko [97] and Reed *et al.* [96]).

In the transition process, different kind of instabilities can be excited: Görtler vortices or more generally centrifugal instabilities, in the local inviscid instability framework; instabilities in jets and wakes, related to layer inviscid instabilities; Tollmien–Schlichting waves, typical of layer viscous flow (boundary layer), or finally algebraic instabilities, which explain bypass transition. In all these cases, since the phenomena are different, also the excitation and receptivity process are different.

Here, since our main objectives is the study of fluid dynamic instabilities in a boundary layer, we concentrate only on Tollmien–Schlichting waves and algebraic growth.

1.2.2 Transition due to Tollmien–Schlichting waves

As far as the two-dimensional boundary layer is concerned, it is well known that acoustic disturbances present in the freestream can become resonant with the Tollmien–Schlichting waves, leading to transition, only when associated to another mechanism. This is widely described by Murdock [89], Tam [106], Goldstein [51], Goldstein *et al.* [56], Goldstein and Hultgren [54].

The acoustic wave, in fact, does not have the typical wavelength of the Tollmien–Schlichting waves⁴, so that, in order to have an amplified wave, a “wavelength conversion” mechanism is needed (see the review by Reshotko [97]). This is obtained through a rapid variation of the boundary layer characteristics due, for example, to the boundary layer growth close to the leading edge or to the presence of wall roughness or suction/blowing velocity at the wall.

The basic mechanism that allows this “wave adaptation” is related to the nonlinear interaction between the disturbance originated by the acoustic wave and the one originated by the wall roughness. Their mixing produces a forcing term in the equation for the resonant wave so that Tollmien–Schlichting waves can be excited.

The excited wave can be amplified or not, depending on the growth or decay determined by the linear theory. Experiments actually show a good agreement with linear theory when the amplitude of Tollmien–Schlichting wave is small (order of a few tenths of a percent with respect to the free-stream velocity).

On the contrary, when the unstable wave amplitude u_{rms} is of the order of 1% of the free-stream velocity, two dimensional Tollmien–Schlichting waves become three dimensional (Klebanoff *et al.* [72]). This phenomenon is today believed to be caused by a further instability of the Tollmien–Schlichting waves called secondary instability, which eventually leads to turbulence. For a complete and detailed review regarding physical mechanisms of laminar–boundary–layer transition the reader is referred to Kachanov [67].

1.2.3 Transition due to non-modal disturbance growth

Laminar boundary layers may exhibit a rapid breakdown to turbulence, which cannot be explained by the traditional scenario based on the growth of Tollmien–Schlichting waves. This mechanism is therefore denoted as bypass transition. It represents an alternative amplification phenomenon and can be defined as *transition emanating from linear mechanisms other than exponential instabilities* [59]. Basically, bypass transition is related to transient growth mechanisms and algebraic instabilities.

One of the most important disturbance sources leading to bypass transition is free-stream turbulence (FST). This kind of excitation is of great interest in engineering and practical applications, especially for transition prediction on turbine blades or on airplane wings, and more generally for wind-tunnel tests for which it is desirable to reduce the FST level in order to reproduce the free-flight conditions.

Experiments carried out by Matzubara and Alfredsson [81], regarding the effects of FST on the boundary layer past a flat plate, show an initial growth proportional to the square root of the streamwise coordinate, in accordance with theoretical results by

⁴in the incompressible case, the acoustic disturbance wavelength is infinity

Luchini [79]. Moreover, also the profile of u_{rms} (the streamwise velocity disturbance) experimentally obtained at different streamwise stations is in agreement with the theoretical profiles computed by Luchini [79] and Andersson *et al.* [4], with the difference that u_{rms} reaches the asymptotic free-stream value in the experiments whereas is zero in computations (where the boundary conditions at infinity are homogeneous).

The same experiments, by using flow visualizations and hot-wire measurements, prove that a boundary layer subjected to FST develops unsteady streaky structure with regions of high and low streamwise velocity. The following breakdown of these streaky structures seems to be associated with the secondary instability eventually leading to turbulence.

Algebraic instability studies can therefore actually explain bypass transition. A wide overview concerning this topic can be found in Henningson and Alfredsson [59] and references therein.

1.3 Transition prediction

Since different kinds of transition processes can occur leading a laminar flow to turbulence (those presented in the previous sections are just some of them), it may seem too optimistic to expect simple but still accurate methods for transition prediction. In principle, direct numerical simulation (DNS) or large eddy simulation (LES) could provide the transition location for simple flow. However, the cost of such computations for engineering applications is prohibitive and therefore more simple methods should be provided. Since these simpler approaches are usually based on empirical correlations, they are not aimed at modeling any physical process leading to transition, but just at providing an acceptable prediction of transition location.

Several limitations characterize this kind of methods. For instance, they cannot take into account phenomena like transient growth or secondary instability and the external disturbances, when considered, are usually introduced in a very rudimentary way, very far from the receptivity process.

1.3.1 Correlation methods

Very simple transition prediction methods do not require stability computations but are based on empirical correlations.

Cebeci and Smith [22] proposed a relationship between R_θ and R_x at transition. The former is defined as $R_\theta = U_\infty \theta / \nu$ where U_∞ is the free-stream velocity, θ is the momentum thickness and ν the fluid kinematic viscosity, whereas the latter as $R_x = U_\infty x / \nu$ where x is the streamwise location. The equation which relates R_θ and R_x at transition is

$$R_\theta = 1.174 \left(1 + \frac{22400}{R_x} \right) R_x^{0.46} \quad (1.3.1)$$

If R_θ and R_x are determined solving the boundary layer equations starting from the leading edge and then plotted together with the curve $R_\theta = R_\theta(R_x)$ obtained by (1.3.1), the point of intersection gives the location of transition onset.

Another simple method, reported by Cebeci and Cousteix [21], was proposed by Granville. It relates R_θ and $R_{\theta_{cr}}$ ($R_{\theta_{cr}}$ is R_θ at the critical point “cr” of instability onset) by the expression

$$R_\theta - R_{\theta_{cr}} = 375 + e^{6.1+55\lambda_\theta} \quad \text{with} \quad -0.04 \leq \lambda_\theta \leq 0.024 \quad (1.3.2)$$

where

$$R_{\theta_{cr}} = \begin{cases} \frac{54.2124}{H(H-2.48)} + \frac{31.6}{H} & \text{for } H > 2.591 \\ \frac{520}{H} + \frac{2.5 \cdot 10^6}{H} \left(\frac{1}{H} - \frac{1}{2.591} \right)^{1.95} & \text{for } H \leq 2.591 \end{cases}$$

H is shape factor ($H = \delta^*/\theta$, with δ^* displacement thickness and θ momentum thickness) and

$$\lambda_\theta = \frac{4}{45} - \frac{1}{5} \frac{R_\theta^2 - (U_\infty/U_{cr})R_{\theta_{cr}}^2}{R_x - U_\infty/U_{cr})R_{x_{cr}}^2}$$

Basically, the method works in the following way: boundary layer computations are performed marching in the streamwise direction x . H is known and $R_{\theta_{cr}}$ can be computed, so that $\Delta = R_\theta - R_{\theta_{cr}}$ is calculated. On the other hand, λ_θ can be computed and $R_\theta - R_{\theta_{cr}}$ evaluated via (1.3.2): when this difference equals Δ transition is considered reached.

This method was later modified in order to account for the influence of the free-stream turbulence level T_u :

$$R_\theta - R_{\theta_{cr}} = -206e^{25.7\lambda_\theta} [\ln(16.8T_u) - 2.77\lambda_\theta]$$

1.3.2 e^N method

One of the main drawbacks of the previous methods is that the stability equations are not taken into account, but only empirical correlations are used. On the contrary, e^N method is based on the linear behavior of instability waves as described by the Orr–Sommerfeld equation. It has been successfully applied to a variety of flows revealing a fairly accurate transition prediction for simple cases (boundary layer past a flat plate) or even more complex flows.

This method was developed independently by van Ingen and Smith & Gamberoni in 1956. The idea was to find a correlation between the amplification of linear waves with the onset of transition. It is obviously clear that before transition is reached, the waves become nonlinear so that e^N method cannot take into account the physics of these nonlinear processes.

Transition is assumed to occur when the wave amplitude A is e^N times the wave amplitude at the beginning of amplification A_I , corresponding to the first neutral point of the neutral stability curve in the ω – R plane. The factor N is defined as

$$N = - \int_{x_I}^x \alpha_i(x') dx' \quad (1.3.3)$$

where x_I is the streamwise location corresponding to the first neutral point and α_i is the imaginary part of the wavenumber $\alpha = \alpha_r + i\alpha_i$. At the neutral point $\alpha_i = 0$.

In a low disturbance environment, transition is experimentally observed when the factor N is between 8 and 11. This feature was first noticed by the people who proposed this method and that is the reason why it is the main transition prediction technique used for wing design in aeronautical industry.

One of the limitations is that e^N method does not account for the amplitude of the disturbance before the start of the amplification, i.e. upstream of the first neutral point. This basically means that the receptivity mechanism is completely neglected. In order to overcome this drawback, Mack suggested a correction for N which consider the presence of free-stream turbulence

$$N = -8.43 - 2.4 \ln(T_u)$$

and gives reasonable transition locations in the range $0.1\% < T_u < 2\%$.

In order to find the streamwise transition point, N is determined from linear stability computations, as a function of the streamwise location x at a fixed frequency, applying the definition (1.3.3). When the value of $N(x)$ is equal to a value previously decided (usually between 8 and 11, or computed assuming a certain turbulence intensity T_u), the corresponding streamwise location x is considered the transition location.

This method can be applied to parallel flows or to nonparallel flows, allowing to account for boundary layer growth and nonparallel effects in complex boundary layers.

1.3.3 H - R_x method

This method represents a useful shortcut for transition prediction in a wide class of boundary-layer flows, being simple to use and a good substitute to the e^N method, previously described, for two-dimensional and axial symmetric flows with pressure gradient, suction and wall heating or cooling. The N factor at transition is assumed to be with $N = 9$ (see Cebeci and Cousteix [21]). The simple relationship characterizing this method is between H and R_x :

$$\log [R_x e^9] = -40.4557 + 64.8066H - 26.7538H^2 + 3.3819H^3; \quad 2.1 < H < 2.8 \quad (1.3.4)$$

where H and R_x are respectively the shape factor and the Reynolds number as previously defined.

This method, like those described in section 1.3.1, is not based on stability calculations but only on boundary layer computations. However, it differs from the other correlation methods because they are strictly for two-dimensional incompressible flows and are not applicable to two-dimensional flow with heating and suction or axial symmetric flows, whereas H - R_x method can be used in such situations.

1.4 Transition control

From the previous sections, it should be quite clear that delaying transition from laminar to turbulent flow has many obvious advantages. Actually, the ability of manipulating a flow field actively or passively, in order to obtained a desired change, has a great

technological importance because of the potential benefits achievable. Depending on the Reynolds number, the skin-friction drag in a laminar flow can be an order of magnitude smaller than in turbulent conditions (Gad-el-Hak [46]), implying the savings of a great amount of money in fuel costs for land, air and water vehicles.

Flow control aims not only at transition delay but also at more general goals: separation postponement, lift increase, drag reduction, turbulence control, relaminarization and noise suppression. In aerodynamics, flow control usually means the ability to avoid transition, separation or turbulence; on the contrary, in other fields (e.g. chemistry) high and fast mixing is required and therefore transition, separation and turbulence are desirable.

Control strategies can be classified in different ways. One possibility is to consider the energy or power required in order to control the flow field, obtaining a first main division in *passive* or *active* control. In the former case no energy is needed (see the successful development of NACA 6-series airfoils for which transition was delayed just by shaping the wall in a specific way), in the latter energy is required. Active control can be further divided into open-loop or reactive. Open-loop control consists in the application of steady or unsteady energy input without regard to the particular state of the flow. For this reason, no sensors are required. On the other hand, when a variable characterizing the flow field is measured and used in order to change the flow itself, reactive control is applied. Therefore, reactive control is a special class of active control where the control input is continuously adjusted based on measurements of some kind.

This field is clearly very wide, however here we briefly discuss only some possibilities in order to delay transition. On the contrary, a wide overview of the subject of flow control is provided by Gad-el-Hak *et al.* [48], Gad-el-Hak [46], Gad-el-Hak [47] and the numerous references therein.

As far as boundary layer transition is concerned, apart from the previous subdivision in *passive* or *active* control, another possible classification can be based on whether the control technique directly modifies the shape of the base flow, making it more stable, or directly influences the perturbation generated inside the boundary layer, avoiding its amplification. Suction at the wall, shaping, wall heating/cooling, wall motion, stream-wise or spanwise pressure gradient can be grouped in the former class of techniques, whereas wave cancellation belong to the techniques that directly act on the disturbance.

In the following sections some examples of transition control methods are reported.

1.4.1 Suction at the wall

The application of wall suction was the first method historically introduced in order to delay boundary-layer transition. It was used by Prandtl in 1904 to prevent flow separation from the surface of a cylinder, becoming the demonstration that withdrawing near-wall fluid can actually be feasible (at least in lab experiments).

The main effect of suction at the wall is the modification of the velocity profile in the neighborhood of the surface, implying the change of the stability characteristics of the flow. Additionally, suction inhibits the growth of boundary layer and thus the critical Reynolds number based on boundary-layer thickness may never be reached.

Although laminar flow can be maintained to extremely high Reynolds numbers, pro-

vided that enough fluid is sucked away, the goal is to reach the delay of transition with the minimum suction flow rate, since this will reduce the power necessary and the momentum loss due to suction.

The theoretical treatment of the problem is considerably simplified by assuming continuous and uniform suction (for instance through a porous wall). In fact, under the further hypothesis of suction weak enough so that the flow outside the boundary layer is not affected by the loss of mass at the wall, the asymptotic velocity profile inside the boundary layer is an exact solution of the Navier–Stokes equations and is expressed as

$$U(y) = U_\infty \left[1 - \exp\left(-\frac{|v_w|y}{\nu}\right) \right]$$

where v_w is a negative constant representing the value of the uniform suction velocity at the wall (see Schlichting [102]).

Suction may be applied on porous surfaces, perforated plates or slots carefully actuated. It is of course structurally impossible to make the whole surface of an aircraft wing of porous material. On the other hand, the surface smoothness and rigidity of the wings could be negatively affected by the use of perforated plates. Finally, slots are expensive to fabricate accurately and the mass–flow rate associated to them could result in other instabilities, with separations and backflows.

Another problem is related to the protection of the delicate suction surface of an aircraft wing from insect impacts, ice formations or other small particles. Moreover, suction is less suited for underwater vehicles because of the suspended ocean particulate (Gad–el–Hak [46]).

Delaying transition using suction at the wall seems therefore to be useful in experiments, whereas more difficulties are encountered in industrial applications (airplanes, submarines and other vehicles) due to problems related to maintainability and reliability of suction surfaces. Moreover, as in all the other active techniques, if the gain in drag reduction obtained through transition delay is smaller than the effort necessary to reach it, the control has no practical relevance.

1.4.2 Shaping

Shaping is probably the simplest method in order to delay laminar–to–turbulent transition. It basically involves the use of suitably shaped bodies to manipulate the pressure distribution. It was born as a passive technique, in order to find the “best aerodynamic shape” for a body moving in a fluid, but it can be used also as an active control method if the surface is modified via large–scale actuators.

Choosing the best shape of a body to prevent separation and to delay transition is quite an old art. However, the stabilization of a boundary layer over an airplane wing by pushing the longitudinal location of the pressure minimum as far as possible downstream dates 1930s and led to the successful development of NACA 6–series airfoils.

For a lifting surface, beyond the location of pressure minimum, the adverse pressure gradient has negative effects on the boundary layer, leading directly to separation or first to transition and then to turbulence, depending on the shape of the body, angle of attack, Reynolds number, surface roughness and other factors. The main goal of

transition delay via body shaping is therefore to maintain attached and laminar flow in the adverse pressure gradient region as long as possible.

Factors that limit the utility of this technique include performance degradation at angles of attack different from the one for which the shape was optimized, insect impact, dirty particulates, ice formation.

The main advantage is that it is a passive control technique and does not require power support.

1.4.3 Wave cancellation

An alternative approach to the previously proposed methods is wave cancellation.

This technique is not based on the modification of the boundary layer profile, but aims at acting directly on the perturbation. If the frequency, orientation and phase angle of the dominant element of the spectrum of a linear growing disturbance is detected, a control system and appropriate located disturbance generators may then be used to produce a desired cancellation or suppression of the detected disturbance. Wave cancellation is feasible only when the disturbances are still relatively small, their growth is governed by linear equations and the principle of superimposition is still valid.

In an early experiment, Milling [85] showed the possible application of this approach in a water tunnel. He excited the Tollmien–Schlichting waves by a vibrating ribbon at one station on a flat plate and by introducing another wave at a downstream location, in opposite phase with respect to the first, caused the transition location to move beyond the plate's end.

The same principle of wave superimposition can be applied using wall heating and cooling, plate vibration or periodic suction and blowing (Cathalifaud and Luchini [20]).

The transition delay achieved by active wave cancellation is modest, typically a factor of two or less increase in the transitional Reynolds number based on the distance from the leading edge can be reached. Moreover, delaying transition using this technique would require an extensive array of disturbance detectors and generators as well as a prohibitively complicated control system that could cancel both the primary and residual disturbance spectra. Significant delay transition is more readily achieved via the stabilizing techniques described in sections 1.4.1 and 1.4.2.

Chapter 2

Boundary layer receptivity to external disturbances using multiple-scale approach

2.1 Introduction

The receptivity problem has been receiving large attention in the last decades because it relates the response of the boundary layer to external disturbances and thus it allows the transition prediction criteria to be improved by accounting for the environmental conditions. The term “receptivity” was introduced by Morkovin in the late 1960s [87] in order to describe the physical phenomenon by which external perturbations enter the boundary layer. However, this represents only a *qualitative* idea. An effort has recently been made in order to define the *quantitative* response of the boundary layer relating the final amplitude of the excited wave to the exciting external disturbance amplitude. The typical scenario leading to transition is the following. (I) A perturbation (acoustic wave, vorticity wave, wall vibration, wall roughness, etc.) is introduced in the base flow by the receptivity mechanism. The disturbance follows the evolution determined by the linearized Navier–Stokes equations so that (II) a linear amplification or decay is found. If the amplitude of the excited wave is greater than a certain threshold, (III) non-linear breakdown can lead to transition from laminar to turbulent flow. If this amplifying mechanism is considered exponential, the instability is monitored by the exponential growth of Tollmien–Schlichting waves. However, the latter scenario can be bypassed by another strongly amplifying mechanism, leading to the definition of bypass transition as *transition emanating from linear mechanisms other than exponential instabilities* [59]. Basically, bypass transition regards transient growth mechanisms and algebraic instabilities. From the depicted scenarios, it is clear that transition strictly depends on the environmental perturbation sources. Moreover, the external disturbances usually enter the boundary layer via non homogeneous initial or boundary conditions. Unfortunately, current transition prediction criteria are based on the solution of the homogeneous Orr–Sommerfeld equation which is an eigenvalue problem and simply describes the stability characteristics of the boundary layer, without relating them to the free-stream perturbations.

The goal of a receptivity study is therefore to improve the transition prediction methods extending the transition criteria to include the free-stream disturbance environment. In other words, it allows us to relate the amplitude of the instability wave produced inside the boundary layer (Tollmien–Schlichting waves) to the physical amplitude of the external exciting disturbance.

2.1.1 Different receptivity configurations

Different receptivity configurations have been studied and can be found in the literature. As far as Tollmien–Schlichting waves in a two-dimensional incompressible boundary layer past a flat plate are concerned, the typical external disturbances can be acoustic waves, free stream vorticity waves or wall vibrations. For all of them, even if the temporal frequency is the same as that of TS waves, the typical wavelength is much greater than the TS one. This means that such a kind of disturbance cannot create any coupling with the boundary layer instability waves and energy cannot be transferred to the unsteady perturbation. In other words, these kinds of disturbance are not resonant with the TS waves and a “wavelength conversion” mechanism is needed, as Reshotko [97] recognized, in order to allow the “adaptation” of the exciting wavelength to the TS one. This wavelength–conversion effect can be provided by the growth of the boundary layer near the leading edge or every time a rapid variation of the wall boundary conditions produces a fast adaptation of the boundary layer (typically in the neighborhood of a surface variation like wall roughness). Therefore two main receptivity configurations can be identified: (a) leading edge receptivity and (b) sudden boundary layer forced adjustment receptivity.

For case (a), the receptivity to acoustic waves or vorticity waves have been widely analyzed. Ackerberg and Philips [1] provided the first analytical studies concerning the coupling between the acoustic wave and the boundary layer growth in the leading edge region, while later on Murdock [89], Tam [106], Goldstein [51], Goldstein *et al.* [56], Goldstein and Hultgren [54] produced the first numerical results using asymptotic methods based on the assumption of infinite Reynolds number. More recently, certain configurations were solved by direct numerical simulation (DNS) by Casalis *et al.* [18]. From the experimental viewpoint, Leehey and Shapiro [75] provided a study on the effect of sound excitation on the leading edge boundary layer region. As far as the vorticity wave excitation is concerned, less work can be found in the literature. Probably the first experiments were those by Kachanov *et al.* [69] who showed that if the vortex core generated by a vibrating ribbon passes close to the leading edge of a flat plate, TS waves are observed. Heinrich *et al.* [58] applied asymptotic theory to study the receptivity for a range of free-stream disturbances, including convected gusts. Butter and Reed [16] numerically investigated the receptivity to free-stream vorticity of the boundary layer over a flat plate with an elliptic leading edge by solving the Navier–Stokes equations. Later, Liu *et al.* [77] studied the leading-edge receptivity of two-dimensional and three-dimensional airfoils to free-stream vortical disturbances by incompressible DNS as well. Finally, Hammerton and Kerschen [57] considered the effect of the nose of a body in the case of a parabolic leading edge using asymptotic methods supplemented by numerical results for the incompressible flow.

In the second case (*b*), a wide range of configurations that produce a sudden change in the boundary layer can be mentioned, such as surface irregularities, humps, steps, or changes in boundary conditions due to suction, blowing and heating. A first classification is in localized receptivity, where the sudden change in the boundary conditions is single, local and isolated (single hump, single blow or suction strip), and distributed receptivity where a sequence of the previous humps or strips is studied. In both cases, a further subdivision can be made in receptivity to acoustic wave, vorticity wave and excitation coming from the wall (vibrating ribbon problem or wall rigid-vibration) to different possible sudden boundary layer forced adjustment receptivity mechanisms.

For the problem of receptivity to acoustic wave, notable experimental contributions are those by Kachanov [69] and Saric *et al.* [100]. From the theoretical point of view, Goldstein [52] analyzed a sudden change in the wall geometry using the linearized triple-deck approach. In the same year, Ruban [98] stressed the important role of the surface geometry on acoustic receptivity. Goldstein and Hultgren [53] considered a sudden change in the surface curvature. Bodonyi *et al.* [15] extended the linear analysis of Goldstein to a roughness height which requires the nonlinear triple-deck approach providing a numerical study of the problem. Finally, Tadjfar and Bodonyi [105] dealt with a three-dimensional hump by applying non-linear triple-deck theory and solving the equations numerically.

Parallel to the asymptotic analysis, the receptivity problem to acoustic waves has been attacked using the Orr-Sommerfeld approach. Crouch [33] and Choudhari and Streett [29] independently developed the same approach to the receptivity problem obtaining a linear dependence of the unsteady wave amplitude on the roughness height. The advantage, with respect to the asymptotic analysis, is that the Reynolds number and the frequency are no more related but can be chosen separately. This allows a finite Reynolds number study. The limitation of the linear approach with respect to the roughness height, was overcome by Nayfeh and Ashour [92]: they used an interacting boundary layer scheme for the base flow obtaining very good agreement with Crouch [33] and Choudhari and Streett [29] for the low roughness heights and with the experimental results by Saric *et al.* [100] for greater heights. This approach allows the localized receptivity problem to be solved for finite roughness heights at finite Reynolds numbers.

For the receptivity to acoustic wave, in addition to roughness, also suction and blowing have been considered: Choudhari and Kershen [28] focused the attention on roughness and suction in three-dimensional configurations using an Orr-Sommerfeld approach. Bodonyi and Duck studied the acoustic receptivity to steady wall suction applying the triple-deck theory. Finally, Crouch and Spalart [37] compared their Orr-Sommerfeld approach to DNS computations.

A less extensively studied configuration is the receptivity due to rapid static pressure variation or to marginally separated flows (Goldstein *et al.* [55] and Goldstein and Hultgren [54]); while Asai *et al.* [6] performed DNS computations on a descending step.

As far as the non localized receptivity to acoustic waves is concerned, Crouch [34] [35] considered a periodic roughness having a sinusoidal behavior, while Choudhari [26] studied a periodic suction configuration.

The problem of receptivity to vorticity waves was first studied in order to understand the effect of the turbulence present in the free-stream flow. It was modeled as a

vorticity wave which interacts with sudden boundary layer change creating a coupling between TS waves and vorticity waves (Kerschen [71]). Kerschen [70] and Choudhari and Kerschen [27] studied respectively the two-dimensional and three-dimensional vorticity waves and Duck *et al.* [42] modeled the problem introducing a four-deck asymptotic expansion.

Finally, non localized receptivity to vorticity waves was approached by Crouch [36].

A very good overview and references concerning the problem of receptivity to convected free-stream disturbances (i. e. acoustic waves or vorticity waves) can be found in Diets [39].

Up to this point of our overview, we considered only the receptivity to an external forcing coming from the free-stream flow. On the contrary, an unsteady forcing source can be produced at the wall and historically this was the first problem studied. The typical configuration, in this case, is the one of the vibrating ribbon experimentally investigated by Schubauer and Skramstad [103] in the late forties. A localized unsteady periodic exciter was positioned at the wall along a line and its effect was to excite a spatially evolving wave inside the oncoming Blasius boundary layer. The first theoretical results concerning this experiment were given by Gaster [49] who verified Schubauer and Skramstad's observations that in the long-time limit the ribbon excites the spatial eigenmodes of the flow at its own frequency. More recently, Ashpis and Reshotko [7] discussed the theoretical aspects related to the Bromwich contour, Gaster and Sengupta [50] numerically treated this kind of problem and Sengupta *et al.* [104] studied the receptivity approach examining the time dependent response of the Blasius boundary layer to small wall excitations localized in space. The excitation of instability waves in wall boundary layers with adverse pressure gradients by various types of Dirac sources was investigated by Michalke and Neemann [84] who extended the previous works to the boundary layers close to separation since they are more unstable than the Blasius one. The three-dimensional receptivity mechanism related to the surface perturbations in two-dimensional boundary layers have been much less investigated. Michalke [82] first analyzed the receptivity of axisymmetric boundary layers due to excitation by Dirac point source at the wall and gave numerical results for velocity profiles with inflection point. Michalke [83] also treated the excitation of a three-dimensional wavetrain by Dirac point source at the wall and its growth in decelerating laminar boundary layers using the linearized theory and the locally-parallel flow approximation. Here we do not extend the review to the three-dimensional case neither to the swept-wing boundary layers, but very good references can be found in Kachanov [68].

As far as it is known to the authors, the receptivity to structural vibration is not so easily found in literature. Chiu *et al.* [25] considered the receptivity to transverse structural vibration on the leading edge and compare their experimental results with calculations performed by Chiu and Norton [24].

2.1.2 Possible modeling approaches

The receptivity problem can be analyzed using different theoretical approaches: asymptotic expansions based on high Reynolds number, Orr-Sommerfeld formulation, parabolized stability equations or direct numerical simulation (DNS). All these techniques can

be coupled with an adjoint formulation in order to obtain the sensitivity of the physical phenomenon to a certain excitation cause.

The first studies on receptivity made use of the triple-deck modeling. Goldstein [51] and [52], Goldstein *et al.* [55], and Goldstein and Hultgren [54] considered the solution as the sum of a steady base flow, a steady perturbation due to the presence of the wall and an unsteady perturbation due to the acoustic wave. If the roughness height is small, the equations for the perturbation can be linearized obtaining ([52]) an analytical expression for the receptivity coefficient. This coefficient is independent of the wall shape, but the perturbation wave amplitude contains the Fourier transform of the wall geometry. In general, the asymptotic approach reduces the two degrees of freedom Re (Reynolds number) and F (dimensionless frequency) to only one, $S_0 = FRe^{3/4}$, losing the possibility of computing the receptivity for a finite Reynolds number at different frequencies. If the roughness height is large and a linearization is not allowed the receptivity problem can be numerically solved, as Bodonyi *et al.* [15] did for the two-dimensional case via triple-deck theory. The steady perturbation was computed following a nonlinear approach, while the unsteady perturbation was still dealt with linearly. The three-dimensional finite height hump was studied by Tadjfar and Bodonyi [105] using a triple-deck approach. Another asymptotic approach was the double-deck one used by Bessiere [11]: instead of three different regions he dealt with only two and solved the problem for finite heights. A set of coupled equations between the two decks was numerically solved and the results showed a good agreement with the DNS performed by Casalis *et al.* [18] including the deviations from the linear behavior. Bessiere considered also a wall roughness coupled with vibration leading to unsteady humps like the ones examined by Duck [41]. The main disadvantage of all the asymptotic methods is that they work well only for very high Reynolds numbers, in the vicinity of the lower branch and for specific dimensions of the hump which are on a scale specified in the formulation.

As far as the Orr–Sommerfeld approach is concerned, in the same year (1992) and independently, Crouch [33] and Choudhari and Streett [29] developed a study of the acoustic receptivity. They considered a locally-parallel Blasius boundary layer over a flat plate, a two-dimensional localized change in the surface characteristic and an acoustic wave in the free-stream. The solution was subdivided in the Blasius boundary layer $v_0(y)$ independent of x , in an unsteady flow $v_\epsilon(x, y, t)$ due to the interaction between the boundary layer and the unsteady acoustic wave (Stokes flow), in a steady flow $v_\delta(x, y)$ due to the interaction between the wall disturbance and the boundary layer and an unsteady flow $v_{\epsilon\delta}(x, y, t)$ due to the interaction of the previous ones. The latter is the resonant wave. The boundary conditions are moved from the location at the wall shape $y = \delta h(x)$ to $y = 0$ using a Taylor expansion. They determined the instability wave amplitude as the residue corresponding to the appropriate pole of the Fourier transform solution. These analyses are valid for finite Reynolds numbers both near and away from branch I, in contrast with the asymptotic analysis valid only near the branch I. In addition, they allowed the study of the frequency effects at different Reynolds numbers. The accuracy of the approach of Crouch [33] and Choudhari and Streett [29] is limited by the assumptions of small hump heights and locally parallel mean flow. Actually, their results agree with the experimental results of Saric *et al.* [100] only for small hump heights. In order to solve the problem of the linearity of the amplitude TS wave with

the roughness height, Nayfeh and Ashour [92] proposed an alternative approach. The base flow was calculated by using interacting boundary layers (IBL) thus accounting for viscous/inviscid interactions and separation bubbles. The unsteady motion was assumed to be the sum of a Stokes wave and a traveling wave. The latter is governed by a set of non-homogeneous partial differential equations with variable coefficients. The inhomogeneity reflects the interaction between the Stokes flow and the steady disturbance caused by the roughness element. The solution of this set of equations is projected onto quasi-parallel eigenmode by using the quasi-parallel adjoint. The result is a first-order complex-valued non-homogeneous ordinary differential equation governing the amplitude and phase of the traveling wave. The results were in good agreement with the experimental results of Saric *et al.* [100] for all the tested hump heights at the two tested sound pressure levels.

Parabolized stability equations (PSE) can incorporate non-homogeneous initial and boundary conditions as numerical solutions of the Navier–Stokes equations do, but they can be obtained at a modest computational expense. For this reason they have been applied for receptivity studies and transition prediction, accounting also for non-parallel effects: Bertolotti *et al.* [10], Herbert [62], Airiau [2] and Pralits *et al.* [94]. Unfortunately, depending on the way in which the equations are implemented in a code, numerical stability problems can arise due to the x -step and a lack of convergence is encountered as the computational step tends to zero so that special stabilization techniques are required.

A more direct approach is the DNS which does not use any modeling and solve directly the unsteady Navier–Stokes equations. Casalis *et al.* [18] [19] studied the sensitivity of the TS wave amplitude to the acoustic frequency, to the hump height and hump length. The results are in good agreement with the experimental results by Saric *et al.* [100] for all the heights and with the linear Goldstein approach [52] for small heights. The numerical results from DNS confirm also the experimental results of Kobashi *et al.* [73] for the influence of the hump length.

For all the previous cases it is possible to introduce an adjoint formulation. The aim is to obtain the sensitivity of the TS wave amplitude to modifications of the base flow or boundary conditions without repeating the calculations for different initial or boundary conditions. This is done for the flat plate boundary layer receptivity coupling the adjoint formulation with the Orr–Sommerfeld approach by Hill [63] and for the Görtler vortices by Luchini and Bottaro [80] using a backward-in-time approach. It is possible to combine the regular PSE solutions with its adjoint: in contrast with the regular PSE, the calculation is marching in upstream direction (Herbert [62], Airiau [2] and Pralits *et al.* [94]).

2.1.3 Multiple-scale technique

The distinguishing feature of boundary layer flows is that variations of fluid dynamic quantities are much faster in the wall-normal direction than in the streamwise one. This implies that the results obtained for a boundary layer, with parallel-flow assumptions (i.e. velocity independent of the streamwise coordinate x , and v -component equal to zero), can be generalized accounting for the weak dependence on x . The basis of such a generalization is the multiple-scale technique: it is a fundamental mathematical method

for the asymptotic analysis applied in physics every time it is necessary to solve a problem which differs from an already solved one just because certain parameters, previously constant, are replaced by slowly varying functions. An extended explanation of this method and its applications to dissipative and dispersive phenomena can be found in Whitham [109] and Bender and Orszag [9]. The condition for applying multiple scales is the existence of two separated scales. This characteristic allows to write the solution as the product of a slow and a fast varying function. Originally one-dimensional, multiple scales can be applied to multi-dimensional and nonlinear problems. In the linear case, if the fast varying scale produce a constant coefficients equation, the fast contribution to the solution has an exponential behavior. In the cited reference book, the solution $y(x)$ is supposed to behave as $y(x) \sim A(x)e^{\phi(x)/\tilde{\epsilon}}$ where $\tilde{\epsilon}$ is a small parameter accounting for the slow variation (for example the boundary layer thickness) and the exponential part $e^{\phi(x)/\tilde{\epsilon}}$ comes from the consideration that both dissipative and dispersive phenomena are characterized by exponential behavior [9]. The function $A(x)$ represents the slowly varying amplitude, that can be expanded in series of the small parameter $\tilde{\epsilon}$ leading to different problems at different orders with respect to $\tilde{\epsilon}$. In the appendix, the one-dimensional version of multiple scales, better known as WKB approximation (after Wentzel, Kramers and Brillouin), is reported in the homogeneous case in order to show how the problem is formulated.

As far as the fluid dynamic field is concerned, Saric and Nayfeh [101] applied the multiple-scale technique to study the stability of a two-dimensional incompressible boundary layer, allowing the possibility to account for nonparallel effects. Later, De Matteis *et al.* [38] used the multiple scales in order to analyze the stability of three-dimensional incompressible boundary layers.

Compared to the receptivity approaches previously described, this technique can be more preferable for the study of boundary-layer receptivity, because of different reasons. First, it allows to include nonparallel effects due to boundary-layer growth, which become very important especially when the boundary layer is more complex than the one past a flat plate (an accelerating or decelerating boundary layer due to a streamwise pressure gradient or the boundary layer on a swept wing with induced cross-flow). Second, in contrast with asymptotic methods like triple deck, which work for very high Reynolds numbers where the flow in practical application is already turbulent, multiple scales can be applied at finite Reynolds numbers, allowing the parametric study of the influence of both Reynolds number and frequency. From the numerical point of view, multiple scales do not have numerical stability problems and are not computationally expensive, so that they can be included in industrial codes for transition prediction used, for example, in real cases for wing design. The last, but not the least, consideration is that the problem we are dealing with is resonant, requiring a singular perturbation technique, that multiple scales can provide.

2.1.4 Motivations for the present work

From the previous review concerning the possible mechanisms that can excite the Tollmien-Schlichting waves in a two-dimensional incompressible laminar boundary layer, it can be viewed that the main excitation sources are acoustic waves, vorticity waves and wall vi-

brations. However, their temporal frequency and spatial wavelength are not in the same range as those of the Tollmien–Schlichting waves, so that resonance can be reached only via an “adaptation mechanism”. The latter is easily produced by the presence of wall roughness. The aim of the present work is therefore a detailed investigation concerning the possible disturbance interactions leading to unstable waves resonant with those of Tollmien–Schlichting. Acoustic waves and vorticity waves interacting with wall roughness are found in cited works, while it seems that not much attention has been paid to the problem of structural vibration. On the contrary, wall vibration is a very common environment for an airplane wing or for the blade of a turbo-machine so that it could be very interesting investigating what happens to the Tollmien–Schlichting waves excited by a vibrating wall and developing in a Blasius boundary layer. What we expect is that the wall vibration plays the role of the acoustic wave for the receptivity to sound. As far as the methodology is concerned, the multiple-scale approach is introduced in the non homogeneous case. The interactions here analyzed are between an acoustic wave and wall roughness, between a vorticity wave and wall roughness, between a wall vibration and wall roughness and between acoustic wave and vorticity wave.

2.2 Problem formulation

The starting point for the analysis is the system of Navier–Stokes equations for an incompressible flow, written in dimensionless form:

$$\begin{aligned} \hat{u}_{\hat{x}} + \hat{v}_{\hat{y}} + \hat{w}_{\hat{z}} &= 0 \\ \hat{u}_{\hat{t}} + \hat{u}\hat{u}_{\hat{x}} + \hat{v}\hat{u}_{\hat{y}} + \hat{w}\hat{u}_{\hat{z}} &= -\hat{p}_{\hat{x}} + R^{-1}(\hat{u}_{\hat{x}\hat{x}} + \hat{u}_{\hat{y}\hat{y}} + \hat{u}_{\hat{z}\hat{z}}) \\ \hat{v}_{\hat{t}} + \hat{u}\hat{v}_{\hat{x}} + \hat{v}\hat{v}_{\hat{y}} + \hat{w}\hat{v}_{\hat{z}} &= -\hat{p}_{\hat{y}} + R^{-1}(\hat{v}_{\hat{x}\hat{x}} + \hat{v}_{\hat{y}\hat{y}} + \hat{v}_{\hat{z}\hat{z}}) \\ \hat{w}_{\hat{t}} + \hat{u}\hat{w}_{\hat{x}} + \hat{v}\hat{w}_{\hat{y}} + \hat{w}\hat{w}_{\hat{z}} &= -\hat{p}_{\hat{z}} + R^{-1}(\hat{w}_{\hat{x}\hat{x}} + \hat{w}_{\hat{y}\hat{y}} + \hat{w}_{\hat{z}\hat{z}}) \end{aligned} \quad (2.2.1)$$

where the hat $\hat{\cdot}$ indicates dimensionless quantities. The velocities are made dimensionless with the outer velocity U_{∞}^* (the starred quantities \cdot^* are dimensional), the streamwise, wall-normal and spanwise coordinates x , y and z with respect to a certain length $\delta_0^* = \sqrt{x_0^* \nu^* / U_{\infty}^*}$, where x_0^* is the first neutral point of the neutral curve, and time with respect to $\delta_0^* / U_{\infty}^*$. The Reynolds number is therefore defined as

$$R = \frac{\delta_0^* U_{\infty}^*}{\nu^*} = \sqrt{\frac{x_0^* U_{\infty}^*}{\nu^*}} = \sqrt{Re_{x_0^*}}$$

The Navier–Stokes equations (2.2.1) require three boundary conditions at the wall and three at infinity. Usually, in the former case the velocity field is specified, while in the latter the \hat{v} component is free and \hat{u} , \hat{w} and \hat{p} specified :

$$\begin{aligned} \hat{u} = \hat{u}_0 \quad \text{at} \quad \hat{y} = 0 & \quad \hat{u} = \hat{u}_{\infty} \quad \text{for} \quad \hat{y} \rightarrow \infty \\ \hat{v} = \hat{v}_0 \quad \text{at} \quad \hat{y} = 0 & \quad \hat{w} = \hat{w}_{\infty} \quad \text{for} \quad \hat{y} \rightarrow \infty \\ \hat{w} = \hat{w}_0 \quad \text{at} \quad \hat{y} = 0 & \quad \hat{p} = \hat{p}_{\infty} \quad \text{for} \quad \hat{y} \rightarrow \infty \end{aligned} \quad (2.2.2)$$

The Navier–Stokes equations are nonlinear and their solution is computationally quite heavy. However, our interest is in the growth or decay of a perturbation produced by the

interaction of two disturbances and developing in a given boundary layer. The velocity field is therefore decomposed in different contribution and the previous Navier–Stokes system linearized about the base flow.

2.2.1 Velocity decomposition and linearization

Referring to figure (2.1), we consider a general steady incompressible boundary layer

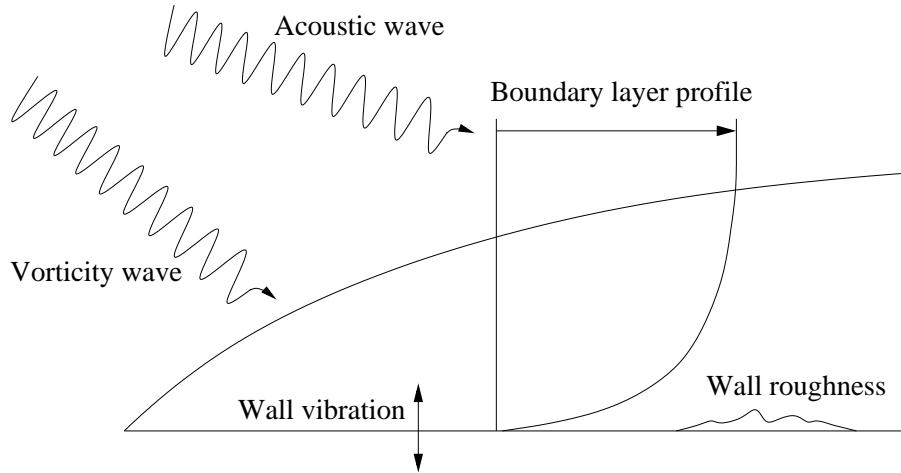


Figure 2.1: External disturbances inducing turbulence

past a flat plate. The oncoming flow can be obtained from calculations with or without an external pressure gradient or experimental data. The possible disturbances can come from the upstream and external flow, like acoustic waves and vorticity waves, or can act at the wall, like in the wall vibration or wall roughness case. Each excitation source produces a contribution to the velocity field at order ϵ or δ , depending on what ϵ or δ represents (the amplitude of the acoustic wave, of the vorticity wave, of the wall displacement due to the vibration or the typical wall roughness size), and their interaction produces a resonant wave at order $\epsilon\delta$.

Following what was already done by others, we introduce two small disturbances $\epsilon\hat{\mathbf{v}}_\epsilon(\hat{x}, \hat{y}, \hat{z})e^{-i\omega_\epsilon\hat{t}}$ and $\delta\hat{\mathbf{v}}_\delta(\hat{x}, \hat{y}, \hat{z})e^{-i\omega_\delta\hat{t}}$, where $\hat{\mathbf{v}} = (u, v, w)$, which represent respectively an unsteady wave of amplitude ϵ generated by a general unsteady excitation source behaving as $e^{-i\omega_\epsilon\hat{t}}$ and an unsteady wave of amplitude δ due to another general unsteady excitation source behaving as $e^{-i\omega_\delta\hat{t}}$. These two perturbations are superimposed to a two-dimensional steady base flow $\hat{\mathbf{V}}(\hat{x}, \hat{y})$ (Blasius flow in our case) and their interaction generates other beat waves, respectively $\epsilon\delta\hat{\mathbf{v}}_{\epsilon\delta}^+(\hat{x}, \hat{y})e^{-i(\omega_\epsilon+\omega_\delta)\hat{t}}$ and $\epsilon\delta\hat{\mathbf{v}}_{\epsilon\delta}^-(\hat{x}, \hat{y})e^{-i(\omega_\epsilon-\omega_\delta)\hat{t}}$ at order $\epsilon\delta$ plus other waves at higher orders. The waves at order ϵ and order δ , in general, do not have the right spatial wavelength and time frequency which characterize the Tollmien–Schlichting wave. However, their interaction at order $\epsilon\delta$ could have and could generate a resonance phenomenon. If we assume that the resonant wave is $\epsilon\delta\hat{\mathbf{v}}_{\epsilon\delta}^+(\hat{x}, \hat{y})e^{-i(\omega_\epsilon+\omega_\delta)\hat{t}}$, its amplitude is much larger than the amplitude of $\epsilon\delta\hat{\mathbf{v}}_{\epsilon\delta}^-(\hat{x}, \hat{y})e^{-i(\omega_\epsilon-\omega_\delta)\hat{t}}$ so that the latter can be neglected. The velocity inside the boundary layer $\hat{\mathbf{v}}(\hat{x}, \hat{y}, \hat{z}, \hat{t})$ is therefore decomposed into different contributions due to the base

flow, to different excitation sources and to their mutual interaction:

$$\begin{aligned} \hat{\mathbf{v}}(\hat{x}, \hat{y}, \hat{z}, \hat{t}) &= \hat{\mathbf{V}}(\hat{x}, \hat{y}) + \epsilon \hat{\mathbf{v}}_\epsilon(\hat{x}, \hat{y}, \hat{z}) e^{-i\omega_\epsilon \hat{t}} + \delta \hat{\mathbf{v}}_\delta(\hat{x}, \hat{y}, \hat{z}) e^{-i\omega_\delta \hat{t}} + \\ &\quad \epsilon \delta \hat{\mathbf{v}}_{\epsilon\delta}(\hat{x}, \hat{y}, \hat{z}) e^{-i(\omega_\epsilon + \omega_\delta) \hat{t}} + \mathcal{O}(\epsilon^2) + \mathcal{O}(\delta^2) + \dots \end{aligned} \quad (2.2.3)$$

We have considered both perturbations at order ϵ and δ as unsteady, but in real cases it is possible to have one of them steady. It typically happens when the wall roughness is introduced at order δ , imposing $\omega_\delta = 0$.

If the previous velocity decomposition (2.2.3) is introduced in the Navier–Stokes system of equations (2.2.1), neglecting terms of order greater than ϵ , δ or $\epsilon\delta$, one finds three linear problems at the three orders ϵ , δ and $\epsilon\delta$ (the base flow already satisfies the equations) which can be formally and compactly written as

$$\begin{aligned} \mathbf{L}_\epsilon(\hat{\mathbf{V}}, R) \hat{\mathbf{f}}_\epsilon &= \hat{\mathbf{y}}_\epsilon \\ \mathbf{L}_\delta(\hat{\mathbf{V}}, R) \hat{\mathbf{f}}_\delta &= \hat{\mathbf{y}}_\delta \\ \mathbf{L}_{\epsilon\delta}(\hat{\mathbf{V}}, R) \hat{\mathbf{f}}_{\epsilon\delta} &= \hat{\mathbf{y}}_{\epsilon\delta} \end{aligned} \quad (2.2.4)$$

where $\hat{\mathbf{f}} = (\hat{u}, \hat{v}, \hat{w}, \hat{p})$, $\mathbf{L}(\hat{\mathbf{V}}, R)$ is a linear operator, function of the base flow $\hat{\mathbf{V}} = (\hat{U}(\hat{x}, \hat{y}), \hat{V}(\hat{x}, \hat{y}), \hat{W}(\hat{x}, \hat{y}))$ and Reynolds number R . The known terms $\hat{\mathbf{y}}$ are originated at order ϵ and δ by the possible non homogeneous boundary conditions at the wall or at infinity, while at order $\epsilon\delta$ not only the boundary conditions are included but also the coupling terms coming from the nonlinear part of the original Navier–Stokes equations:

$$\hat{\mathbf{y}}_{\epsilon\delta} = \begin{pmatrix} 0 \\ \hat{u}_\epsilon(\hat{u}_\delta)_x + \hat{u}_\delta(\hat{u}_\epsilon)_x + \hat{v}_\epsilon(\hat{u}_\delta)_y + \hat{v}_\delta(\hat{u}_\epsilon)_y + \hat{w}_\epsilon(\hat{u}_\delta)_z + \hat{w}_\delta(\hat{u}_\epsilon)_z \\ \hat{u}_\epsilon(\hat{v}_\delta)_x + \hat{u}_\delta(\hat{v}_\epsilon)_x + \hat{v}_\epsilon(\hat{v}_\delta)_y + \hat{v}_\delta(\hat{v}_\epsilon)_y + \hat{w}_\epsilon(\hat{v}_\delta)_z + \hat{w}_\delta(\hat{v}_\epsilon)_z \\ \hat{u}_\epsilon(\hat{w}_\delta)_x + \hat{u}_\delta(\hat{w}_\epsilon)_x + \hat{v}_\epsilon(\hat{w}_\delta)_y + \hat{v}_\delta(\hat{w}_\epsilon)_y + \hat{w}_\epsilon(\hat{w}_\delta)_z + \hat{w}_\delta(\hat{w}_\epsilon)_z \end{pmatrix} \quad (2.2.5)$$

Once the equations have been linearized about the base flow and with respect to the small parameters ϵ , δ and $\epsilon\delta$, also the boundary conditions at the wall can be linearized about the wall shape and with respect to the same small parameters. Two possible sources of excitation at the wall are wall roughness and wall vibration. In the former case the wall is expressed as a function of the streamwise coordinate by $\delta h(\hat{x})$, where δ is the typical wall roughness scale, and $h(\hat{x})$ is an order–one function which describes the wall shape. If wall roughness is acting at order δ , since it is stationary, $\omega_\delta = 0$. On the other hand, an exciting source at the wall is represented by a rigid vibration. In this case the wall can move in the streamwise, spanwise or wall–normal direction. However, in the first two cases the problem reduces to the well–known flow near an oscillating flat plate (Stokes’s second problem [102]) and thus we concentrate only on the wall–normal rigid vibration. The position of the wall as a function of time can be described by $\epsilon e^{-i\omega_\epsilon \hat{t}}$ where ϵ is the typical amplitude of the vibration with a characteristic time frequency ω_ϵ . If both of the disturbances are acting at the wall, the wall shape can be expressed by the function

$$H(\hat{x}, \hat{t}) = \delta h(\hat{x}) + \epsilon e^{-i\omega_\epsilon \hat{t}}$$

Since δ and ϵ are small parameters, $H(\hat{x}, \hat{t})$ is small as well so that the boundary conditions defined at $\hat{y} = H(\hat{x}, \hat{t})$ for the velocity field $\hat{\mathbf{v}} = (\hat{u}, \hat{v}, \hat{w})$ can be shifted to $\hat{y} = 0$ via linearization. Introducing a Taylor expansion about the position $\hat{y} = 0$, one gets

$$\begin{aligned} \hat{\mathbf{v}}(\hat{x}, \hat{y}, \hat{z}, \hat{t}) &= \hat{\mathbf{v}}(\hat{x}, 0, \hat{z}, \hat{t}) + \left[\delta h(\hat{x}) + \epsilon e^{-i\omega\epsilon\hat{t}} \right] \frac{\partial \hat{\mathbf{v}}(\hat{x}, \hat{y}, \hat{z}, \hat{t})}{\partial \hat{y}} \Big|_{\hat{y}=0} + \\ &\quad \frac{1}{2} \left[\epsilon^2 e^{-2i\omega\epsilon\hat{t}} + \delta^2 h^2(\hat{x}) + 2\epsilon\delta h(\hat{x}) e^{-i\omega\epsilon\hat{t}} \right] \frac{\partial^2 \hat{\mathbf{v}}(\hat{x}, \hat{y}, \hat{z}, \hat{t})}{\partial \hat{y}^2} \Big|_{\hat{y}=0} + \dots \\ &= \hat{\mathbf{v}}_0 \end{aligned} \tag{2.2.6}$$

where the vector $\hat{\mathbf{v}}_0 = (\hat{u}_0, \hat{v}_0, \hat{w}_0)$ contains the boundary conditions at the wall. If the vibration is only in the wall normal direction, since the velocity there is simply the time derivative of the displacement, the velocity vector at $\hat{y} = 0$ is $\hat{\mathbf{v}}_0 = \epsilon(0, -i\omega\epsilon, 0)e^{-i\omega\epsilon\hat{t}}$. If the expansion (2.2.3) is introduced in (2.2.6), non-homogeneous boundary conditions are obtained at order ϵ , δ and $\epsilon\delta$:

$$\begin{aligned} \hat{\mathbf{V}}(\hat{x}, 0, \hat{z}) &= 0 \\ \hat{\mathbf{v}}_\epsilon(\hat{x}, 0, \hat{z}) &= - \frac{\partial \hat{\mathbf{V}}(\hat{x}, \hat{y}, \hat{z})}{\partial \hat{y}} \Big|_{\hat{y}=0} - i\omega\epsilon \\ \hat{\mathbf{v}}_\delta(\hat{x}, 0, \hat{z}) &= -h(\hat{x}) \frac{\partial \hat{\mathbf{V}}(\hat{x}, \hat{y}, \hat{z})}{\partial \hat{y}} \Big|_{\hat{y}=0} \\ \hat{\mathbf{v}}_{\epsilon\delta}(\hat{x}, 0, \hat{z}) &= -h(\hat{x}) \frac{\partial \hat{\mathbf{v}}_\epsilon(\hat{x}, \hat{y}, \hat{z})}{\partial \hat{y}} \Big|_{\hat{y}=0} - \frac{\partial \hat{\mathbf{v}}_\delta(\hat{x}, \hat{y}, \hat{z})}{\partial \hat{y}} \Big|_{\hat{y}=0} - h(\hat{x}) \frac{\partial^2 \hat{\mathbf{V}}(\hat{x}, \hat{y}, \hat{z})}{\partial \hat{y}^2} \Big|_{\hat{y}=0} \end{aligned} \tag{2.2.7}$$

It is important to remark that the previous non homogeneous boundary conditions are referred to the case in which both wall roughness and wall vibration are considered. If one of them does not act, for example the wall does not move and only the wall roughness is present, then the boundary conditions at the wall reduce to

$$\begin{aligned} \hat{\mathbf{V}}(\hat{x}, 0, \hat{z}) &= 0 \\ \hat{\mathbf{v}}_\epsilon(\hat{x}, 0, \hat{z}) &= 0 \\ \hat{\mathbf{v}}_\delta(\hat{x}, 0, \hat{z}) &= -h(\hat{x}) \frac{\partial \hat{\mathbf{V}}(\hat{x}, \hat{y}, \hat{z})}{\partial \hat{y}} \Big|_{\hat{y}=0} \\ \hat{\mathbf{v}}_{\epsilon\delta}(\hat{x}, 0, \hat{z}) &= -h(\hat{x}) \frac{\partial \hat{\mathbf{v}}_\epsilon(\hat{x}, \hat{y}, \hat{z})}{\partial \hat{y}} \Big|_{\hat{y}=0} \end{aligned} \tag{2.2.8}$$

which are already known from previous works found in the literature. If the wall surface is perfectly flat (no roughness) and it moves up and down, the wall boundary conditions are

$$\begin{aligned}
 \hat{\mathbf{V}}(\hat{x}, 0, \hat{z}) &= 0 \\
 \hat{\mathbf{v}}_\epsilon(\hat{x}, 0, \hat{z}) &= - \left. \frac{\partial \hat{\mathbf{V}}(\hat{x}, \hat{y}, \hat{z})}{\partial \hat{y}} \right|_{\hat{y}=0} - i\omega_\epsilon \\
 \hat{\mathbf{v}}_\delta(\hat{x}, 0, \hat{z}) &= 0 \\
 \hat{\mathbf{v}}_{\epsilon\delta}(\hat{x}, 0, \hat{z}) &= - \left. \frac{\partial \hat{\mathbf{v}}_\delta(\hat{x}, \hat{y}, \hat{z})}{\partial \hat{y}} \right|_{\hat{y}=0}
 \end{aligned} \tag{2.2.9}$$

Obviously, if the wall does not move and the surface is without roughness, all the boundary conditions are homogeneous, while if both wall roughness and wall vibration are present, also the second derivative of the base flow enters in the boundary conditions at order $\epsilon\delta$.

2.2.2 Order ϵ and δ

In the previous paragraphs, the linearized Navier–Stokes equations have been derived for three problems at three different orders. Also the boundary conditions at the wall have been linearized about $\hat{y} = 0$, obtaining non homogeneous boundary conditions defined at $\hat{y} = 0$ instead of the original homogeneous boundary conditions defined at $\hat{y} = H(\hat{x})$.

In this section we solve the problem at first order with respect to ϵ and δ , which actually means the problems of acoustic wave, vorticity wave, wall vibration and wall roughness. It should be kept in mind that each disturbance, by itself, is not resonant and therefore it does not satisfy the dispersion relation of the Tollmien–Schlichting waves, requiring an “adaptation mechanism” (their interaction at order $\epsilon\delta$) for the resonance condition.

Acoustic wave disturbance

We suppose that the acoustic wave, present in the outer flow, is plane and characterized by a streamwise velocity amplitude equal to ϵ and a typical time frequency ω_ϵ . This wave, interacting with the boundary layer on the flat plate, produces a perturbation that can be described by the linearized Navier–Stokes equations about the given base flow $\mathbf{V} = (U(x, y), V(x, y), W(x, y))$, where the variables with the hat $\hat{\cdot}$ have been replaced by variables without it. The perturbation produced is two–dimensional and independent of the streamwise coordinate x and spanwise coordinate z , so that the governing equations

are

$$\begin{aligned} \frac{\partial v_\epsilon}{\partial y} &= 0 \\ -i\omega_\epsilon u_\epsilon - \frac{1}{R} \frac{\partial^2 u_\epsilon}{\partial y^2} &= 0 \\ \frac{\partial p_\epsilon}{\partial y} &= 0 \end{aligned}$$

with boundary conditions

$$\begin{aligned} u_\epsilon &= 0 & \text{at } y &= 0 \\ v_\epsilon &= 0 & \text{at } y &= 0 \\ u_\epsilon &\rightarrow 1 & \text{for } y &\rightarrow \infty \\ v_\epsilon &\rightarrow 0 & \text{for } y &\rightarrow \infty \end{aligned}$$

The problem is easily solvable and the solution corresponds to the well known Stokes's flow, where $v_\epsilon = 0$ and u_ϵ depends only on y :

$$\epsilon \mathbf{v}_\epsilon(x, y) e^{-i\omega_\epsilon t} = \epsilon (1 - e^{-\sqrt{-i\omega_\epsilon R} y}, 0) e^{-i\omega_\epsilon t}$$

Vorticity wave disturbance

A vorticity wave represents a gust traveling in the free stream. Let ϵ be the amplitude of the streamwise velocity disturbance and ω_ϵ its characteristic time frequency. The main difference with the acoustic wave disturbance is that the vorticity wave is characterized by a certain spatial wavelength α_ϵ different from zero. In fact, the non-viscous flow, which represents the outer conditions, admits disturbances with non-zero vorticity which behave like $e^{-i\omega_\epsilon t + i\alpha_\epsilon x}$ with $\alpha_\epsilon = \omega_\epsilon / U_\infty$. This free-stream traveling disturbance produces a perturbation inside the boundary layer, where the viscous equations are used. The boundary conditions at the wall for such a disturbance are obviously homogeneous, while for $y \rightarrow \infty$ the solution must reach the asymptotic values of the external flow in which the perturbation is present, satisfying also the asymptotic behavior of the perturbation equations. The problem is governed by the Navier-Stokes linearized about the base flow. For simplicity we consider a two-dimensional disturbance and write the equations in the stream-function variable ψ_ϵ , so that

$$u_\epsilon = \frac{\partial \psi_\epsilon}{\partial y}; \quad v_\epsilon = -\frac{\partial \psi_\epsilon}{\partial x}$$

The equations for the perturbation reduce to the Orr-Sommerfeld one. In the $y \rightarrow \infty$ limit it reads

$$-i(\omega - \alpha U_e) \left(\frac{\partial^2 \psi_\epsilon}{\partial y^2} - \alpha^2 \psi_\epsilon \right) = R^{-1} \left(\frac{\partial^2}{\partial y^2} - \alpha^2 \right)^2 \psi_\epsilon$$

which is a simple constant-coefficient ordinary differential equation and therefore the solution can be expressed as:

$$\psi_\epsilon = \sum_{i=1}^4 C_i e^{\lambda_i y}$$

with

$$\lambda_1 = \alpha; \lambda_2 = -\alpha; \lambda_3 = \sqrt{\alpha^2 + iR(\alpha U_e - \omega)}; \lambda_4 = -\sqrt{\alpha^2 + iR(\alpha U_e - \omega)}$$

In general, the upstream disturbance is supposed to be a function of the wall-normal coordinate and expandable in a Fourier series, requiring the real part of λ_i to be zero. However, the wave traveling from upstream undergoes a certain attenuation and has more possibility to reach the boundary layer if its wavelength is large compared to the boundary layer thickness. Therefore $\lambda = 0$ is a reasonable choice and implies a polynomial dependence on y instead of an exponential one. For $\lambda = 0$, one gets

$$\alpha_\epsilon = \frac{-iU_e + i\sqrt{U_e^2 - 4i\omega_\epsilon R^{-1}}}{2R^{-1}} \quad (2.2.10)$$

The asymptotic solution is therefore:

$$\psi_\epsilon = (C_1 e^{-\alpha_\epsilon y} + C_3 + C_4 y) e^{i(\alpha_\epsilon x - \omega_\epsilon t)}$$

which implies:

$$\begin{aligned} u_\epsilon &= \frac{\partial \psi_\epsilon}{\partial y} = (-\alpha_\epsilon C_1 e^{-\alpha_\epsilon y} + C_4) e^{i(\alpha_\epsilon x - \omega_\epsilon t)} \\ v_\epsilon &= -\frac{\partial \psi_\epsilon}{\partial x} = -i\alpha_\epsilon (C_1 e^{-\alpha_\epsilon y} + C_3 + C_4 y) e^{i(\alpha_\epsilon x - \omega_\epsilon t)} \end{aligned}$$

The boundary conditions at infinity must thus behave like

$$\begin{aligned} u_\epsilon &\rightarrow (-\alpha_\epsilon C_1 e^{-\alpha_\epsilon y} + C_4) e^{i(\alpha_\epsilon x - \omega_\epsilon t)} \\ v_\epsilon &\rightarrow -i\alpha_\epsilon (C_1 e^{-\alpha_\epsilon y} + C_3 + C_4 y) e^{i(\alpha_\epsilon x - \omega_\epsilon t)} \end{aligned} \quad (2.2.11)$$

with C_1 and C_3 free constants and C_4 given and equal to 1. The value α_ϵ obtained by (2.2.10) imposing $\lambda = 0$ furnishes the correct parameter to be introduced in the Orr–Sommerfeld operator. In fact, the equations for the vorticity wave problem are the same as the Orr–Sommerfeld problem with non homogeneous boundary conditions (2.2.11) at infinity instead of homogeneous ones. Since $\alpha_\epsilon \neq \alpha_{TS}$, and $\omega_\epsilon \neq \omega_{TS}$, the problem is not singular and, after the discretization, can be reduced to:

$$\mathbf{A}_\epsilon(\alpha_\epsilon, \omega_\epsilon, R) \mathbf{f}_\epsilon(x) = \mathbf{y}_\epsilon(x) e^{i \int \alpha_\epsilon dx'}$$

where $\mathbf{y}_\epsilon(x)$ contains only the non homogeneous boundary conditions at infinity. Finally,

$$\epsilon \mathbf{v}_\epsilon(x, y) e^{-i\omega_\epsilon t} = \epsilon (u_\epsilon(y), v_\epsilon(y)) e^{i \int \alpha_\epsilon dx' - i\omega_\epsilon t}$$

Wall vibration disturbance

A structural rigid vibration of the wall may be of different forms: the surface can be finite or infinite and the vibration can be parallel or normal to the wall. If an infinite surface is considered, the vibration parallel to the wall is a well-known problem with a closed-form solution (Stokes's second problem [102]) and is treated as the acoustic disturbance. The

vibration of an infinite surface in the direction normal to the wall will be the object of this section. On the other hand, if the wall is finite, a wall-normal vibration originates an induced flow in both parallel and normal directions with respect to the wall. The problem is thus decomposed into the known Stokes's second problem and the wall normal rigid-vibration problem. For the latter case, let us consider a structural rigid vibration of the wall which produces a wall normal displacement $\epsilon e^{-i\omega_\epsilon t}$, where ϵ is the vibration amplitude and ω_ϵ its time frequency. The governing equations are the Navier-Stokes ones linearized about the given base flow. As in the acoustic wave case, since the wall is infinite, the induced flow is independent of x , so that the equations to be solved read

$$\begin{aligned} \frac{\partial v_\epsilon}{\partial y} &= 0 \\ -i\omega_\epsilon u_\epsilon - \frac{1}{R} \frac{\partial^2 u_\epsilon}{\partial y^2} + \frac{\partial U}{\partial y} v_\epsilon &= 0 \\ -i\omega_\epsilon v_\epsilon - \frac{1}{R} \frac{\partial^2 v_\epsilon}{\partial y^2} + \frac{\partial p_{0\epsilon}}{\partial y} &= 0 \end{aligned}$$

supplemented by the boundary conditions

$$\begin{aligned} u_\epsilon &= -U_y & \text{at } y &= 0 \\ v_\epsilon &= -V_y - i\omega & \text{at } y &= 0 \\ u_\epsilon &\rightarrow 0 & \text{for } y &\rightarrow \infty \\ v_\epsilon &\rightarrow 0 & \text{for } y &\rightarrow \infty \end{aligned}$$

The solution for v_ϵ is trivial: $v_\epsilon = -V_y - i\omega$, while u_ϵ has to satisfy the equation:

$$\frac{1}{R} \frac{\partial^2 u_\epsilon}{\partial y^2} + i\omega_\epsilon u_\epsilon = \frac{\partial U}{\partial y} v_\epsilon$$

with boundary conditions

$$\begin{aligned} u_\epsilon &= -U_y & \text{at } y &= 0 \\ u_\epsilon &\rightarrow 0 & \text{for } y &\rightarrow \infty \end{aligned}$$

The solution can be obtained solving numerically the ordinary constant-coefficients differential equation or analytically using the Green function technique. In the latter case, starting from the equation

$$u_\epsilon'' + i\omega_\epsilon R u_\epsilon = R \frac{\partial U}{\partial y}$$

we seek a solution $g(y, y')$ which satisfies:

$$g'' + i\omega_\epsilon R g = \delta(y - y')$$

in such a way that it is continuous at $y = y'$ and its first derivative has a discontinuity with unitary jump there. The function is:

$$g(y, y') = -\frac{1}{2\sqrt{-i\omega_\epsilon R}} e^{-\sqrt{-i\omega_\epsilon R}|y - y'|}$$

so that the solution u_ϵ is:

$$u_\epsilon = -\frac{R}{2\sqrt{-i\omega_\epsilon R}} \int_0^\infty \frac{\partial U}{\partial y} e^{-\sqrt{-i\omega_\epsilon R}|y-y'|} dy' + C e^{-\sqrt{-i\omega_\epsilon R}y}$$

The boundary condition $u_\epsilon(0) = -U_y(0)$ allows us to obtain the constant

$$C = -U_y(0) + \frac{R}{2\sqrt{-i\omega_\epsilon R}} \int_0^\infty \frac{\partial U}{\partial y} e^{-\sqrt{-i\omega_\epsilon R}|y'|} dy'$$

from which the final solution

$$u_\epsilon(y) = -\frac{R}{2\sqrt{-i\omega_\epsilon R}} \int_0^\infty \frac{\partial U}{\partial y} \left[e^{-\sqrt{-i\omega_\epsilon R}|y-y'|} - e^{-\sqrt{-i\omega_\epsilon R}|y'|} \right] dy' - U_y(0) e^{-\sqrt{-i\omega_\epsilon R}y}$$

Finally,

$$\epsilon \mathbf{v}_\epsilon(x, y) e^{-i\omega_\epsilon t} = \epsilon(u_\epsilon(y), v_\epsilon(y)) e^{-i\omega_\epsilon t}$$

Wall roughness disturbance

The wall-roughness shape is described by a function $\hat{y} = \delta h(\hat{x})$, where δ is the typical roughness scale and $h(\hat{x})$ an order-one function which actually describes the shape as a function of \hat{x} . In principle, the latter has a wide wavenumber spectrum when decomposed in Fourier series. However, we are interested in the combination between a generic disturbance and the wall roughness in order to create a resonance with the Tollmien-Schlichting wave, that occurs for a specific value of the wall-roughness wavenumber. Therefore, we concentrate on a particular α_δ , keeping in mind that the same analysis can be performed for different wavenumbers. The steady perturbation induced in the boundary layer by the wall roughness can be expressed as a wave in the form $(u(x, y), v(x, y)) e^{i \int \alpha_\delta dx'}$, where α_δ is related to the inverse of the typical roughness wavelength. Also in this case the equations are the same as in the Orr-Sommerfeld formulation, but solved for $\omega_\delta = 0$ (since the perturbation is steady) and with non-homogeneous boundary conditions coming from the linearization at the wall:

$$\begin{aligned} u_{0\delta}(x, 0) &= -h(x) \left. \frac{\partial U}{\partial y} \right|_{y=0} e^{-i \int \alpha_\delta dx'} \\ v_{0\delta}(x, 0) &= -h(x) \left. \frac{\partial V}{\partial y} \right|_{y=0} e^{-i \int \alpha_\delta dx'} \end{aligned}$$

after the discretization of the equations and boundary conditions, the problem at order δ reduces to the linear system

$$\mathbf{A}_\delta(\alpha_\delta, R) \mathbf{f}_\delta(x) = \mathbf{y}_\delta(x) h(x) e^{-i \int \alpha_\delta dx'}$$

where $\mathbf{y}_\delta(x)$ contains only the terms provided by the boundary conditions and the matrix \mathbf{A}_δ is the Orr-Sommerfeld operator evaluated at the value of α_δ that produces at second order $\epsilon\delta$ a wave resonant with the Tollmien-Schlichting one.

2.2.3 Order $\epsilon\delta$

It has been said that the perturbations analyzed in the previous sections (at order ϵ or δ) cannot create, by themselves, a resonant condition with the Tollmien–Schlichting wave because their spatial wavenumber α and time frequency ω do not satisfy its dispersion relation. On the contrary, the resonance can be achieved by the combination of at least two of the previous disturbances: the nonlinear terms in the Navier–Stokes equations produce an exciting term at order $\epsilon\delta$ that has the spatial wavenumber α and time frequency ω due to the summation of the wavenumbers and frequencies of each disturbance. This fact allows the possibility to have α and ω of the forcing term within the Tollmien–Schlichting range and therefore resonance.

At order $\epsilon\delta$ the problem to be solved is thus resonant. One possible approach is to use the multiple–scale technique which allows the treatment of a singular problem and offers several advantages related to the possibility to include nonparallel–flow effects without numerical stability problems. In the next sections, the theory of multiple scales will be presented in a non homogeneous case and then applied to the Navier–Stokes equations, formulating the resonant problem at order $\epsilon\delta$.

2.3 Multiple scales

The multiple–scale technique is usually applied in physics in order to solve a problem which slightly differs from an already solved one because some coefficients previously constant are substituted by slowly varying functions. This is the case of the boundary layer, where strong variations of fluid dynamic quantities occur in the wall–normal direction, while the dependence on the streamwise coordinate is much weaker. For this reason, it is reasonable to assume a non parallel boundary layer as a quasi–parallel flow with slowly varying characteristics with the streamwise coordinate x .

The multiple–scale method exists in different forms and has been applied to both linear and nonlinear problems. Our stability analysis is linear and thus we use the linear version, developed especially in quantum mechanics in the 1920s with the name of “Adiabatic perturbation theory”, where “adiabatic” means “slowly varying” from the theory of reversible thermodynamic processes. In appendix B the classical multiple–scale theory without forcing sources is reported, while here we describe the non–homogeneous version and its application to the Navier–Stokes equations.

2.3.1 Non–homogeneous multiple–scale theory

In order to explain the multiple–scale technique in the non homogeneous case, let us consider the simple one–dimensional system

$$\mathbf{H}(t) \frac{d\mathbf{x}(t)}{dt} + \mathbf{A}(t) \mathbf{x}(t) = \tilde{\epsilon} \mathbf{y}(t)$$

where the matrices \mathbf{H} and \mathbf{A} are slowly varying with time t , \mathbf{x} represents the state vector, $\tilde{\epsilon}$ is a small parameter that accounts for the slow variation with respect to t and \mathbf{y} is the known forcing term. Since all the quantities are supposed to be weak functions

of the only variable t , a new corresponding variable $T = \tilde{\epsilon}t$ is introduced in order to account for that, and the solution \mathbf{x} is assumed to be representable in the form

$$\mathbf{x}(T) = \mathbf{f}(T)e^{\frac{\phi(T)}{\tilde{\epsilon}}} = (\mathbf{f}_0(T) + \tilde{\epsilon}\mathbf{f}_1(T) + \tilde{\epsilon}^2\mathbf{f}_2(T) + \dots) e^{\frac{\phi(T)}{\tilde{\epsilon}}}$$

where the exponential is a fast varying oscillating function while the vector $\mathbf{f}(T)$ represents the slowly varying part and is expanded in a series of the small parameter $\tilde{\epsilon}$. The derivative with respect to t therefore becomes

$$\begin{aligned} \frac{d\mathbf{x}(t)}{dt} &= \tilde{\epsilon} \frac{d\mathbf{x}(T)}{dT} \\ &= \tilde{\epsilon} \left[\left(\frac{d\mathbf{f}_0(T)}{dT} + \tilde{\epsilon} \frac{d\mathbf{f}_1(T)}{dT} + \dots \right) e^{\frac{\phi(T)}{\tilde{\epsilon}}} + \frac{1}{\tilde{\epsilon}} \frac{d\phi(T)}{dT} (\mathbf{f}_0(T) + \tilde{\epsilon}\mathbf{f}_1(T) + \dots) e^{\frac{\phi(T)}{\tilde{\epsilon}}} \right] \\ &= \left[\frac{d\phi(T)}{dT} \mathbf{f}_0(T) + \tilde{\epsilon} \left(\frac{d\phi(T)}{dT} \mathbf{f}_1(T) + \frac{d\mathbf{f}_0(T)}{dT} \right) + \mathcal{O}(\tilde{\epsilon}^2) \right] e^{\frac{\phi(T)}{\tilde{\epsilon}}} \end{aligned}$$

by introducing the previous derivative in the original system and separating the different orders with respect to $\tilde{\epsilon}$, a linear system is found at each order:

$$\begin{aligned} \left(\frac{d\phi}{dT} \mathbf{H}(T) \mathbf{f}_0(T) + \mathbf{A}(T) \mathbf{f}_0(T) \right) e^{\frac{\phi(T)}{\tilde{\epsilon}}} &= 0 \\ \tilde{\epsilon} \left(\frac{d\phi}{dT} \mathbf{H}(T) \mathbf{f}_1(T) + \frac{d\mathbf{f}_0}{dT} + \mathbf{A}(T) \mathbf{f}_1(T) \right) e^{\frac{\phi(T)}{\tilde{\epsilon}}} &= \tilde{\epsilon} \mathbf{y}(T) \\ \dots &= \dots \\ \tilde{\epsilon}^n \left(\frac{d\phi}{dT} \mathbf{H}(T) \mathbf{f}_n(T) + \frac{d\mathbf{f}_{n-1}}{dT} + \mathbf{A}(T) \mathbf{f}_n \right) e^{\frac{\phi(T)}{\tilde{\epsilon}}} &= 0 \end{aligned}$$

At order zero, $\tilde{\epsilon}^0$, a homogeneous system is obtained so that, in order for the solution to exist, it is necessary for the determinant of the matrix to be zero. This consideration leads to the eigenvalue problem

$$[\mathbf{A}(T) + \lambda_k(T) \mathbf{H}(T)] \mathbf{f}_0(T) = 0 \quad (2.3.1)$$

where $d\phi/dT$ must equal $\lambda_k(T)$. By solving (2.3.1), the eigenvalue $\lambda_k(T)$ and eigenvector $\tilde{\mathbf{u}}_k(T)$ are computed. However, the latter is not unique because it is defined up to a multiplicative factor and thus it can be normalized in different ways. In order to express this feature, the solution at order zero $\mathbf{f}_0(T)$ can be written as $c_k(T) \tilde{\mathbf{u}}_k(T)$ where $c_k(T)$ is still unknown.

At order $\tilde{\epsilon}$ the following problem is obtained

$$[\mathbf{A}(T) + \lambda_k(T) \mathbf{H}(T)] \mathbf{f}_1(T) = -\frac{d\mathbf{f}_0}{dT} + \mathbf{y}(T) e^{-\frac{\phi(T)}{\tilde{\epsilon}}} \quad (2.3.2)$$

It is a non homogeneous linear system with a singular matrix, because the coefficient matrix is exactly the same as the one at order $\tilde{\epsilon}^0$. Therefore the RHS must satisfy the compatibility condition, recalled in appendix A, which requires the dot product between

the RHS term and the left eigenvector corresponding to the vanishing eigenvalue to be zero:

$$\tilde{\mathbf{v}}_k(T) \cdot \left(-\frac{d\mathbf{f}_0}{dT} + \mathbf{y}(T)e^{-\frac{\phi(T)}{\tilde{\epsilon}}} \right) = 0 \quad (2.3.3)$$

By expanding the previous equation and considering that $\mathbf{f}_0(T) = c_k(T)\tilde{\mathbf{u}}_k(T)$, an equation for the unknown $c_k(T)$ is derived:

$$\tilde{\mathbf{v}}_k(T) \cdot \tilde{\mathbf{u}}_k(T) \frac{dc_k}{dT} + \tilde{\mathbf{v}}_k(T) \cdot \frac{d\tilde{\mathbf{u}}_k(T)}{dT} c_k = \tilde{\mathbf{v}}_k(T) \cdot \mathbf{y}(T)e^{-\frac{\phi(T)}{\tilde{\epsilon}}} \quad (2.3.4)$$

It is easy to verify that (2.3.4) is a first order non homogeneous ordinary differential equation, for which a closed-form solution exists. Its solution provides the multiplicative factor $c_k(T)$ from which the product $c_k(T)\tilde{\mathbf{u}}_k(T)$ is computed. It is important to remark that the latter vector is unique, independent of the normalization, while $\tilde{\mathbf{u}}_k(T)$ was not. Finally, the state vector $\mathbf{x}(T_f)$ is expressed in the form

$$\mathbf{x}(T_f) = c_k(T_f)\tilde{\mathbf{u}}_k(T_f)e^{\frac{\phi(T_f)}{\tilde{\epsilon}}} + \mathcal{O}(\tilde{\epsilon})$$

or more compactly as

$$\mathbf{x}(T_f) = \tilde{\mathbf{u}}_k(T_f) \int_{T_0}^{T_f} \mathbf{r}(T) \cdot \mathbf{y}(T) dT + \mathcal{O}(\tilde{\epsilon})$$

The state vector is thus given by the right eigenvector obtained at order $\tilde{\epsilon}^0$ and normalized in a certain way, multiplied by the integral of the dot product between the forcing term $\mathbf{y}(T)$ and a vector $\mathbf{r}(T)$ that we call ‘‘receptivity vector’’. Basically, $\mathbf{r}(T)$ represents the sensitivity of the solution to the forcing $\mathbf{y}(T)$ and contains the left eigenvector of problem (2.3.1), that can be also viewed as the solution of the adjoint problem corresponding to (2.3.1).

2.3.2 Application to the Navier–Stokes equations

The main feature of the receptivity problem we are dealing with is that at order $\epsilon\delta$ resonance with the Tollmien–Schlichting wave is achieved thanks to the fact that two interacting disturbances produce a wave with the characteristic time frequency and spatial wavenumber in the range of Tollmien–Schlichting ones. At order $\epsilon\delta$ a singular perturbation problem thus needs to be solved. One possibility is to express the unknowns using a wave propagation approach and since a very slight variation with \hat{x} is expected, and a singular problem encountered, the multiple-scale technique is here applied. We derive the governing equations for a three dimensional base flow dependent only on the stream-wise x and wall normal y coordinates, so that the perturbation is three dimensional. However, the results will be presented only for a two dimensional base flow (Blasius profile) and a two dimensional perturbation ($\beta = 0$)

Following the same steps corresponding the one dimensional case, if $\tilde{\epsilon}$ is a small parameter that accounts for the small variations in the \hat{x} and \hat{z} directions, a new reference frame may be introduced:

$$x = \tilde{\epsilon}\hat{x}, \quad y = \hat{y}, \quad z = \tilde{\epsilon}\hat{z}, \quad t = \hat{t}$$

while the base flow can be expressed in the new reference frame as

$$U(x, y) = \hat{U}(\hat{x}, \hat{y}), \quad V(x, y) = \frac{\hat{V}(\hat{x}, \hat{y})}{\tilde{\epsilon}}, \quad W(x, y) = \hat{W}(\hat{x}, \hat{y})$$

The derivatives, considering the previous substitutions, become:

$$(\cdot)_{\hat{x}} = \tilde{\epsilon}(\cdot)_x \quad (\cdot)_{\hat{y}} = (\cdot)_y \quad (\cdot)_{\hat{z}} = \tilde{\epsilon}(\cdot)_z \quad (\cdot)_{\hat{t}} = (\cdot)_t$$

and the derivatives of the base flow

$$\hat{U}_{\hat{x}} = \tilde{\epsilon}U_x \quad \hat{U}_{\hat{y}} = U_y \quad \hat{V}_{\hat{x}} = \tilde{\epsilon}^2V_x \quad \hat{V}_{\hat{y}} = \tilde{\epsilon}V_y \quad \hat{W}_{\hat{x}} = \tilde{\epsilon}W_x \quad \hat{W}_{\hat{y}} = W_y$$

The general quantity $\hat{q}(\hat{x}, \hat{y}, \hat{z}, \hat{t})$ (which corresponds to \hat{u} , \hat{v} , \hat{w} or \hat{p} previously introduced) in the multiple-scale framework has the form

$$\hat{q}(\hat{x}, \hat{y}, \hat{z}, \hat{t}) = (q_0(x, y) + \tilde{\epsilon}q_1(x, y) + \dots) e^{\frac{i\theta(x)}{\tilde{\epsilon}} + i\beta z - i\omega t} \quad (2.3.5)$$

where $q_0(x, y, z)$ and $q_1(x, y, z)$ are functions with a weak dependence on the streamwise coordinate, $\theta(x)$ is a fast-varying function of x , β is the spanwise wavenumber and ω the time frequency. By introducing the expansion (2.3.5) in the first derivatives expressed in the new reference frame, one obtains:

$$\begin{aligned} (\hat{q})_{\hat{x}} &= \tilde{\epsilon}((q_0)_x + \tilde{\epsilon}(q_1)_x + \dots) e^{\frac{i\theta(x,z)}{\tilde{\epsilon}} - i\omega t} + \frac{i\alpha}{\tilde{\epsilon}} (q_0 + \tilde{\epsilon}q_1 + \dots) e^{\frac{i\theta(x)}{\tilde{\epsilon}} + i\beta z - i\omega t} \\ &= \tilde{\epsilon} \left(\frac{i\alpha}{\tilde{\epsilon}} q_0 + (q_0)_x + i\alpha q_1 + \tilde{\epsilon}(q_1)_x + \dots \right) e^{\frac{i\theta(x)}{\tilde{\epsilon}} + i\beta z - i\omega t} \\ &= (i\alpha q_0 + \tilde{\epsilon}(q_0)_x + \tilde{\epsilon}i\alpha q_1 + \tilde{\epsilon}^2(q_1)_x + \dots) e^{\frac{i\theta(x)}{\tilde{\epsilon}} + i\beta z - i\omega t} \\ &= [i\alpha q_0 + \tilde{\epsilon}[i\alpha q_1 + (q_0)_x] + \mathcal{O}(\tilde{\epsilon}^2)] e^{\frac{i\theta(x)}{\tilde{\epsilon}} + i\beta z - i\omega t} \\ (\hat{q})_{\hat{y}} &= [(q_0)_y + \tilde{\epsilon}(q_1)_y + \mathcal{O}(\tilde{\epsilon}^2)] e^{\frac{i\theta(x)}{\tilde{\epsilon}} + i\beta z - i\omega t} \\ (\hat{q})_{\hat{z}} &= [i\beta q_0 + \tilde{\epsilon}i\beta q_1 + \mathcal{O}(\tilde{\epsilon}^2)] e^{\frac{i\theta(x)}{\tilde{\epsilon}} + i\beta z - i\omega t} \\ (\hat{q})_{\hat{t}} &= -i\omega t [(q_0) + \tilde{\epsilon}(q_1) + \mathcal{O}(\tilde{\epsilon}^2)] e^{\frac{i\theta(x)}{\tilde{\epsilon}} + i\beta z - i\omega t} \end{aligned}$$

where the streamwise wavenumber α is defined as

$$\alpha = \frac{\partial \theta}{\partial x}$$

For the second derivatives, one gets

$$\begin{aligned} (\hat{q})_{\hat{x}\hat{x}} &= \tilde{\epsilon}^2 \left(-\frac{\alpha^2}{\tilde{\epsilon}^2} + \frac{2i\alpha}{\tilde{\epsilon}}(q_0)_x - \frac{\alpha^2}{\tilde{\epsilon}}q_1 + \frac{i\alpha_x}{\tilde{\epsilon}}q_0 + (q_0)_{xx} + \right. \\ &\quad \left. 2i\alpha(q_1)_x + i\alpha_x q_1 + \tilde{\epsilon}(q_1)_{xx} + \dots \right) e^{\frac{i\theta(x)}{\tilde{\epsilon}} + i\beta z - i\omega t} \\ &= [-\alpha^2 q_0 + \tilde{\epsilon}2i\alpha(q_0)_x - \tilde{\epsilon}\alpha^2 q_1 + \tilde{\epsilon}i\alpha_x q_0 + \mathcal{O}(\tilde{\epsilon}^2)] e^{\frac{i\theta(x)}{\tilde{\epsilon}} + i\beta z - i\omega t} \\ &= [-\alpha^2 q_0 + \tilde{\epsilon}[-\alpha^2 q_1 + 2i\alpha(q_0)_x + i\alpha_x q_0] + \mathcal{O}(\tilde{\epsilon}^2)] e^{\frac{i\theta(x)}{\tilde{\epsilon}} + i\beta z - i\omega t} \\ (\hat{q})_{\hat{y}\hat{y}} &= [(q_0)_{yy} + \tilde{\epsilon}(q_1)_{yy} + \mathcal{O}(\tilde{\epsilon}^2)] e^{\frac{i\theta(x)}{\tilde{\epsilon}} + i\beta z - i\omega t} \\ (\hat{q})_{\hat{z}\hat{z}} &= [-\beta^2 q_0 - \tilde{\epsilon}\beta^2 q_1 + \mathcal{O}(\tilde{\epsilon}^2)] e^{\frac{i\theta(x)}{\tilde{\epsilon}} + i\beta z - i\omega t} \end{aligned}$$

so that the Laplacian in the new framework is

$$\nabla^2 \hat{q} = [-(\alpha^2 + \beta^2)q_0 + (q_0)_{yy} + \tilde{\epsilon} [-(\alpha^2 + \beta^2)q_0 + (q_0)_{yy} + 2i\alpha(q_0)_x + i\alpha_x q_0] + \mathcal{O}(\tilde{\epsilon}^2)] e^{\frac{i\theta(x)}{\tilde{\epsilon}} + i\beta z - i\omega t}$$

If the base flow (U, V, W) , the perturbation (u, v, w, p) , the derivatives of the base flow and the derivatives of the perturbation are introduced in the linearized Navier–Stokes equations and boundary conditions, different systems of equations can be derived at each $\tilde{\epsilon}$ -order. In particular, at order $\tilde{\epsilon}^0$, one gets

$$\mathbf{A}_{\epsilon\delta}(\alpha_{\epsilon\delta}, \omega_{\epsilon\delta}, R) \mathbf{f}_{0\epsilon\delta} = \mathbf{y}_{0\epsilon\delta} e^{-i \int \alpha_{\epsilon\delta} dx' + i\omega_{\epsilon\delta} t} \quad (2.3.6)$$

where the matrix $\mathbf{A}_{\epsilon\delta}$ is the Orr–Sommerfeld operator:

$$\mathbf{A}(\alpha, \omega, R) = \begin{pmatrix} i\alpha & (\cdot)_y & i\beta & 0 \\ T & U_y & 0 & i\alpha \\ 0 & T & 0 & (\cdot)_y \\ 0 & W_y & T & i\beta \end{pmatrix}$$

with $T = [i(\alpha U + \beta W - \omega) + R^{-1}(\alpha^2 + \beta^2 - (\cdot)_{yy})]$, and the unknown vector $\mathbf{f}_{0\epsilon\delta}$ is defined as

$$\mathbf{f}_0 = \begin{pmatrix} u_0(x, y) \\ v_0(x, y) \\ w_0(x, y) \\ p_0(x, y) \end{pmatrix}$$

The forcing $\mathbf{y}_{0\epsilon\delta}$ arises from the non homogeneous boundary conditions at the wall and from the nonlinear interactions between the solutions at order ϵ and δ . These perturbations, in principle, have a wide spectrum and therefore does not need to be represented by wave packets. However, since the resonance is achieved only for the wavenumber and frequency corresponding to the Tollmien–Schlichting ones, we assume that each disturbance velocity at order ϵ and δ is in the form $\epsilon[u(x, y), v(x, y)]e^{i \int \alpha_{\epsilon} dx' - i\omega_{\epsilon} t}$ or $\delta[u(x, y), v(x, y)]e^{i \int \alpha_{\delta} dx' - i\omega_{\delta} t}$. Under these hypotheses, the forcing term at order $\epsilon\delta$ reduces to

$$\mathbf{y}_{0\epsilon\delta} = \begin{pmatrix} i\alpha_{\delta} u_{\epsilon} u_{0\delta} + i\alpha_{\epsilon} u_{0\delta} u_{\epsilon} + v_{\epsilon} (u_{0\delta})_y + v_{0\delta} (u_{\epsilon})_y \\ i\alpha_{\delta} u_{\epsilon} v_{0\delta} + i\alpha_{\epsilon} u_{0\delta} v_{\epsilon} + v_{\epsilon} (v_{0\delta})_y + v_{0\delta} (v_{\epsilon})_y \\ 0 \\ 0 \end{pmatrix}$$

Basically, this feature means that when $\alpha_{\epsilon\delta} \approx \alpha_{TS}$ and $\omega_{\epsilon\delta} \approx \omega_{TS}$ the matrix is singular and the solution of the non homogeneous problem at order $\epsilon\delta$ is non trivial.

The Orr–Sommerfeld problem

Before solving the problem (2.3.6) at order $\epsilon\delta$ for the case $\alpha_{\epsilon\delta} \approx \alpha_{TS}$ and $\omega_{\epsilon\delta} \approx \omega_{TS}$, we briefly recall how the homogeneous Orr–Sommerfeld formulation is derived in the

multiple-scale framework. By linearizing the Navier–Stokes equations about a given base flow and assuming the perturbation in the form (2.3.5), one finds at order $\tilde{\epsilon}^0$ a homogeneous system:

$$\mathbf{A}_{\text{TS}}(\alpha_{\text{TS}}, \omega_{\text{TS}}, R) \mathbf{f}_0 = 0 \quad (2.3.7)$$

Equation (2.3.7) is clearly an eigenvalue problem and if ω_{TS} and R are given and fixed, α_{TS} is found requiring the determinant of \mathbf{A}_{TS} to be zero, that is equivalent to satisfying the dispersion relation $D(\alpha_{\text{TS}}, \omega_{\text{TS}}, R) = 0$ for the Tollmien–Schlichting waves.

At order $\tilde{\epsilon}^1$, the equation is

$$\mathbf{A}_{\text{TS}}(\alpha_{\text{TS}}, \omega_{\text{TS}}, R) \mathbf{f}_1 = -\mathbf{H}(\alpha_{\text{TS}}, R) \frac{d\mathbf{f}_0}{dx} - \mathbf{C}(\alpha_{\text{TS}}, R) \mathbf{f}_0 \quad (2.3.8)$$

However, as seen in the multiple-scale framework applied to the one dimensional case, the linear system (2.3.8) is singular because the singularity of the same matrix \mathbf{A}_{TS} was required at order $\tilde{\epsilon}^0$. Since the RHS is different from zero, in order for the multiple-scale expansion to exist it is necessary to impose the “compatibility condition”, which stands that the dot product between the RHS and the the left eigenvector must be zero.

The resonant problem

The resonant problem at order $\epsilon\delta$

$$\mathbf{A}_{\epsilon\delta}(\alpha_{\epsilon\delta}, \omega_{\epsilon\delta}, R) \mathbf{f}_{0\epsilon\delta} = \mathbf{y}_{0\epsilon\delta} \quad (2.3.9)$$

presents the same singularity encountered in the Orr–Sommerfeld formulation at order $\tilde{\epsilon}^1$. In fact, the matrix $\mathbf{A}_{\epsilon\delta}$ is formally the same as \mathbf{A}_{TS} , used in the Orr–Sommerfeld problem so that when the system (2.3.9) is solved for $\alpha_{\epsilon\delta} \approx \alpha_{\text{TS}}$ and $\omega_{\epsilon\delta} \approx \omega_{\text{TS}}$, the determinant $|\mathbf{A}_{\epsilon\delta}|$ becomes zero as a function of $\alpha_{\epsilon\delta}$, if $\omega_{\epsilon\delta}$ and R are fixed. This implies that, if all the eigenvalues are distinct, one and only one eigenvalue λ_i of $\mathbf{A}_{\epsilon\delta}$ goes to zero as a function of $\alpha_{\epsilon\delta}$. Using the spectral decomposition of a matrix, the solution \mathbf{x} of a general linear system $\mathbf{A}\mathbf{x} = \mathbf{b}$, when the eigenvalue λ_i goes to zero as a function of a parameter, can be expressed as

$$\mathbf{x} \rightarrow \frac{1}{\lambda_i} \mathbf{u}_i (\mathbf{v}_i^T \mathbf{b}) \quad \text{for } \lambda_i \rightarrow 0 \quad (2.3.10)$$

where \mathbf{u}_i and \mathbf{v}_i are the right and left eigenvectors corresponding to the eigenvalue λ_i and $\mathbf{v}_i^T \mathbf{b}$ is a dot product. The expression (2.3.10), applied to the singular problem (2.3.9) at order $\epsilon\delta$, is extremely important because it says that in a resonant condition the solution behaves like the right eigenvector \mathbf{u}_i , corresponding to the singular eigenvalue λ_i , producing an effect of order λ_i^{-1} .

Since both the Orr–Sommerfeld problem (2.3.8) at order $\tilde{\epsilon}^1$ and the resonant problem (2.3.9) produce an effect at order λ_{TS}^{-1} , it is reasonable to include the forcing term $\mathbf{y}_{0\epsilon\delta}$ at order $\tilde{\epsilon}$ in the multiple-scale expansion together with the RHS of (2.3.8). This leads to the equation

$$\mathbf{A}(\alpha, \omega, R) \mathbf{f}_1 = -\mathbf{H}(\alpha, R) \frac{d\mathbf{f}_0}{dx} - \mathbf{C}(\alpha, R) \mathbf{f}_0 + \mathbf{y} e^{-\int \alpha dx + i\omega t} \quad (2.3.11)$$

where

$$\begin{aligned}\alpha &= \alpha_{\epsilon\delta} = \alpha_\epsilon + \alpha_\delta \approx \alpha_{TS} \\ \omega &= \omega_{\epsilon\delta} = \omega_\epsilon + \omega_\delta \approx \omega_{TS}\end{aligned}$$

and the matrices \mathbf{H} and \mathbf{C} are respectively

$$\mathbf{H}(\alpha, R) = \begin{pmatrix} 1 & 0 & 0 & 0 \\ U - 2R^{-1}i\alpha & 0 & 0 & 1 \\ 0 & U - 2R^{-1}i\alpha & 0 & 0 \\ 0 & 0 & U - 2R^{-1}i\alpha & 0 \end{pmatrix} = -i \frac{\partial \mathbf{A}}{\partial \alpha}$$

$$\mathbf{C}(\alpha, R) = \begin{pmatrix} 0 & 0 & 0 & 0 \\ U_x + V(\cdot)_y - R^{-1}i\alpha_x & 0 & 0 & 0 \\ 0 & V_y + V(\cdot)_y - R^{-1}i\alpha_x & 0 & 0 \\ W_x & 0 & V_y + V(\cdot)_y - R^{-1}i\alpha_x & 0 \end{pmatrix}$$

By solving equation (2.3.7) at order $\tilde{\epsilon}^0$, for a fixed frequency ω_{TS} and Reynolds number R , the Tollmien–Schlichting wavenumber α_{TS} and the corresponding eigenvector \mathbf{f}_0 are obtained. However, \mathbf{f}_0 is not unique and can be normalized in different ways, for example by requiring the maximum absolute value of the u -velocity-perturbation to be 1. If $\tilde{\mathbf{f}}_0$ is the eigenvector normalized in this way, the general solution \mathbf{f}_0 can be expressed by $\mathbf{f}_0 = c(x)\tilde{\mathbf{f}}_0$, where $c(x)$ is an unknown multiplicative factor to be determined.

On the other hand, the problem (2.3.11) is singular and therefore the “compatibility condition”, which imposes that the dot product between the left eigenvector and RHS must be zero, is needed:

$$\mathbf{y}^* \cdot \left(-\mathbf{H}(\alpha, R) \frac{d\mathbf{f}_0}{dx} - \mathbf{C}(\alpha, R) \mathbf{f}_0 + \mathbf{y} e^{-\int \alpha dx + i\omega t} \right) = 0$$

where \mathbf{y}^* is the left eigenvector. By replacing \mathbf{f}_0 with $c(x)\tilde{\mathbf{f}}_0$, the compatibility condition provides an equation necessary in order to determine the unknown $c(x)$:

$$\frac{dc}{dx} + \frac{a_2}{a_1} c = \frac{\mathbf{y}^* \cdot \mathbf{y}}{a_1} e^{-i \int_{x_0}^x \alpha dx' + i\omega t} \quad (2.3.12)$$

where

$$a_1 = \mathbf{y}^* \cdot (\mathbf{H}\tilde{\mathbf{f}}_0); \quad a_2 = \mathbf{y}^* \cdot \left(\mathbf{H} \frac{d\tilde{\mathbf{f}}_0}{dx} + \mathbf{C}\tilde{\mathbf{f}}_0 \right)$$

As it can be easily noticed, (2.3.12) is a non-homogeneous first-order linear differential equation for which a closed-form solution is known. The coefficient a_2 accounts for the non-parallel corrections to the amplitude of the solution. In fact, in the case of parallel-flow assumptions ($U = U(y)$ and $V = 0$) a_2 is zero because the derivative $d\tilde{\mathbf{f}}_0/dx$ is

null (the vector \mathbf{f}_0 is constant) and the matrix \mathbf{C} is zero everywhere (it contains the derivatives of U with respect to x and the V -component of the base flow). Considering only the order-zero contribution in the multiple-scale expansion, the solution at order $\epsilon\delta$, reads

$$\mathbf{f}_{\epsilon\delta}(x_f) = c(x_f)\tilde{\mathbf{f}}_0(x_f)e^{i\int_{x_0}^{x_f}\alpha dx'} + \mathcal{O}(\tilde{\epsilon})$$

where the multiplicative factor $c(x_f)$ is obtained solving (2.3.12):

$$c(x_f) = \int_{x_0}^{x_f} \frac{\mathbf{y}^*(x) \cdot \mathbf{y}(x) e^{-i\int_{x_0}^x \alpha dx'}}{a_1(x)} e^{\int_x^{x_f} -\frac{a_2(x')}{a_1(x')} dx'} dx$$

The final solution for the resonant perturbation at order $\epsilon\delta$ is therefore written as

$$\mathbf{f}_{\epsilon\delta}(x_f) = \left[\int_{x_0}^{x_f} \frac{\mathbf{y}^*(x) \cdot \mathbf{y}(x) e^{-i\int_{x_0}^x \alpha dx'}}{a_1(x)} e^{\int_x^{x_f} -\frac{a_2(x')}{a_1(x')} dx'} dx \right] \tilde{\mathbf{f}}_0(x_f)e^{i\int_{x_0}^{x_f}\alpha dx'} + \mathcal{O}(\tilde{\epsilon}) \quad (2.3.13)$$

or in a more compact form as

$$\mathbf{f}_{\epsilon\delta}(x_f) = \tilde{\mathbf{f}}_0(x_f) \int_{x_0}^{x_f} \mathbf{r}(x) \cdot \mathbf{y}(x) dx + \mathcal{O}(\tilde{\epsilon}) \quad (2.3.14)$$

It is important to notice that the solution is expressed as the product of the eigenvector obtained at order zero and the integral of a dot product which contains the known forcing term $\mathbf{y}(x)$ and the vector $\mathbf{r}(x)$ which we call receptivity and that expresses the sensitivity of the solution to the forcing source term.

2.4 Interacting disturbances

The multiple-scale method was previously introduced in order to treat the resonant problem originated by the interaction between acoustic wave, vorticity wave, wall vibration and wall roughness. The single disturbances, in fact, for their intrinsic features cannot create any resonance with the Tollmien–Schlichting wave because they do not have the right spatial wavenumber α and time frequency ω corresponding to α_{TS} and ω_{TS} . For example, the acoustic wave, in the incompressible case, is characterized by an infinite spatial wavelength so that the wavenumber is zero and therefore different from α_{TS} , while the frequency could be the same as ω_{TS} . The same happens for the wall vibration disturbance, for which $\alpha = 0$ and the frequency could be the right one. A perturbation characterized by both wavenumber and frequency different from zero is that due to vorticity waves. However, in this case $\alpha = \omega/U_\infty$ so that it is different from α_{TS} anyway. The last disturbance considered is the one induced by the wall roughness, but since it is stationary, it cannot excite Tollmien–Schlichting waves (at least as long as swept wings are not considered). The resonant wave, with the typical wavenumber and frequency close to the Tollmien–Schlichting ones, originates at order $\epsilon\delta$, thanks to the nonlinear interactions between the disturbances at previous orders. Since

$$\alpha_{\epsilon\delta} = \alpha_\epsilon + \alpha_\delta \quad \omega_{\epsilon\delta} = \omega_\epsilon + \omega_\delta$$

in order for $\alpha_{\epsilon\delta}$ and $\omega_{\epsilon\delta}$ to be different from zero, at least one of the two interacting disturbances must be non stationary and one with α different from zero.

2.4.1 Wall vibration – wall roughness interaction

The perturbation originating from the interaction between wall vibration and wall roughness deserves a special remark because one can prove that it does not produce a resonant wave. Let us concentrate on the problem of a rigid wall vibrating in the normal direction. In this case, the wall is described by a function of time $y(t) = \epsilon e^{-i\omega_\epsilon t}$ where ϵ is the amplitude of the wall vibration. It can be proved that the Navier–Stokes equations are invariant with respect to a coordinate transformation

$$Y = y - \epsilon e^{-i\omega_\epsilon t}$$

which means that the solution in the reference frame moving with the wall is the solution obtained with the wall at rest and expressed as a function of $y - \epsilon e^{-i\omega_\epsilon t}$ instead of y . In order to prove that, we introduce a new reference frame

$$X = x; \quad Y = y - \epsilon e^{-i\omega_\epsilon t}; \quad Z = z; \quad T = t$$

so that the new unknowns are

$$U = u; \quad V = v + \epsilon i\omega_\epsilon e^{-i\omega_\epsilon t}; \quad W = w; \quad P = p$$

and the derivatives, as a function of the variables in the new reference frame, read

$$(\cdot)_t = (\cdot)_T + \epsilon i\omega_\epsilon e^{-i\omega_\epsilon t}; \quad (\cdot)_x = (\cdot)_X; \quad (\cdot)_y = (\cdot)_Y; \quad (\cdot)_z = (\cdot)_Z;$$

By substituting the previous expressions in the original Navier–Stokes equations, one gets:

$$\begin{aligned} U_X + V_Y + W_Z &= 0 \\ U_T + \epsilon i\omega_\epsilon e^{-i\omega_\epsilon T} U_Y + U U_X + (V - \epsilon i\omega_\epsilon e^{-i\omega_\epsilon T}) U_Y + W U_Z &= \\ &= -P_X + R^{-1}(U_{xx} + U_{yy} + U_{zz}) \\ V_T + \epsilon i\omega_\epsilon e^{-i\omega_\epsilon T} V_Y + U V_X + (V - \epsilon i\omega_\epsilon e^{-i\omega_\epsilon T}) V_Y + W V_Z &= \\ &= -P_Y + R^{-1}(V_{xx} + V_{yy} + V_{zz}) \\ W_T + \epsilon i\omega_\epsilon e^{-i\omega_\epsilon T} W_Y + U W_X + (V - \epsilon i\omega_\epsilon e^{-i\omega_\epsilon T}) W_Y + W W_z &= \\ &= -P_z + R^{-1}(W_{xx} + W_{yy} + W_{zz}) \end{aligned}$$

after some simplifications, the previous equations read

$$\begin{aligned} U_X + V_Y + W_Z &= 0 \\ U_T + U U_X + V U_Y + W U_Z &= -P_X + R^{-1}(U_{xx} + U_{yy} + U_{zz}) \\ V_T + U V_X + V V_Y + W V_Z &= -P_Y + R^{-1}(V_{xx} + V_{yy} + V_{zz}) \\ W_T + U W_X + V W_Y + W W_z &= -P_z + R^{-1}(W_{xx} + W_{yy} + W_{zz}) \end{aligned}$$

which are the incompressible Navier–Stokes equations in the common form.

Returning to the original transformation $Y = y - \epsilon e^{-i\omega_\epsilon t}$, since the quantity $\epsilon e^{-i\omega_\epsilon t}$ is very small, it is possible to linearize the solution $\mathbf{v}(x, y - \epsilon e^{-i\omega_\epsilon t})$ about y by a Taylor expansion:

$$\mathbf{v}(x, y - \epsilon e^{-i\omega_\epsilon t}) = \mathbf{v}(x, y) - \epsilon \mathbf{v}_y(y) e^{-i\omega_\epsilon t} + \mathcal{O}(\epsilon^2)$$

When the wall roughness is introduced on a wall at rest, the solution is in the form

$$\mathbf{v}(x, y) = \mathbf{V}(x, y) + \delta \mathbf{v}_\delta(x, y) + \mathcal{O}(\delta^2) \quad (2.4.1)$$

where \mathbf{V} is the base flow and \mathbf{v}_δ the disturbance velocity induced by the wall roughness. If the wall roughness and wall vibration effects are coupled, so that the equations are written in the reference frame $y - \epsilon e^{-i\omega_\epsilon t}$, the solution (2.4.1) becomes

$$\mathbf{v}(x, y - \epsilon e^{-i\omega_\epsilon t}) = \mathbf{V}(x, y) - \epsilon \mathbf{V}_y(x, y) e^{-i\omega_\epsilon t} + \delta \mathbf{v}_\delta(x, y) - \epsilon \delta \frac{\partial \mathbf{v}_\delta(x, y)}{\partial y} e^{-i\omega_\epsilon t} + \mathcal{O}(\epsilon^2) + \mathcal{O}(\delta^2)$$

However, in section 2.2.1 devoted to the problem formulation and velocity decomposition, the velocity field due to the base flow and two interacting perturbations was assumed in the form (2.2.3) which reduces to

$$\mathbf{v}(x, y) = \mathbf{V}(x, y) + \epsilon \mathbf{v}_\epsilon(x, y) e^{-i\omega_\epsilon t} + \delta \mathbf{v}_\delta(x, y) + \epsilon \delta \mathbf{v}_{\epsilon\delta}(x, y) e^{-i\omega_\epsilon t} + \mathcal{O}(\epsilon^2) + \mathcal{O}(\delta^2)$$

in the case wall roughness – wall vibration interaction ($\omega_\delta = 0$ corresponds to the disturbance due to the wall roughness). From this considerations, it is clear that

$$\begin{aligned} \mathbf{v}_\epsilon(x, y) &= -\frac{\partial \mathbf{V}(x, y)}{\partial y} \\ \mathbf{v}_{\epsilon\delta}(x, y) &= -\frac{\partial \mathbf{v}_\delta(x, y)}{\partial y} \end{aligned} \quad (2.4.2)$$

and therefore the velocity disturbance at order $\epsilon\delta$ is not originated by the interaction between the two disturbances at order ϵ and δ but is the exact solution of the velocity perturbation induced by the wall roughness on a wall vibrating in the normal direction.

2.4.2 Possible disturbance interactions

The resonant condition is

$$\begin{aligned} \alpha_\delta + \alpha_\epsilon &\approx \alpha_{TS} \\ \omega_\delta + \omega_\epsilon &\approx \omega_{TS} \end{aligned}$$

so that only certain couplings between perturbations at order ϵ or δ can satisfy this constraint. Possible disturbance interactions are therefore:

- Acoustic wave and wall roughness. The acoustic wave problem is considered at order ϵ and the wall roughness at order δ . $\alpha_\epsilon = 0$ and $\omega_\delta = 0$ so that the resonance is guaranteed by

$$\alpha_\delta \approx \alpha_{TS} \quad \omega_\epsilon \approx \omega_{TS}$$

The boundary conditions to be used at the wall, after the linearization, are (2.2.8) so that at order $\epsilon\delta$ the boundary conditions involve the first derivative of the Stokes solution at the wall.

- Vorticity wave and wall roughness. The vorticity wave problem is solved at order ϵ and the wall roughness one at order δ . Since the vorticity wave dispersion relation admits $\alpha_\epsilon \neq 0$ and $\omega_\epsilon \neq 0$, the resonant condition becomes

$$\alpha_\delta + \alpha_\epsilon \approx \alpha_{TS} \quad \omega_\epsilon \approx \omega_{TS}$$

The boundary conditions at the wall, after the linearization, are still (2.2.8) so that at order $\epsilon\delta$ the boundary conditions involve the first derivative of the vorticity wave solution at the wall.

- Acoustic wave and vorticity wave. The acoustic wave, solved at order δ , is characterized by $\alpha_\delta = 0$ and $\omega_\delta \neq 0$. The vorticity wave, on the contrary, admits both $\alpha_\epsilon \neq 0$ and $\omega_\epsilon \neq 0$, so that the resonant condition reads

$$\alpha_\epsilon \approx \alpha_{TS} \quad \omega_\delta + \omega_\epsilon \approx \omega_{TS}$$

Since the combination between the acoustic wave and vorticity wave is not related to wall roughness or wall vibration, the boundary conditions at the wall for the problem at order $\epsilon\delta$ are homogeneous. The only exciting source is therefore the nonlinear interaction in the x -momentum and y -momentum equations.

Other combinations, like wall vibration and acoustic wave are obviously not interesting because they do not produce any resonance.

2.4.3 Receptivity function

The aim of the receptivity study is to relate the amplitude of the unstable wave generated inside the boundary layer with the amplitude of the physical disturbance that generated it. However, since most of the possible disturbance couplings previously introduced, a part from the acoustic wave – vorticity wave interaction, are characterized by the “adapting mechanism” due to the wall roughness, it is possible to relate the unstable wave amplitude also to the wall roughness shape $h(x)$. In these cases, in fact, the corresponding solution at order δ is a linear function of $h(x)$ (because of the related boundary condition), so that the solution at order $\epsilon\delta$ is a linear function of $h(x)$ as well. This allows us to rewrite the forcing vector $\mathbf{y}(x)$ appearing in (2.3.11) as

$$\mathbf{y}(x) = \tilde{\mathbf{y}}(x)h(x)$$

so that the integral in (2.3.14) can be written as

$$\int_{x_0}^{x_f} \mathbf{r}(x) \cdot \mathbf{y}(x) dx = \int_{x_0}^{x_f} \mathbf{r}(x) \cdot \tilde{\mathbf{y}}(x)h(x) dx = \int_{x_0}^{x_f} r_h(x)h(x) dx$$

and the solution at order $\epsilon\delta$ is expressed in the form

$$\mathbf{f}_{\epsilon\delta}(x_f) = \tilde{\mathbf{f}}_0(x_f) \left(\int_{x_0}^{x_f} r_h(x)h(x) dx \right) e^{-i\omega_\epsilon t} + \mathcal{O}(\tilde{\epsilon}) \quad (2.4.3)$$

It is important to remark that the solution $\mathbf{f}_{\epsilon\delta}$, in the general case, is expressed by a convolution and not by an integral. The simplification to an integral is due to the fact that we are focusing on a certain mode selected by the Tollmien–Schlichting problem. In fact, in the general case where the wall roughness is involved, the exciting source $\mathbf{y}(x)$, containing the nonlinear interaction between two disturbances, can be written using the Green function \mathbf{g} as

$$\mathbf{y}(x) = \int \mathbf{g}(x, x') h(x') dx'$$

and therefore the solution $\mathbf{f}_{\epsilon\delta}$ involving the left eigenvector $\mathbf{y}^*(x)$ reads

$$\mathbf{f}_{\epsilon\delta}(x_f) = \tilde{\mathbf{f}}_0(x_f) \left(\int \int \mathbf{y}^*(x) \mathbf{g}(x, x') h(x') dx' dx \right) e^{-i\omega\epsilon t} + \mathcal{O}(\tilde{\epsilon})$$

which shows that the dependence of $\mathbf{f}_{\epsilon\delta}$ on the roughness shape, in the general case, is more complicated than the simple integral (2.4.3).

Considering the expression (2.4.3), if the eigensolution $\tilde{\mathbf{f}}_0(x_f)$ has been normalized in such a way that $\max |\tilde{u}_0(x_f, y)| = 1$, the amplitude at the final station, defined as the maximum value of $u_0(x_f, y)$, is

$$A(x_f) = \left| \epsilon\delta \int_{x_0}^{x_f} r_h(x) h(x) dx \right|$$

This expression is extremely important because it relates the final amplitude of the TS wave $A(x_f)$ to ϵ (corresponding to the amplitude of the acoustic wave, vorticity wave or wall displacement due to the wall vibration), to δ (the amplitude of the wall roughness) and to the shape of the wall roughness $h(x)$. An essential role is played by $r_h(x)$ which is the receptivity to the wall roughness and represents the sensitivity of the final amplitude to the wall shape $h(x)$. The amplitude $A(x_f)$, as previously defined, depends on the normalization chosen for the eigenvector, while the amplitude of the solution (2.4.3) does not.

By rearranging expression (2.3.13), the receptivity function $r_h(x)$ becomes

$$r_h(x) = \frac{\mathbf{y}^* \cdot \tilde{\mathbf{y}}}{\mathbf{y}^* \cdot (\mathbf{H}\tilde{\mathbf{f}}_0)} \text{EXP} \left[- \int_x^{x_f} \left(\frac{\mathbf{y}^* \cdot \left(\mathbf{H} \frac{d\tilde{\mathbf{f}}_0}{dx} + \mathbf{C}\tilde{\mathbf{f}}_0 \right)}{\mathbf{y}^* \cdot (\mathbf{H}\tilde{\mathbf{f}}_0)} - i\alpha \right) dx' \right] \quad (2.4.4)$$

where the left eigensolution \mathbf{y}^* represents a weight for the known term at order $\epsilon\delta$. The previous expression can be rewritten in a more compact form as

$$r_h(x) = \hat{r}_h(x) e^{-\int_x^{x_f} a(x') dx'} \quad (2.4.5)$$

If we suppose that the receptivity function $r_h(x)$ and the wall roughness shape $h(x)$ vanish as $x \rightarrow -\infty$ and $x \rightarrow x_f$, the final amplitude can be written as

$$A(x_f) = \left| \epsilon\delta \int_{-\infty}^{\infty} h(x) \hat{r}_h(x) e^{-\int_x^{x_f} a(x') dx'} dx \right|$$

The receptivity function $r_h(x)$ is calculated for a fixed final station x_f , so that the amplitude $A(x_f)$ can be easily computed for different shapes $h(x)$. However, in order to let $r_h(x)$ be independent of x_f , it is possible to separate the integral between x and x_f introducing the first neutral point x_I :

$$A(x_f) = \left| \epsilon \delta e^{-\int_{x_I}^{x_f} a(x') dx'} \int_{-\infty}^{\infty} h(x) \hat{r}_h(x) e^{-\int_x^{x_I} a(x') dx'} dx \right|$$

or better

$$A(x_f) = \left| \epsilon \delta e^{-\int_{x_I}^{x_f} a(x') dx'} \int_{-\infty}^{\infty} h(x) \bar{r}_h(x) dx \right|$$

The functions

$$\hat{r}_h(x) = \frac{\mathbf{y}^* \cdot \tilde{\mathbf{y}}}{\mathbf{y}^* \cdot (\mathbf{H} \tilde{\mathbf{f}}_0)}$$

and

$$\bar{r}_h(x) = \hat{r}_h(x) e^{-\int_x^{x_I} a(x') dx'}$$

are called respectively receptivity coefficient and receptivity function. In the parallel assumptions $\hat{r}_h(x)$ simply reduces to the coefficient computed by Crouch [33], Choudhari and Streett [29] and Hill [63].

The interaction between the acoustic wave and vorticity wave does not allow the possibility to introduce a receptivity function varying with x . In this case, since the boundary condition at the wall is already defined at $y = 0$ ($h(x) = 0$), the linearization at the wall is not needed and therefore the boundary condition at the wall is homogeneous at order ϵ (vorticity wave perturbation), at order δ (acoustic wave perturbation) and at order $\epsilon\delta$. The amplitude at the final station is written as

$$A(x_f) = \left| \epsilon \delta A_I e^{-\int_{x_I}^{x_f} a(x') dx'} \right|$$

where A_I is a constant given by the integral on the streamwise coordinate

$$A_I = \int_{-\infty}^{\infty} \hat{r}_h(x) e^{-\int_x^{x_I} a(x') dx'} dx$$

2.5 Results

For each of the perturbation interactions considered, the corresponding results are shown in the following figures. The structure of the presentation is common: first the two interacting perturbation are reported in order to check where their influence is greater. Than the forcing terms originating from their interaction and the corresponding terms of the left eigensolution are shown. Finally, the receptivity coefficient $\hat{r}_h(x)$, which is actually the dot product between the forcing term and the left eigensolution, and the receptivity function $\bar{r}_h(x)$ are plotted versus the Reynolds number R .

2.5.1 Acoustic wave – wall roughness interaction

In figure (2.2)–a the perturbation induced by the acoustic wave present in the free–stream is reported for the streamwise location corresponding to the first neutral point x_I . The corresponding boundary layer reference length δ_0 is therefore $\delta_0 = \sqrt{\nu x_I / U_\infty}$

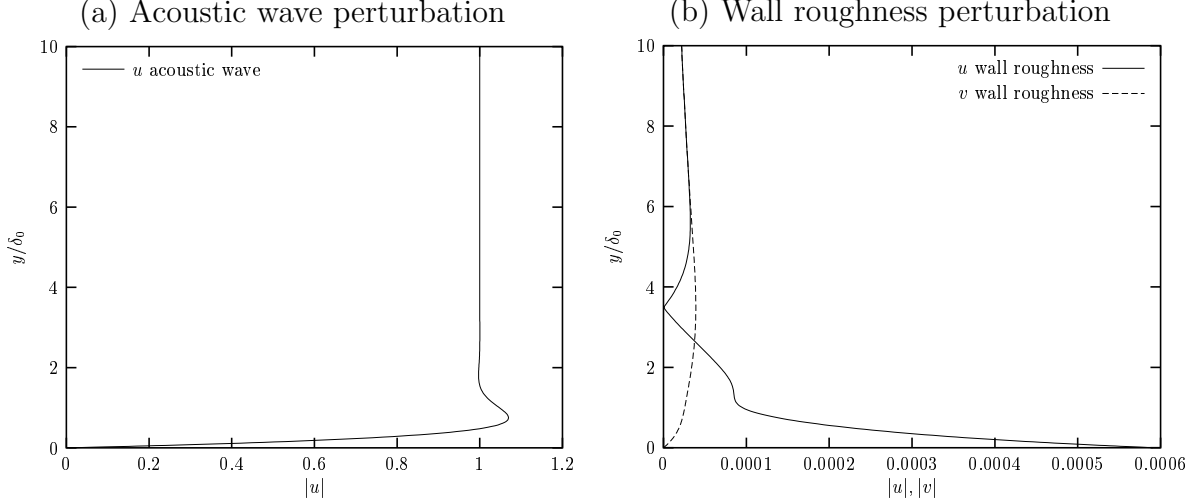


Figure 2.2: Perturbations. $F = \omega / (\nu U_\infty^2) = 5.9 \cdot 10^{-5}$, $R_I = 557$, $\delta_0 = \sqrt{\nu x_I / U_\infty}$

and the corresponding Reynolds number $R_I = U_\infty \delta_0 / \nu$, where $R = \sqrt{Re_x} = \sqrt{U_\infty x / \nu}$. The dimensionless frequency $F = \omega / (\nu U_\infty^2)$ has been chosen as $F = 5.9 \cdot 10^{-5}$ because for this value the amplification reaches a maximum with respect to F at fixed Reynolds number. The v –component is identically zero, whereas the u –component, independent of x , is Stokes’ solution. It is clear that the main influence of the acoustic perturbation occurs inside the boundary layer; on the contrary, u is constant for $y / \delta_0 > 3$, reaching the asymptotic value (this means that the wall–normal derivatives in the exciting terms will be zero). In figure (2.2)–b the perturbation induced by the wall roughness is shown. It is computed at $\alpha_\delta \approx \alpha_{TS}$ and its main influence seems to be localized inside the boundary layer, going asymptotically to zero as $y / \delta_0 \rightarrow \infty$. The y –scale of the plot is limited to 10, but the computations are performed with $y_{\max} / \delta_0 = 180$ and an outer zoom is proposed in section 2.5.2 for the coupling between vorticity wave and wall roughness. The interaction at order $\epsilon \delta$ between the previous perturbations produces the forcing terms reported in figure (2.3)–a. Both the x –momentum and y –momentum forcings are shown. The strongest is the one corresponding to the x –momentum and it is mainly concentrated inside the boundary layer, as a consequence of the previous perturbations. An important remark regarding the forcing terms is that there is also a contribution coming from the non homogeneous boundary condition at the wall for the problem at order $\epsilon \delta$. Usually, this term is much higher than the values reported in figure (2.3)–a.

In figure (2.3)–b the left eigenfunction is shown. The terms corresponding to the x –momentum and y –momentum are separated and they can be viewed as weights for the forcing terms. It is clear that also in this case the highest values are concentrated inside the boundary layer, so that the receptivity coefficient is expected to be quite strong. In figure (2.4)–a the dot product between the forcing terms and their relative weight

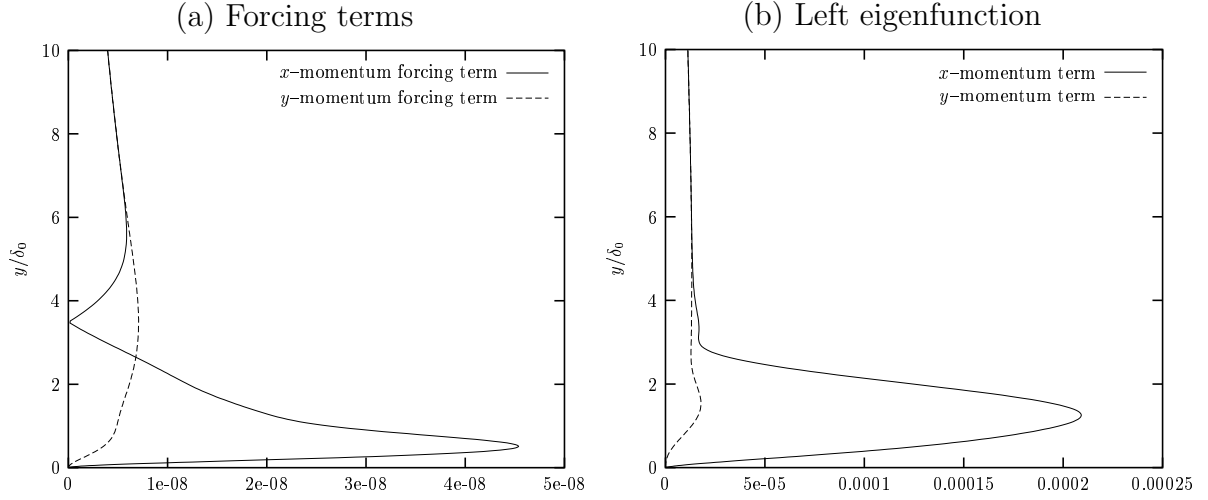


Figure 2.3: Interaction between acoustic wave and wall roughness at order $\epsilon\delta$. $F = \omega/(\nu U_\infty^2) = 5.9 \cdot 10^{-5}$, $R_I = 557$, $\delta_0 = \sqrt{\nu x_I/U_\infty}$

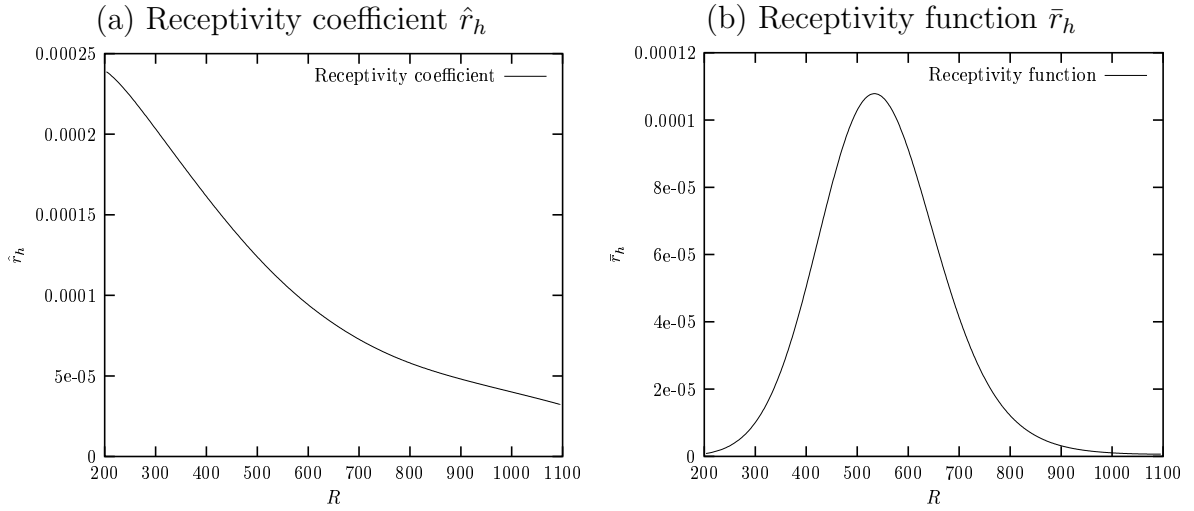


Figure 2.4: Receptivity characteristics for the interaction between acoustic wave and wall roughness. $F = \omega/(\nu U_\infty^2) = 5.9 \cdot 10^{-5}$, $R_I = 557$, $\delta_0 = \sqrt{\nu x_I/U_\infty}$

(the left eigenfunction) is reported. It represents the receptivity coefficient \hat{r}_h defined in (2.4.5) and it is clear that it monotonically decreases with R . Finally, in figure (2.4)–b the receptivity function \bar{r}_h is reported. It is referred to the neutral point, which means that the value of the receptivity coefficient and the receptivity function are the same at the neutral point, found at $R = 557$. The meaning of the receptivity function is that it allows us to compute the amplitude of the excited wave at the first neutral point simply from the integral

$$A(x_I) = \left| \epsilon\delta \int_{-\infty}^{\infty} h(x)\bar{r}_h(x) dx \right|$$

for a given wall-roughness shape $h(x)$.

2.5.2 Vorticity wave – wall roughness interaction

The perturbation induced by a vorticity wave present in the free-stream is reported in figure (2.5)–a. It has been computed for the dimensionless frequency $F = \omega/(\nu U_\infty^2)$ equal

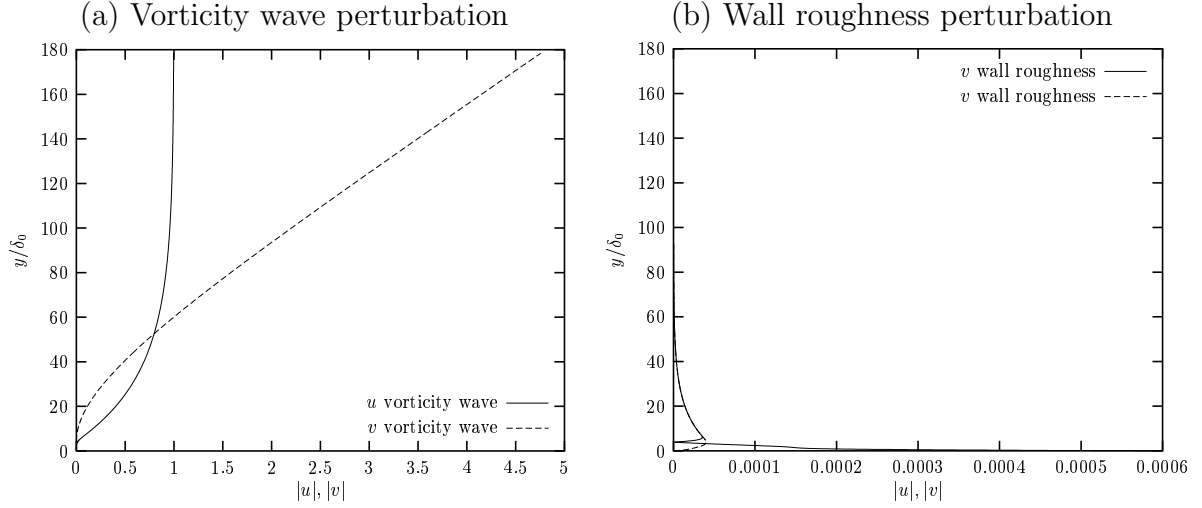


Figure 2.5: Perturbations. $F = \omega/(\nu U_\infty^2) = 5.9 \cdot 10^{-5}$, $R_I = 557$, $\delta_0 = \sqrt{\nu x_I/U_\infty}$

to $F = 5.9 \cdot 10^{-5}$ (the same used in the previous section) and it is referred to the first neutral point, corresponding to $R_I = 557$, where the TS wavenumber is $\alpha_{\text{TS}}\delta_0 = 0.1$. The correct value of the spatial wavenumber to be inserted in the computation of vorticity wave perturbation α_ϵ is furnished by (2.2.10) so that $\alpha_\epsilon\delta_0 = 0.0329$. Since $\alpha_\delta = \alpha_{\text{TS}} - \alpha_\epsilon$, the value of the wavenumber to be used for the wall roughness perturbation turns out to be $\alpha_\delta\delta_0 = 0.067$. The first remark regarding figure (2.5)–a is that a very large value of y/δ_0 is required in order to achieve the asymptotic values of u and v imposed by the outer vorticity wave. It is clear that the u -component of the vorticity wave perturbation reaches a constant value equal to 1 as $y/\delta_0 \rightarrow \infty$, whereas the v -component behaves like a linear function, as described by the expressions (2.2.11). The main influence of this perturbation is located outside the boundary layer, as reported by Wu [111], and confirms the “shear sheltering” mechanism described by Hunt [66]. On the contrary, figure (2.5)–b reports the perturbation due to the wall roughness which is mainly located inside the boundary layer. As previously described, the wavenumber α_δ is chosen so as to produce a resonance with the TS waves. The forcing terms, produced by the interaction of the perturbations reported in figure (2.5), are shown in figure (2.6)–a. In contrast with the acoustic wave – wall roughness interaction, here the forcing is concentrated in the outer part of the boundary layer (about $y/\delta_0 = 15$), primarily due to the vorticity wave perturbation. In fact, u and v generated by the vorticity wave behave respectively like a constant and a linear function of y/δ_0 . The perturbation due to the wall roughness exponentially decays with distance from the wall, so that the forcing term goes to zero with y/δ_0 . However, the distance required is much higher than in the previous case. The receptivity characteristics are reported in figure (2.7). The receptivity coefficient monotonically decreases with R just as in the acoustic wave – wall roughness interaction. However, in this case the slope of the curve is larger than in the

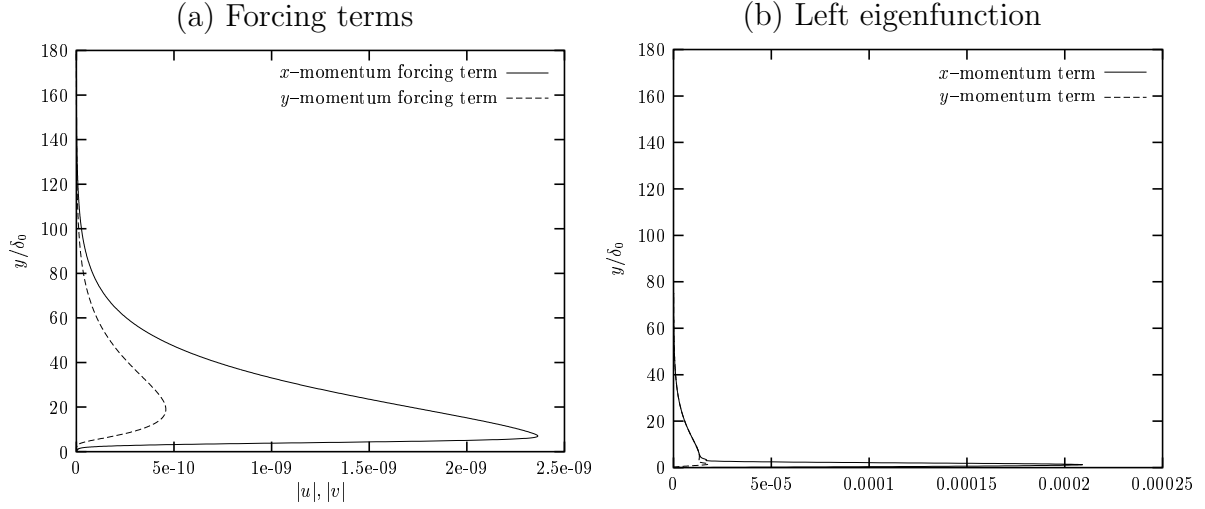


Figure 2.6: Interaction between vorticity wave and wall roughness at order $\epsilon\delta$. $F = \omega/(\nu U_\infty^2) = 5.9 \cdot 10^{-5}$, $R_I = 557$, $\delta_0 = \sqrt{\nu x_I/U_\infty}$

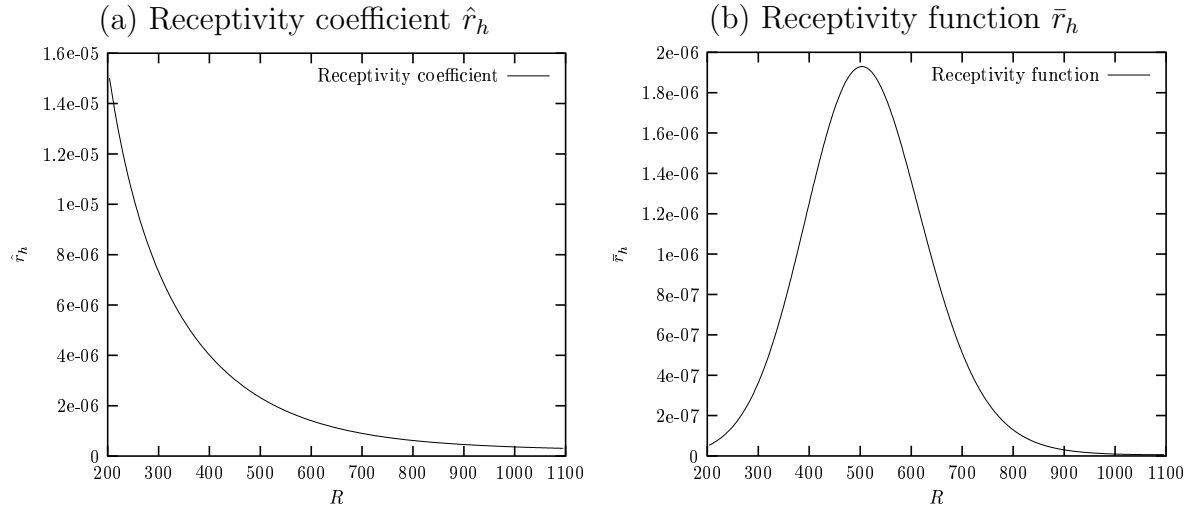


Figure 2.7: Receptivity characteristics for the interaction between vorticity wave and wall roughness. $F = \omega/(\nu U_\infty^2) = 5.9 \cdot 10^{-5}$, $R_I = 557$, $\delta_0 = \sqrt{\nu x_I/U_\infty}$

previous one. In figure (2.7)–b the receptivity function is plotted. It is referred to the first neutral point. Obviously the shape is the same as the one observed for the acoustic wave – wall roughness interaction. The main difference is in the peak amplitude, three orders of magnitude smaller. This feature could let us think that vorticity wave – wall roughness interaction is a negligible phenomenon (shear sheltering [66]). It can be true, but the final amplitude has to be multiplied by ϵ , the amplitude of the u -component vorticity wave in the free-stream, and δ , the amplitude of the wall roughness. Therefore, the relative importance of one phenomenon with respect to the other depends on the actual environmental disturbances involved.

2.5.3 Acoustic wave – vorticity wave interaction

In figure (2.8) the acoustic wave (order δ) and vorticity wave (order ϵ) perturbations are reported. They are computed for $F = 5.9 \cdot 10^{-5}$ (the same as in the previous cases) and they are referred to the first neutral point, corresponding to $R_I = 557$, where the TS wavenumber is $\alpha_{\text{TS}}\delta_0 = 0.1$. The resonant condition is $\alpha_\epsilon \approx \alpha_{\text{TS}}$ and $\omega_\epsilon + \omega_\delta \approx \omega_{\text{TS}}$. The

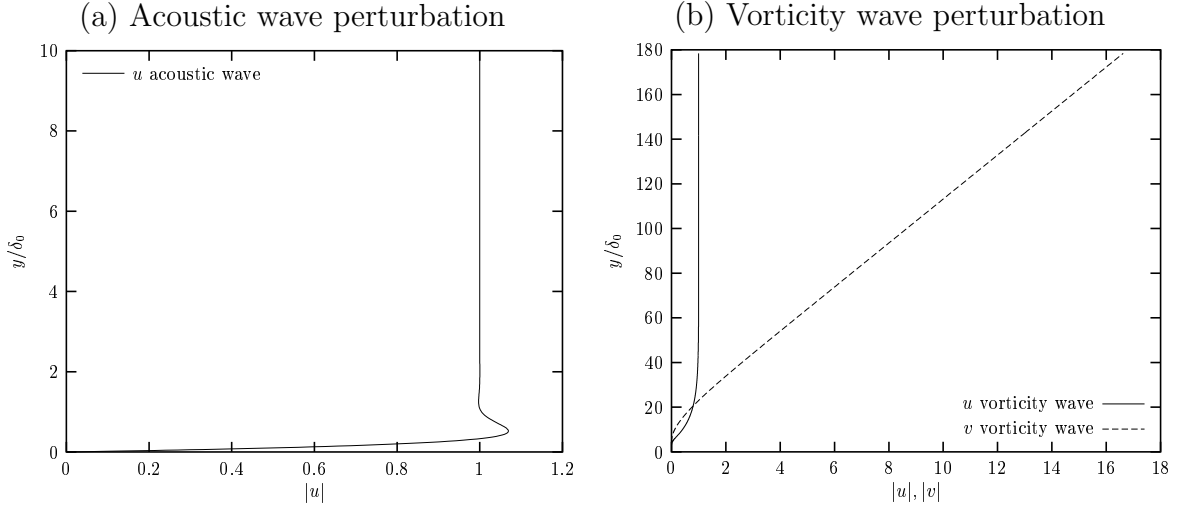


Figure 2.8: Perturbations. $F = \omega/(\nu U_\infty^2) = 5.9 \cdot 10^{-5}$, $R_I = 557$, $\delta_0 = \sqrt{\nu x_I/U_\infty}$

wavenumber for the vorticity wave is thus $\alpha_\epsilon = 0.1$, whereas the frequency ω_ϵ can be obtained by (2.2.10),

$$\omega_\epsilon = \frac{\alpha_\epsilon^2 + i\alpha_\epsilon U_\epsilon R}{iR}$$

The frequency of the acoustic wave is then computed as $\omega_\delta = \omega_{\text{TS}} - \omega_\epsilon$. The velocity perturbation due to the acoustic wave is reported in figure (2.8)–(a) and the vorticity wave perturbation in figure (2.8)–(b). The behavior of the latter as a function of y shows a slight difference with figure (2.5)–(a): for the present case, the u -velocity component reaches the asymptotic value at $y/\delta_0 \approx 60$, while $u = 1$ was previously reached at $y/\delta_0 \approx 140$ (figure (2.5)–(a)). The nonlinear interaction between the two disturbances of figure (2.8) is shown in figure (2.9)–(a). As usual, the x -momentum and y -momentum are separated. The main difference with the previous cases is that the forcing source does not vanish as y/δ_0 goes to infinity. This is obviously due to the profiles of the interacting disturbances: the streamwise velocity component reaches an asymptotic value for both acoustic wave and vorticity wave, while the v -component of the vorticity wave perturbation grows linearly. This produces a forcing term that behaves almost as the vorticity wave perturbation (a part from the scale). The left eigenfunction is reported in figure (2.9)–(b) in order to show that when the weight is maximum, the forcing term is very small, while when the weight goes exponentially to zero, the forcing behaves like a constant (x -momentum) or linearly (y -momentum). The coupling between acoustic wave and vorticity wave does not allow the introduction of a wall receptivity function because the boundary conditions at the wall are homogeneous. On the contrary, in this case, a constant A_I can be introduced (see section 2.4.3) so that $A(x_f) = |\epsilon\delta A_I e^{-\int_{x_I}^{x_f} a(x') dx'}|$.

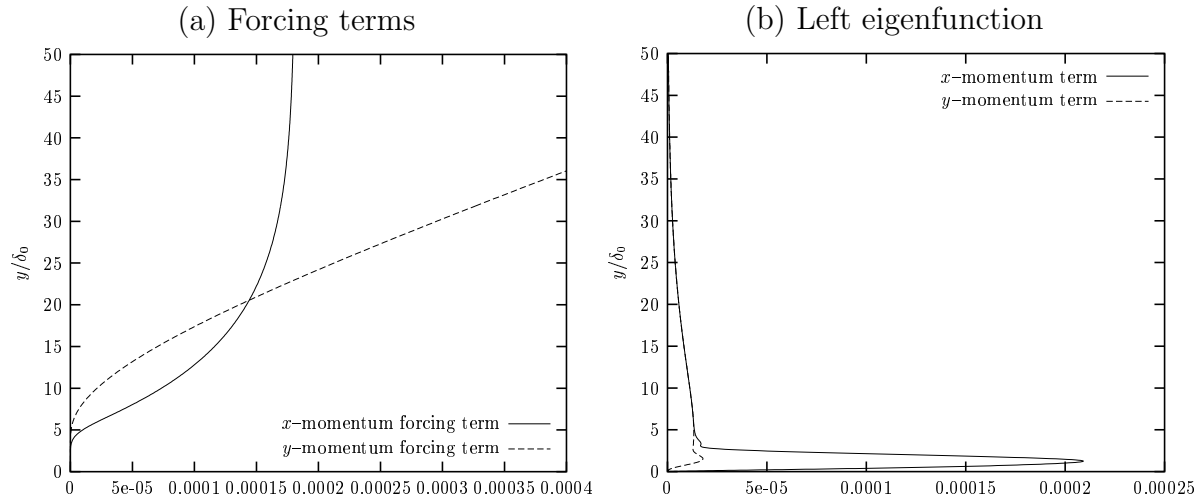


Figure 2.9: Interaction between acoustic wave and vorticity wave at order $\epsilon\delta$. $F = \omega/(\nu U_\infty^2) = 5.9 \cdot 10^{-5}$, $R_I = 557$, $\delta_0 = \sqrt{\nu x_I/U_\infty}$

For this test $A_I = 2.92$, but the spectrum as function of α_{TS} can be obtained performing different tests changing ω_{TS} .

2.6 Conclusions

In this study the receptivity to the quadratic mixing of different disturbances has been considered. The resonant singular problem is solved introducing a multiple-scale expansion of the solution. A receptivity function is obtained: it relates the amplitude of the unstable wave to the physical amplitude of the disturbances which produced it.

The possible interacting perturbations here considered are those due to an acoustic wave or vorticity wave, present in the free-stream, or due to wall vibration and wall roughness. The former induce a corresponding velocity disturbance into the boundary layer thanks to boundary conditions at infinity, whereas the latter induce a perturbation in the boundary layer because of non homogeneous forcing terms at the wall arising from the linearization of the homogeneous wall boundary conditions. However, each of these disturbances cannot create any resonance with the Tollmien–Schlichting waves, because the typical time frequency and spatial wavenumber are different from those which satisfy the Tollmien–Schlichting dispersion relation.

The right values in order to originate resonance can be obtained from the nonlinear mixing of at least two interacting disturbances. In fact, in this case, the time frequency and spatial wavenumber of the resonant wave are given by the sum or difference of the corresponding frequency and wavenumber of the interacting disturbances. For example, in the acoustic wave – wall roughness interaction, the correct time frequency is furnished by the acoustic wave and the spatial wavenumber is due to the wall roughness; for the interaction between a vorticity wave and the wall roughness, the frequency is due only to the vorticity wave traveling in the free-stream, whereas the spatial wavenumber is the sum of the contributions coming from the vorticity wave and wall roughness. For

the interaction between an acoustic wave and a vorticity wave, the correct wavenumber originates only from the vorticity wave, whereas the contribution to the time frequency is due to both disturbances. Finally, for the interaction between the wall vibration and wall roughness, the correct time frequency is given by the unsteady wall vibration and the correct spatial wavenumber by the wall roughness.

Results show that the acoustic wave and wall roughness perturbations can enter in the boundary layer, creating a forcing term that is mainly concentrated close to the wall. Moreover, the weight function by which the forcing term is multiplied, that is represented by the left eigensolution, reaches its maximum inside the boundary layer, in the neighborhood of the maximum of the forcing source. This feature leads to a receptivity coefficient and receptivity function which are quite strong. On the contrary, the vorticity wave interacting with wall roughness produces a coupling which is located outside the boundary layer. The main reason is that the asymptotic behavior of the streamwise and wall-normal velocity perturbations, induced by the free-stream vorticity, is respectively like a constant and a linear function. The forcing term produced by this interaction is therefore shifted far from the wall and the dot product with the left eigenfunction, which reaches its maximum in the middle of the boundary layer, makes the receptivity coefficient and the receptivity function smaller than in the previous case. Moreover, the forcing term is one order of magnitude smaller than for the acoustic wave – wall roughness interaction, explaining the reason why, in this case, the receptivity function is smaller. The interaction between the acoustic wave and vorticity wave show a forcing term which does not vanish at infinity because the interacting disturbances behave like a constant or a linear function of the wall-normal coordinate. On the contrary, the left eigenfunction exponentially decreases with the distance from the wall. Finally, it has been proved that the interaction between the wall-normal vibration and wall roughness is unable to create resonant conditions with the TS waves.

In all these cases, however, it should be kept in mind that the amplitude of the excited wave is given by a constant or the integral of the product between the receptivity function and the wall shape, multiplied by ϵ and δ . The latter are respectively the amplitude of the acoustic wave, vorticity wave and wall displacement (ϵ) and the amplitude of the typical wall roughness (δ). This basically implies that even if the receptivity function for the vorticity wave – wall roughness interaction is smaller than for the acoustic wave – wall roughness interaction, if the amplitude ϵ of the vorticity wave is much greater than the amplitude of the acoustic wave, the product $\epsilon\delta$ could produce a much larger effect in the former case than in the latter.

The main conclusion from this study is that the amplitude of the resonant wave is obtained as a function of the wall shape and the physical amplitude of the external disturbances, for different interacting excitation sources.

Non-parallel effects are taken into account thanks to the multiple-scale approach, which is here introduced in the non-homogeneous form. From the numerical point of view, the multiple-scale method is not computationally expensive and does not have numerical stability problems. Moreover, the formulation is general and can be applied to any base flow, obtained from computations or experimental data. Therefore, receptivity analysis using multiple scales can be efficiently included in industrial codes for transition prediction.

Chapter 3

Optimal perturbations, optimal control and robust control of the algebraic instability in the nonlinear regime

3.1 Introduction

The aim of the present work is the study of the the three-dimensional, algebraically growing instability of a Blasius boundary layer in the nonlinear regime. Adjoint-based optimization is used to determine the “optimal” steady, but spanwise-sinusoidal leading-edge excitation that provides the maximum energy growth for a given initial energy. A similar technique is then used to find a control in the form of a spanwise-uniform wall suction that optimally opposes this instability’s growth. Finally, since the presence of the control at the wall makes the optimal initial perturbation different from the uncontrolled case, robust optimal control is applied. Results show, in the framework of a general agreement with previous linear computations, a non negligible variation of the maximally amplified wavenumber with initial and controlling amplitude.

3.1.1 Algebraic instability

The linear theory for the instability analysis sometimes fails predicting a stable behavior for flows, which experiments show to be unstable. For instance, the theory applied to a pipe flow reveals that all the eigenvalues are stable and thus the only possible state is the stable one. Despite this consideration, Reynolds found that if the parameter Re (Reynolds number) is greater than a certain threshold, transition is observed. Moreover, for certain flows, for example plane Poiseuille flow, transition practically occurs at a Re number smaller than the critical value expected from the theory. This means that there must be another instability growing mechanism which cannot be seen in the classical Orr-Sommerfeld formulation.

Ellingsen and Palm [43] and Landhal [74] explained this kind of growth identifying a new amplification mechanism of the disturbances, according to which a longitudinal

vortex superimposed to a two dimensional boundary layer can lift up low-velocity fluid from the wall and push down high-velocity fluid towards the wall. Since the structure of the boundary layer is elongated in the streamwise direction, with a typical length $Re^{1/2}$ greater than the boundary layer thickness, the disturbance accumulated in the streamwise direction can be $Re^{1/2}$ times greater than the original one.

The combination of this basically inviscid amplification mechanism with the damping effect of viscosity leads to what is nowadays called *algebraic growth* or *transient growth*. This mechanism is also believed to be at the origin of the Klebanoff modes giving rise to the so-called bypass transition (see Morkovin [86] and Morkovin and Reshotko [88]). Recent studies (Luchini [78]) show that viscosity is not sufficient in order to damp the algebraic growth observed in the boundary layer, so that the receptivity to this kind of exciting source (low-amplitude streamwise vortices) can play an important role in boundary layer transition.

3.1.2 Previous work

In the framework of algebraic instability, receptivity to upstream disturbances which can lead to boundary layer transition was first faced by searching the initial conditions, for the boundary layer past a flat plate, that produce the strongest energy growth. This is known as the “optimal perturbation” approach.

Previously published work in this field is all in a linear framework. As far as the temporal stability problem is concerned, optimal perturbations were first so named by Farrell [44], as the input disturbance of the boundary layer that produces the maximum gain, defined as the ration between the perturbation kinetic energy and the initial perturbation energy. This first approach was in the two dimensional plane channel flow framework. Actually, Boberg and Brosa [14] had already introduced a similar concept for flow in a pipe, but Butler and Farrell [17] formulated the definition and considered three-dimensional optimal perturbations with respect to temporal growth for not only plane Couette and Poiseuille flow, but also for a parallel approximation of Blasius boundary layer. Corbett and Bottaro [32] found the temporal-growth optimal perturbations for parallel boundary layers subject to streamwise pressure gradient considering Falkner-Skan base flow profiles and Corbett and Bottaro [31] studied the temporal growth in swept boundary layers described by Falkner-Skan-Cooke similarity solution.

The problem of spatial stability was recently tackled by Luchini [79] and Andersson *et al.* [4]. They both found that the optimal initial disturbance is in the form of stationary streamwise vortices and the velocity field induced by them is dominated by streamwise streaks. The maximum amplification is observed in the stationary case (frequency $\omega = 0$) and for a certain value of the spanwise wavenumber $\beta\delta = 0.45$. In all these cases, however, the boundary layer equations linearized about a given base flow are used, looking for the initial perturbation which maximizes the gain. On the other hand, it is interesting to investigate the non linear regime by solving the complete boundary layer equations and searching the initial perturbation which produces, via non linear interaction between different modes, the highest gain.

Andersson *et al.* [5] investigated via direct numerical simulation the nonlinear evolution of the optimal perturbations found with the linear approach (those computed

by Luchini [79] and Andersson *et al.* [4]). Therefore they did not find the optimal perturbations in the nonlinear case, but they focused on the temporal inviscid instability of these streamwise vortices, called streaks, retaining the nonlinear terms in the Navier–Stokes equations. Results show that the streak’s critical amplitude, beyond which streamwise travelling waves are excited, is about 26% of the free–stream velocity.

If the term “optimal perturbation” identifies the perturbation that produces the worst effects as far as the stability of the flow is concerned, the idea of “optimal control” is exactly the opposite, because its aim is to find the best way of controlling the worst initial perturbations. Let us suppose that a perturbation is present, in the worst case the optimal perturbation, as initial condition for the boundary layer equations and we want to control the evolution of the perturbation in order to delay transition. This can be done by controlling the perturbation energy and requiring, for instance, the energy at the final station to be the lowest, or the integral of the energy over the whole domain to be the lowest. In order to do that, it appears from the literature that a control by blowing and suction at the wall would be the most convenient (see Florian and Saric [45] and Myose and Blackwelder [90] [91]). Pralits *et al.* [94], using an adjoint–based optimization technique in the framework of Parabolized Stability Equations, found the steady suction for disturbance control in incompressible flows. Their approach is linear and considers Tollmien–Schlichting waves, steady streamwise streaks and oblique waves. Bewley and Liu [13] applied modern control theory to determine optimal and robust control, in a linear framework and at a fixed Reynolds number, via wall–normal velocity at the wall for waves and non–modal disturbances in plane channel flows. Corbett [30] studied the control of parallel temporal optimal perturbations via blowing/suction at the wall using a cost function which combined a weighted sum of the terminal and average disturbance growth and the control effort in a linear framework and for Falkner–Skan–Cooke similarity solutions. Cathalifaud and Luchini [20] considered the control of algebraic growth in boundary layers by blowing and suction at the wall. In their work, the boundary layer equations linearized about the Blasius base flow are solved using the optimal perturbation as initial condition. Suction at the wall is applied, in the form of a given v –component of the perturbation velocity. This is a cancellation control, in which the oscillating flow induced by the wall suction and blowing is optimized so as to linearly cancel as much as possible the perturbation. In a nonlinear framework, on the other hand, one can also resort to a mean–flow motion of the type classically proposed for transition control (see chapter XIV of Schlichting [102]). This kind of control can be more easily implemented because the controlling suction is spanwise–uniform rather than oscillating and requires no feedback.

Usually optimal control is applied in order to opposite a previously computed optimal perturbation. However, the optimal perturbation was computed without any control, so that the presence of the control makes the optimal perturbation different from the one used. For this reason, optimal control sometimes is not the correct solution, but robust control is needed. The latter allows to compute simultaneously the worst initial perturbation in the presence of a control and the best optimal control to that initial perturbation. In this framework, Bewley *et al.* [12] presented in a rigorous form the optimal control problem for the Navier–Stokes equations. Conditions on the initial data, the parameters in the cost functional and the regularity of the problem are established

such that existence and uniqueness of the solution to the robust control problem can be proved. Both linear and nonlinear cases are treated, and numerical algorithm based on the repeated computation of an adjoint field are proposed.

3.1.3 Goal of the present work

Boundary layer equations are parabolic partial differential equations and for this reason they need initial conditions at $x = 0$ and boundary conditions at the wall and at infinity. They can be seen as a ‘black box’ which receives initial conditions and boundary conditions as inputs and amplifies or damps them, at the output. It is therefore reasonable to ask the following questions: what is the initial condition which provokes the maximum energy growth and that thus represents the greatest danger as far as transition is concerned? And, what is the best boundary condition to apply at the wall for the mean v -velocity component in order to control the energy growth due to the worst initial condition? The answers are respectively the optimal perturbation and the optimal control.

In previous work concerning optimal perturbations or optimal control the linearized boundary layer equations have always been used. This means that the result is qualitatively independent of the initial energy of the perturbation, since the whole perturbation field is defined up to a constant. Basically, the main difference between a linear and nonlinear study is that in the latter there exists a certain minimum threshold for the initial energy, above which the nonlinear interactions are such that the exponential damping is no more able to attenuate the instability. A saturation state is thus reached and the disturbance energy remains more or less constant with streamwise position

The main goal of this work is therefore to consider the complete boundary layer equations without any linearization. The velocity is decomposed in a Fourier series along the spanwise direction so that the use of different modes allows us to consider their interaction and the nonlinear effects introduced by them.

Optimal steady spanwise-sinusoidal leading-edge excitation that provides the maximum energy growth for a given initial energy will first be found. Then it will be optimally controlled using a spanwise-uniform wall suction velocity in order to obtain the minimum energy’s growth. Finally, since the presence of the control at the wall makes the optimal initial perturbation different from the uncontrolled case, robust optimal control is studied.

3.2 Problem formulation

The problem of algebraic instability in an incompressible boundary layer over a flat plate is studied by considering the general three dimensional incompressible boundary layer equations. They are more simple than the Navier–Stokes equations and, since they are parabolic in the streamwise direction, a marching technique is allowed in order to numerically solve them. However, two different three-dimensional formulations of the boundary-layer approximation can generally be adopted, depending on whether the spanwise scale of the considered phenomenon is comparable to the streamwise scale L

or to the normal scale $\delta = (\nu L/U_\infty)^{1/2}$ (see Luchini [78]). The first case is typically produced by a three-dimensional outer stream, while the second one is typical of three-dimensionalities originating inside the boundary layer itself. For this reason we use the second formulation. The equations, written in boundary layer variables, and in conservative form, which offers several advantages, read:

$$\begin{aligned} u_x + v_y + w_z &= 0 \\ (uu)_x + (uv)_y + (uw)_z - u_{yy} - u_{zz} &= 0 \\ (uv)_x + (vv)_y + (vw)_z + p_y - v_{yy} - v_{zz} &= 0 \\ (uw)_x + (vw)_y + (ww)_z + p_z - w_{yy} - w_{zz} &= 0 \end{aligned} \tag{3.2.1}$$

where the u velocity component is made dimensionless with respect to the outer velocity U_∞ , whereas the v and w (respectively the wall-normal and spanwise) components are made dimensionless with respect to $Re^{-1/2}U_\infty$. Re is the Reynolds number defined as $Re = U_\infty L/\nu$. The streamwise coordinate x is normalized with a reference length L , the wall-normal coordinate y and the spanwise coordinate z are made dimensionless with $\delta = Re^{-1/2}L = (\nu L/U_\infty)^{1/2}$. The system (3.2.1) requires six boundary conditions, three at the wall, where $y = 0$, and three for $y \rightarrow \infty$

$$\begin{aligned} u = 0 \quad \text{at} \quad y = 0 \quad u = 1 \quad \text{for} \quad y \rightarrow \infty \\ v = v_w \quad \text{at} \quad y = 0 \quad w = 0 \quad \text{for} \quad y \rightarrow \infty \\ w = 0 \quad \text{at} \quad y = 0 \quad p = 0 \quad \text{for} \quad y \rightarrow \infty \end{aligned} \tag{3.2.2}$$

where $v_w(x, z)$ is the wall-normal velocity component due to blowing or suction at the wall (zero if no control is applied). The system (3.2.1) is parabolic in x and therefore also initial conditions are required. However, only two initial conditions are allowed for the boundary layer equations, so that if u is fixed, v and w must be related. This can be proved by combining the continuity equation and the x -momentum equation eliminating the x -derivative from them, and obtaining an equation without x -derivative. The latter represents a constraint to be satisfied at $x = 0$: three initial conditions related by an equation imply two free initial conditions for the boundary layer equations. Moreover, when the streamwise component, upstream of the leading edge, is $u = 1$ uniformly in x , the equation relating the initial conditions simply reduces to the continuity. The initial conditions therefore are

$$\begin{aligned} u(0, y, z) &= 1 \\ v(0, y, z) &= v_0(y, z) \end{aligned} \tag{3.2.3}$$

and $w(0, y, z)$ is consequently derived from the continuity.

The system (3.2.1) with initial conditions (3.2.3) and boundary conditions (3.2.2) represents the direct or forward problem to be solved. It can be easily seen as a black box that receives initial and boundary conditions as inputs and produces a certain flow field as output. The aim of the present work is to find the initial conditions and boundary conditions at the wall which produce a certain effect on the output in such a way to give rise to the worst effect regarding transition (optimal perturbations) or in order to delay transition (optimal control). Therefore, the next step in the formulation of the problem consists in identifying an objective function which is related to the stability characteristics of the flow and that can be maximized, for optimal perturbations, or minimized, in the optimal control case.

3.2.1 Choice of the objective function and initial conditions

In previous work concerning the linear algebraic instability, optimal perturbations and optimal control, the perturbation kinetic energy was usually taken as a measure of the level of perturbations. However, this is not the only possibility even if it seems to be a reasonable physical quantity. In our problem, since a complete nonlinear calculation is performed, the flow field is not decomposed in the classical base flow plus a small perturbation, but as a summation of Fourier modes in the spanwise direction. For instance, the streamwise velocity component is:

$$u(x, y, z) = \sum_{n=-\infty}^{\infty} U_n(x, y) e^{in\beta z}$$

where $U_n(x, y)$ is the n^{th} Fourier's mode. The zero mode corresponds to the unperturbed flow (Blasius if we are dealing with a flat plate and homogeneous boundary conditions at the wall) plus a "mean flow correction" due to the interactions of the other modes. After these considerations, the previous expression of the velocity can be written as

$$u(x, y, z) = U_0(x, y) + \sum_{n=-\infty}^{-1} U_n(x, y) e^{in\beta z} + \sum_{n=1}^{\infty} U_n(x, y) e^{in\beta z} = U_0(x, y) + \bar{u}(x, y, z)$$

where $U_0(x, y)$ is the flow component independent of z and \bar{u} contains the modes which do depend on the spanwise coordinate $(1, 2, 3, \dots, -1, -2, -3, \dots)$. Different energy definitions are possible. The first could be the integral along y of the kinetic energy of all the modes, including mode zero. However, since both u and v velocity components tend to a constant as $y \rightarrow \infty$, this energy is infinite. Another possibility is the energy of all the modes, excluding mode zero, but considering the mean flow correction. The latter can be obtained in the following way. A first calculation is performed with all the modes with n different from zero set to zero, and appropriate boundary conditions at the wall, obtaining the unperturbed base flow (Blasius if the boundary conditions at the wall are homogeneous). Then a second calculation is performed with the perturbations turned on. Finally, subtracting the mode zero of the first calculation (base flow), from mode zero of the second one (base flow plus mean flow correction), the mean flow correction is obtained. However, the mean flow perturbation usually does not represent a dangerous disturbance as far as transition is concerned. For this reason, we consider the kinetic energy of only $\bar{u}(x, y, z)$, the velocity contribution which depends on the spanwise coordinate. Since the unknowns are expressed in boundary layer variables, the perturbation energy to be considered as a measure of the stability behavior of the system is (see Luchini [79]):

$$E(x) = \int_{-Z}^Z \int_0^{\infty} [|\bar{u}|^2 + Re^{-1}(|\bar{v}|^2 + |\bar{w}|^2)] dy dz \quad (3.2.4)$$

The expression (3.2.4) represents the perturbation energy as a function of the streamwise coordinate x . However, coming back to the black-box boundary layer representation, the most interesting quantity is the ratio between the output energy and the input energy, because it gives the gain of the system and allows the comparison with the linear case.

The objective function to be maximized or minimized is therefore the gain G , which can have at least two expressions. The first is the one used by Luchini [79] and Andersson *et al.* [4] for the optimal perturbation problem. It is defined as the ratio between the energy at the final station and the energy at the initial station:

$$G_{\text{out}} = \frac{E_{\text{out}}}{E_{\text{in}}} = \frac{\left[\int_{-Z}^Z \int_0^{\infty} [|\bar{u}|^2 + Re^{-1}(|\bar{v}|^2 + |\bar{w}|^2)] dy dz \right]_{x=X}}{\left[\int_{-Z}^Z \int_0^{\infty} [|\bar{u}|^2 + Re^{-1}(|\bar{v}|^2 + |\bar{w}|^2)] dy dz \right]_{x=0}} \quad (3.2.5)$$

Another possible definition of the gain is the integral of $E(x)$ over the whole domain divided by the initial energy:

$$G_{\text{mean}} = \frac{E_{\text{mean}}}{E_{\text{in}}} = \frac{\int_0^X E(x) dx}{E_{\text{in}}} = \frac{\int_{-Z}^Z \int_0^{\infty} \int_0^X [|\bar{u}|^2 + Re^{-1}(|\bar{v}|^2 + |\bar{w}|^2)] dx dy dz}{\left[\int_{-Z}^Z \int_0^{\infty} [|\bar{u}|^2 + Re^{-1}(|\bar{v}|^2 + |\bar{w}|^2)] dy dz \right]_{x=0}} \quad (3.2.6)$$

Expression (3.2.6) seems to be much more effective when dealing with optimal control problems. As shown by Cathalifaud and Luchini [20], optimal control based on minimizing the gain (3.2.5) can produce very large energy growth before the final station with undesired consequences on boundary layer transition, whereas minimizing (3.2.6) produces an almost monotonic energy growth along x . Since the aim of this work is to find optimal perturbations and optimal control, more attention will be given to gain (3.2.6) than to gain (3.2.5). On looking at expression (3.2.6), two possible cases can be analyzed: homogeneous initial conditions for the u -component $\bar{u}_{x=0} = 0$, or non homogeneous initial conditions $\bar{u}_{x=0} \neq 0$. Obviously, if we want to maximize G , the best choice is to consider $\bar{u}_{x=0} = 0$ which gives a gain of order Re when $Re \rightarrow \infty$, while in the other case the gain is of order one and therefore certainly smaller. The expression (3.2.6) thus becomes

$$G_{\text{mean}} = \frac{E_{\text{mean}}}{E_{\text{in}}} = Re \frac{\int_{-Z}^Z \int_0^{\infty} \int_0^X [|\bar{u}|^2 + Re^{-1}(|\bar{v}|^2 + |\bar{w}|^2)] dx dy dz}{\left[\int_{-Z}^Z \int_0^{\infty} [|\bar{v}|^2 + |\bar{w}|^2] dy dz \right]_{x=0}} \quad (3.2.7)$$

At this point it is important to observe that, within the boundary layer approximation, retaining the term $Re^{-1}(|\bar{v}|^2 + |\bar{w}|^2)$ does not make sense if further terms are not considered when deriving the boundary layer equations. Therefore the expression for G reduces to

$$G_{\text{mean}} = \frac{E_{\text{mean}}}{E_{\text{in}}} = Re \frac{\int_{-Z}^Z \int_0^{\infty} \int_0^X [|\bar{u}|^2] dx dy dz}{\left[\int_{-Z}^Z \int_0^{\infty} [|\bar{v}|^2 + |\bar{w}|^2] dy dz \right]_{x=0}} \quad (3.2.8)$$

which contains the Reynolds number Re as a scale factor only.

3.2.2 Constrained optimization and linear adjoint problem

Once the objective function to be maximized or minimized has been chosen, the next step is to build up an optimization technique in order to find the input parameters that make the objective function on extremum. We want, in fact, to solve two different problems. The first is to find the initial condition $\bar{v}_0(y, z)$ for the wall-normal velocity component at $x = 0$ which makes the objective function (for instance the mean gain G_{mean} or the gain at the outlet G_{out}) maximum for a given boundary condition at the wall $v_w(x, z)$. The other is to find the boundary condition at the wall $v_w(x, z)$ which makes the objective function (in this case it is usually much better to choose the mean gain G_{mean} instead of the gain at the outlet G_{out}) minimum for a given initial condition $\bar{v}_0(y, z)$. For each problem, there is one free function. However, in order to choose either the initial energy or the control energy at the wall, two constraints have to be satisfied:

$$E_{\text{in}} = E_0, \quad E_w = E_{w0}$$

For the initial energy E_{in} we have

$$E_{\text{in}} = \left[\int_{-Z}^Z \int_0^\infty [|\bar{v}|^2 + |\bar{w}|^2] dy dz \right]_{x=0} = E_0$$

but since at $x = 0$ \bar{w}_0 is related to \bar{v}_0 by an equation obtained combining the continuity and x -momentum equations, the initial perturbation energy can be seen as dependent only on \bar{v}_0 :

$$E_{\text{in}}(\bar{v}_0) = E_0 \tag{3.2.9}$$

As far as the control energy at the wall is concerned,

$$E_w = \left[\int_{x_{\text{in}}}^X |v_w|^2 dx \right]_{y=0} = E_{w0}$$

so that

$$E_w(v_w) = E_{w0} \tag{3.2.10}$$

In order to have the possibility to test different objective functions, we define

$$\mathcal{J} = \alpha G_{\text{out}} + \beta G_{\text{mean}}$$

so that for $\alpha = 1$ and $\beta = 0$ the objective is the energy at the final station whereas for $\alpha = 0$ and $\beta = 1$ the objective is the integral of the energy over the whole domain. Using the Lagrange multiplier technique to solve our constrained optimization problem,

we introduce the functional

$$\begin{aligned}
\mathcal{L} = & \mathcal{J} + \int_{-Z}^Z \int_0^\infty \int_0^X a[u_x + v_y + w_z] dx dy dz \\
& + \int_{-Z}^Z \int_0^\infty \int_0^X b[(uv)_x + (uv)_y + (uv)_z - u_{yy} - u_{zz}] dx dy dz \\
& + \int_{-Z}^Z \int_0^\infty \int_0^X c[(uv)_x + (vz)_y + (vw)_z + p_y - v_{yy} - v_{zz}] dx dy dz \\
& + \int_{-Z}^Z \int_0^\infty \int_0^X d[(uw)_x + (vw)_y + (wz)_z + p_x - w_{yy} - w_{zz}] dx dy dz \\
& + \lambda_0[E_{in}(\bar{v}_0) - E_0] + \lambda_w[E_w(v_w) - E_{w0}]
\end{aligned} \tag{3.2.11}$$

where

$$a = a(x, y, z); \quad b = b(x, y, z); \quad c = c(x, y, z); \quad d = d(x, y, z); \quad \lambda_0 = \text{const}; \quad \lambda_w = \text{const}$$

are the Lagrange multipliers. Maximizing or minimizing \mathcal{L} implies that $\delta\mathcal{L} = 0$:

$$\begin{aligned}
& \frac{\delta\mathcal{L}}{\delta u} \delta u + \frac{\delta\mathcal{L}}{\delta v} \delta v + \frac{\delta\mathcal{L}}{\delta w} \delta w + \frac{\delta\mathcal{L}}{\delta p} \delta p + \frac{\delta\mathcal{L}}{\delta \bar{v}_0} \delta \bar{v}_0 + \frac{\delta\mathcal{L}}{\delta v_w} \delta v_w + \\
& \frac{\delta\mathcal{L}}{\delta a} \delta a + \frac{\delta\mathcal{L}}{\delta b} \delta b + \frac{\delta\mathcal{L}}{\delta c} \delta c + \frac{\delta\mathcal{L}}{\delta d} \delta d + \frac{\delta\mathcal{L}}{\delta \lambda_0} \delta \lambda_0 + \frac{\delta\mathcal{L}}{\delta \lambda_w} \delta \lambda_w = 0
\end{aligned} \tag{3.2.12}$$

where, for example, $\frac{\delta\mathcal{L}}{\delta u} \delta u$ denotes

$$\frac{\delta\mathcal{L}}{\delta u} \delta u = \lim_{\epsilon \rightarrow 0} \frac{\mathcal{L}(u + \epsilon \delta u, v, w, p, \bar{v}_0, v_w, a, b, c, d, \lambda_0, \lambda_w) - \mathcal{L}(u, v, w, p, \bar{v}_0, v_w, a, b, c, d, \lambda_0, \lambda_w)}{\epsilon}$$

Since $\delta\mathcal{L}$ must be nullified for unconstrained variations in all the parameters, every term in (3.2.12) must be zero:

$$\begin{aligned}
\frac{\delta\mathcal{L}}{\delta u} = 0; & \quad \frac{\delta\mathcal{L}}{\delta v} = 0; & \quad \frac{\delta\mathcal{L}}{\delta w} = 0; & \quad \frac{\delta\mathcal{L}}{\delta p} = 0; & \quad \frac{\delta\mathcal{L}}{\delta \bar{v}_0} = 0; & \quad \frac{\delta\mathcal{L}}{\delta v_w} = 0; \\
\frac{\delta\mathcal{L}}{\delta a} = 0; & \quad \frac{\delta\mathcal{L}}{\delta b} = 0; & \quad \frac{\delta\mathcal{L}}{\delta c} = 0; & \quad \frac{\delta\mathcal{L}}{\delta d} = 0; & \quad \frac{\delta\mathcal{L}}{\delta \lambda_0} = 0; & \quad \frac{\delta\mathcal{L}}{\delta \lambda_w} = 0
\end{aligned}$$

It can be easily seen that the derivatives of the functional \mathcal{L} with respect to the Lagrange multipliers $a, b, c, d, \lambda_0, \lambda_w$ give the original constrains, respectively system (3.2.1) and the energy constrains (3.2.9) and (3.2.10). On the other hand, the derivatives of the functional with respect to the direct variables u, v, w, p , after integration by parts, produce the set of adjoint equations:

$$\begin{aligned}
& c_y + d_z = 0 \\
a_x + 2b_x u + b_y v + b_z w + c_z v + d_x v + d_x w + b_{yy} + b_{zz} &= \beta u \\
a_y + b_y u + c_x u + 2c_y v + d_y w + c_z w + c_{yy} + c_{zz} &= 0 \\
a_z + b_z u + c_z v + d_y v + d_x u + 2d_z w + d_{yy} + d_{zz} &= 0
\end{aligned} \tag{3.2.13}$$

A system of second-order linear partial differential equations has been derived. They are parabolic, but the “natural” marching direction is from the outlet $x = X$ to $x = 0$ so that “initial conditions” are required at $x = X$. These are provided by the set of conditions arising from the boundary terms (at $x = 0$, $x = X$, $y = 0$ and for $y \rightarrow \infty$) due the integration by parts. Such a set of conditions can be divided into “initial conditions” for the adjoint problem at $x = X$ and boundary conditions for (3.2.13) at $y = 0$ and for $y \rightarrow \infty$. Moreover, “coupling conditions” at $x = 0$ and $y = 0$, due to the derivatives with respect to the controlling parameters \bar{v}_0 and v_w , are obtained: they are not necessary in order to solve (3.2.13), but relate the direct solution to the adjoint one in the framework of the constrained optimization. The boundary conditions for system (3.2.13) are:

$$\begin{aligned} b = 0 & \quad \text{at } y = 0 & c = 0 & \quad \text{for } y \rightarrow \infty \\ a + c_y = 0 & \quad \text{at } y = 0 & a + ub + c_y = 0 & \quad \text{for } y \rightarrow \infty \\ d = 0 & \quad \text{at } y = 0 & d = 0 & \quad \text{for } y \rightarrow \infty \end{aligned} \quad (3.2.14)$$

and the initial conditions at $x = X$ read

$$\begin{aligned} \int_{-Z}^Z \int_0^\infty [a + 2ub] dy dz + \alpha \frac{\partial G_{\text{out}}}{\partial u} = 0 & \quad \text{at } x = X \\ c = 0 & \quad \text{at } x = X \\ d = 0 & \quad \text{at } x = X \end{aligned} \quad (3.2.15)$$

The coupling conditions at $x = 0$ and $y = 0$, which relate the direct and adjoint problem, reduce to

$$\int_{-Z}^Z \int_0^\infty c dy dz + \lambda_0 \frac{\delta E_{\text{in}}}{\delta \bar{v}} = 0 \quad \text{at } x = 0 \quad (3.2.16)$$

$$\int_0^X c dx - \lambda_w \frac{\delta E_w}{\delta v_w} = 0 \quad \text{at } y = 0$$

On introducing $a^* = a + 2bu$, the system (3.2.13) can be written as

$$\begin{aligned} c_y + d_z &= 0 \\ a_x^* - 2u_x b + b_y v + b_z w + c_z v + d_x v + d_x w + b_{yy} + b_{zz} &= \beta u \\ a_y^* - 2bu_y - b_y u + c_x u + 2c_y v + d_y w + c_z w + c_{yy} + c_{zz} &= 0 \\ a_z^* - 2bu_z - b_z u + c_z v + d_y v + d_x u + 2d_z w + d_{yy} + d_{zz} &= 0 \end{aligned} \quad (3.2.17)$$

with boundary conditions:

$$\begin{aligned} b = 0 & \quad \text{at } y = 0 & c = 0 & \quad \text{for } y \rightarrow \infty \\ a^* - 2bu + c_y = 0 & \quad \text{at } y = 0 & a^* - ub + c_y = 0 & \quad \text{for } y \rightarrow \infty \\ d = 0 & \quad \text{at } y = 0 & d = 0 & \quad \text{for } y \rightarrow \infty \end{aligned} \quad (3.2.18)$$

and “initial conditions” at $x = X$

$$\begin{aligned} c = 0 & \quad \text{at } x = X \\ d = 0 & \quad \text{at } x = X \\ \int_{-Z}^Z \int_0^\infty a^* dy dz + \alpha \frac{\delta G_{\text{out}}}{\delta u} = 0 & \quad \text{at } x = X \end{aligned} \quad (3.2.19)$$

while the coupling conditions (3.2.16) are not affected by the substitution.

3.2.3 Iterative optimization

In the previous section, starting from boundary layer equations (3.2.1) with boundary conditions (3.2.2) and initial conditions (3.2.3) (direct or forward problem), under the constraints (3.2.9) and (3.2.10), the set of adjoint equations (3.2.17) with related boundary conditions (3.2.18) and “initial conditions” (3.2.19) (adjoint or backward problem) has been derived. In addition, in order to nullify $\delta\mathcal{L}$ (optimality condition), it is necessary to satisfy also the “coupling conditions” (3.2.16).

All these equations and conditions can be satisfied solving at the same time the complete forward and backward problems together with the coupling conditions. However, this represents a very large nonlinear system of equations which turns out to require quite a heavy computational effort in order to be solved.

On the other hand, the equations are parabolic in the forward (direct problem) or backward (adjoint problem) direction, suggesting the idea of an iterative technique. The latter involves first the solution of the direct equations, with related initial conditions and boundary conditions, and then of the adjoint ones (with related initial conditions and boundary conditions), linked by the “coupling conditions”, until $\delta\mathcal{L} = 0$. This was done, in the linear framework, by Luchini [79]. In that case, since the initial problem was linear and the optimization of a quadratic function was required, a Rayleigh quotient was generated, which converged to the optimal solution.

In the nonlinear case, convergence is not assured. However, the parabolic nature of the equations allows the use of an iterative technique summarized in the following steps:

1. Guess is given for the initial condition $v_0^{(1)}$ at $x = 0$ and boundary condition, $v_w^{(1)}$ at $y = 0$
2. The parabolic direct problem (3.2.1) is solved using the initial and boundary conditions of point 1 and introducing a marching technique forward in space from $x = 0$ to $x = X$
3. At $x = X$ the objective function $\mathcal{J}^{(1)}$ is evaluated and the “initial condition” for $a^{*(1)}$, knowing $\frac{\delta G_{\text{out}}^{(1)}}{\delta u}$, is obtained from the relationship

$$\int_{-Z}^Z \int_0^\infty a^{*(1)} dy dz = -\alpha \frac{\delta G_{\text{out}}^{(1)}}{\delta u}$$

If the objective is the integral of the energy over the whole domain (i.e. if $\alpha = 0$), the condition is obviously $a^{*(1)} = 0$.

4. The adjoint problem (3.2.17) is solved together with the “initial conditions” ($a^{*(1)}$ is known from point 3) and boundary conditions, using a marching technique backward in space from $x = X$ to $x = 0$. If the objective is the energy at the final station, $\beta = 0$ and the adjoint equations are homogeneous, otherwise there is a source term βu in the equation corresponding to the x -momentum.

5. When the adjoint solution is known, the “coupling conditions” (3.2.16) are actually used. The initial condition $\bar{v}_0^{(2)}$ at $x = 0$ is obtained from the equation

$$\int_{-Z}^Z \int_0^\infty c^{(1)} dy dz + \lambda_0 \frac{\delta E_{\text{in}}^{(2)}}{\delta v} = 0$$

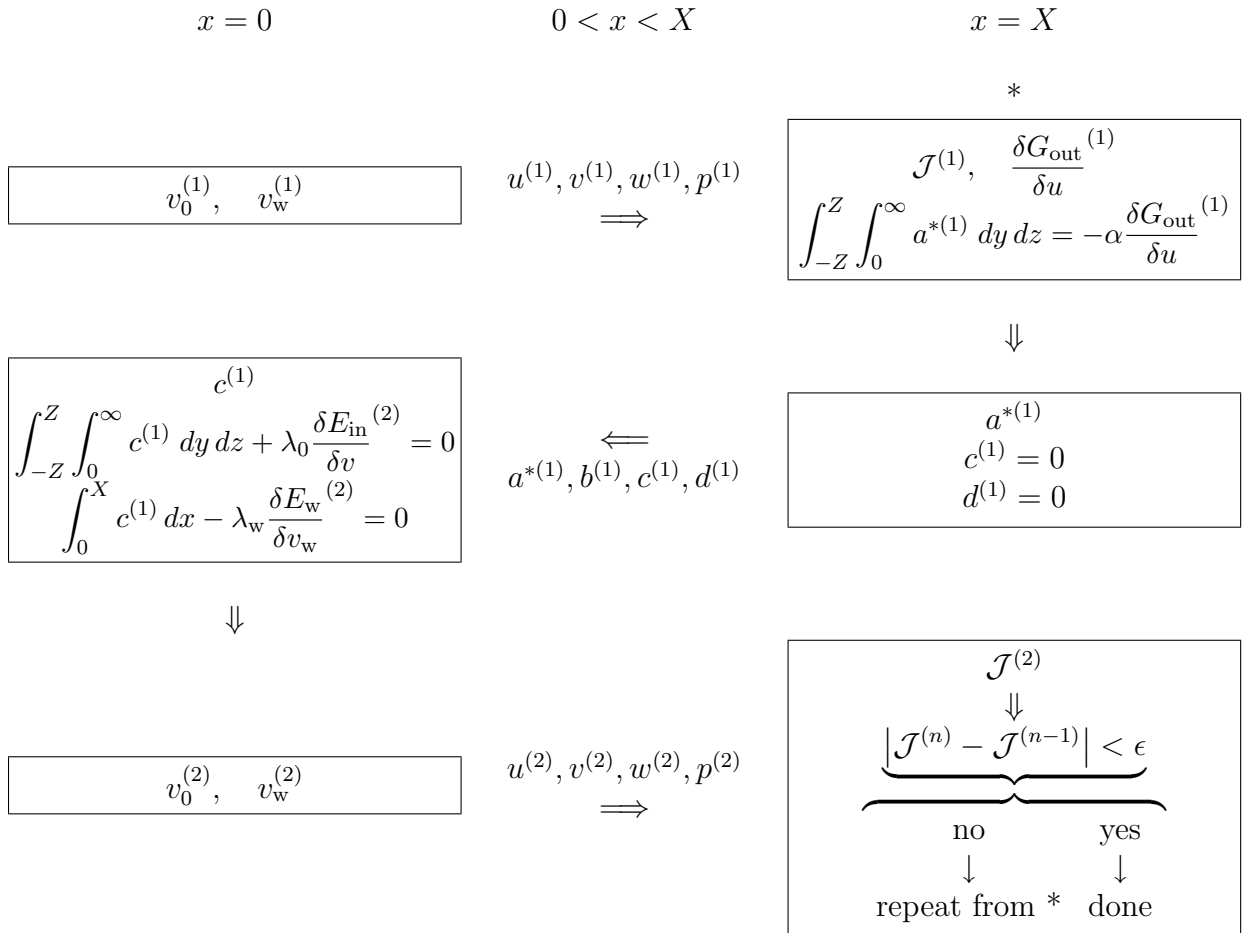
and a new boundary condition $v_w^{(2)}$ at the wall ($y = 0$) is computed from

$$\int_0^X c^{(1)} dx - \lambda_w \frac{\delta E_w^{(2)}}{\delta v_w} = 0$$

If one of the two conditions is given and fixed, like in the optimal perturbation or optimal control problem, only the optimized one is updated. The two Lagrange multipliers λ_0 and λ_w are obtained satisfying the condition $E_{\text{in}}(v_0^{(2)}) - E_0 = 0$ and $E_w(v_w^{(2)}) - E_{w0} = 0$ respectively

6. Step 2 is repeated using initial and boundary conditions coming from step 5. The objective function $\mathcal{J}^{(2)}$ is evaluated again and if the difference in \mathcal{J} between two following iterations is smaller than a certain threshold then the procedure is finished, otherwise steps from 3 to 6 are repeated

The iterative procedure needed for the solution of the problem is here sketched:



3.2.4 Implementation and numerical solution

In the following sections the numerical discretization of the direct and adjoint problems and the implementation of the iterative procedure will be described.

Direct nonlinear problem

In order to account for the nonlinearities, the solution of the direct problem is expanded in Fourier modes along the spanwise direction:

$$\begin{aligned} u(x, y, z) &= \sum_{n=-\infty}^{\infty} U_n(x, y)e^{in\beta z}; & v(x, y, z) &= \sum_{n=-\infty}^{\infty} V_n(x, y)e^{in\beta z}; \\ w(x, y, z) &= \sum_{n=-\infty}^{\infty} W_n(x, y)e^{in\beta z}; & p(x, y, z) &= \sum_{n=-\infty}^{\infty} P_n(x, y)e^{in\beta z}; \end{aligned} \quad (3.2.20)$$

If

$$f(x, y, z) = \sum_{n=-\infty}^{\infty} F_n(x, y)e^{in\beta z}$$

represents the general quantity u, v, w, p , the function $F_n(x, y)$ is the n^{th} mode and depends only on x and y . Under the previous expansions, the nonlinear terms in equations (3.2.1) produce a double summation similar to a convolution. For example, indicating with $f(x, y, z)$ and $g(x, y, z)$ two generic variables (u, v, w, p), one has:

$$\begin{aligned} f(x, y, z)g(x, y, z) &= \sum_{k=-\infty}^{\infty} F_k(x, y)e^{ik\beta z} \sum_{j=-\infty}^{\infty} G_j(x, y)e^{ij\beta z} \\ &= \sum_{n=-\infty}^{\infty} e^{in\beta z} \left[\sum_{k=-\infty}^{\infty} F_k(x, y)G_{n-k}(x, y) \right] \\ &= \sum_{n=-\infty}^{\infty} e^{in\beta z} C_n^{FG}(x, y); \end{aligned} \quad (3.2.21)$$

where $n = j + k$. The coefficient

$$C_n^{FG}(x, y) = \sum_{k=-\infty}^{\infty} F_k(x, y)G_{n-k}(x, y)$$

depends on n , and obviously on $F(x, y)$ and $G(x, y)$, whereas k is a mute index inside the summation. Introducing expressions (3.2.20) and (3.2.21) in the equations (3.2.1)

yields:

$$\begin{aligned}
\sum_{n=-\infty}^{\infty} [(U_n)_x + (V_n)_y + in\beta W_n] e^{in\beta z} &= 0 \\
\sum_{n=-\infty}^{\infty} [(C_n^{UU})_x + (C_n^{UV})_y + in\beta C_n^{UW} - (U_n)_{yy} + n^2\beta^2 U_n] e^{in\beta z} &= 0 \\
\sum_{n=-\infty}^{\infty} [(C_n^{UV})_x + (C_n^{VV})_y + in\beta C_n^{VW} - (V_n)_{yy} + n^2\beta^2 V_n + (P_n)_y] e^{in\beta z} &= 0 \\
\sum_{n=-\infty}^{\infty} [(C_n^{UW})_x + (C_n^{VW})_y + in\beta C_n^{WW} - (W_n)_{yy} + n^2\beta^2 W_n + in\beta P_n] e^{in\beta z} &= 0
\end{aligned} \tag{3.2.22}$$

Since each equation is satisfied if each term in the summation is zero, the following system is obtained:

$$\begin{aligned}
(U_n)_x + (V_n)_y + in\beta W_n &= 0 \\
(C_n^{UU})_x + (C_n^{UV})_y + in\beta C_n^{UW} - (U_n)_{yy} + n^2\beta^2 U_n &= 0 \\
(C_n^{UV})_x + (C_n^{VV})_y + in\beta C_n^{VW} - (V_n)_y + n^2\beta^2 V_n + (P_n)_y &= 0 \\
(C_n^{UW})_x + (C_n^{VW})_y + in\beta C_n^{WW} - (W_n)_{yy} + n^2\beta^2 W_n + in\beta P_n &= 0
\end{aligned} \tag{3.2.23}$$

Up to this moment, no approximations have been introduced in order to solve the non-linear system of equations (3.2.1) (the solution has been expanded in an infinite number of Fourier modes).

On the contrary, in order to numerically determine the solution, a finite number of modes N must be used, so that the discretization in spanwise direction is straightforwardly defined. If the unknowns are expressed on a finite basis as

$$\begin{aligned}
u(x, y, z) &= \sum_{n=-N}^N U_n(x, y) e^{in\beta z}; & v(x, y, z) &= \sum_{n=-N}^N V_n(x, y) e^{in\beta z}; \\
w(x, y, z) &= \sum_{n=-N}^N W_n(x, y) e^{in\beta z}; & p(x, y, z) &= \sum_{n=-N}^N P_n(x, y) e^{in\beta z};
\end{aligned} \tag{3.2.24}$$

the product between two generic functions f and g (which represent u, v, w, p) becomes

$$\begin{aligned}
f(x, y, z)g(x, y, z) &= \sum_{k=-N}^N F_k(x, y) e^{ik\beta z} \sum_{j=-N}^N G_j(x, y) e^{ij\beta z} \\
&= \sum_{n=-N}^N e^{in\beta z} \left[\sum_{k=a}^b F_k(x, y) G_{n-k}(x, y) \right] \\
&= \sum_{n=-N}^N e^{in\beta z} C_n^{FG}(x, y);
\end{aligned} \tag{3.2.25}$$

where the coefficient $C_n^{FG}(x, y)$ is defined as

$$C_n^{FG}(x, y) = \sum_{k=a}^b F_k(x, y) G_{n-k}(x, y) \quad (3.2.26)$$

and the two constants a and b are introduced in order to bound the summation on k because of the finite number of modes N :

$$a = \max(-N, n + N); \quad b = \min(N, n - N)$$

As far as the discretization in the streamwise direction is concerned, since system (3.2.1) is parabolic, we choose a backward discretization. In addition, to account for the fact that boundary layer equations are singular at $x = 0$, and thus a very high density grid is required close to the leading edge, a non uniform grid is used. Moreover in order to conserve the second-order accuracy, the x -derivative is discretized as follows:

$$\mathbf{h}_x = C_0 \mathbf{h}_i + C_1 \mathbf{h}_{i-1} + C_2 \mathbf{h}_{i-2}$$

where

$$C_0 = \frac{\Delta_1 + 2\Delta_2}{\Delta_1(\Delta_1 + \Delta_2)}, \quad C_1 = -\frac{\Delta_1 + 2\Delta_2}{\Delta_1\Delta_2}, \quad C_2 = \frac{\Delta_1}{\Delta_2(\Delta_1 + \Delta_2)}$$

and

$$\Delta_1 = x_i - x_{i-1}, \quad \Delta_2 = x_{i-1} - x_{i-2}$$

Clearly, for a uniformly spaced grid $\Delta_1 = \Delta_2 = \Delta = x_i - x_{i-1}$ and the coefficients reduce to the well known values $C_0 = 1.5/\Delta$, $C_1 = -2/\Delta$, $C_2 = 0.5/\Delta$. If a first order scheme is used, then $C_0 = 1/\Delta$, $C_1 = -1/\Delta$ and $C_2 = 0$.

In the wall-normal direction, second-order central finite differences are used. Since boundary layer quantities vary much faster close rather than far from the wall, a non uniform grid is introduced also in y direction with more points located near the wall.

After the discretization, system (3.2.23) is yet nonlinear and couples the general unknown $F_n(x, y)$ with $G_k(x, y)$ because of the coefficient $C_n^{FG}(x, y)$. Therefore a Newton-like iterative technique is needed to solve the discretized nonlinear problem. However, different possibilities are available.

The first is to write a very large and sparse linear system where the unknowns are all the modes (from $-N$ to N) for each variable (u, v, w, p). In this way the modes are coupled and when the Newton-like iteration ends, because convergence is reached, all the modes are known at the same time. The main drawback of this technique is that a very large system needs to be solved and thus a large amount of memory is required.

Another possibility is to decouple the different modes n in order to solve a small system for each n . Mode zero is first found and then all the others using the solution of mode zero. When all the modes are known, the residue is computed and if it is greater than a certain threshold all the modes are computed again using the results from the previous iteration, otherwise convergence is considered reached.

In any case, both iterative techniques can be applied to the discretized problem and provide its exact solution.

Following the second approach, in order to linearize (3.2.23), we separate the mode F_n in two contributions

$$F_n = \bar{F}_n + f_n;$$

where \bar{F}_n is considered known and f_n is small in such a way that, neglecting terms like $f_k(x, y)g_{n-k}(x, y)$ in the coefficient $C_n^{FG}(x, y)$, which was the origin of the nonlinearity in the system, one gets:

$$C_n^{FG}(x, y) = \sum_{k=a}^b F_k(x, y)G_{n-k}(x, y) = \sum_{k=a}^b (\bar{F}_k\bar{G}_{n-k} + \bar{F}_kg_{n-k} + f_k\bar{G}_{n-k})$$

Since \bar{F}_n and \bar{G}_{n-k} are known, the unknowns reduce to f_n and g_{n-k} . In the previous expression the coefficient $C_n^{FG}(x, y)$ is linear in the unknowns g_{n-k} and f_k , but it still couples the unknowns corresponding to different modes.

Since our aim is to decouple different modes so that a small linear system can be solved for each mode n , in the summations

$$\sum_{k=a}^b \bar{F}_kg_{n-k} \quad \text{and} \quad \sum_{k=a}^b f_k\bar{G}_{n-k}$$

we retain only the terms \bar{F}_0g_n and $f_n\bar{G}_0$. This reduces C_n^{FG} to

$$C_n^{FG}(x, y) = \sum_{k=a}^b \bar{F}_k\bar{G}_{n-k} + \bar{F}_0g_n + f_n\bar{G}_0 = C_n^{\bar{F}\bar{G}} + \bar{F}_0g_n + f_n\bar{G}_0$$

where obviously $C_n^{\bar{F}\bar{G}} = \sum_{k=a}^b \bar{F}_k\bar{G}_{n-k}$.

Under these assumptions, the original nonlinear coupling coefficient $C_n^{FG}(x, y)$ has been simplified in a linear form and couples only mode n and mode zero.

The discretized direct problem therefore, after the linearization, can be rewritten in the simple form

$$\mathbf{T}_n^i \mathbf{f}_n^i = \mathbf{y}_n^i \quad (3.2.27)$$

where the index \cdot_n denotes the n -th mode, the apex \cdot^i denotes the i -th station in x , the vector \mathbf{f}_n^i is the vector of unknowns

$$\mathbf{f}_n^i = \begin{pmatrix} u_n^i \\ v_n^i \\ w_n^i \\ p_n^i \end{pmatrix} \quad (3.2.28)$$

and the matrix \mathbf{T}_n^i depends on n and is defined as

$$\mathbf{T}_n^i = C_0 \mathbf{A}_0^i + \mathbf{B}_n^i$$

Matrix \mathbf{A}_0^i contains only the mode zero of the solution and both \mathbf{A}_0^i and \mathbf{B}_n^i account for the y -discretization of the derivatives. The vector \mathbf{y}_n^i is due to all known terms:

$$\mathbf{y}_n^i = -C_1 \mathbf{A}_0^{i-1} \mathbf{f}_n^{i-1} - C_2 \mathbf{A}_0^{i-2} \mathbf{f}_n^{i-2} - C_0 \mathbf{r}_x^i - C_1 \mathbf{r}_x^{i-1} - C_2 \mathbf{r}_x^{i-2} - \mathbf{r}_0^i$$

where the residue \mathbf{r} , which contains the complete nonlinear coupling between all the modes, has been decomposed in two parts: $(\mathbf{r}_x)_x$, which accounts the x -derivative, and \mathbf{r}_{0n} which contains all the other terms so that

$$\mathbf{r}_n = (\mathbf{r}_x)_x + \mathbf{r}_0$$

The complete expressions of \mathbf{r}_x and \mathbf{r}_0 can be found in appendix D, together with the matrices \mathbf{A}_0 and \mathbf{B}_n .

The numerical solution of the direct problem is obtained marching in x -direction, from $x = 0$ to $x = X$.

Linear adjoint problem

The adjoint problem formulated in section 3.2.2 can be solved by discretizing the system (3.2.17). However this implies writing another code, based on the direct one, which could be source of programming errors. On the other hand, it is possible to solve the adjoint problem by taking the adjoint of the discrete direct problem. This corresponds to the same steps followed in the continuous case: the discretized direct equations are left-multiplied by a vector which represents the adjoint unknowns so that, after a summation equivalent to the integration by parts, a discretized system is obtained for the adjoint unknowns. Obviously, the optimization technique applied to the discretized equations provides the optimal solution of the discretized problem. On the other hand, the solution of the adjoint problem of the discretized equations tends to the solution obtained discretizing the continuous adjoint equations (3.2.17) when the discretization is finer (the discretized direct solution tends to the continuous one as $\Delta x \rightarrow 0$, $\Delta y \rightarrow 0$ and $N \rightarrow \infty$). For more details about this, the reader is referred to Cathalifaud and Luchini [20] and Luchini and Bottaro [80].

The adjoint problem is solved from $x = X$ to $x = 0$, using a marching technique as done for the direct problem, but in the backward direction.

Iterative optimization

As remarked in section 3.2.3, the optimization problem we are dealing with can be attacked by considering a very large system of equations including the direct and adjoint problems with related initial, boundary and “coupling” conditions, and solving it (after the Newton-like linearization on the discretized system) with a quite hard computational effort, or by an iterative technique.

This iterative procedure was used, in the linear framework, by Luchini [79]. The iterative optimization technique reduces, in that case, to a Rayleigh quotient, which converges to the optimal solution.

Here the problem is nonlinear and although the direct equations can be recast in a linear system using a Newton-like linearization of the discretized nonlinear equations, unfortunately the optimization does not reduce to a Rayleigh quotient and therefore convergence cannot be assured. For this reason, a slightly more sophisticated technique than the one used by Luchini [79] is here required in the discretization of the “coupling conditions” at $x = 0$ and $y = 0$.

On the contrary, the discretization of the “initial condition” for the adjoint problem at $x = X$ is straightforward. Its continuous form reads

$$\int_{-Z}^Z \int_0^\infty a^* dy dz = -\alpha \frac{\delta G_{\text{out}}}{\delta u}$$

If $\alpha = 0$ the initial condition is simply $a^* = 0$, whereas if $\alpha \neq 0$ the discretized form of the condition is

$$a^*(y) = -\alpha \mathbf{L}_u(y) u^*(y)$$

where everything is a function of y only and u^* denotes the complex conjugate of u . The previous formula gives directly the initial condition for the adjoint solution, once $u^*(y)$ is known at $x = X$ (at the end of the forward calculation).

As far as the condition at $x = 0$ is concerned, from the continuous formulation we have

$$\int_{-Z}^Z \int_0^\infty c dy dz + \lambda_0 \frac{\delta E_{\text{in}}}{\delta v} = 0$$

which can be written in a discretized form as

$$c(y) + \lambda_0 \mathbf{L}_v(y) v^*(y) = 0 \quad (3.2.29)$$

In the optimal-perturbation framework $v(y)$ represents the unknown of the problem. It is directly given by the adjoint solution $c(y)$ at $x = 0$ once $\mathbf{L}_v(y)$ and λ_0 (Lagrange multiplier) are known. $\mathbf{L}_v(y)$ is an operator which depends only on the discretization, whereas the λ_0 is found by imposing the constrain

$$E_{\text{in}}(v_0(\lambda_0)) = E_0$$

which implies a second order algebraic equation for λ_0 .

Once the forward solution and the corresponding adjoint one have been obtained during a general iteration t , the initial condition $v_0(y)^{t+1}$ for the next forward-backward iteration $t + 1$ can be evaluated by solving (3.2.29):

$$v_0(y)^{t+1} = -\frac{1}{\lambda^t} \mathbf{L}_v(y)^{-1} c_0(y)^t \quad (3.2.30)$$

where the index \cdot_0 denotes the station $x = 0$. The iterative loop ends when the difference between the gain computed for a forward-backward iteration and the previous one is smaller than a certain threshold. However, convergence difficulties are encountered when equation (3.2.30) is straightforwardly applied. The problem is due to the fact that this technique does not reduce to the optimization of a Rayleigh quotient in the nonlinear case so that convergence is even not guaranteed.

The obstacle can be bypassed if a relaxation is introduced in such a way that the solution at the previous step is taken into account when computing $v_0(y)^{t+1}$:

$$v_0(y)^{t+1} = v_0(y)^t + k \left[-v_0(y)^t - \left[\frac{1}{\lambda_0^t} \mathbf{L}_v(y)^{-1} c_0(y)^t \right]^* \right] \quad (3.2.31)$$

or in a more compact form

$$v_0(y)^{t+1} = v_0(y)^t(1 - k) - k \left[\frac{1}{\lambda^t} \mathbf{L}_v(y)^{-1} c_0(y)^t \right]^* \quad (3.2.32)$$

It is evident that expression (3.2.32) reduces to (3.2.30) for $k = 1$.

One of the most delicate problem is the choice of k . When it is zero, the optimal solution is not updated ($v_0(y)^{t+1} = v_0(y)^t$), whereas $k = 1$ implies no contribution of $v_0(y)^t$ to $v_0(y)^{t+1}$. For $0 < k < 1$, the solution $v_0(y)^{t+1}$ is obtained from a mixing of the initial perturbation $v_0(y)^t$ and the adjoint solution $c_0(y)^t$, applying equation (3.2.32) where λ^t satisfies the energy constrain. The main problem is related to the fact that k can make the solution tend to the optimal one or diverge. Basically, when dealing with optimal perturbations, we look for the maximum gain produced by the worst initial condition. For this reason, if the objective function at the end of iteration $t + 1$ is smaller than the objective function at iteration t , the value of k used in (3.2.32) is not correct since the solution is not converging to a maximum (it is decreasing). In this case a smaller value of k is chosen, for example half of the previous one.

When dealing with the optimal–control problem, the new boundary condition to be applied at the wall is updated using the adjoint solution in a way very similar to the condition at $x = 0$ in the optimal–perturbation framework. The coupling condition at $y = 0$, in a continuous form, reads

$$\int_0^X c_w(x) dx - \lambda \frac{\delta E_w}{\delta v_w} = 0$$

whereas in a discretized form it can be written as

$$c_w(x) - \lambda_w \mathbf{L}_w(x) v_w^*(x) = 0$$

Again, $v_w(x)$ represents the solution of the optimal control problem for a given initial condition and can be obtained directly from the solution of the adjoint problem $c_w(x)$, once $\mathbf{L}_w(x)$ and λ_w are known. The former depends on the discretization while the Lagrange multiplier λ_w is determined by imposing the energy constraint

$$E_w(v_w(\lambda)) = E_{w0}$$

If the procedure is applied iteratively:

$$v_w(x)^{t+1} = \left[\frac{1}{\lambda^t} \mathbf{L}_w(x)^{-1} c_w(x)^t \right]^* \quad (3.2.33)$$

The solution v_w is considered the optimal one when the relative difference between the gain at a forward–backward iteration and the previous one is smaller than a certain threshold. A relaxation for $v_w(y)^{t+1}$ can be introduced in the same way as done for the optimal perturbation (3.2.31) by taking into account the solution at the previous forward–backward iteration:

$$v_w(x)^{t+1} = v_w(x)^t + k \left[-v_w(x)^t + \left[\frac{1}{\lambda^t} \mathbf{L}_w(x)^{-1} c_w(x)^t \right]^* \right] \quad (3.2.34)$$

or more compactly

$$v_w(x)^{t+1} = v_w(x)^t(1 - k) + k \left[\frac{1}{\lambda^t} \mathbf{L}_w(x)^{-1} c_w(x)^t \right]^* \quad (3.2.35)$$

Again, for $k = 0$ the solution is not updated, whereas for $k = 1$ the previous expression reduces to (3.2.33). If the objective function at the end of iteration $t + 1$ is greater than the objective function at iteration t , the value of k was not correct (the solution is not converging to a minimum) and a smaller value of k is chosen (for instance, half of the previous one).

The discretized form of the objective function

$$\mathcal{J} = \alpha G_{\text{out}} + \beta G_{\text{mean}} \quad (3.2.36)$$

is straightforwardly defined once the output gain $G_{\text{out}} = E_{\text{out}}/E_{\text{in}}$ and the mean gain $G_{\text{mean}} = E_{\text{mean}}/E_{\text{in}}$ are themselves written in the discretized form. The initial energy

$$E_{\text{in}} = \left[\int_{-Z}^Z \int_0^\infty [|\bar{v}|^2 + |\bar{w}|^2] dy dz \right]_{x=0}$$

for a finite number of modes becomes

$$E_{\text{in}} = \sum_{n \neq 0} \frac{2\pi}{\beta} \int_0^\infty [|V_n(0, y)|^2 + |W_n(0, y)|^2] dy \quad (3.2.37)$$

while the energy of the u -velocity component, as a function of x , reads

$$E_u(x) = \sum_{n \neq 0} \frac{2\pi}{\beta} \int_0^\infty |U_n(x, y)|^2 dy$$

The mean energy E_{mean} and final energy E_{out} thus are respectively

$$E_{\text{mean}} = \int_0^X E_u(x) dx, \quad E_{\text{out}} = E_u(X)$$

Since the initial energy is fixed, maximizing or minimizing $\alpha G_{\text{out}} + \beta G_{\text{mean}}$ is the same as maximizing or minimizing

$$\mathcal{J} = \alpha E_{\text{out}} + \beta E_{\text{mean}} \quad (3.2.38)$$

3.2.5 Optimal perturbation, optimal control and robust control

The formulation developed in the previous sections considers the boundary layer system as a black box. Input parameters are the initial condition v_0 (the wall-normal velocity component) at $x = 0$ and the wall boundary condition v_w (v component at $y = 0$). As far as the initial condition is concerned, different choices are possible: the simplest is to consider a sinusoidal dependence on the spanwise coordinate z , so that the relevant initial conditions at $x = 0$ are only mode zero, $[U_0(x, y), V_0(x, y), W_0(x, y)]$, which represents the

contribution to the velocity independent of z , and mode 1, $[U_1(x, y), V_1(x, y), W_1(x, y)]e^{i\beta z}$, which represents a sinusoidal perturbation. The set of initial conditions therefore is:

$$\begin{array}{lll}
 \text{mode } n = 0 & \text{mode } n = 1 & \text{mode } n > 1 \\
 U_0(0, y) = 1 & U_1(0, y) = 0 & U_n(0, y) = 0 \\
 V_0(0, y) = 0 & V_1(0, y) = V_1^0(y) & V_n(0, y) = 0 \\
 W_0(0, y) = 0 & W_1(0, y) = W_1^0(V_1^0(0, y)) & W_n(0, y) = 0
 \end{array} \quad (3.2.39)$$

where $W_1^0(V_1^0(0, y))$ formally means that V_1^0 and W_1^0 are related by continuity equation. This implies that, when dealing with the optimal perturbation problem, the only unknown is the function $V_1^0(y)$ which is the initial condition to be sought for. Once $V_1^0(y)$ is found, also $W_1^0(y)$ is available so that the initial conditions are completely known in order to perform the direct calculation.

For the optimal control problem, we observed that applying suction/blowing at the wall could be an effective way of controlling the boundary layer transition. Moreover, if the velocity applied at the wall is finite and uniform with z , boundary conditions at $y = 0$ are different from zero for the wall-normal component of mode zero only:

$$\begin{array}{ll}
 \text{mode } n = 0 & \text{mode } n > 0 \\
 U_0(x, 0) = 0 & U_n(x, 0) = 0 \\
 V_0(x, 0) = v_w(x) & V_n(x, 0) = 0 \\
 W_0(x, 0) = 0 & W_n(x, 0) = 0
 \end{array} \quad (3.2.40)$$

Functions $V_1(0, y)$ and $V_0(x, 0)$ are respectively the unknowns of the optimal perturbation and optimal control problem. In the first case, the boundary condition at the wall is fixed and is usually $V_0(x, 0) = 0$. The aim is therefore to find the optimal perturbations for the boundary layer over a flat plate without blowing/suction at the wall. In the second case, the initial condition $V_1(0, y)$ is fixed and usually equal to the optimal perturbation, and the aim is to control this worst-possible case.

However, when a finite control is applied at the wall, the non homogeneous boundary condition $V_0(x, 0) \neq 0$ can make the optimal disturbance different from the one computed for $V_0(x, 0) = 0$. In order to compute the correct optimal perturbation, robust control is needed. Basically, robust control is the combination of optimal perturbation and optimal control: the initial optimal perturbation is first found, then it is controlled by blowing/suction at the wall. Then, with the control acting at the wall, a new initial optimal perturbation is found which accounts for the non homogeneous boundary condition at the wall. A new control is performed again and the loop ends when the objective function does not change anymore. In the following sections, we present results regarding optimal perturbations, optimal control and robust control.

A remark concerning sinusoidal optimal perturbations

We said that the simplest form of the initial optimal perturbation is a sinusoidal dependence on the spanwise coordinate z , which means that each n^{th} mode with $n > 1$ is zero at $x = 0$. However, some tests have been performed considering initial optimal

perturbations with all Fourier modes different from zero. Results show that, for low values of the initial energy E_0 , mode zero of the optimal perturbation is much larger than the higher modes. This behavior is what was expected and allows us to consider few modes in the z -discretization.

A much stranger optimal solution is obtained for high initial energy. In this case, since nonlinear effects are supposed to act, more modes must be used. However, for a fixed value of E_0 , when N increases, the energy content of the higher modes increases instead of decreasing. In particular, the energy of the mode N is always the highest. This is shown in figure (3.1). E_n is the energy content of mode n , corresponding to the

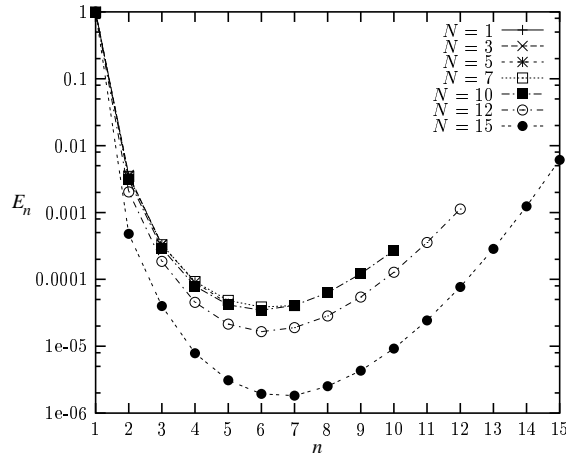


Figure 3.1: Energy “shift” towards higher modes when the number of modes N increases

optimal perturbation, and different curves are reported for different numbers of modes N . Tests regarding 1, 3, 5, 7, 10, 12 and 15 modes are considered. It is clear that when the number of modes is $N \leq 7$, all the curves collapse on one curve, meaning that mode $n = 1$ is dominant and the higher modes are on different scales and much smaller than the lower modes. On the contrary, for a number of modes $N \geq 10$, more energy (rather than less energy) is associated to modes greater than $n = 6$. For $N = 15$, the energy content of the highest mode ($n = 15$) is even greater than the energy of the second mode. This is quite strange and exactly the opposite of what one would expect, since higher modes should be negligible with respect to the lower ones.

The main problem is that such a solution cannot be accepted because it is highly grid-dependent. In fact, when a finer z -discretization is used (more Fourier modes in z), the solution changes a lot instead of converging to only one.

We first verified that it is actually the optimal solution (the one that maximizes the gain) by changing a bit some numerical values (of the solution) and finding a lower gain. Moreover we checked the dependence on the x - and y -discretization, without observing any better behavior.

It is therefore reasonable that such a strange optimal solution could be the solution of the discretized problem. The reason why we found this behavior could be that the objective function we considered is inadequate for this kind of optimization.

3.3 Optimal perturbations: results

Results concerning optimal perturbations are reported in this section. In all the following cases, the z -dependence of the solution at $x = 0$ is sinusoidal, as previously remarked. The boundary conditions at the wall are homogeneous ($V_0(x, 0) = 0$) and the calculation is extended from $x = 0$ to $x = 1$, which means that the surface length L introduced in section 3.2 is the total length of the plate.

First the dependence of the solution on the choice of different objective functions will be investigated for the linear case and then comparisons will be shown for three different conditions: at fixed wavenumber $\beta\delta$, at fixed initial energy E_0 and at the optimal wavenumber, defined as the wavenumber which maximizes the gain for the same initial energy.

3.3.1 Different objective functions – linear case

In figure (3.2) the results obtained using two different objective functions \mathcal{J} are compared. In one case $\mathcal{J} = E_{\text{out}}$, which corresponds to $\alpha = 1$ and $\beta = 0$ in expression (3.2.38), in the other case $\mathcal{J} = E_{\text{mean}}$, corresponding to $\alpha = 0$ and $\beta = 1$. In both cases a very low initial energy, $E_0 = 10^{-12}$, is applied in order to make the response linear. In figure (3.2)–a the energy of the streamwise perturbation u , made dimensionless with respect to the initial energy E_0 , is represented as a function of the streamwise coordinate x . Results are as expected: if the aim is the maximization of the energy at

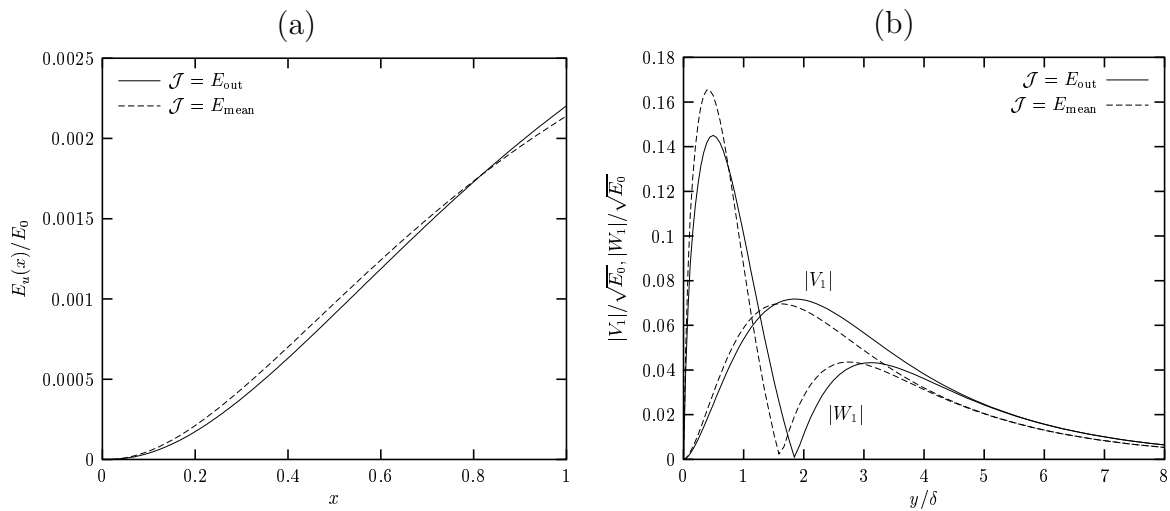


Figure 3.2: Comparison between two different objective functions. (a) energy of the streamwise velocity perturbation u as a function of x , normalized with respect to the initial energy E_0 . (b) optimal perturbations normalized with respect to $\sqrt{E_0}$. $\beta\delta = 0.45$, $E_0 = 10^{-12}$, linear behavior.

the final station, the maximum value is reached at $x = 1$. On the contrary, if the aim is the integral of the energy along the streamwise coordinate, the energy at the end is somewhat lower, but for a certain range of x values ($x < 0.8$) it is greater than in the first case (in order to render the integral higher). It is remarkable that the two curves

are very close to each other. On the contrary, when an opposition control is applied (Cathalifaud and Luchini [20]), the use of different objective functions produces different energy behaviors. In figure (3.2)–b the optimal initial velocity perturbation profiles

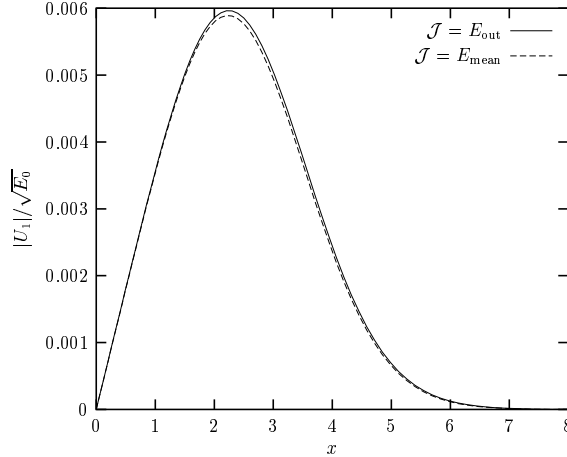


Figure 3.3: Comparison between two different objective functions. streamwise velocity component u at the final station $x = 1$, normalized with respect to $\sqrt{E_0}$, mode zero. $\beta\delta = 0.45$, $E_0 = 10^{-12}$, linear behavior.

are reported. Since the initial energy E_0 is very low and the regime is still linear, results regarding the maximization of the final energy E_{out} are the same as found by Luchini [79] and Andersson *et al.* [4]. For the case $\mathcal{J} = E_{\text{out}}$ the results are slightly different from the case $\mathcal{J} = E_{\text{mean}}$ in the sense that the maximum of V_1 is reached for smaller values of y/δ . In figure (3.3) the first mode of the direct solution is shown. It is referred to the final station $x = 1$, normalized with respect to $\sqrt{E_0}$ and corresponds to the initial conditions reported in figure (3.2). Since v and w are of the order of $Re^{-1/2}$ with respect to u , and therefore much smaller, only the modulus of the u component is reported. It can be easily observed that the shape of the solution at the final station does not change much depending on the objective function and on the initial conditions. This is in agreement with what already found by Luchini [79] regarding the “near universality” of the output velocity profile in the linear framework (for an extended discussion about this topic, see Luchini [79]).

3.3.2 Comparisons for varying $\beta\delta$ and E_0

In figure (3.4) the behavior of the mean gain $G_{\text{mean}} = E_{\text{mean}}/E_0$ is shown as a function of the wavenumber β for different values of the initial energy E_0 . The linear result (solid line) is obtained with a very low initial energy $E_0 = 10^{-12}$ and it can be noticed that increasing E_0 up to $E_0 = 1$ makes no difference, meaning that the nonlinear regime is not yet reached. In figure (3.4)–a β is normalized with respect to the characteristic length $\delta = \sqrt{\nu L/U_\infty}$. All the curves present a maximum at a certain wavenumber $\beta\delta$ depending on the value of E_0 . We call that particular wavenumber the optimal one since it provides the highest gain at a fixed E_0 . With increasing E_0 the maximum gain shifts

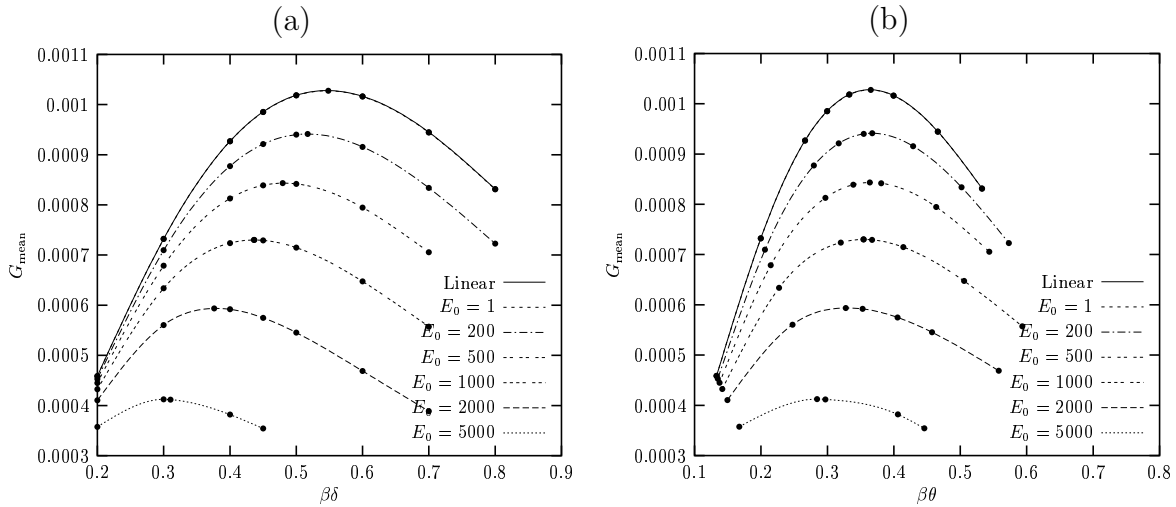


Figure 3.4: Gain $G_{\text{mean}} = E_{\text{mean}}/E_0$ for different initial energy values E_0 and different wavenumbers. (a) β made dimensionless with respect to $\delta = \sqrt{\nu L/U_\infty}$, (b) β made dimensionless with respect to the momentum thickness $\theta = \int_0^{+\infty} \frac{U_0}{U_\infty} \left(1 - \frac{U_0}{U_\infty}\right) dy$

towards lower wavenumbers and this dependence is stronger and more evident for high E_0 .

If the wavenumber β is normalized with respect to the momentum thickness θ^1 , figure (3.4)–b, a different dependence on the initial energy is found. The optimal wavenumber $\beta\theta$ does not move but remains almost constant with E_0 ($\beta\theta \approx 0.36$). If the initial energy is high, so that nonlinearities cause quite a strong deviation from the unperturbed base flow, a slight discrepancy to such a behavior is found. However, the fact that the optimal wavenumber remains almost constant with $\beta\theta$ is a very important feature because enforces the idea that the spanwise dimension of the vortices generated by the optimal perturbations scales with a typical boundary layer length (the momentum thickness). The same good scaling is not obtained if the displacement thickness is used. The reason why this happens is not yet clear.

From figure (3.4), different comparisons can be derived among the optimal perturbations. The first is at fixed $\beta\delta$ and increasing initial energy so as to test the influence of the nonlinear interactions as E_0 grows (section 3.3.3). Another possibility is to fix the initial energy E_0 and change the wavenumber $\beta\delta$ in order to check if there is any common dependence on the wavenumber, possibly comparing the results for two different values of E_0 (section 3.3.4). Finally, the last possibility is the comparison at the optimal wavenumber $\beta\delta$ (the one at which the gain is maximum at fixed E_0) for different values of E_0 (section 3.3.5).

¹We thank Prof. Henrik Alfredsson for suggesting the normalization of the wavenumber β with respect to the momentum thickness θ

3.3.3 Comparisons at fixed $\beta\delta$

In figure (3.5)–a the behavior of the velocity perturbation energy E_u , normalized with respect to the initial energy E_0 , is reported as a function of x for different values of E_0 at a fixed wavenumber $\beta\delta = 0.45$. Since the energy is normalized with E_0 , the ratio $E_u(x)/E_0$

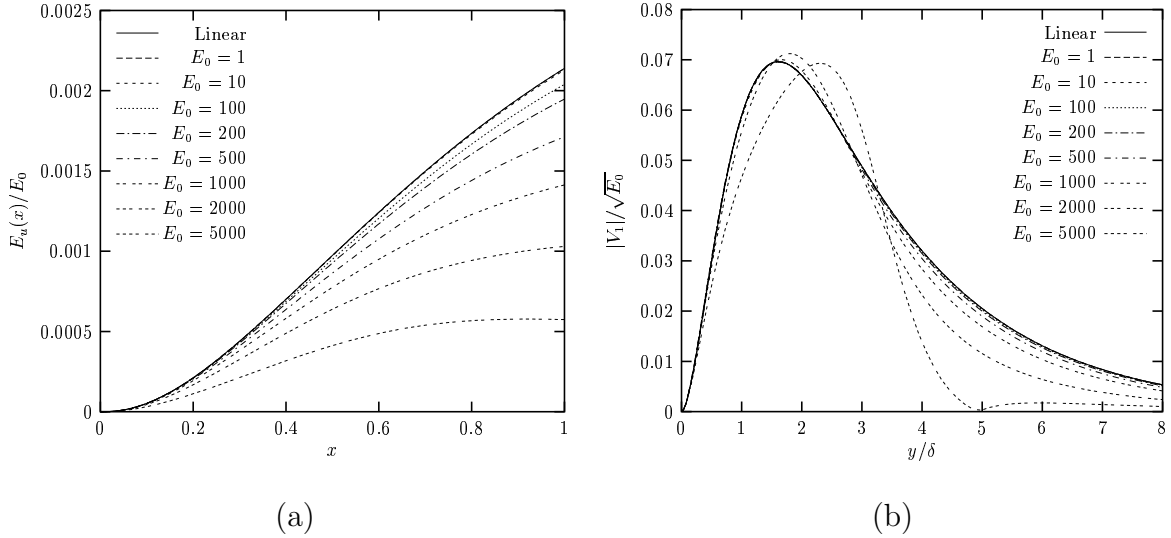


Figure 3.5: Results at fixed wavenumber $\beta\delta = 0.45$ for increasing initial energy E_0 . (a) streamwise perturbation energy $E_u(x)/E_0$; (b) optimal perturbation $|V_1|/\sqrt{E_0}$

can be interpreted as the ratio between the output and the input of the boundary–layer system. From figure (3.5)–a, therefore, one can have an idea of the deviation from the linear response of the system. A linear behavior of the solution is clearly observed for $E_0 \leq 10$, since all the curves collapse on the linear result (solid one), whereas for higher initial energies the curves show a plateau region probably due to saturation effects (the flat region observable for $E_0 = 5000$ and $0.8 < x < 1$). However, it is important to remember that the comparison is done at a fixed wavenumber $\beta\delta = 0.45$, which is not the optimal wavenumber for each energy E_0 and thus the solution found is not the optimal perturbation which produces the highest gain for that E_0 . In figure (3.5)–b the modulus of the first mode of the initial optimal perturbation $|V_1(y/\delta)|$ normalized with the square root of the initial energy E_0 is reported for fixed $\beta\delta = 0.45$ and increasing initial energies. Only the wall–normal velocity component is shown because $W_1(y/\delta)$ is nothing but the derivative of $V_1(y/\delta)$ with respect to the wall–normal coordinate (V_1 and W_1 are related by continuity). Again, a linear behavior can be observed up to $E_0 = 10$, whereas for higher values of E_0 the maximum shifts further from the wall and the shape of the optimal solution changes, going to zero with y faster than in the linear case. For $E_0 = 5000$ a different behavior of the solution is found: $V_1(y/\delta)$ changes sign around $y/\delta = 5$.

The effects of the nonlinearities due to the increase of the initial energy can be realized also by looking at the u and v components of the solution for mode zero at the final station. Mode zero represents the mean flow contribution independent of z and is reported in figure (3.6), where also the Blasius solution is plotted for comparison. For

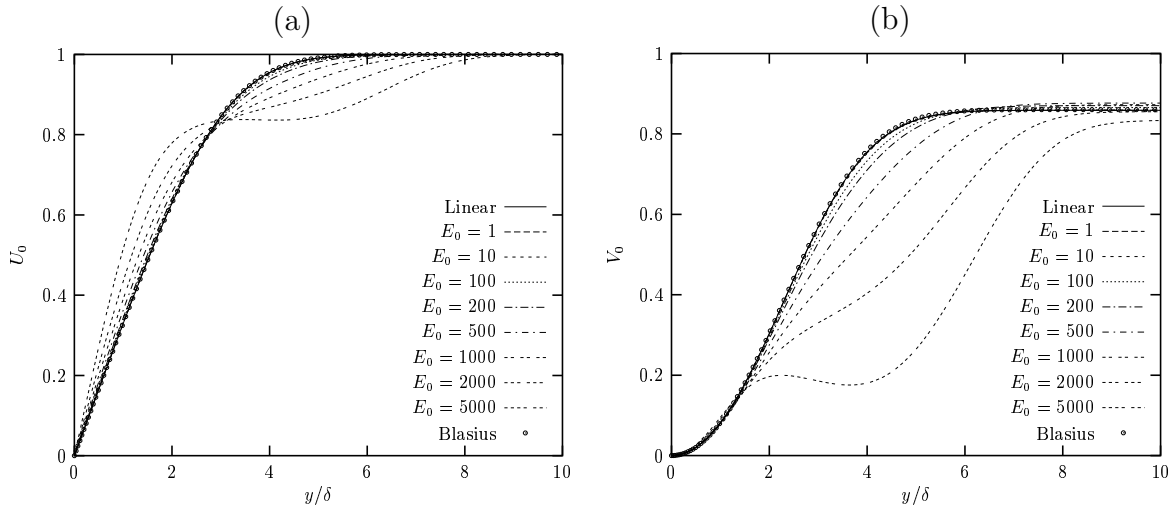


Figure 3.6: Comparisons at fixed wavenumber $\beta\delta = 0.45$. Mode zero at $x = 1$ for increasing E_0 . (a) streamwise component u ; (b) wall-normal component v

low values of E_0 , the solution is the same as Blasius', as was expected since nonlinear effects are not yet active. For $E_0 > 10$ the difference from Blasius's solution can easily be noticed, and for very high initial energies, for example $E_0 = 5000$, the solution at $x = 1$ inside the boundary layer is definitely different from Blasius' with remarkable flow distortions.

3.3.4 Comparisons at fixed E_0

Another possible way of analyzing results reported in figure (3.4) is to consider a fixed initial energy and see what happens with changing the wavenumber $\beta\delta$. This can be done, for instance, at low initial energy, where the response is still linear ($E_0 = 1$), or at high initial energy, where nonlinear effects are already evident ($E_0 = 1000$). In figure (3.7) the energy behavior as a function of x and the optimal perturbation are reported for low initial energy $E_0 = 1$. The solid line is referred to the optimal wavenumber. The energy, figure (3.7)-a, shows that the plateau observed for high E_0 at fixed $\beta\delta = 0.45$ (figure (3.5)-a) is found also at very low initial energy, but at high wavenumbers. The straightforward conclusion is that the plateau is not directly related to the initial energy E_0 or to the action of nonlinearities, but seems to be a characteristic of wavenumbers higher than the optimal one. This is actually confirmed by figure (3.8)-a, where the energy behavior for $E_0 = 1000$ is shown. In this case, nonlinear effects are supposed to produce a different response of the system. However, the plateau is present only at high wavenumbers, leading to the conclusion that this feature depends on $\beta\delta$ and not on the initial energy or nonlinear effects.

Such a plateau can be observed also in Andersson [3] and Andersson *et al.* [5], who solved (without optimization) the nonlinear boundary layer equations for a fixed initial condition corresponding to the optimal perturbation found in the linear framework by Luchini [79] and Andersson *et al.* [4] at $\beta\delta = 0.45$. In that case, results are shown for different initial energy E_0 and the plateau is observed at high E_0 ($\beta\delta$ is fixed). According

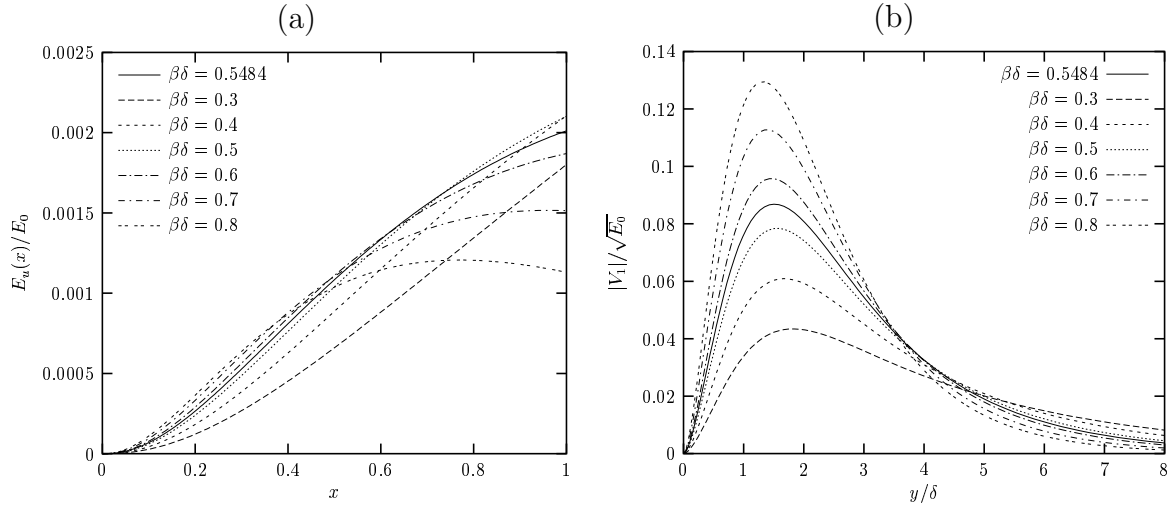


Figure 3.7: Comparisons at fixed initial energy $E_0 = 1$ for different values of the wavenumber $\beta\delta$. (a) streamwise perturbation energy $E_u(x)/E_0$; (b) optimal perturbation $|V_1|/\sqrt{E_0}$

to figure (3.7)–a and figure (3.8)–a, what found by Andersson [3] and Andersson *et al.* [5] seems to be due just to the fact that for those initial energies the wavenumber is higher than the optimal one.

From figure (3.7)–b and figure (3.8)–b one can notice that the shape of the optimal

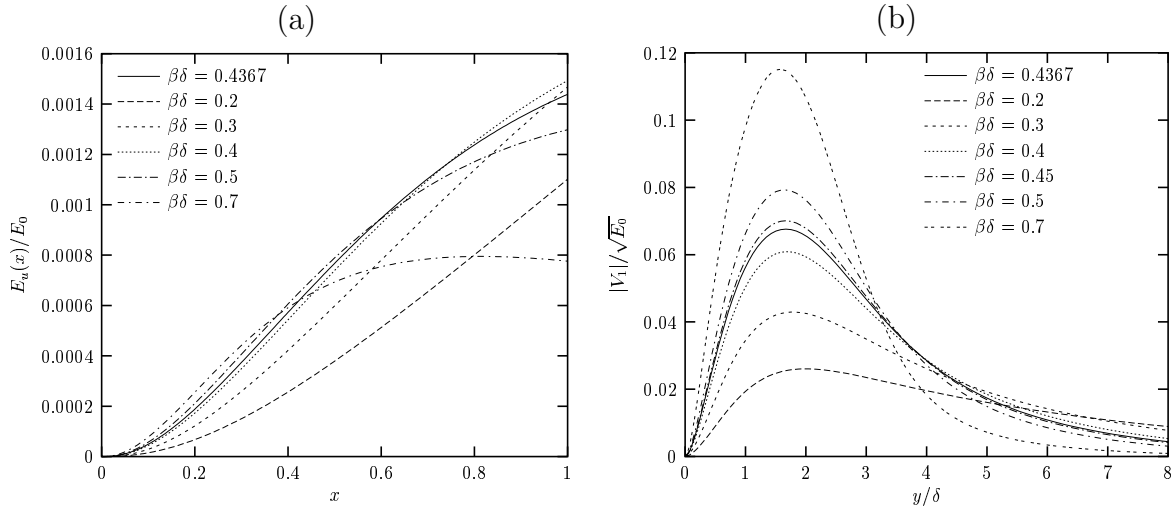


Figure 3.8: Comparisons at fixed initial energy $E_0 = 1000$ for different values of the wavenumber $\beta\delta$. (a) streamwise perturbation energy $E_u(x)/E_0$; (b) optimal perturbation $|V_1|/\sqrt{E_0}$

perturbation also changes with wavenumber, and the same trend characterizes low and high initial energy cases. For low $\beta\delta$ the profile goes to zero very slowly with y/δ , as shown in figure (3.7)–b for $\beta\delta = 0.2$ and in figure (3.8)–b for $\beta\delta = 0.3$. On the contrary, as the wavenumber increases, the velocity goes to zero much faster with y/δ . This feature is independent of the initial energy.

The conclusion from this kind of comparison is therefore that the wavenumber seems to have much greater influence than the initial energy E_0 on the shape of the initial optimal perturbation and on energy growth.

3.3.5 Comparisons at optimal $\beta\delta$

The last, and probably most interesting, way of comparing optimal perturbations is to plot the solution for each initial energy E_0 at the wavenumber corresponding to maximum gain at that particular energy. We call this wavenumber the optimal one. Results are shown in figure (3.9). The first remark is that the big differences previously observed

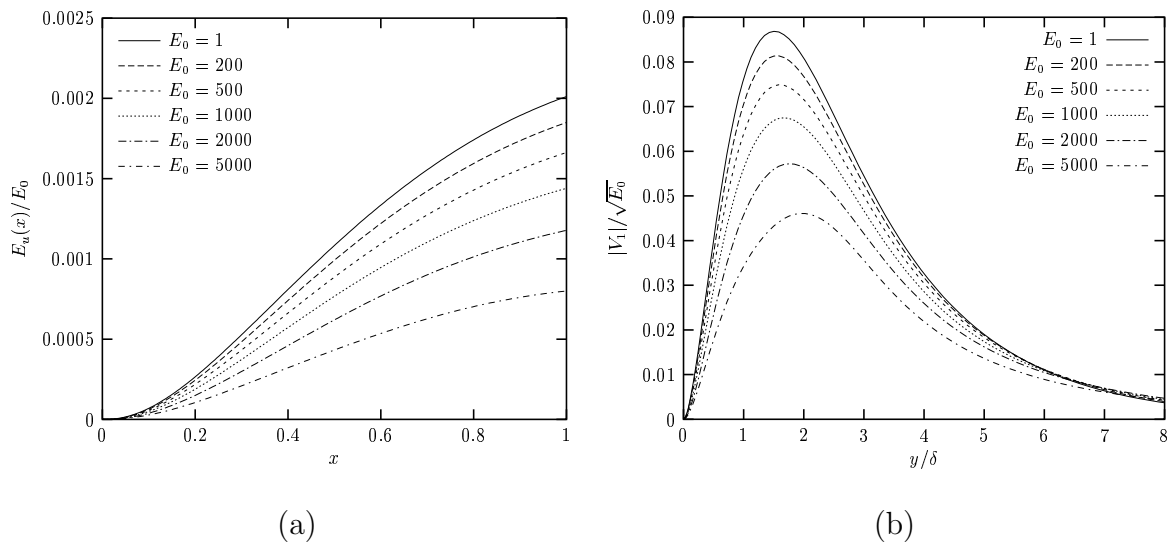


Figure 3.9: Comparisons at optimal wavenumber $\beta\delta$ (defined as the wavenumber for which the curve of the gain reaches its maximum at fixed initial energy E_0) for different values of E_0 . (a) streamwise perturbation energy $E_u(x)/E_0$; (b) optimal perturbation $|V_1|/\sqrt{E_0}$

at fixed wavenumber or at fixed E_0 are no longer present. Increasing the initial energy E_0 induces a variation in the energy behavior and in the shape of the optimal solution at $x = 0$, but the change is much smoother than what happened at fixed $\beta\delta$ or fixed E_0 . In figure (3.10) the u and v component of mode zero at the final station are plotted at the optimal wavenumber and increasing E_0 . The aim of figure (3.10) is to give an idea of how much the mean velocity field, which represents the sum of unperturbed flow and the mean-flow correction, is affected by nonlinearities with increasing values of E_0 . It is clear that, for $E_0 > 10$, nonlinear effects are strong enough in order to cause a considerable change in the solution.

3.4 Optimal control: results

In the previous section, which deals with optimal perturbations, we found the worst possible initial condition for the nonlinear boundary layer equations in order to generate

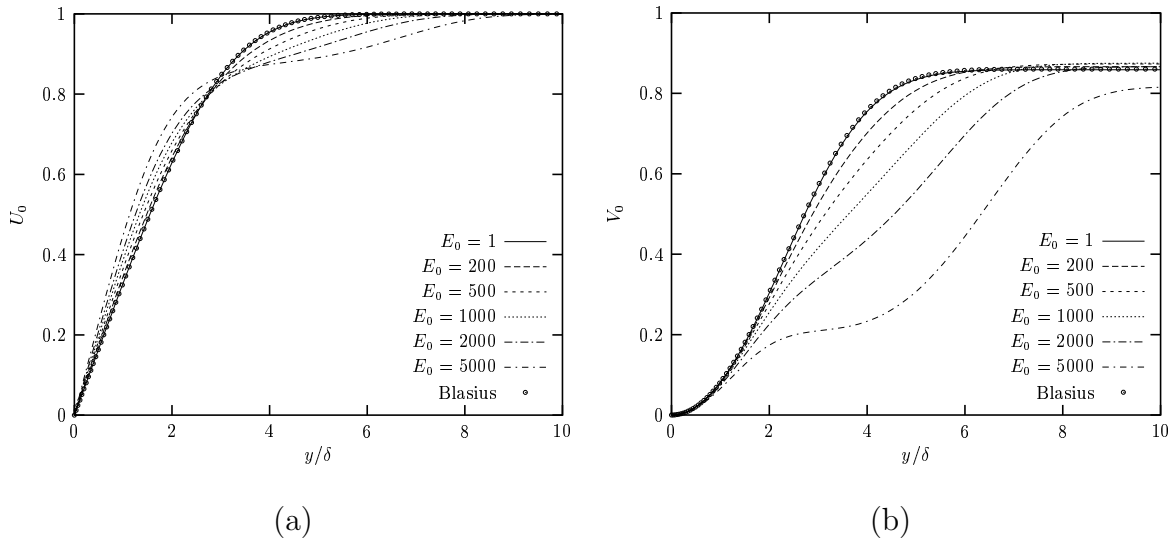


Figure 3.10: Comparisons at optimal wavenumber $\beta\delta$ for different values of E_0 . Mode zero at $x = 1$ for increasing E_0 . (a) streamwise component u ; (b) wall-normal component v

the highest integral of the energy density over the complete domain. Once these initial conditions have been found, another reasonable question that can be asked is: what is the best way to oppose the energy growth caused by those initial optimal perturbations? This question is addressed in optimal control. Our aim will be to find the best blowing/suction profile to apply at the wall in order to obtain the lowest integral of the energy over the whole domain for a given initial condition, namely the optimal perturbation found at that particular wavenumber $\beta\delta$.

Different possible controlling strategies are available. We choose to act only on the wall-normal velocity component $V_0(x, 0)$ of mode zero at $y = 0$. One reason is that a control independent of the spanwise coordinate z seems to be more feasible in practical applications. Therefore, in all the following cases, the control energy at the wall is defined as

$$E_w = \int_0^X |V_0(x, 0)|^2 dx \quad (3.4.1)$$

3.4.1 Different objective functions – linear case

In order to determine the best blowing/suction profile at the wall in order to control the algebraic growth due to initial sinusoidal optimal perturbations, the first test is to observe the differences generated by two objective functions $\mathcal{J} = E_{\text{out}}$ and $\mathcal{J} = E_{\text{mean}}$. When the former is chosen, the aim is to minimize the energy at the final streamwise station; with the second choice, the aim is the minimization of the integral of the energy over the whole domain. Results are shown in figure (3.11) for a very low initial energy, $E_0 = 10^{-12}$, where the behavior is still linear, and for a quite strong control energy $E_w = 1$. The initial optimal perturbations for these tests are respectively the ones reported in figure (3.2). If the objective function is the energy at the end, obviously the energy can grow for $x < 1$ and be larger than the one at the final station. This actually

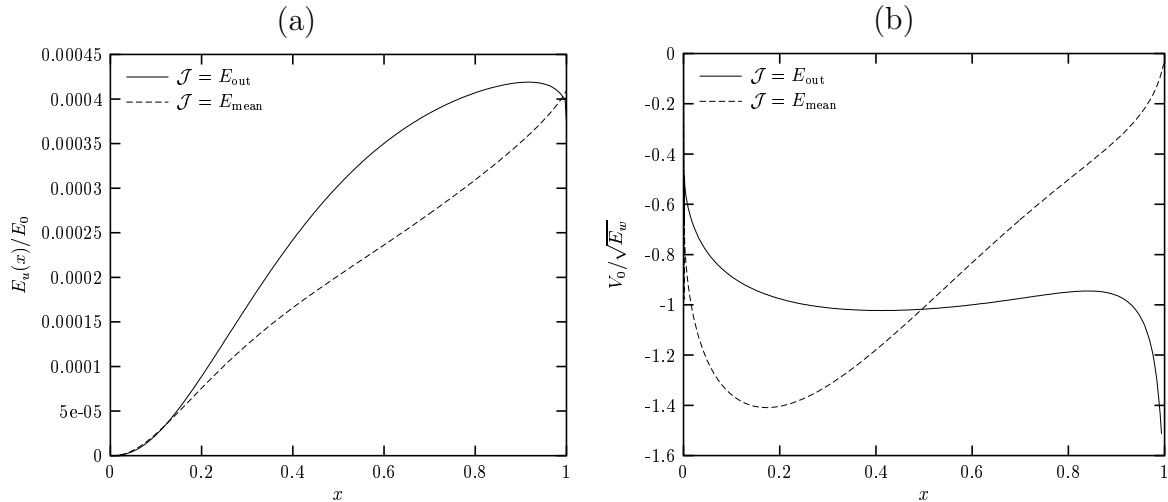


Figure 3.11: Comparison between two different objective functions, $\beta\delta = 0.45$, $E_0 = 10^{-12}$, linear behavior. (a) energy of the streamwise velocity perturbation u as a function of x , normalized with respect to the initial energy E_0 . (b) optimal suction at the wall normalized with respect to the control energy $\sqrt{E_w}$.

happens, as reported in figure (3.11)–a. Moreover, for $\mathcal{J} = E_{\text{out}}$, even if the optimal suction profile is quite flat for $0.2 < x < 0.8$ (figure (3.11)–b), the velocity profile V_0 goes to $-\infty$ for $x > 0.8$, becoming quite difficult to be implemented in practical applications. Therefore, the minimization of the final energy seems to have at least two drawbacks: the first is that for $x < 1$ the energy can grow a lot and lead to transition before reaching the final station, just as pointed out (in a different situation) by Cathalifaud and Luchini [20]. The second drawback is the feasibility of such a solution: since a very high suction velocity (in modulus) is required at the trailing edge, non trivial problems could be found in designing the suction system. On the other hand, if the objective function is $\mathcal{J} = E_{\text{mean}}$, where the integral of the energy over the whole domain is minimized, the energy behavior does not present any maximum for $0 < x < 1$ (the curve grows monotonically), as shown in figure (3.11)–a. The highest energy is reached at the final station and the energy inside the domain, for $x < 1$, is lower than in the previous case. This could be much better as far as the stability characteristics of the flow are concerned. In addition, for $\mathcal{J} = E_{\text{mean}}$, the suction velocity profile, in figure (3.11)–b, seems to be more feasible than the previous one: it does not go to infinity, but tends to a finite value for $x = 0$ and $x = 1$.

From these considerations it is clear that if the purpose is to control the energy growth, it is much better to minimize the integral of the energy along the streamwise direction instead of the energy at the final station. For this reason, in the following tests, we consider only the objective function $\mathcal{J} = E_{\text{mean}}$.

3.4.2 Comparisons for varying $\beta\delta$ and E_w

Results presented in the following figures, as done for optimal perturbations, are referred to $E_0 = 1$, for which the behavior is still linear, and $E_0 = 1000$, where nonlinear inter-

actions between the different modes produce visible effects (see figure (3.5)—a regarding optimal perturbations).

The initial conditions correspond to the optimal perturbations previously computed and the optimal control, in order to oppose them, is in the form of a spanwise uniform blowing/suction at the wall.

In figure (3.12) the mean gain $G_{\text{mean}} = E_{\text{mean}}/E_0$ is reported for $E_0 = 1$ and $E_0 = 1000$ as a function of the spanwise wavenumber $\beta\delta$ and for different values of the control energy at the wall E_w . The solid lines in figure (3.12)—a and figure (3.12)—b represent

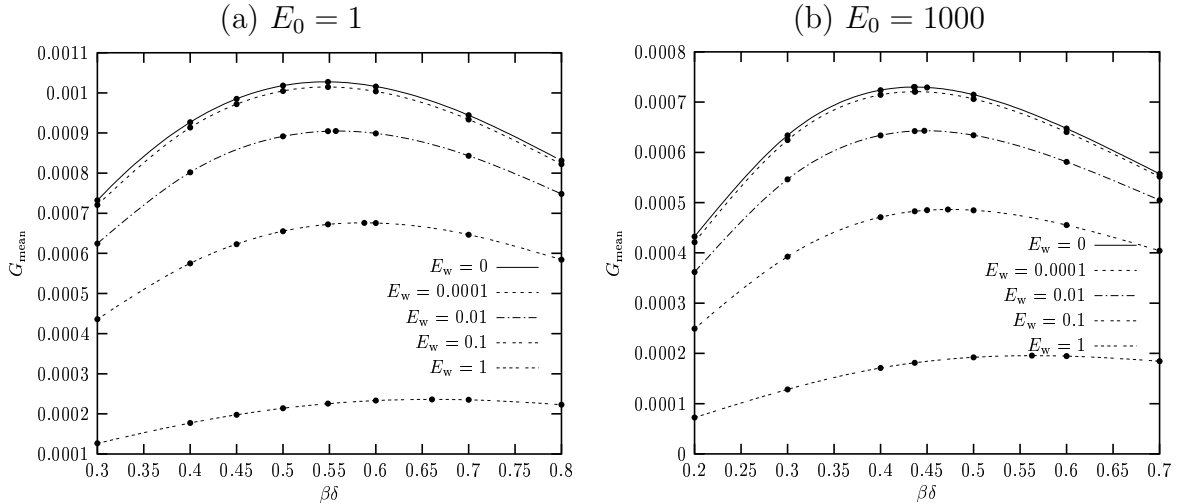


Figure 3.12: Gain $G_{\text{mean}} = E_{\text{mean}}/E_0$ as a function of the spanwise wavenumber $\beta\delta$ for different values of the control energy at the wall E_w . (a) initial energy $E_0 = 1$; (b) initial energy $E_0 = 1000$

the uncontrolled case (they are the same curves already shown in figure (3.4)). With reference to low initial energy, figure (3.12)—a, it can be seen that if the control energy is low, $E_w = 0.0001$, there is not much difference with the uncontrolled case $E_w = 0$, as one could expect. The maximum of the curve is still at the same wavenumber $\beta\delta = 0.55$ and the gain is just slightly lower, because of the control. If the control energy at the wall is increased, $E_w = 0.01$, the maximum of the curve shifts towards higher wavenumbers $\beta\delta$ and the difference with the uncontrolled case becomes more evident. The same behavior characterizes also the case $E_w = 0.1$ and for the highest control $E_w = 1$, the maximum of the curve is located at $\beta\delta = 0.66$ which is 20% more than the optimal wavenumber without control. For higher initial energy, $E_0 = 1000$, the same dependence on the control energy E_w is found. Referring to figure (3.12)—b, for very low control, $E_w = 0.0001$, the maximum is close to the uncontrolled case, whereas for higher control at the wall the optimal wavenumber monotonically moves to higher values. For the strongest control, $E_w = 1$, the maximum of the curve is located at $\beta\delta = 0.56$ whereas without control it was around $\beta\delta = 0.437$.

Exactly as done in the optimal perturbations framework, also for optimal control different comparisons can be analyzed. However, we prefer to keep two fixed initial energy values, one in the linear regime, $E_0 = 1$, and one in the nonlinear regime, $E_0 = 1000$, and for both of them to compare the results in different ways. The first possibility is

at a fixed wavenumber $\beta\delta$, equal to that corresponding to the maximum gain without control. Comparisons, in this case, can be done for different control energies at the wall E_w (section 3.4.3). Another choice is to fix the control energy E_w and to follow the dependence on the wavenumber varying $\beta\delta$ (section 3.4.4). The last possibility is to compare results at the optimal wavenumber for each E_w (section 3.4.5). The optimal wavenumber is defined, like in the optimal perturbation framework, as the wavenumber for which the curve $G_{\text{mean}}(\beta\delta)$ reaches its maximum.

3.4.3 Comparisons at fixed $\beta\delta$

For comparisons at fixed $\beta\delta$ we chose the optimal wavenumber of the uncontrolled case as the reference wavenumber. Since two values of initial energy are considered ($E_0 = 1$ and $E_0 = 1000$), two values of $\beta\delta$ are presented: $\beta\delta = 0.548$ for $E_0 = 1$ and $\beta\delta = 0.437$ for $E_0 = 1000$ (see figure (3.12)). In figure (3.13) the energy behavior $E_u(x)/E_0$ is

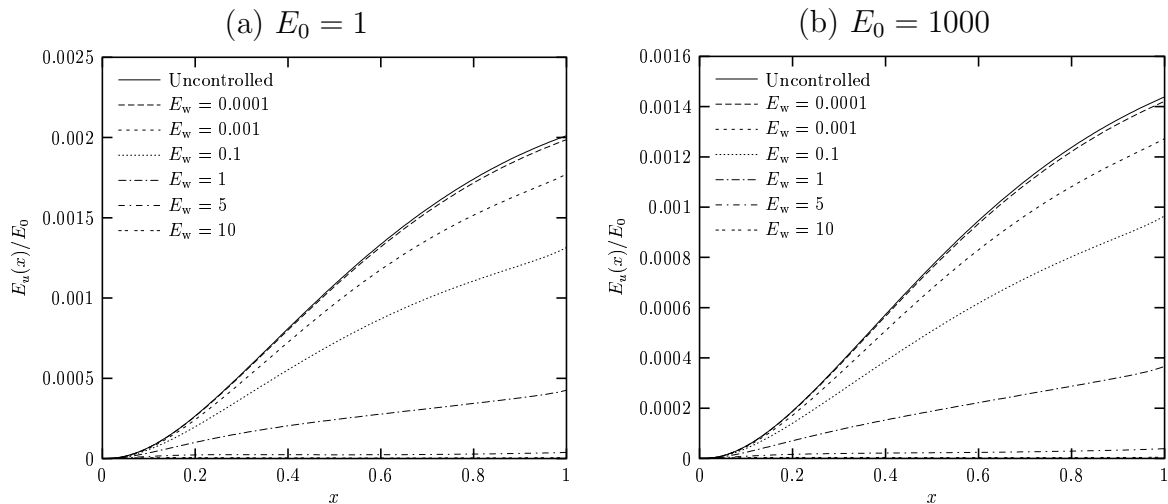


Figure 3.13: Comparisons at fixed wavenumber $\beta\delta$: streamwise perturbation energy $E_u(x)/E_0$ for increasing control energy E_w at the wall. (a) $E_0 = 1$ and $\beta\delta = 0.548$; (b) $E_0 = 1000$ and $\beta\delta = 0.437$

reported for increasing control energy E_w . It is clear that a small control energy at the wall, $E_w = 0.0001$ produces a very small effect on the energy growth, as expected, and this is true for both initial energies $E_0 = 1$ and $E_0 = 1000$. On the other hand, if the control energy increases, a deviation of the energy growth from the uncontrolled case can be much better appreciated. For very high control, $E_w = 5$ and $E_w = 10$, the reduction in $E_u(x)$ is very strong and cannot be seen from figure (3.13). If a zoom is made for the lower part of the figure, it can be seen that also the energy profile changes when a strong control is applied (figure (3.14)). In fact, whereas for small E_w the maximum of the energy is reached at $x = 1$, for the highest control ($E_w = 10$) the maximum is reached at smaller streamwise positions, as shown in figure (3.14). This is true for both low and high initial energy E_0 .

In figure (3.15) the optimal blowing/suction profile at the wall is presented for the cases reported in figure (3.13). Each profile has been normalized with respect to $\sqrt{E_w}$ in

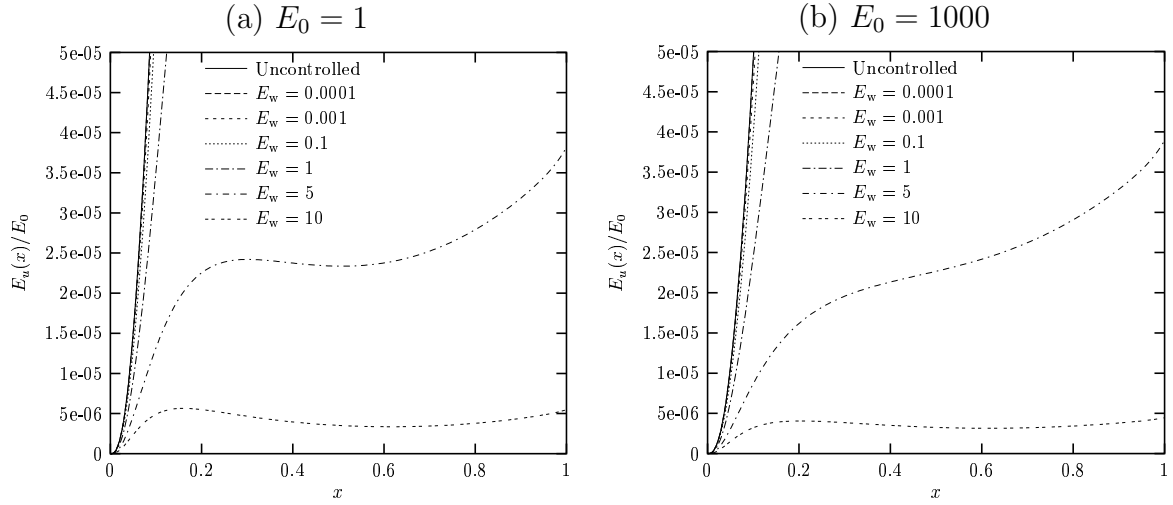


Figure 3.14: Comparisons at fixed wavenumber $\beta\delta$: streamwise perturbation energy $E_u(x)/E_0$ for increasing control energy E_w at the wall. (a) $E_0 = 1$ and $\beta\delta = 0.548$; (b) $E_0 = 1000$ and $\beta\delta = 0.437$

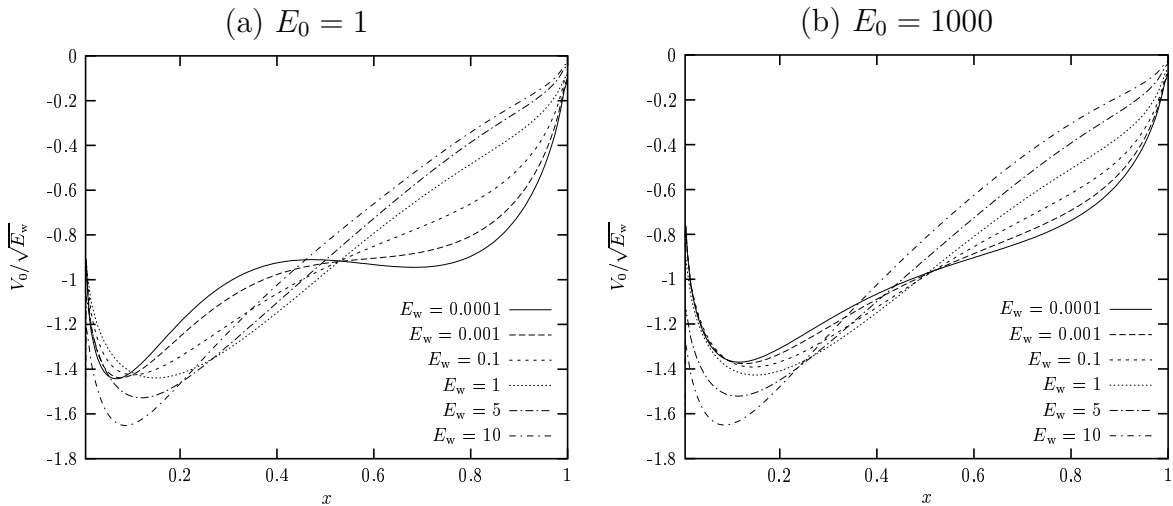


Figure 3.15: Comparisons at fixed wavenumber $\beta\delta$: optimal suction profile at the wall $V_0/\sqrt{E_w}$ for increasing control energy E_w . (a) $E_0 = 1$ and $\beta\delta = 0.548$; (b) $E_0 = 1000$ and $\beta\delta = 0.437$

order to have the possibility to evaluate the difference in the shape for different control energy. The first remark is that the control velocity at the wall is always negative, so that only suction is applied. For low initial energy $E_0 = 1$, the optimal suction profile seems to change a lot depending on the control energy E_w = (figure (3.15)–a), whereas for higher initial energy $E_0 = 1000$ all the profiles have more or less the same shape. What is interesting from figure (3.15) is that the maximum of the absolute value of the velocity at the wall shifts toward higher x if $E_w < 1$, whereas for $E_w > 1$ the behavior is exactly the opposite. This happens for both low and high initial energy. In any case, the highest control is performed close to the leading edge, at low values of x , as expected since the boundary layer equations are parabolic in x and therefore the first streamwise

stations are important for the downstream development of the flow.

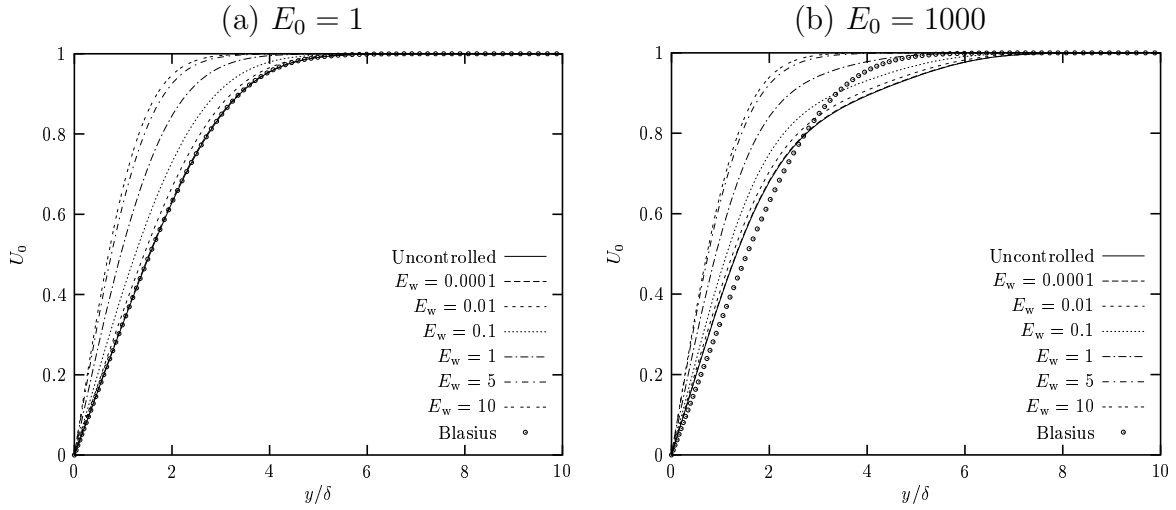


Figure 3.16: Comparisons at fixed wavenumber $\beta\delta$: streamwise velocity component u of mode zero at $x = 1$ for increasing control energy E_w at the wall. (a) $E_0 = 1$ and $\beta\delta = 0.548$; (b) $E_0 = 1000$ and $\beta\delta = 0.437$

In order to investigate the influence of the control on the flow, we reported in figure (3.16) the mode zero at the final station for $E_0 = 1$ and $E_0 = 1000$. From the

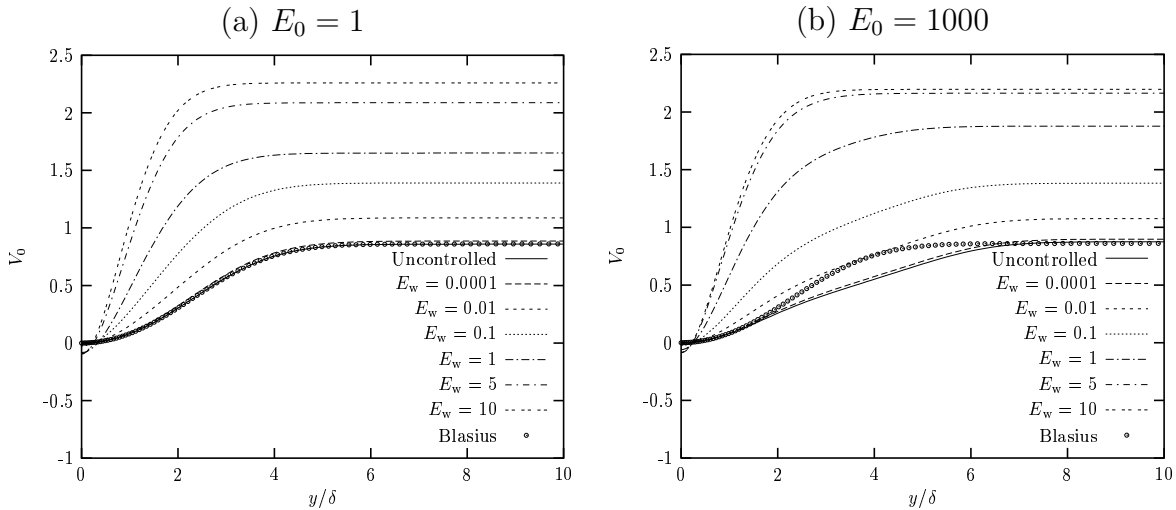


Figure 3.17: Comparisons at fixed wavenumber $\beta\delta$: wall-normal velocity component v of mode zero at $x = 1$ for increasing control energy E_w . (a) $E_0 = 1$ and $\beta\delta = 0.548$; (b) $E_0 = 1000$ and $\beta\delta = 0.437$

optimal perturbation analysis, it was clear that for $E_0 = 1$ nonlinear effects are not yet evident and this is confirmed by figure (3.16)–a where Blasius and uncontrolled profiles coincide. The only effect caused by the increase of the control energy is the modification of the mean flow velocity in order to make it closer to accelerating Falkner–Skan profiles. For high initial energy, $E_0 = 1000$, the mode zero in the uncontrolled case is completely different from Blasius because of strong distortions induced by nonlinear effects. If the

control is applied, from figure (3.16)–b one can deduce that stronger the control, closer the profile is to the one for low initial energy. For example for $E_w = 10$ the profiles at $E_0 = 1$ and $E_0 = 1000$ are almost the same. In figure (3.17) also the v -component of the mode zero is reported. The same considerations done for the streamwise component are still valid for the wall-normal one. It can be noticed that V_0 is negative close to the wall due to the suction velocity at $y = 0$. In any case, the effect of suction is basically to move the profile closer to the wall making it to look like an accelerating one.

From the physical point of view, it is worth to investigate how the optimal control attenuates the disturbance induced by the optimal perturbation. This can be done by looking at the velocity vectors (v, w) or the streamwise velocity (u) contour in the (z, y) plane, at different streamwise locations. In figure (3.18) results are shown for high initial energy $E_0 = 1000$ and $\beta\delta = 0.437$. The values of control energy E_w are some of those presented in figure (3.13) ($E_w = 0$, uncontrolled case, $E_w = 0.1$, $E_w = 1$, $E_w = 5$ and $E_w = 10$), and three x -locations are considered: $x = 0.1$ (since the control is very strong about this position), $x = 0.5$ (inside the domain) and $x = 1$ (the final station).

Without control ($E_w = 0$, figure (3.13)–1), the optimal perturbation causes streamwise vortices which grow with x , as can be realized by comparing plots at different streamwise locations (a1, b1, c1). When a slight control is applied ($E_w = 0.1$, figure (3.13)–2), the most evident effects can be noticed at the final station, where the shape of the vortices changes and their dimension seems to be smaller than in the uncontrolled case. On the contrary, close to the leading edge ($x = 0.1$) and in a middle position ($x = 0.5$) no remarkable attenuation of the disturbance can be appreciated. For a higher control, $E_w = 1$, figure (3.13)–3, a reduction of vortices size can be seen at $x = 0.1$, whereas at $x = 0.5$ one can observe that the core of the vortices moves towards $z = 0$. The strongest effect is visible at $x = 1$, where the original vortices are highly deformed. For $E_w = 5$, figure (3.13)–4, which corresponds to a remarkable disturbance attenuation as reported in figure (3.14)–b, close to the leading edge the vortices are still recognizable, whereas at $x = 0.5$ they have been sucked away and at $x = 1$ the flow is quite regular and completely different from the uncontrolled case. The last test, for $E_w = 10$, figure (3.13)–5, shows a very strong suction close to the leading edge, a disappearance of the vortices at $x = 0.5$ and a very regular flow field at the final station. From figure (3.18), it seems that the effect of the control at the wall is to suck away the vortices from the boundary layer.

The contour of the streamwise velocity u , reported in figure (3.19), confirms the hypothesis regarding the stabilization of the flow. For a Blasius profile, the contour plot corresponds to lines parallel to z so that the deviation from such a behavior can give an idea of how strong the disturbance is. Without control, figure (3.19)–1, the flow field is quite regular close to the leading edge ($x = 0.1$), whereas the effects of the streamwise vortices are more evident at $x = 0.5$. At the final position $x = 1$, figure (3.19)–c1, the flow distortion induced by the optimal perturbation is definitely clear. When the control at the wall is applied and the disturbance reduced, two effects are visible on the plots. The first is that the contour lines become parallel to z axes, the second is the reduction of the perturbed region along z . For instance, comparing plots at $x = 1$, figure (3.19)–c, one can notice that without control the contour lines are highly nonparallel and the region where this happens is between $z = -8$ and $z = 8$. For increasing control energy

E_w at the wall, more parallel patterns are observed and, for the highest control $E_w = 10$, the unperturbed region reduces between $z = -3$ and $z = 3$.

Plots shown in figure (3.19) visually confirm that the main effect of a suction velocity profile at the wall is to control the disturbance by sucking away the boundary layer, confining it closer to the wall.

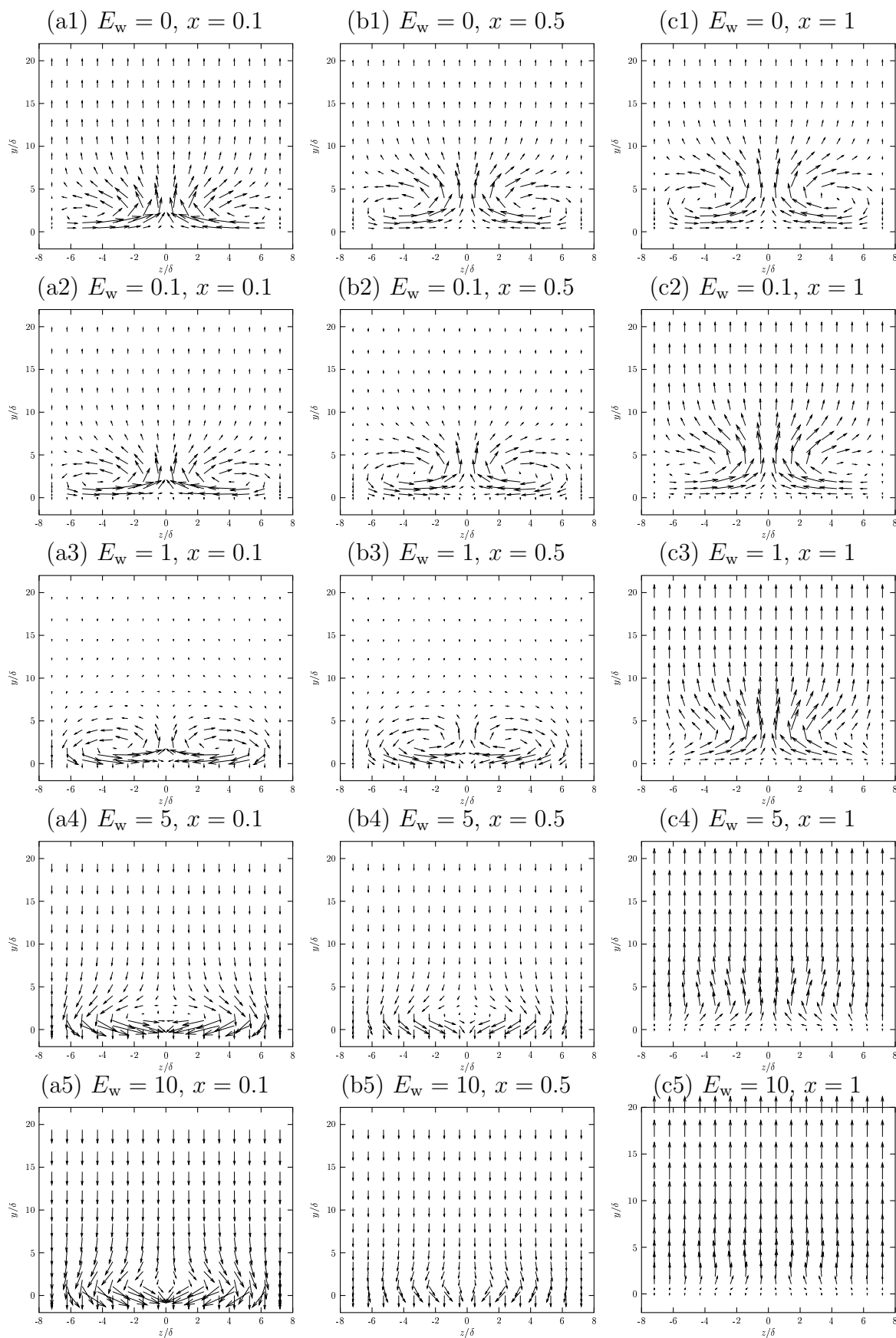


Figure 3.18: $E_0 = 1000$, $\beta\delta = 0.437$. Velocity vectors (v, w) in the (z, y) plane.

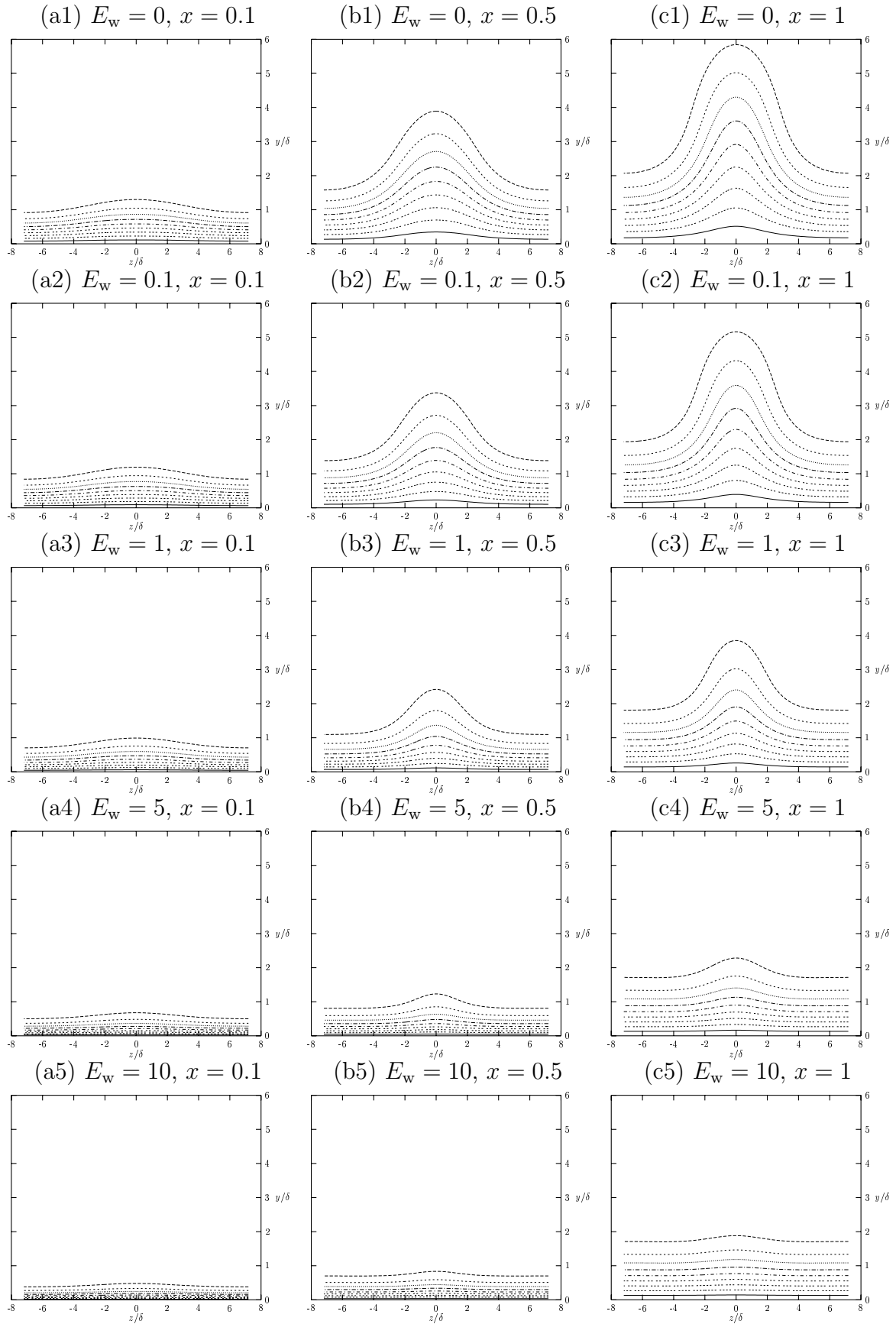


Figure 3.19: $E_0 = 1000, \beta\delta = 0.437$. Streamwise velocity u contour in the (z, y) plane.

3.4.4 Comparisons at fixed E_w

Another possible comparing approach is to consider the evolution of the solution as a function of the wavenumber $\beta\delta$, at a fixed control energy E_w . In figure (3.20) the energy $E_u(x)/E_0$ is reported for two initial energies ($E_0 = 1$ and $E_0 = 1000$) and $E_w = 0.01$. The

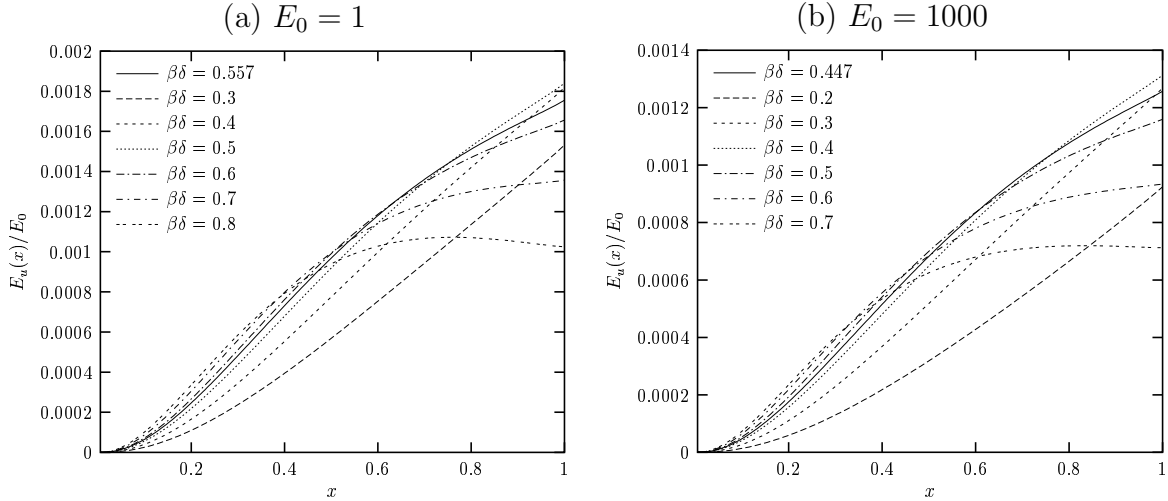


Figure 3.20: Comparisons at fixed control energy $E_w = 0.01$ for increasing wavenumbers $\beta\delta$: streamwise perturbation energy $E_u(x)/E_0$. (a) $E_0 = 1$; (b) $E_0 = 1000$

solid line corresponds to the optimal wavenumber for that initial energy and the plots are normalized with the corresponding E_0 , in order to make it possible to compare the results on the same scale. One can easily see that there is not much difference between low and high initial energy profiles. For both initial energies, when the wavenumber

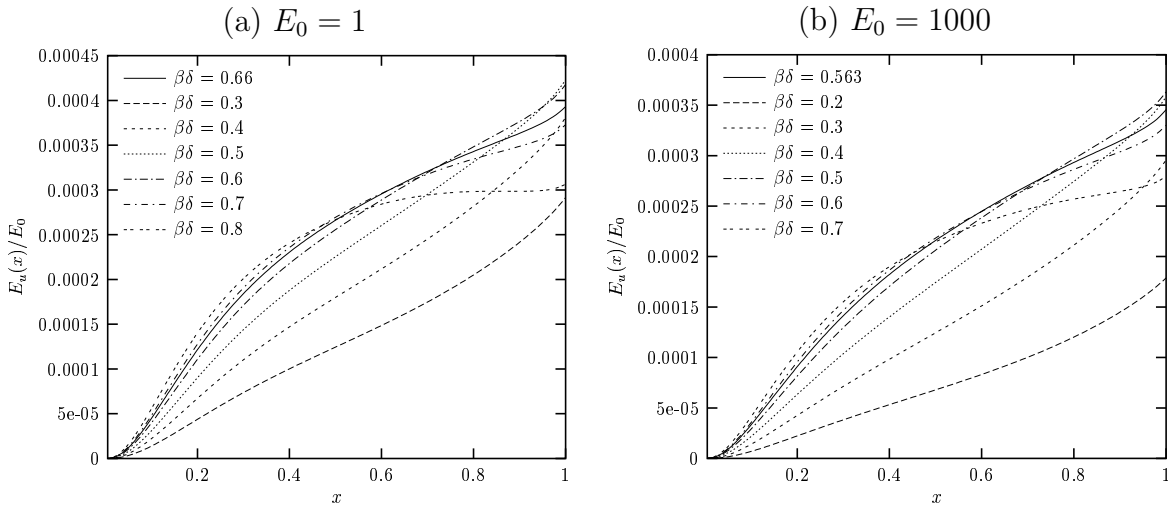


Figure 3.21: Comparisons at fixed control energy $E_w = 1$ for increasing wavenumbers $\beta\delta$: streamwise perturbation energy $E_u(x)/E_0$. (a) $E_0 = 1$; (b) $E_0 = 1000$

is increased, the shape of the energy profile presents the typical plateau seen in the optimal perturbation framework. The presence of this characteristic also in the optimal

control framework is probably due to the fact that the control energy, $E_w = 0.01$, is not strong enough in order to reduce the effects produced by optimal perturbations. This hypothesis is actually confirmed by figure (3.21) where the energy profiles are reported for a stronger control, $E_w = 1$. The curves do not show any plateau and in all the cases the maximum of $E_u(x)$ is always reached at the final station. In figure (3.22) the optimal suction profiles at the wall for $E_w = 0.01$ are reported. Also in this case the solid line corresponds to the optimal wavenumber for that initial energy. It seems

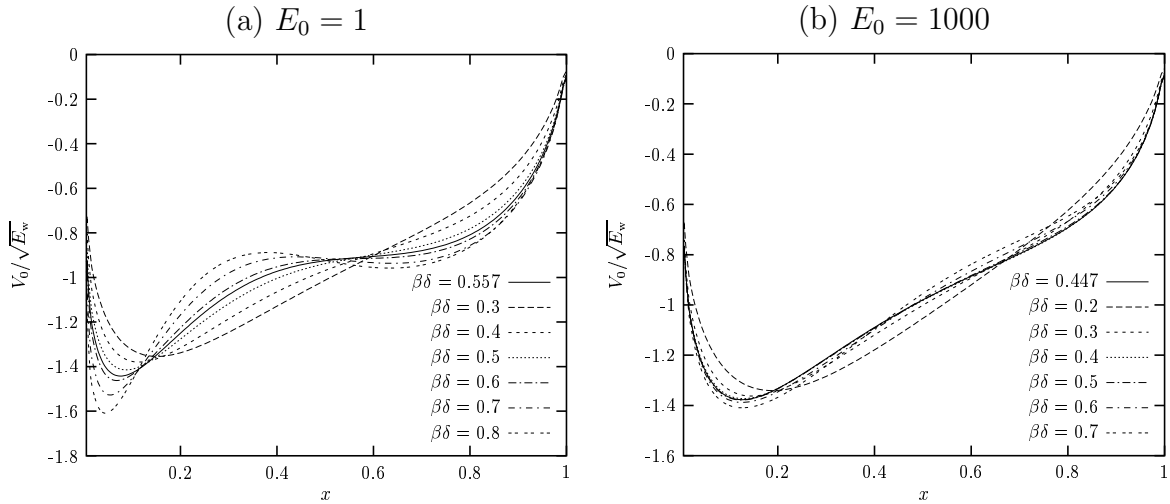


Figure 3.22: Comparisons at fixed control energy $E_w = 0.01$ for increasing wavenumbers $\beta\delta$: optimal suction profile at the wall $V_0/\sqrt{E_w}$. (a) $E_0 = 1$; (b) $E_0 = 1000$

that low initial energy $E_0 = 1$ makes the optimal control profile more sensitive to the wavenumber $\beta\delta$ than $E_0 = 1000$. Referring to figure (3.22)–a, the strongest suction is

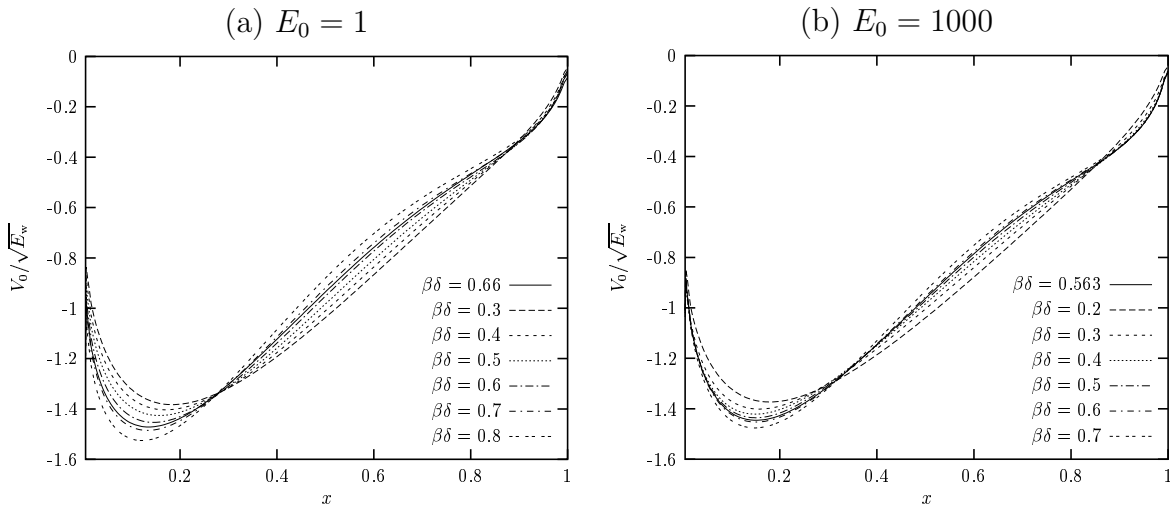


Figure 3.23: Comparisons at fixed control energy $E_w = 1$ for increasing wavenumbers $\beta\delta$: optimal suction profile at the wall $V_0/\sqrt{E_w}$. (a) $E_0 = 1$; (b) $E_0 = 1000$

always close to the leading edge, but the shape of the profile changes quite a lot with $\beta\delta$. For small wavenumbers only one minimum is found for $0.1 < x < 0.2$, whereas if

$\beta\delta$ grows, the main minimum shifts towards smaller x but oscillations with two minima are observed. This is particularly evident for $\beta\delta = 0.8$. On the contrary, for high initial energy $E_0 = 1000$, the optimal control suction profile is not affected too much by the value of the spanwise wavenumber $\beta\delta$. If the control energy is increased to $E_w = 1$, figure (3.23), the strong dependence of the optimal suction profile on the wavenumber disappears. In figure (3.23) results are shown for the two initial energies $E_0 = 1$ and $E_0 = 1000$. It is clear that the evolution of the suction profile for different wavenumbers $\beta\delta$ at fixed $E_w = 1$ seems to be the same for both low and high E_0 . This is probably due to the stronger effects induced by a higher control energy at the wall which makes the profiles closer each another.

3.4.5 Comparisons at optimal $\beta\delta$

The last comparison we present is at the optimal wavenumber, the one for which the curve of the gain reaches its maximum for that particular control energy E_w . As far as

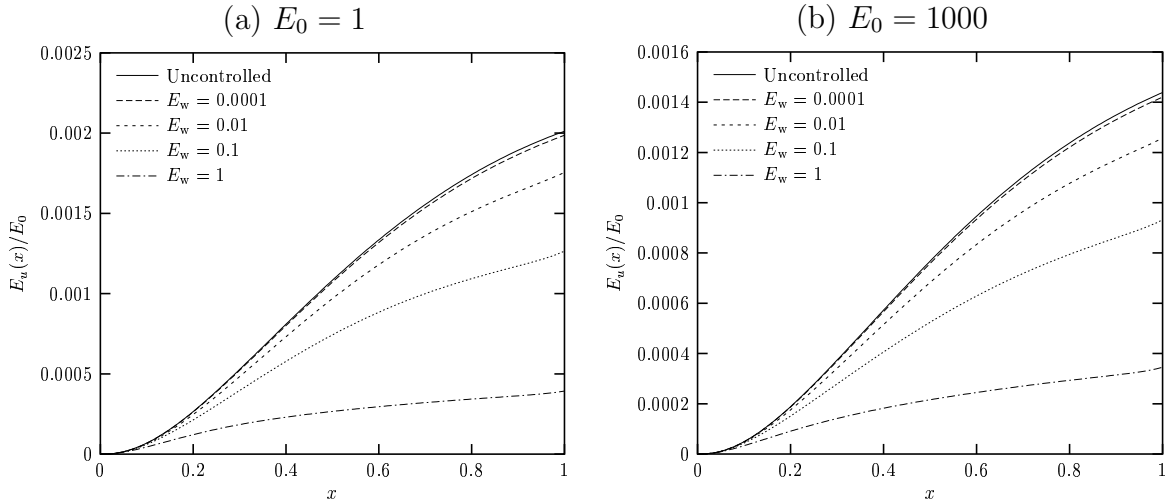


Figure 3.24: Comparisons at optimal wavenumber $\beta\delta$ for different values of the control energy E_w : streamwise perturbation energy $E_u(x)/E_0$. (a) $E_0 = 1$; (b) $E_0 = 1000$

the energy behavior is concerned, there is not much difference between the results at low initial energy $E_0 = 1$, figure (3.24)–a, and high initial energy $E_0 = 1000$, figure (3.24)–b. Obviously, when the control energy is higher, the curve is lower. The comparison between suction profiles, on the contrary, seem to be much more interesting. For $E_0 = 1$, the optimal suction profile at the wall is very sensitive to the control energy E_w . From figure (3.25)–a it is clear that for low E_w the velocity profile has two minima, whereas when E_w increases, the profile becomes more regular with a single minimum. For high initial energy $E_0 = 1000$, all the profiles have more or less the same shape, independently of the control energy E_w . This dependence of the profiles on the varying parameter was noticed also at fixed control energy. In any case, the highest absolute values of the control at the wall is always reached close to the leading edge. Moreover, when the control E_w is increased the main minimum moves downstream. From the results shown, it seems that if the initial energy is sufficiently low in such a way that the response of the system is

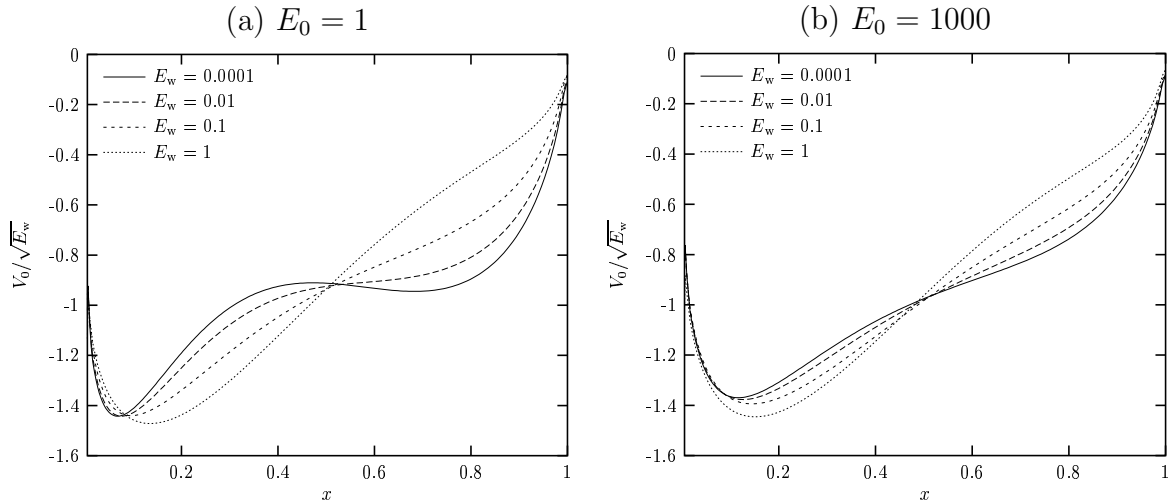


Figure 3.25: Comparisons at optimal wavenumber $\beta\delta$ for different values of the control energy E_w : optimal suction profile at the wall $V_0/\sqrt{E_w}$. (a) $E_0 = 1$; (b) $E_0 = 1000$

linear (figure (3.25)–a and figure (3.22)–a), the optimal suction profile can change a lot. On the other hand, if the initial energy is high, (figure (3.25)–b and figure (3.22)–b), all the suction profiles are less sensitive to the wavenumber or to the control energy E_w .

3.4.6 Controlling on a finite window

In the previous sections, the control has always been applied from the leading edge to the trailing edge. However, in practical applications to aircraft industry this solution could be not feasible, because of the installation of other systems at the leading or trailing edge. For this reason, it is worth to check what happens if the control is applied only on a certain window, in the range $x_1 < x < x_2$ where $x_1 \neq 0$ and $x_2 \neq 1$. Instead of producing a discontinuity in the wall velocity profile, here we use a weight function $k(x)$ in the form

$$k(x) = \begin{cases} 1 - \left[\sin \left(\pi \frac{x - x_1}{x_2 - x_1} - \frac{\pi}{2} \right) \right]^{20} & \text{for } x_1 < x < x_2 \\ 0 & \text{for } x < x_1 \text{ and } x > x_2 \end{cases}$$

In figure (3.26) results are shown at fixed control $E_w = 1$ for low and high initial energy, at the wavenumber which is the optimal one in the uncontrolled case ($\beta\delta = 0.548$ for $E_0 = 1$; $\beta\delta = 0.437$ for $E_0 = 1000$). Different configurations are compared: without control (solid line), controlling from $x = 0$ to $x = 1$ or controlling on one or two windows. The energy behavior normalized with respect to E_0 , figure (3.26), shows that if the control is applied from $x = 0$ to $x = 1$ the lowest integral of the energy over the whole domain is achieved. In the other two cases, for the same control energy $E_w = 1$, the control is less effective and in any case it seems that controlling over the complete domain gives the best results. The same conclusions can be drawn looking at the results for high initial energy $E_0 = 1000$, figure (3.26)–b, where no substantial difference from $E_0 = 1$ is

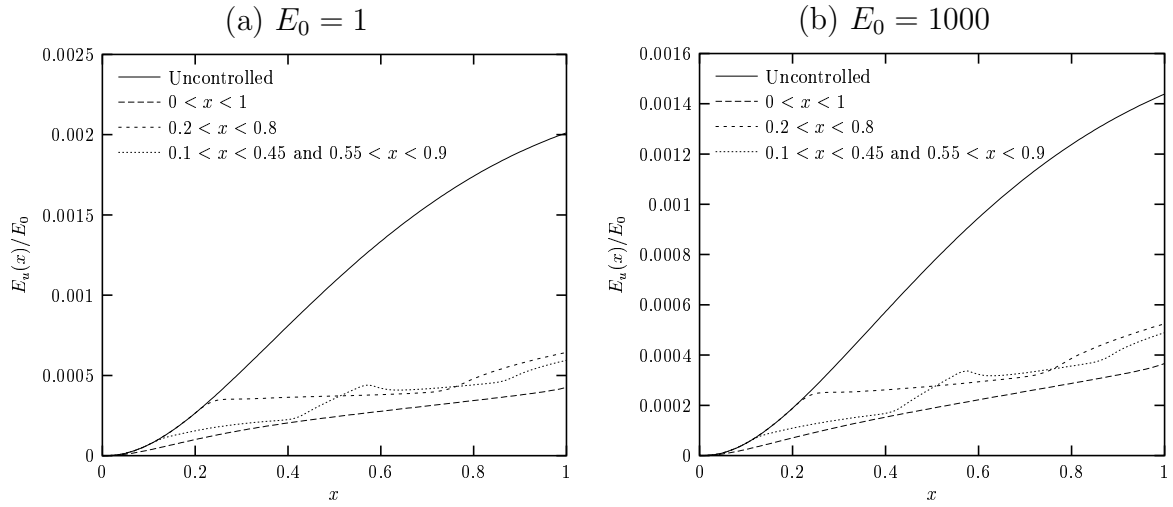


Figure 3.26: Comparisons for different suction windows at fixed control energy $E_w = 1$: streamwise perturbation energy $E_u(x)/E_0$. (a) $E_0 = 1$ and $\beta\delta = 0.548$; (b) $E_0 = 1000$ and $\beta\delta = 0.437$

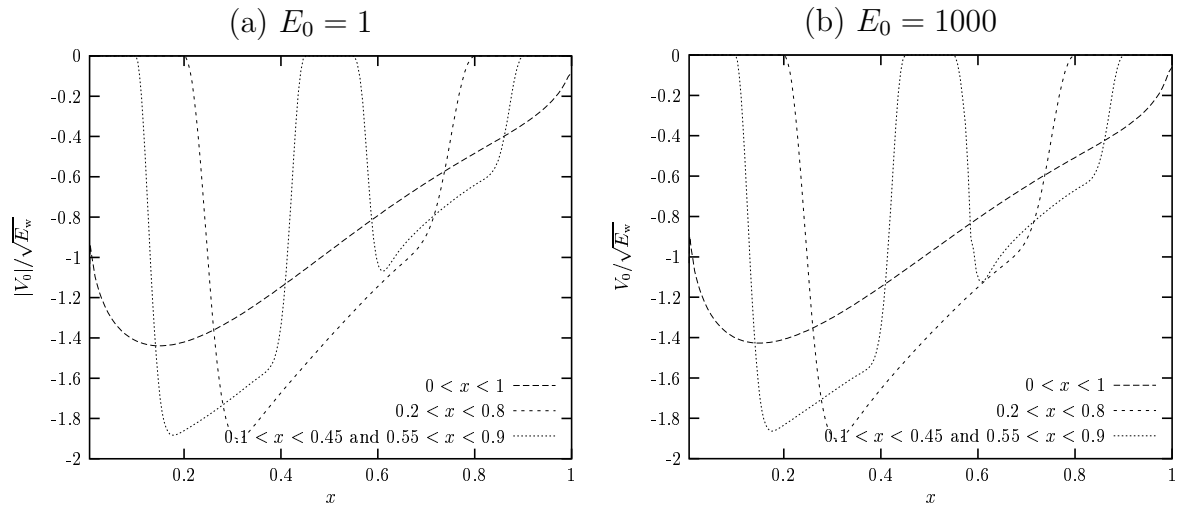


Figure 3.27: Comparisons for different suction windows at fixed control energy $E_w = 1$: optimal suction profile at the wall $V_0/\sqrt{E_w}$. (a) $E_0 = 1$ and $\beta\delta = 0.548$; (b) $E_0 = 1000$ and $\beta\delta = 0.437$

found. From the optimal suction profile at the wall, figure (3.27), it is evident that for the same $E_w = 1$ if the control window is shorter then the velocity values are higher (in absolute value), as obviously expected. What is interesting is that the strongest control is always applied close to the leading edge, as already observed in the previous cases. For high initial energy $E_0 = 1000$, almost the same curves are found also when two control windows are used. This is probably due to the fact that when the control energy is high enough, there is a weaker dependence on the initial energy E_0 .

3.5 Robust control: results

In the previous sections, two different problems have been analyzed. The first was to find the best sinusoidal initial condition for the nonlinear boundary layer equations in order to generate the maximum energy growth (optimal perturbation). Then, using that initial condition, we computed the best velocity distribution at the wall in order to control the algebraic growth due to sinusoidal optimal perturbations, with the aim of minimizing the integral of the perturbation energy over the whole domain. The latter is well-known as optimal control. However, the optimal perturbations were found with homogeneous boundary conditions at $y = 0$, whereas the optimal control obviously implies non homogeneous boundary conditions at the wall. This means that the optimal perturbations, when the control is on, are no longer the ones found when the control was off. A new question can therefore be asked: what is the initial condition to apply at $x = 0$ in order to generate the maximum energy growth when a suction velocity is applied at the wall, and what is the best control to apply at the wall in order to oppose that initial condition? This approach is called “robust control”: it allows us to find both the optimal perturbation and the optimal control at the same time and accounting for each other.

3.5.1 Comparisons for varying $\beta\delta$, E_0 and E_w

In figure (3.28) the gain $G_{\text{mean}} = E_{\text{mean}}/E_{\text{in}}$ as a function of the wavenumber $\beta\delta$ is reported. Two different initial energies E_0 are considered: $E_0 = 1$, in the linear regime,

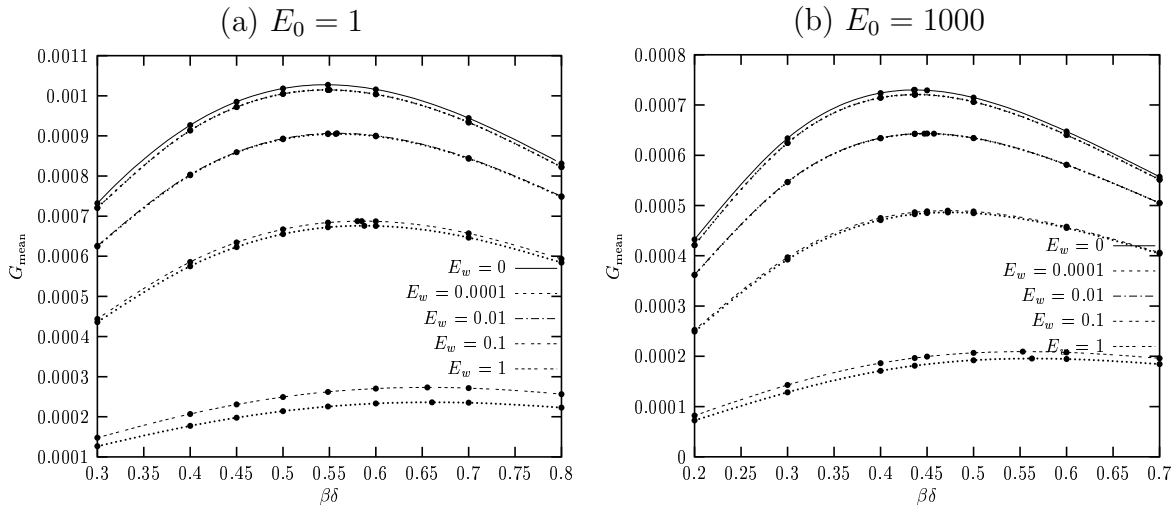


Figure 3.28: Comparisons between optimal control and robust control: gain $G_{\text{mean}} = E_{\text{mean}}/E_0$ as a function of the spanwise wavenumber $\beta\delta$ for different values of the control energy at the wall E_w . (a) initial energy $E_0 = 1$; (b) initial energy $E_0 = 1000$

figure (3.28)–a, and $E_0 = 1000$, figure (3.28)–b, for which nonlinear effects, as shown for the optimal perturbations, are well visible. Different control energies at the wall are applied, from $E_w = 0.0001$ to $E_w = 1$. The solid lines represent the optimal perturbation results, which means without any control, and the small dot curves are referred to the

optimal control results previously presented. The first remark is that, exactly as found in the case of optimal control, an increase in the control energy makes the maximum of the curves shift towards higher wavenumbers and this feature is even more evident if E_w is high. Results regarding the robust control are very close to the ones found in the case of optimal control. If the control energy is low, $E_w = 0.0001$, no difference can be graphically appreciated between the optimal control and robust control curves. This is true for both initial energies $E_0 = 1$ and $E_0 = 1000$ as one can easily see in figure (3.28)–a and figure (3.28)–b. For $E_w > 0.01$ the difference between optimal and robust control can be noticed for both initial energies $E_0 = 1$ and $E_0 = 1000$. What is clear is that the robust control curves always above the optimal control ones. This behavior was expected: the aim of robust control is to find the most dangerous initial condition when suction is applied at the wall, which means that the control, in the robust case, is less efficient than what it can be in the optimal control case.

In order to compare results, we follow the same structure used in the case of optimal perturbations and optimal control: first at constant wavenumber and increasing control energy (section 3.5.2), then at fixed control energy E_w and varying the wavenumber $\beta\delta$ (section 3.5.3), and finally at the optimal wavenumber (section 3.5.4).

3.5.2 Comparisons at fixed $\beta\delta$

As done for optimal control, comparisons at fixed $\beta\delta$ are performed at the wavenumber corresponding to the one for which the curve of the gain reaches its maximum in the uncontrolled case. The energy behavior at this wavenumber is reported in figure (3.29) for $E_0 = 1$ ($\beta\delta = 0.548$) and $E_0 = 1000$ ($\beta\delta = 0.437$). The energy is made dimensionless with respect to E_0 and the small dots represent the results for optimal control. The solid line is referred to the uncontrolled case. It is clear that the energy behavior is almost

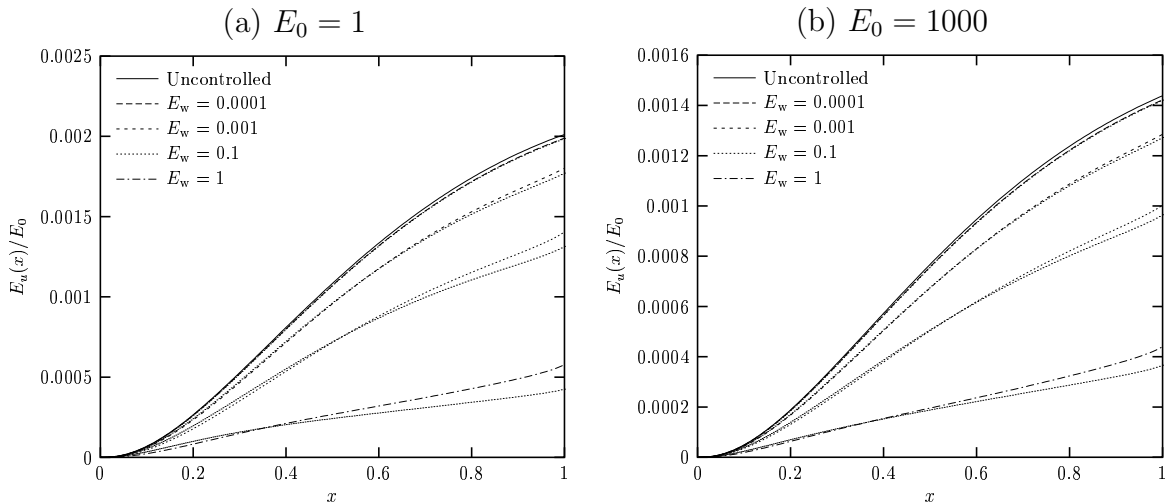


Figure 3.29: Comparisons at fixed wavenumber $\beta\delta$: streamwise perturbation energy $E_u(x)/E_0$ for increasing control energy E_w at the wall. (a) $E_0 = 1$ and $\beta\delta = 0.548$; (b) $E_0 = 1000$ and $\beta\delta = 0.437$

the same for both initial energies, as it was seen in the optimal control framework,

showing a very weak dependence on E_0 . For the largest part of the streamwise domain the curves of robust control are above the ones corresponding to optimal control: this let the mean gain $G_{\text{mean}} = E_{\text{mean}}/E_0$ for robust control become higher than the gain of optimal control (robust control is the worst possible case). In figure (3.30) the optimal perturbations for the same cases of figure (3.29) are reported. The solid line corresponds to the uncontrolled case. The optimal perturbation $|V_1|$ is normalized with respect to the square root of the initial energy E_0 . Looking at figure (3.30) it seems that the qualitative

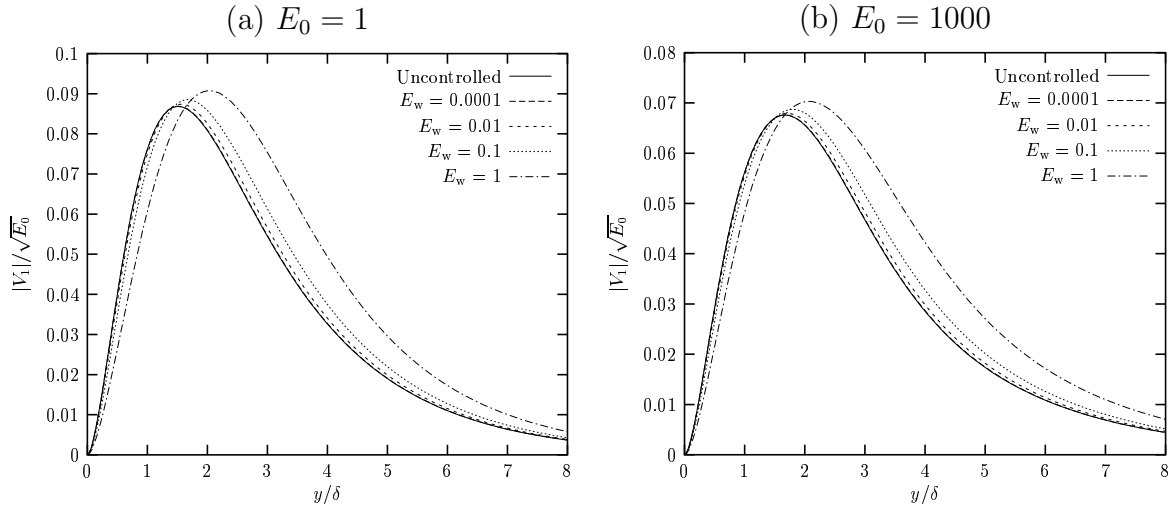


Figure 3.30: Comparisons at fixed wavenumber $\beta\delta$: optimal perturbation $|V_1|/\sqrt{E_0}$ at $x = 0$ for increasing control energy E_w . (a) $E_0 = 1$ and $\beta\delta = 0.548$; (b) $E_0 = 1000$ and $\beta\delta = 0.437$

behavior is the same at low and high initial energy. On the contrary, the initial optimal perturbation shows a dependence on the control energy E_w . For low E_w the initial profile is obviously the same, or at least very close to, the optimal one, without any control. For $E_w > 0.01$ the difference becomes more evident and the maximum of the profile moves towards higher distances from the wall. This characteristic is observed for low and high initial energy. In figure (3.31), the optimal suction profiles are reported. The small dots represent optimal control calculations. For very low control, $E_w = 0.0001$, the results coincide with the ones found in the optimal control framework. This was expected because low control implies low velocity at the wall, which slightly modifies the flow field and thus the optimal perturbation at $x = 0$ (as was observed for figure (3.30)). For low initial energy E_0 , the optimal suction profile shows a quite strong dependence on the control energy: if E_w is low two minima are observed, whereas for higher values of E_w the minimum reduces to only one. This characteristic was noticed also in the optimal control framework. If the control energy is increased to $E_w > 0.01$, then the difference between optimal control and robust control is greater. The main difference seems to be at low streamwise positions: at $x = 0$, for instance, in the robust control case the modulus of the control velocity is lower than in the optimal control case. Moreover, for $E_w = 1$ and $E_0 = 1$, the minimum of the optimal suction profile is reached at about $x = 0.15$ in the optimal control framework and at about $x = 0.25$ in the robust control one.

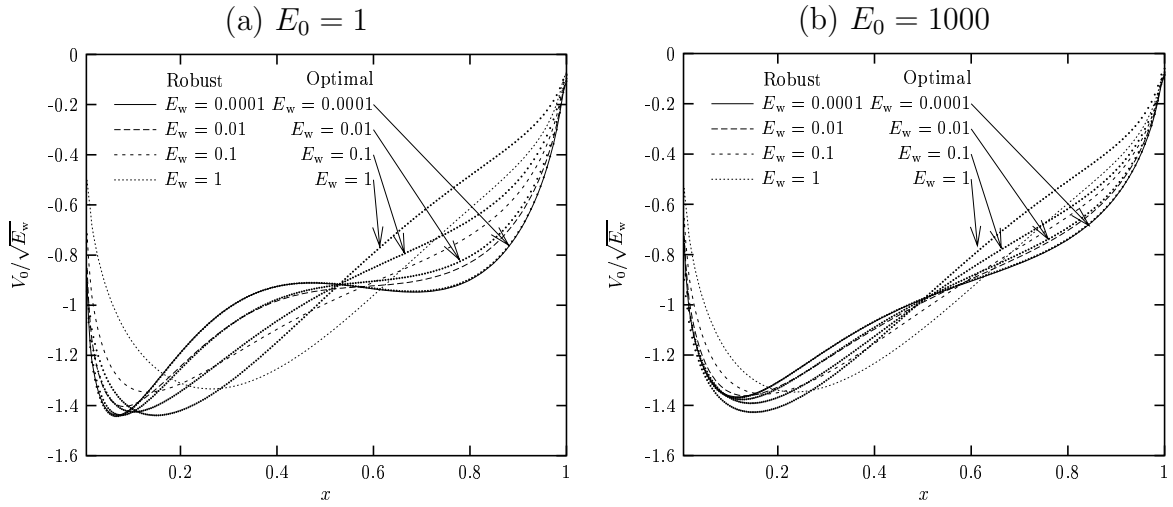


Figure 3.31: Comparisons at fixed wavenumber $\beta\delta$: optimal suction profile at the wall $V_0/\sqrt{E_w}$ for increasing control energy E_w . (a) $E_0 = 1$ and $\beta\delta = 0.548$; (b) $E_0 = 1000$ and $\beta\delta = 0.437$

Finally, for high initial energy $E_0 = 1000$, results from robust control calculations are closer to those from optimal control (figure (3.31)–b) and the dependence on the control energy E_w is much weaker.

3.5.3 Comparisons at fixed E_w

Another possibility is to consider a fixed control energy, for example $E_w = 1$, and to follow the dependence on the wavenumber $\beta\delta$ for two initial energies E_0 . In figure (3.32) the energy behavior normalized with respect to E_0 is reported for $E_0 = 1$ and $E_0 = 1000$. The solid line corresponds to the optimal wavenumber for that initial energy E_0 and

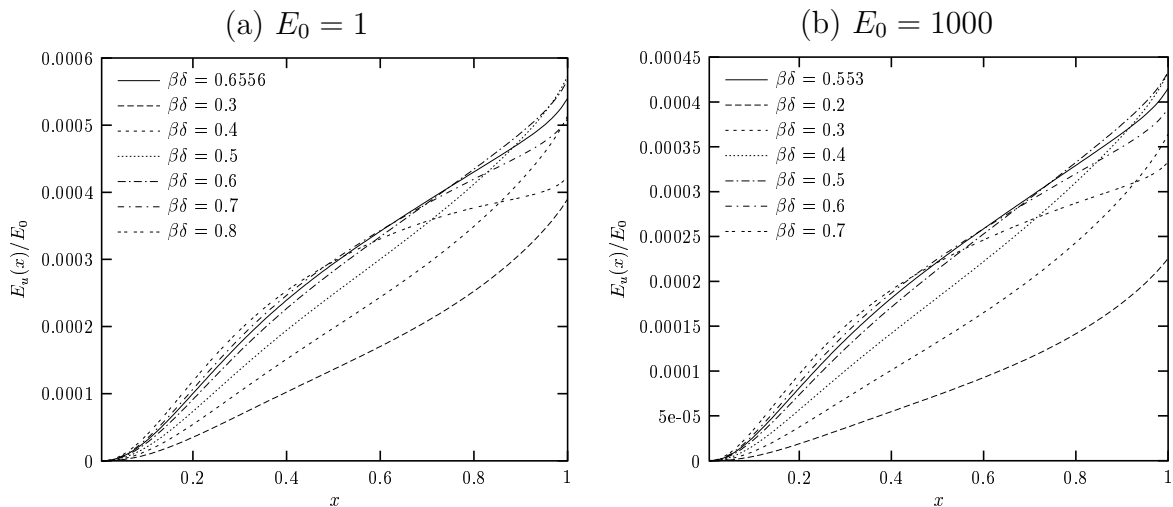


Figure 3.32: Comparisons at fixed control energy $E_w = 1$: streamwise perturbation energy $E_u(x)/E_0$ for increasing wavenumber $\beta\delta$. (a) $E_0 = 1$; (b) $E_0 = 1000$

control energy $E_w = 1$. It is clear that the qualitative behavior is the same for both E_0 . It is interesting to notice that the plateau observed in the optimal perturbation framework for high wavenumbers is no longer present. On the contrary, the energy profile is always monotonically growing.

Optimal perturbations are reported in figure (3.33). An interesting comparison is

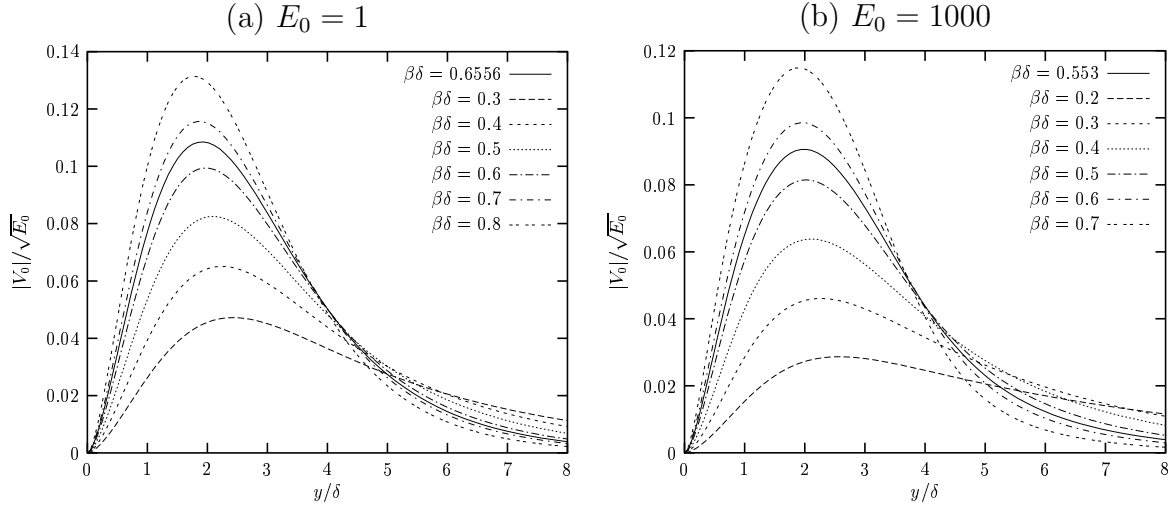


Figure 3.33: Comparisons at fixed control energy $E_w = 1$: optimal perturbation $|V_1|/\sqrt{E_0}$ at $x = 0$ for increasing wavenumber $\beta\delta$. (a) $E_0 = 1$; (b) $E_0 = 1000$

between robust control results, figure (3.33), and optimal perturbations obtained without control for the same initial energy (see figure (3.7)–b for $E_0 = 1$ and figure (3.8)–b for $E_0 = 1000$). The maximum of the wall-normal velocity profiles moves towards higher y/δ values when the wavenumber increases. As far as the shape of the profile is concerned, it changes quite a lot depending on $\beta\delta$. For low wavenumbers, V_1 goes to zero very slowly for $y \rightarrow \infty$ requiring long distances from the wall for V_1 to be negligible. On the other hand, for high wavenumbers, the optimal perturbation goes to zero very fast as $y \rightarrow \infty$. The same features were observed for sinusoidal optimal perturbations without control. The comparison between two different initial energies reveals that E_0 is not a crucial parameter since the curves in figure (3.33)–a and figure (3.33)–b show the same trend with the wavenumber $\beta\delta$.

In figure (3.34) optimal suction profiles at the wall are plotted for the robust control case and for two different initial energies. The maximum absolute value of the control velocity at the wall moves towards lower values of x as the wavenumber is increased. This trend was already observed for the optimal control case, figure (3.23), and it is confirmed also for high initial energy $E_0 = 1000$. We reported extensively the results for high control energy $E_w = 1$ because obviously for low E_w they are expected to be very close to the ones found for optimal control. This is confirmed by figure (3.35) where the optimal perturbation $|V_1|/\sqrt{E_0}$ and optimal suction $V_0/\sqrt{E_w}$ profiles are reported for $E_w = 0.01$ and $E_0 = 1$. For $|V_1|/\sqrt{E_0}$, figure (3.35)–a, the same remarks done for figure (3.33)–a are valid: the profile goes to zero very slowly as $y \rightarrow \infty$ for low wavenumbers, whereas for high wavenumbers it goes to zero very fast with the distance from the wall. The optimal suction profiles reported in figure (3.35)–b confirm what was

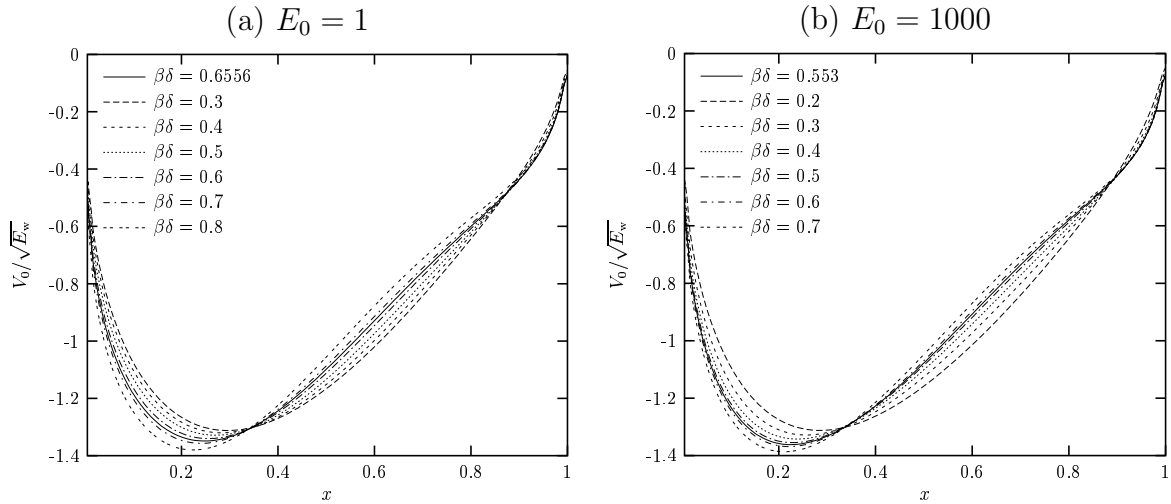


Figure 3.34: Comparisons at fixed control energy $E_w = 1$: optimal suction profile at the wall $V_0/\sqrt{E_w}$ for increasing wavenumber $\beta\delta$. (a) $E_0 = 1$; (b) $E_0 = 1000$

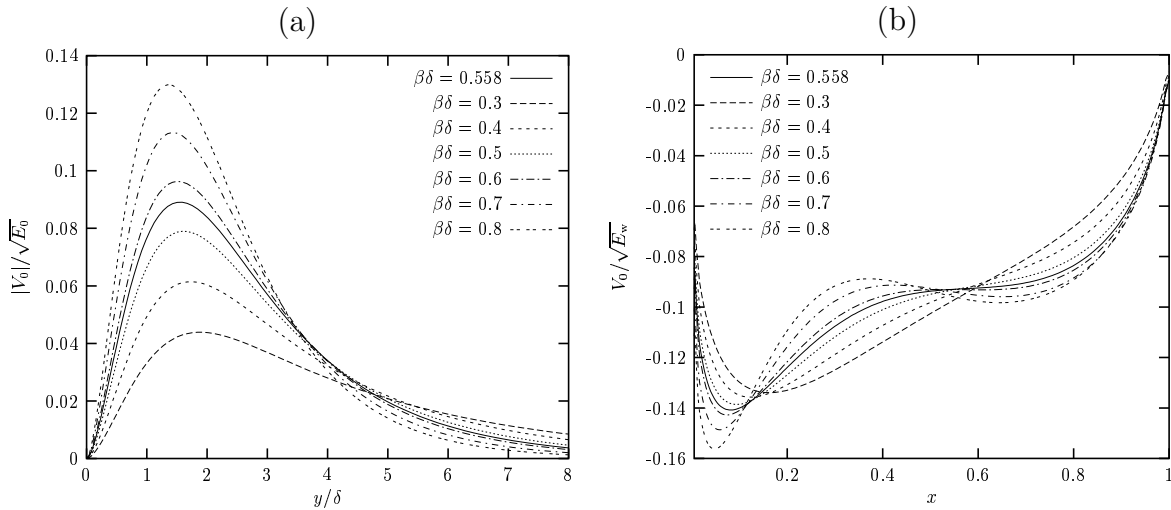


Figure 3.35: Comparisons at fixed control energy $E_w = 0.01$ and initial energy $E_0 = 1$ for increasing wavenumber $\beta\delta$. (a) optimal perturbation $|V_1|/\sqrt{E_0}$ at $x = 0$; (b) optimal suction profile at the wall $V_0/\sqrt{E_w}$

found in the optimal control framework, for low initial energy and low control. Only one minimum can be observed if the wavenumber is low, whereas the profile at the wall becomes more oscillating with two minima at high wavenumbers. The main one moves towards upstream locations with growing $\beta\delta$. Basically, figure (3.35) shows that, for low control energy, results are very close to the ones already found for optimal control.

3.5.4 Comparisons at optimal $\beta\delta$

The last comparison is done at the wavenumber for which the gain as a function of $\beta\delta$ reaches its maximum, for a fixed control energy at the wall E_w . The evolution of $E_u(x)/E_0$ for $E_0 = 1$ and $E_0 = 1000$ is shown in figure (3.36). The behavior is the

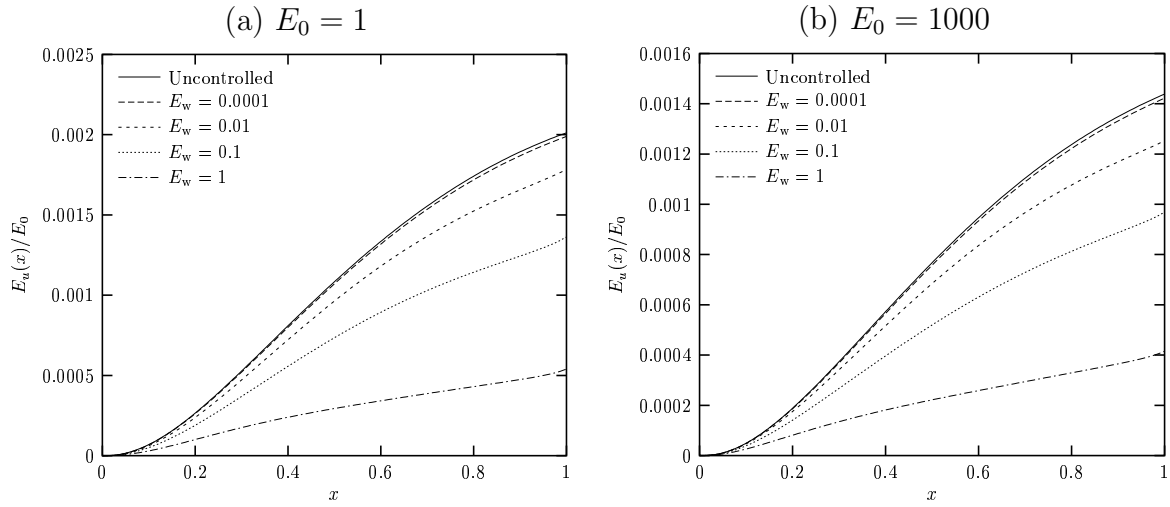


Figure 3.36: Comparisons at optimal wavenumber $\beta\delta$ for different values of the control energy E_w : streamwise perturbation energy $E_u(x)/E_0$. (a) $E_0 = 1$; (b) $E_0 = 1000$

one already seen for the optimal control. What seems to be more interesting is the sinusoidal optimal perturbation reported in figure (3.37). It is referred to the robust control framework, for different values of the control energy E_w . Results at very low E_w

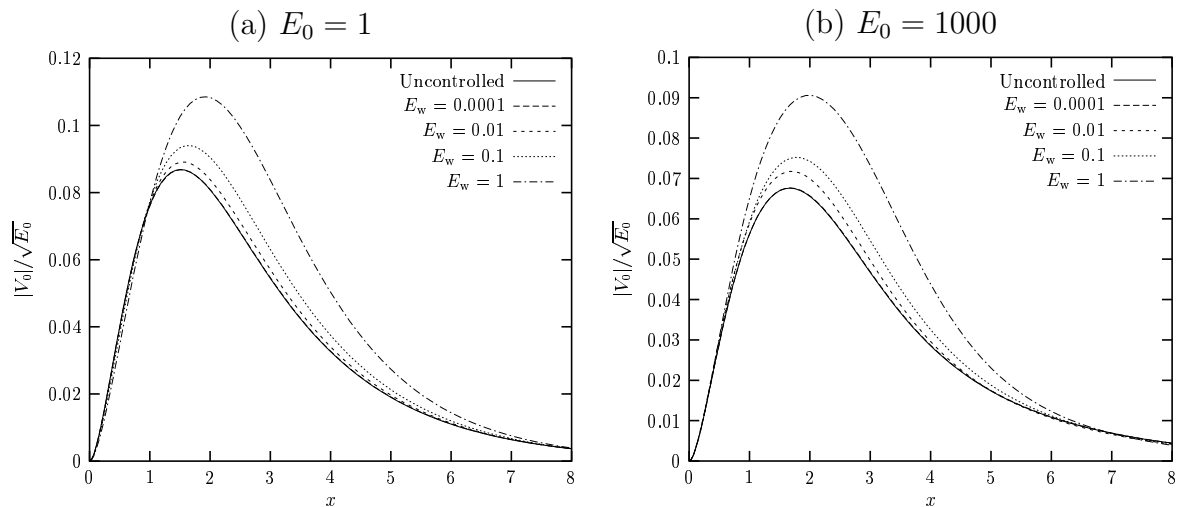


Figure 3.37: Comparisons at optimal wavenumber $\beta\delta$ for different values of the control energy E_w : optimal perturbation $|V_1|/\sqrt{E_0}$ at $x = 0$ (a) $E_0 = 1$; (b) $E_0 = 1000$

are not distinguishable from the uncontrolled ones, for both initial energies $E_0 = 1$ and $E_0 = 1000$. For $E_w > 0.0001$, however, the maximum moves further from the wall for increasing control energy E_w . Moreover, the value of the maximum increases with E_w and all the profiles go to zero in the same way as $y/\delta \rightarrow \infty$. The latter behavior reveals a new feature in the profile of V_1 . In figure (3.38) the optimal suction profile $V_0/\sqrt{E_w}$ is reported for different values of the control energy, at the optimal wavenumber. The first difference between low and high initial energy, $E_0 = 1$ and $E_0 = 1000$, is that in the first case, figure (3.38)–a, the dependence on the control energy is much more evident than in

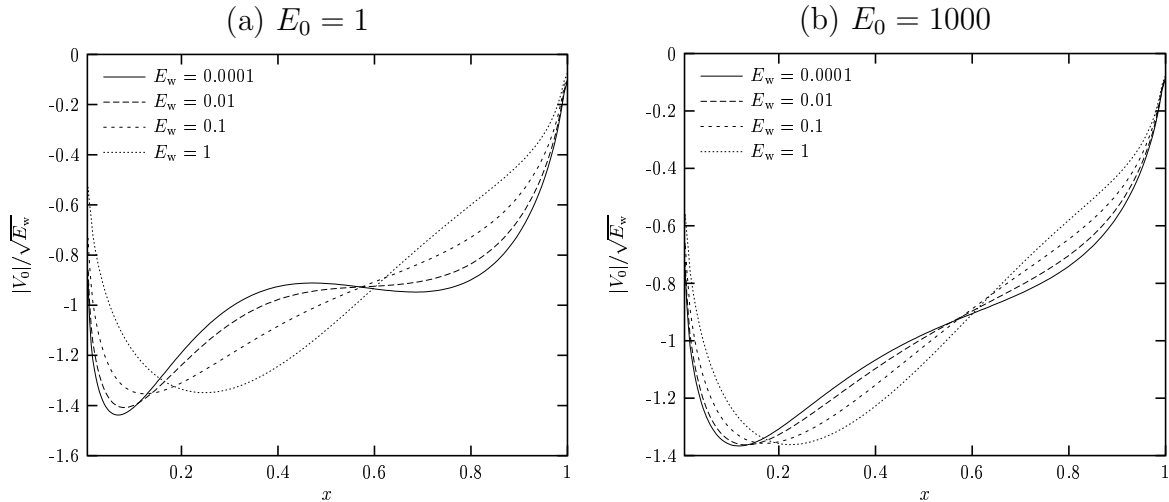


Figure 3.38: Comparisons at optimal wavenumber $\beta\delta$ for different values of the control energy E_w : optimal suction profile at the wall $V_0/\sqrt{E_w}$. (a) $E_0 = 1$; (b) $E_0 = 1000$

the second one. If E_w is very low, the optimal suction at the wall presents two minima, whereas if E_w increases the main maximum moves downstream and the profile becomes less oscillating with only one minimum. The same behavior is valid also for $E_0 = 1000$, even if in this case the profiles are much more regular than those for $E_0 = 1$.

3.6 Concluding summary

This work is devoted to the study of steady three-dimensional, algebraically growing instability of an incompressible boundary layer past a flat plate in the completely nonlinear regime.

An adjoint-based optimization technique is used in order to determine first sinusoidal optimal perturbations at the leading edge which provide the maximum energy growth for a given initial energy, and then the steady spanwise-uniform optimal suction to be applied at the wall in order to reduce the energy growth to a minimum for that initial perturbation.

The solution is decomposed in a finite number of Fourier modes along the spanwise direction z and discretized using finite differences in x and y . The velocity field can be viewed as the sum of a spanwise-uniform contribution due to mode zero, which represents the unperturbed base flow plus mean flow correction, and a spanwise-varying contribution due to all the other modes. The energy of the streamwise velocity component of the latter contribution is taken as a measure of the growth of algebraic instability.

Results are compared at constant wavenumber, at constant initial or control energy and at optimal wavenumber, defined as $\beta\delta$ for which the gain is maximum.

In the optimal perturbation framework, the already published results by Luchini [79] and Andersson *et al.* [4] are reproduced using a very low value of the initial energy (so that the mutual interactions between different modes do not produce nonlinear effects) and maximizing the energy at the final station. An extended study for a large range of

wavenumbers and initial energies is then performed with the aim of maximizing the integral of the energy over the whole domain. Curves of the mean gain $G_{\text{mean}} = E_{\text{mean}}/E_0$ as a function of the wavenumber at constant E_0 present a maximum at a certain wavenumber $\beta\delta$, identified as the optimal wavenumber for that initial energy E_0 . If E_0 increases, the curve representing $G_{\text{mean}} = E_{\text{mean}}/E_0$ becomes lower and the optimal wavenumber moves toward smaller values. A threshold is found such that if the initial energy is below it, nonlinear effects are negligible and the spanwise–uniform velocity profile at the final station is not distinguishable from Blasius’, whereas for an initial energy larger than the threshold, nonlinear effects are clearly seen, especially from the normalized energy curve which is lower and flatter, showing a characteristic plateau. The presence of the same plateau for very low E_0 and high wavenumber, however, seems to indicate a greater dependence on wavenumber than on initial energy. Low values of $\beta\delta$ produce a mode–one wall–normal velocity profile that goes to zero very slowly with the distance from the wall whereas increasing wavenumber changes its shape and makes it go to zero very fast with y/δ .

Once the initial perturbations have been found, the steady spanwise–uniform wall–suction profile that optimally opposes them is computed, for the corresponding wavenumber and initial energy values. The curves of mean gain $G_{\text{mean}} = E_{\text{mean}}/E_0$ as a function of the wavenumber are calculated for different control energies at the wall E_w and two initial energies, $E_0 = 1$ in the linear regime, and $E_0 = 1000$ in the nonlinear one. Low control energy implies no big difference with the uncontrolled case, whereas high E_w makes the gain curve lower and flatter than in the uncontrolled one. This trend is independent of the initial energy. Increasing the control energy produces a reduction in the curve of energy as a function of x , as expected. If the control is very strong the energy can reach a maximum for $x < 1$ and not far from the leading edge, whereas for low control energy the maximum is monotonically reached at the final station. The corresponding suction velocity at the wall presents more than one maximum (in the absolute value) for low control energies and for high wavenumbers only at low initial energy, whereas high E_0 produces more regular results with only one maximum. The effect of the control on the flow field is basically to make the mode–zero velocity profile similar to an accelerating Falkner–Skan one and to suck away the boundary layer, confining it closer to the wall. The control on a shorter window or on more than a single window is always less efficient than controlling from the leading to the trailing edge because both the gain and the maximum of the absolute value of the suction velocity are higher. The main common feature found in all the tests performed is that the control velocity is always negative (suction without blowing) and the strongest control is always applied close to the leading edge.

Robust control is finally considered because when the optimal control is computed, the boundary condition for V_0 at the wall is no more homogeneous, and the flow field is different from the one without control. This makes the optimal perturbations found in the optimal perturbation framework different from the correct ones. Robust control overcomes this problem by calculating simultaneously the initial optimal perturbations and the corresponding optimal wall suction distribution. Robust–control results show that the gain is always higher than the corresponding case for the optimal control. This was expected, since the perturbation applied in robust control is by definition the worst

possible one. Comparing the gain as a function of the wavenumber for optimal and robust control, almost no difference can be appreciated if E_w is very low, as expected, because the flow field is not very much modified. On the other hand, for increasing control velocity, the gain in the robust control case becomes higher than in optimal control. This feature is found for low and high initial energy. Comparisons at a fixed wavenumber, equal to the optimal $\beta\delta$ without any control, and at a fixed initial energy, reveal a slight difference in the optimal perturbation profile with a shift of the maximum further from the wall for increasing E_w . For low initial energy $E_0 = 1$ and low control, the optimal control profile shows a weak oscillation along x (more than one maximum) which disappears when the control energy E_w is increased. For high initial energy, much smaller differences in the shape of the optimal control profiles are found. From the comparisons at the optimal wavenumber it can be noticed that quite the same behavior regarding dimensionless energy curves and initial optimal perturbations characterizes both low and high initial energies case, whereas the optimal control profile reveals a strong dependence on E_w only if the initial energy is low.

Chapter 4

Conclusions

In this thesis, the problem of transition from laminar to turbulent flow in an incompressible boundary layer has been considered. Tollmien–Schlichting instabilities and algebraically growing instabilities have been analyzed. In the former case attention has been paid to the receptivity process of free–stream and wall disturbances, whereas in the latter optimization of exciting disturbances at the leading edge and their optimal and robust control via suction/blowing at the wall has been investigated.

As far as the boundary layer receptivity to the quadratic mixing of different disturbances is concerned, the resonant singular problem is solved introducing a multiple–scale expansion of the solution. A receptivity function is obtained: it relates the amplitude of the unstable wave, generated inside the boundary layer, to the physical amplitude of the disturbances which produced it.

The possible interacting perturbations are those due to an acoustic wave or vorticity wave, present in the free–stream, or due to wall vibration and wall roughness. Each of these disturbances, however, cannot create by itself any resonance with the Tollmien–Schlichting waves, because the typical time frequency and spatial wavenumber are different from those which satisfy the Tollmien–Schlichting dispersion relation.

The right values in order to originate resonance can be obtained from the nonlinear mixing of at least two interacting disturbances. In this case, the time frequency and spatial wavenumber of the resonant wave are given by the sum or difference of the corresponding frequency and wavenumber of the interacting disturbances.

Results show that the acoustic wave and wall roughness perturbations can enter in the boundary layer, creating a forcing term that is mainly concentrated close to the wall. Moreover, the weight function by which the forcing term is multiplied, that is represented by the left eigensolution, reaches its maximum inside the boundary layer, in the neighborhood of the maximum of the forcing source. This feature leads to a receptivity coefficient and receptivity function which are quite strong for the acoustic wave – wall roughness mixing. On the contrary, the vorticity wave interacting with wall roughness produces a coupling which is located outside the boundary layer. The main reason is that the asymptotic behavior of the streamwise and wall–normal velocity perturbations, induced by the free–stream vorticity, is respectively like a constant and a linear function. The forcing term produced by this interaction is therefore shifted far from the wall and the dot product with the left eigenfunction, which reaches its

maximum in the middle of the boundary layer, makes the receptivity coefficient and the receptivity function smaller than in the previous case. Moreover, the forcing term is one order of magnitude smaller than the one for the acoustic wave – wall roughness interaction, explaining the reason why, in this case, the receptivity function is smaller. The interaction between the acoustic wave and vorticity wave show a forcing term which does not vanish at infinity because the interacting disturbances behave like a constant or a linear function of the wall–normal coordinate. On the contrary, the left eigenfunction exponentially decreases with the distance from the wall. Finally, it has been proved that the interaction between the wall–normal vibration and wall roughness is unable to create resonant conditions with the TS waves.

The amplitude of the resonant wave is obtained as a function of the wall shape and the physical amplitude of the external disturbances, for different interacting excitation sources.

Non–parallel effects are taken into account thanks to the multiple–scale approach, which is here introduced in the non–homogeneous form. From the numerical point of view, the multiple–scale method is not computationally expensive and does not have numerical stability problems, it allows a general formulation and can be applied to any base flow, obtained from computations or experimental data. For all these reasons, the receptivity analysis using multiple scales can be efficiently included in industrial codes for transition prediction.

The second part of the thesis is devoted to the study of steady three–dimensional, algebraically growing instability of an incompressible boundary layer past a flat plate in the completely nonlinear regime. An adjoint–based optimization technique is used in order to determine first sinusoidal optimal perturbations at the leading edge which provide the maximum energy growth for a given initial energy, and then the steady spanwise–uniform optimal suction to be applied at the wall in order to reduce the energy growth to a minimum for that initial perturbation. The solution is decomposed in a finite number of Fourier modes along the spanwise direction and discretized by finite differences in x and y . Results are compared at constant wavenumber, at constant initial or control energy and at optimal wavenumber, defined as $\beta\delta$ for which the gain is maximum.

An extended study for a large range of wavenumbers and initial energies is performed with the aim of maximizing the integral of the energy over the whole domain. Curves of the mean gain as a function of the wavenumber at constant initial energy E_0 present a maximum at a certain wavenumber, identified as the optimal wavenumber for that initial energy. If E_0 increases, the curve representing the gain becomes lower and the optimal wavenumber moves towards smaller values. A threshold is found such that if the initial energy is below it, nonlinear effects are negligible and the spanwise–uniform velocity profile at the final station is not distinguishable from Blasius', whereas for an initial energy larger than the threshold, nonlinear effects are clearly seen.

The optimal control problem is then considered. The aim is to find the steady spanwise–uniform wall–suction profile that optimally opposes the initial perturbations previously computed, for the same values of the wavenumber and initial energy. The curves of mean gain, as a function of the wavenumber, are calculated for different control energies and two initial energies, in the linear and nonlinear regime. Low control energy implies no big difference with the uncontrolled case, whereas high control makes the gain

curve lower and flatter than the uncontrolled one, independently of the initial energy. If the control energy is increased, a more remarkable reduction of energy as a function of x is observed, as expected. If the control is very strong the energy can reach a maximum before the end of the plate, whereas for low E_w the maximum is reached at the final location. The optimal suction velocity at the wall presents a dependence on the control energy or on the wavenumber only for low initial energies, whereas more regular profiles (with only one minimum) are found at high E_0 . The effect of the control on the flow field is basically to make the mode-zero velocity profile similar to an accelerating Falkner–Skan one and to suck away the boundary layer, confining it closer to the wall. The control on a shorter window or on more than a single window is always less efficient than controlling from $x = 0$ to $x = 1$ (the gain and the maximum of the absolute value of the control velocity are higher). The control velocity is always negative (suction without blowing) and the strongest control is always applied close to the leading edge.

When a suction velocity is applied at the wall in order to control optimal perturbations, attention should be paid to the fact that the latter are different from those computed without control. The boundary condition for V_0 at the wall, in fact, is homogeneous when $E_w = 0$, whereas it is non-homogeneous when $E_w > 0$. Robust control is therefore needed. It allows to compute simultaneously the initial optimal perturbations and their optimal control. Robust-control results show that the gain is always higher than the corresponding one for optimal control. This was expected, since the aim of robust control is to find the worst possible case. Comparing the gain as a function of the wavenumber for optimal and robust control, almost no difference can be appreciated if E_w is very low. On the other hand, for increasing control energy, the gain in the robust control case becomes higher than in optimal control, for low and high initial energy. Comparisons at a fixed wavenumber, equal to the optimal $\beta\delta$ without control, and at a fixed initial energy, reveal a slight difference in the optimal perturbation profile for increasing E_w , with a shift of the maximum further from the wall. The optimal suction velocity at the wall is very similar to the one computed using optimal control. If the initial energy is low, the profile shows a dependence on the control energy and wavenumber, whereas more regular profiles are obtained at high initial energy.

Appendix A

Basic matrix properties

Here we briefly recall some basic properties of matrix algebra useful in order to understand the behavior of a resonant system. More detailed informations can be found in dedicated books (Wilkinson [110]).

Let us consider a complex square matrix \mathbf{A} . The eigenvalue problem

$$\mathbf{A}\mathbf{u} = \lambda\mathbf{u}$$

furnishes n generally complex values λ_i (the eigenvalues) and, if all the eigenvalues are distinct, the eigenvector \mathbf{u}_i which are defined up to a constant and can be arbitrarily normalized. Under these hypotheses, the eigenvectors \mathbf{u}_i are linearly independent so that the matrix

$$\mathbf{U} = (\mathbf{u}_1 \ \cdots \ \mathbf{u}_n)$$

is invertible. The problem

$$\mathbf{v}^T \mathbf{A} = \lambda \mathbf{v}^T$$

gives the eigenvalues λ_i and the left eigenvector \mathbf{v}_i , defined up to a constant too. One possibility is to normalize \mathbf{v}_i in such a way that

$$\mathbf{v}_i^T \mathbf{u}_i = 1$$

If all the eigenvalues λ_i are distinct the left eigenvectors \mathbf{v}_i^T are linearly independent and the matrix

$$\mathbf{V} = \begin{pmatrix} \mathbf{v}_1^T \\ \vdots \\ \mathbf{v}_n^T \end{pmatrix}$$

is non singular and therefore invertible.

It can be proved that, if $\mathbf{v}_i^T \mathbf{u}_i = 1$, then $\mathbf{V}\mathbf{U} = \mathbf{I}$. From the right- and left-eigenvalue problems

$$\begin{aligned} \mathbf{A}\mathbf{u}_i &= \lambda_i \mathbf{u}_i \\ \mathbf{v}_j^T \mathbf{A} &= \lambda_j \mathbf{v}_j^T \end{aligned} \tag{A.1}$$

left multiplying the first expression by \mathbf{v}_j^T one gets

$$\mathbf{v}_j^T \mathbf{A}\mathbf{u}_i = \lambda_i \mathbf{v}_j^T \mathbf{u}_i$$

but since $\mathbf{v}_j^T \mathbf{A} = \lambda_j \mathbf{v}_j^T$:

$$\begin{aligned}\lambda_j \mathbf{v}_j^T \mathbf{u}_i &= \lambda_i \mathbf{v}_j^T \mathbf{u}_i \\ (\lambda_j - \lambda_i) \mathbf{v}_j^T \mathbf{u}_i &= 0\end{aligned}$$

$\lambda_j \neq \lambda_i$ implies

$$\mathbf{v}_j^T \mathbf{u}_i = 0$$

This result, together with the normalization $\mathbf{v}_i^T \mathbf{u}_i = 1$ leads to

$$\mathbf{V}\mathbf{U} = \mathbf{I}$$

which is what we wanted to prove and furnishes $\mathbf{U} = \mathbf{V}^{-1}$ so that $\mathbf{U}\mathbf{V} = \mathbf{V}^{-1}\mathbf{V} = \mathbf{I}$ and therefore

$$\mathbf{V}\mathbf{U} = \mathbf{U}\mathbf{V} = \mathbf{I}$$

We now prove a more useful property which allows the decomposition of a matrix in the form:

$$\mathbf{A} = \sum_{k=1}^n \lambda_k \mathbf{u}_k \mathbf{v}_k^T$$

The equations (A.1) can be written in a matrix form as

$$\begin{aligned}\mathbf{A}\mathbf{U} &= \mathbf{\Lambda}\mathbf{U} \\ \mathbf{V}\mathbf{A} &= \mathbf{\Lambda}\mathbf{V}\end{aligned}\tag{A.2}$$

where $\mathbf{\Lambda} = \text{diag}(\lambda_1, \dots, \lambda_n)$ while \mathbf{U} and \mathbf{V} are the ones previously defined. Left multiplying the second equation by \mathbf{U} and remembering that $\mathbf{U}\mathbf{V} = \mathbf{I}$:

$$\begin{aligned}\mathbf{U}\mathbf{V}\mathbf{A} &= \mathbf{U}\mathbf{\Lambda}\mathbf{V} \\ \mathbf{I}\mathbf{A} &= \mathbf{U}\mathbf{\Lambda}\mathbf{V} \\ \mathbf{A} &= \mathbf{U}\mathbf{\Lambda}\mathbf{V}\end{aligned}\tag{A.3}$$

The matrix $\mathbf{U}\mathbf{\Lambda}\mathbf{V}$ is obviously

$$\begin{aligned}\mathbf{U}\mathbf{\Lambda}\mathbf{V} &= \begin{pmatrix} \mathbf{u}_1 & \cdots & \mathbf{u}_n \end{pmatrix} \begin{pmatrix} \lambda_1 & 0 & 0 \\ 0 & \ddots & 0 \\ 0 & 0 & \lambda_n \end{pmatrix} \begin{pmatrix} \mathbf{v}_1^T \\ \vdots \\ \mathbf{v}_n^T \end{pmatrix} \\ &= \begin{pmatrix} \mathbf{u}_1 & \cdots & \mathbf{u}_n \end{pmatrix} \begin{pmatrix} \lambda_1 \mathbf{v}_1^T \\ \vdots \\ \lambda_n \mathbf{v}_n^T \end{pmatrix}\end{aligned}$$

Indicating with

$$\begin{aligned}\mathbf{u}_1 &= \begin{pmatrix} u_1^1 & u_2^1 & \cdots & u_{n-1}^1 & u_n^1 \end{pmatrix} \\ \mathbf{u}_2 &= \begin{pmatrix} u_1^2 & u_2^2 & \cdots & u_{n-1}^2 & u_n^2 \end{pmatrix} \\ \vdots &= \vdots \\ \mathbf{v}_1^T &= \begin{pmatrix} v_1^1 & v_2^1 & \cdots & v_{n-1}^1 & v_n^1 \end{pmatrix} \\ \mathbf{v}_2^T &= \begin{pmatrix} v_1^2 & v_2^2 & \cdots & v_{n-1}^2 & v_n^2 \end{pmatrix} \\ \vdots &= \vdots\end{aligned}$$

the general ij -th term of the matrix $\mathbf{U}\mathbf{\Lambda}\mathbf{V}$ is:

$$(\mathbf{U}\mathbf{\Lambda}\mathbf{V})_{ij} = \sum_{k=1}^n u_i^k \lambda_k v_j^k = \sum_{k=1}^n \lambda_k \bar{a}_{ij}^k$$

Basically, the matrix $\mathbf{U}\mathbf{\Lambda}\mathbf{V}$ has been decomposed in the sum of n matrices $\lambda_k \bar{a}_{ij}^k$ where $\bar{a}_{ij}^k = u_i^k v_j^k$ so that

$$[\bar{a}_{ij}^k] = [u_i^k v_j^k] = \mathbf{u}_k \mathbf{v}_k^T$$

Finally, $\mathbf{A} = \mathbf{U}\mathbf{\Lambda}\mathbf{V}$ implies

$$\mathbf{A} = \sum_{k=1}^n \lambda_k \mathbf{u}_k \mathbf{v}_k^T$$

which is what we wanted to prove.

A couple of other interesting properties can be derived for singular matrices or for matrices with an eigenvalue that goes to zero as a function of a parameter. Referring to the general linear system

$$\mathbf{A}\mathbf{x} = \mathbf{b}$$

if all the eigenvalues λ_i are distinct, the right eigenvalues form a basis so that the solution can be expressed as

$$\mathbf{x} = \mathbf{U}\mathbf{h}$$

and

$$\mathbf{A}\mathbf{U}\mathbf{h} = \mathbf{b}$$

left multiplying by \mathbf{V}

$$\mathbf{V}\mathbf{A}\mathbf{U}\mathbf{h} = \mathbf{V}\mathbf{b}$$

and noticing that from the left-eigenvalue problem $\mathbf{V}\mathbf{A} = \mathbf{\Lambda}\mathbf{V}$

$$\mathbf{V}\mathbf{A}\mathbf{U} = \mathbf{\Lambda}\mathbf{V}\mathbf{U} = \mathbf{\Lambda}\mathbf{I} = \mathbf{\Lambda}$$

the original linear system reduces to

$$\mathbf{\Lambda}\mathbf{h} = \mathbf{V}\mathbf{b}$$

or

$$\lambda_i \mathbf{h} = \mathbf{v}_i^T \mathbf{b}$$

If the initial matrix \mathbf{A} is singular, all the eigenvalues are distinct and $\lambda_i = 0$, the only possibility for the solution \mathbf{h} , and therefore \mathbf{x} , to exist is

$$\mathbf{v}_i^T \mathbf{b} = 0 \tag{A.4}$$

Expression (A.4) is usually called “compatibility condition” for linear systems with a singular matrix and is another way to express the Rouché–Capelli theorem.

Finally, the last interesting feature regards system with an eigenvalue going to zero as a function of a parameter. In this case, from the previous developments, the linear system $\mathbf{A}\mathbf{x} = \mathbf{b}$ can be reduced to $\mathbf{\Lambda}\mathbf{h} = \mathbf{V}\mathbf{b}$ with $\mathbf{x} = \mathbf{U}\mathbf{h}$. The solution is therefore

$$\mathbf{x} = \mathbf{U}\mathbf{\Lambda}^{-1}\mathbf{V}\mathbf{b}$$

Since

$$\mathbf{\Lambda}^{-1} = \text{diag}(\lambda_1^{-1}, \dots, \lambda_n^{-1})$$

when $\lambda_i \rightarrow 0$ the greatest contribution in $\mathbf{\Lambda}^{-1}$ is simply the term λ_i^{-1} so that

$$\mathbf{x} \rightarrow \frac{1}{\lambda_i} \mathbf{u}_i (\mathbf{v}_i^T \mathbf{b}) \quad \text{for } \lambda_i \rightarrow 0 \quad (\text{A.5})$$

This expression leads to the conclusion that the RHS of a linear system with an eigenvalue going to zero as a function of a parameter produces a contribution of order λ_i^{-1} and, moreover, the solution \mathbf{x} behaves like the corresponding right eigenvector \mathbf{u}_i .

Appendix B

Homogeneous multiple scales example

Let

$$\mathbf{B}(t) \frac{d\mathbf{x}(t)}{dt} + \mathbf{C}(t) \mathbf{x}(t) = 0$$

be the evolution equation of a generic time-dependent linear system. If \mathbf{B} is non singular, the previous expression can be written in a more simple form as

$$\frac{d\mathbf{x}(t)}{dt} = \mathbf{A}(t) \mathbf{x}(t) \tag{B.1}$$

where $\mathbf{A} = -\mathbf{B}^{-1}\mathbf{C}$. If the coefficient matrix $\mathbf{A}(t)$ is considered fixed at a certain time $t = t_0$, so that $\mathbf{A}(t) = \mathbf{A}(t_0)$, the solution $\mathbf{x}(t)$ can be expressed as a function of the eigenvalues $\lambda_k(t_0)$ and right eigenvectors $\mathbf{u}_k(t_0)$:

$$\mathbf{x}(t) = \sum_{k=1}^N c_k \mathbf{u}_k(t_0) e^{\lambda_k(t_0)t} \tag{B.2}$$

with N arbitrary coefficients c_k to be determined using the initial conditions. If the matrix \mathbf{A} is not fixed at a certain time t_0 but varies in such a way that a long time (with respect to the typical characteristic time) is required in order to appreciate a variation of the eigenvalues λ_k and eigenvectors \mathbf{u}_k , then \mathbf{A} is said to be slowly varying with t . In this case, a new time scale $T = \tilde{\epsilon}t$ can be introduced so that an order-one variation of T occurs for a long variation of t if $\tilde{\epsilon}$ is a small parameter accounting for the slow dependence of \mathbf{A} on t . With this substitution, equation (B.1) reads

$$\tilde{\epsilon} \frac{d\mathbf{x}(T)}{dT} = \mathbf{A}(T) \mathbf{x}(T) \tag{B.3}$$

and the expression (B.2) becomes

$$\mathbf{x}(T) = \sum_{k=1}^N c_k \mathbf{u}_k(T_0) e^{\lambda_k(T_0)T/\tilde{\epsilon}} \tag{B.4}$$

The asymptotic solution of (B.3) in the limit $\tilde{\epsilon} \rightarrow 0$ can be assumed to maintain the form (B.4), but with $\lambda_k(T)$ and $\mathbf{u}_k(T)$ instead of $\lambda_k(T_0)$ and $\mathbf{u}_k(T_0)$, and with c_k no more constant but function of T and $\tilde{\epsilon}$ and expandable in a power series of the parameter $\tilde{\epsilon}$. A single term in the summation (B.4) (the complete solution can be reconstructed by superimposition), in the case of a constant coefficient matrix $\mathbf{A} = \mathbf{A}(T_0)$, reads

$$\mathbf{x}(T) = \mathbf{u}_k(T_0)e^{\lambda_k(T_0)T/\tilde{\epsilon}}$$

while, when the coefficient matrix \mathbf{A} is slowly varying, the corresponding term can be written as

$$\mathbf{x}(T) = \mathbf{f}(T, \tilde{\epsilon})e^{\phi(T)/\tilde{\epsilon}}$$

so that in the constant-coefficient case $\mathbf{f}(T, \tilde{\epsilon})$ and $\phi(T)$ respectively reduce to $\mathbf{f}(T, \tilde{\epsilon}) = \mathbf{u}_k(T_0)$ and $\phi(T) = \lambda_k(T_0)T$. We now assume that the vector $\mathbf{f}(T, \tilde{\epsilon})$ is expandable in a power series of $\tilde{\epsilon}$ so that

$$\mathbf{f}(T, \tilde{\epsilon}) = \sum_{n=0}^{\infty} \mathbf{f}_n(T)\tilde{\epsilon}^n$$

which implies

$$\mathbf{x}(T) = \mathbf{f}(T, \tilde{\epsilon})e^{\phi(T)/\tilde{\epsilon}} = (\mathbf{f}_0(T) + \tilde{\epsilon}\mathbf{f}_1(T) + \tilde{\epsilon}^2\mathbf{f}_2(T) + \dots) e^{\phi(T)/\tilde{\epsilon}} \quad (\text{B.5})$$

With this expression for the solution $\mathbf{x}(T)$, the term $\tilde{\epsilon}d\mathbf{x}/dT$ becomes

$$\begin{aligned} \tilde{\epsilon} \frac{d\mathbf{x}(T)}{dT} &= \tilde{\epsilon} \left[\left(\frac{d\mathbf{f}_0(T)}{dT} + \tilde{\epsilon} \frac{d\mathbf{f}_1(T)}{dT} + \dots \right) e^{\phi(T)/\tilde{\epsilon}} + \frac{1}{\tilde{\epsilon}} \frac{d\phi(T)}{dT} (\mathbf{f}_0(T) + \tilde{\epsilon}\mathbf{f}_1(T) + \dots) e^{\phi(T)/\tilde{\epsilon}} \right] \\ &= \left[\frac{d\phi(T)}{dT} \mathbf{f}_0(T) + \tilde{\epsilon} \left(\frac{d\phi(T)}{dT} \mathbf{f}_1(T) + \frac{d\mathbf{f}_0(T)}{dT} \right) + \mathcal{O}(\tilde{\epsilon}^2) \right] e^{\phi(T)/\tilde{\epsilon}} \end{aligned}$$

so that by introducing the previous derivative and the expansion (B.5) in the original system (B.3), collecting terms at different orders with respect to $\tilde{\epsilon}$, and dividing by the exponential part, the following hierarchy of equations is found:

$$\begin{aligned} \frac{d\phi}{dT} \mathbf{f}_0(T) &= \mathbf{A}(T) \mathbf{f}_0(T) \\ \tilde{\epsilon} \left(\frac{d\phi}{dT} \mathbf{f}_1(T) + \frac{d\mathbf{f}_0}{dT} \right) &= \tilde{\epsilon} \mathbf{A}(T) \mathbf{f}_1(T) \\ &\vdots = \vdots \\ \tilde{\epsilon}^n \left(\frac{d\phi}{dT} \mathbf{f}_n(T) + \frac{d\mathbf{f}_{n-1}}{dT} \right) &= \tilde{\epsilon}^n \mathbf{A}(T) \mathbf{f}_n \end{aligned}$$

The first equation reduces to the eigenvalue problem

$$\left[\frac{d\phi}{dT} \mathbf{I} - \mathbf{A}(T) \right] \mathbf{f}_0(T) = 0 \quad (\text{B.6})$$

that admits a non trivial solution if

$$\frac{d\phi}{dT} = \lambda_k(T)$$

The solution is actually $\mathbf{f}_0(T) = \mathbf{u}_k(T)$, as expected, but it is defined up to a multiplicative factor since the normalization of the eigenvector $\mathbf{f}_0(T)$ can be performed in different ways. In order to express this feature, the solution at order zero is written as $\mathbf{f}_0(T) = c_k(T)\tilde{\mathbf{u}}_k(T)$ where the coefficient $c_k(T)$ is unknown and $\tilde{\mathbf{u}}_k(T)$ is normalized in a certain way. The second equation, at order $\tilde{\epsilon}$, can be recasted in the form

$$[\lambda_k(T)\mathbf{I} - \mathbf{A}(T)]\mathbf{f}_1(T) = \frac{d\mathbf{f}_0}{dT} \quad (\text{B.7})$$

which represents a singular problem because the coefficient matrix $[\lambda_k(T)\mathbf{I} - \mathbf{A}(T)]$ is the same as the one at order zero, where the singularity of the matrix was required in order to obtain a non trivial solution. However, at order $\tilde{\epsilon}$ an inhomogeneous known term is present: from the basic theory of linear systems it is well known that the solution exists if a proper ‘‘compatibility condition’’ is satisfied (see appendix A), which states that the dot product between the known term and the left eigenvector corresponding to the vanishing eigenvalue must be zero:

$$\tilde{\mathbf{v}}_k(T) \cdot \frac{d\mathbf{f}_0}{dT} = 0 \quad (\text{B.8})$$

By expanding the previous equation and recalling that $\mathbf{f}_0(T) = c_k(T)\tilde{\mathbf{u}}_k(T)$, an equation for the unknown coefficient $c_k(T)$ is obtained:

$$\tilde{\mathbf{v}}_k(T) \cdot \tilde{\mathbf{u}}_k(T) \frac{dc_k}{dT} + \tilde{\mathbf{v}}_k(T) \cdot \frac{d\tilde{\mathbf{u}}_k(T)}{dT} c_k = 0 \quad (\text{B.9})$$

It is easy to verify that (B.9) is a first order homogeneous ordinary differential equation, for which a closed-form solution exists. Its solutions provides the coefficient $c_k(T)$ so that the product $c_k(T)\tilde{\mathbf{u}}_k(T)$ is computed. It is important to remark that the latter vector is unique, independent of the normalization, while $\tilde{\mathbf{u}}_k(T)$ was not.

This analysis can therefore be summarized in the following way. The solution at order zero is not uniquely determined, but it is defined up to a multiplicative factor $c_k(T)$ which depends on T . However, $c_k(T)$ can be an arbitrary function of T because equation (B.6) does not contain derivatives of $\mathbf{f}_0(T)$ with respect to T . On the other hand, the ‘‘compatibility condition’’ (B.8), which allows the problem (B.7) at first order to admit a solution and thus the expansion (B.5) to exist, is used as a constrain in order to determine the unknown factor $c_k(T)$. The same compatibility problem found at order $\tilde{\epsilon}$ is present also at the next orders because the generic equation contains always the same singular matrix $[\lambda_k(T)\mathbf{I} - \mathbf{A}(T)]$. It is therefore necessary to impose a condition like (B.8) at each order. In fact, once the equation for $\mathbf{f}_1(T)$ has been made compatible, the solution is still determined up to a factor that multiplies $\mathbf{u}_k(T)$ and that can be used in order to satisfy the compatibility condition at second order. The same procedure can be repeated at each order.

In practical applications the solution is usually truncated at order zero. However, it is interesting to evaluate the error when order- $\tilde{\epsilon}$ terms are neglected. This can be done using the relation (A.5), so that the solution at order $\tilde{\epsilon}$ is written as

$$\tilde{\epsilon}\mathbf{f}_1(t) = \sum_{h \neq k} [\lambda_h(t) - \lambda_k(t)]^{-1} \left(\mathbf{v}_k^\top(t) \cdot \frac{d\mathbf{u}_k(t)}{dt} \right) \mathbf{u}_k(t)$$

where $t = T/\tilde{\epsilon}$ has been substituted and $\lambda_h(t)$ is another eigenvalue of $\mathbf{A}(t)$. From this expression, it is clear that in order for $\tilde{\mathbf{f}}_1(T)$ to be small and negligible with respect to $\mathbf{f}_0(T)$, the derivative $d\mathbf{u}_k/dT$ must be small with respect to $\lambda_h(t) - \lambda_k(t)$. This basically implies that the multiple-scale approximation can be applied if the parameter of the system are slowly varying with respect to the characteristic frequency given by the difference between the considered eigenvalue and the other eigenvalues of the system. Therefore multiple scales can be applied if the eigenvalues are distinct but sufficiently far, independent of how small they are.

By retaining only the order-zero term, the state vector $\mathbf{x}(T)$ is expressed as

$$\mathbf{x}(T) = c_k(T)\tilde{\mathbf{u}}_k(T)e^{\frac{\phi(T)}{\tilde{\epsilon}}} + \mathcal{O}(\tilde{\epsilon})$$

Appendix C

Example of optimization

In order to show the optimization technique used to find the shape of the optimal perturbation at the initial station which maximizes a certain gain, or the velocity distribution at the wall which minimizes the same (or another) gain, let us consider a simple partial differential equation (Burger's equation) in the form

$$u_t + uu_y - u_{yy} = 0 = \mathbf{F}(u) \quad \text{with } y \in [0, +\infty) \text{ and } t \in [0, T] \quad (\text{C.1})$$

with initial condition, since equation (C.1) is parabolic with respect to time t ,

$$u(y, 0) = u_0(y) \quad (\text{C.2})$$

and boundary conditions at the wall

$$u(0, t) = u_w(t) \quad (\text{C.3})$$

and at infinity

$$u(\infty, t) = 0$$

In order to solve an optimization problem, we should first define an objective function to be minimized or maximized. To do that, we introduce the energy-like norms:

$$\begin{aligned} E(g(y)) &= \frac{1}{2} \int_0^\infty g(y)g(y)dy \\ E_i(p(y, t)) &= \frac{1}{2} \int_{-Z}^Z \int_0^\infty p(y, t)p(y, t)dy dz \\ E_w(h(t)) &= \frac{1}{2} \int_0^T h(t)h(t)dt \end{aligned} \quad (\text{C.4})$$

The aim is to find the initial condition (C.2) and boundary condition (C.3) in such a way that a certain gain G is stationary (maximum or minimum). For seek of generality, we define G as the sum of different energy contributions:

$$G(u, u_T) = \alpha E(u(y, T)) + \beta E_i(u(y, t)) \quad (\text{C.5})$$

respectively coming from the energy of the solution at $t = T$ ($u_T = u(y, T)$), and from the the energy computed over the complete domain.

In this problem we consider both the initial energy $E(u_0)$ and the controlling energy $E_w(u_w)$ fixed. This means that a constrained optimization problem has to be solved, where the constraints are represented by the initial equation (C.1) and the energy constraints:

$$E(u_0) = E_0; \quad E_w(u_w) = E_{0w} \quad (\text{C.6})$$

where E_0 and E_{0w} are given. The problem of constrained optimization can be faced introducing and optimizing a Lagrange functional in the form

$$\mathcal{L}(u, u_0, u_T, u_w, a, b, c) = G(u, u_T, u_w) - \langle \mathbf{F}(u), a \rangle - b [E(u_0) - E_0] - c [E_w(u_w) - E_{0w}] \quad (\text{C.7})$$

where

$$a = a(y, t); \quad b = \text{const}; \quad c = \text{const}$$

are Lagrange multipliers and the inner product is

$$\langle p(y, t), q(y, t) \rangle = \int_0^T \int_0^{+\infty} p(y, t) q(y, t) dy dt$$

Maximizing or minimizing \mathcal{L} means $\delta\mathcal{L} = 0$, that is:

$$\frac{\delta\mathcal{L}}{\delta u} \delta u + \frac{\delta\mathcal{L}}{\delta u_0} \delta u_0 + \frac{\delta\mathcal{L}}{\delta u_0} \delta u_T + \frac{\delta\mathcal{L}}{\delta u_w} \delta u_w + \frac{\delta\mathcal{L}}{\delta a} \delta a + \frac{\delta\mathcal{L}}{\delta b} \delta b + \frac{\delta\mathcal{L}}{\delta c} \delta c = 0 \quad (\text{C.8})$$

where, for example, $\frac{\delta\mathcal{L}}{\delta u} \delta u$ denotes

$$\frac{\delta\mathcal{L}}{\delta u} \delta u = \lim_{\epsilon \rightarrow 0} \frac{\mathcal{L}(u + \epsilon \delta u, u_0, u_T, u_w, a, b, c) - \mathcal{L}(u, u_0, u_T, u_w, a, b, c)}{\epsilon}$$

The derivatives of $\mathcal{L}(u, u_0, u_T, u_w, a, b, c)$ with respect to a, b, c represent respectively the initial equation (C.1) and the energy constraints (C.6), which are supposed to be satisfied, so that

$$\frac{\delta\mathcal{L}}{\delta a} \delta a + \frac{\delta\mathcal{L}}{\delta b} \delta b + \frac{\delta\mathcal{L}}{\delta c} \delta c = 0$$

For this reason, we can concentrate only on the remaining terms in (C.8). From

$$\frac{\delta\mathcal{L}}{\delta u} \delta u + \frac{\delta\mathcal{L}}{\delta u_0} \delta u_0 + \frac{\delta\mathcal{L}}{\delta u_0} \delta u_T + \frac{\delta\mathcal{L}}{\delta u_w} \delta u_w = 0$$

one gets

$$\begin{aligned} & \alpha \int_0^{+\infty} u_T \delta u_T dy + \beta \int_0^T \int_0^{+\infty} u \delta u dy dt - \\ & \int_0^T \int_0^{+\infty} a(y, t) [\delta u_t + \delta u u_y + u(\delta u)_y - \delta u_{yy}] dy dt - \\ & b \int_0^{+\infty} \delta u_0 \delta u_0 dy - c \int_0^T \delta u_w \delta u_w dt = 0 \end{aligned}$$

Integrating by parts leads to:

$$\begin{aligned} & \alpha \int_0^{+\infty} u_T \delta u_T dy + \beta \int_0^T \int_0^{+\infty} u \delta u dy dt - \\ & - \int_0^T \int_0^{+\infty} [(a\delta u)_t - a_t \delta u] dy dt - \int_0^T \int_0^{+\infty} [(a\delta u)_y - a_y u \delta u] dy dt + \\ & \int_0^T \int_0^{+\infty} [(a\delta u)_y - (a_y \delta u)_y + a_{yy} \delta u] dy dt - b \int_0^{+\infty} \delta u_0 \delta u_0 dy - c \int_0^T \delta u_w \delta u_w dt = 0 \end{aligned}$$

so that:

$$\begin{aligned} & \alpha \int_0^{+\infty} u_T \delta u_T dy + \beta \int_0^T \int_0^{+\infty} u \delta u dy dt - \int_0^{+\infty} [a\delta u]_0^T dy + \\ & \int_0^T \int_0^{+\infty} a_t \delta u dy dt - \int_0^T [a\delta u]_0^{+\infty} dt + \int_0^T \int_0^{+\infty} a_y u \delta u dy dt + \int_0^T [a(\delta u)_y]_0^{+\infty} dt - \\ & \int_0^T [a_y \delta u]_0^{+\infty} dt + \int_0^T \int_0^{+\infty} a_{yy} \delta u dy dt - b \int_0^{+\infty} \delta u_0 \delta u_0 dy - c \int_0^T \delta u_w \delta u_w dt = 0 \end{aligned} \quad (C.9)$$

Collecting terms multiplied by δu and appearing inside the double integral, one obtains:

$$a_t + a_y u + a_{yy} = -\beta u \quad \text{with } y \in [0, +\infty) \text{ and } t \in [0, T] \quad (C.10)$$

the term $\int_0^T [a(\delta u)_y]_0^{+\infty} dt$, since there is no reason for requiring $(\delta u)_y = 0$ at $y = 0$ and $y \rightarrow \infty$, implies

$$a(0, t) = a(\infty, t) = 0 \quad (C.11)$$

Collecting terms multiplied by δu_T in the y -integrals leads to:

$$-a_T + \alpha u_T = 0$$

where $a_T = a(y, T)$, while collecting terms multiplied by δu_0 gives

$$a_0 - b u_0 = 0$$

The term $\int_0^T [a\delta u]_0^{+\infty} dt$ is identically zero because of the conditions (C.11) while grouping terms multiplied by $\delta u(0, t) = \delta u_w(t)$ leads to:

$$a_y - c u_w = 0$$

Summarizing, we started from the problem

$$\begin{cases} u_t + u u_y - u_{yy} = 0 \\ u(y, 0) = u_0(y) \\ u(0, t) = u_w(t) \\ u(\infty, t) = 0 \end{cases} \quad (C.12)$$

with the aim of maximizing or minimizing a certain gain defined as

$$G(u, u_T, u_w) = \alpha E(u_T) + \beta E_i(u)$$

with the energy constraints

$$E(u_0) = E_0; \quad E_w(u_w) = E_{0w}$$

where u_w and u_0 can be fixed or unknown depending on the problem we are dealing with. If we are searching for a certain $u_0(y)$ which minimizes G then $u_w(t)$ is fixed (and in general equal to zero), while if we want to minimize a certain G for a given $u_0(y)$ (in general the optimal perturbation), $u_w(t)$ is the unknown. In any case, we ended up to the problem

$$\begin{cases} a_t + a_y u + a_{yy} = -\beta u \\ a(y, T) = \alpha u(y, T) \\ a(0, t) = 0 \\ a(\infty, t) = 0 \end{cases} \quad (\text{C.13})$$

plus conditions at $t = 0$ and $y = 0$ which link the direct problem to the adjoint one and which are respectively the initial and boundary condition for the direct problem:

$$\begin{cases} u_0(y) = \frac{1}{b} a(y, 0) \\ u_w(t) = \frac{1}{c} a_y(0, t) \end{cases}$$

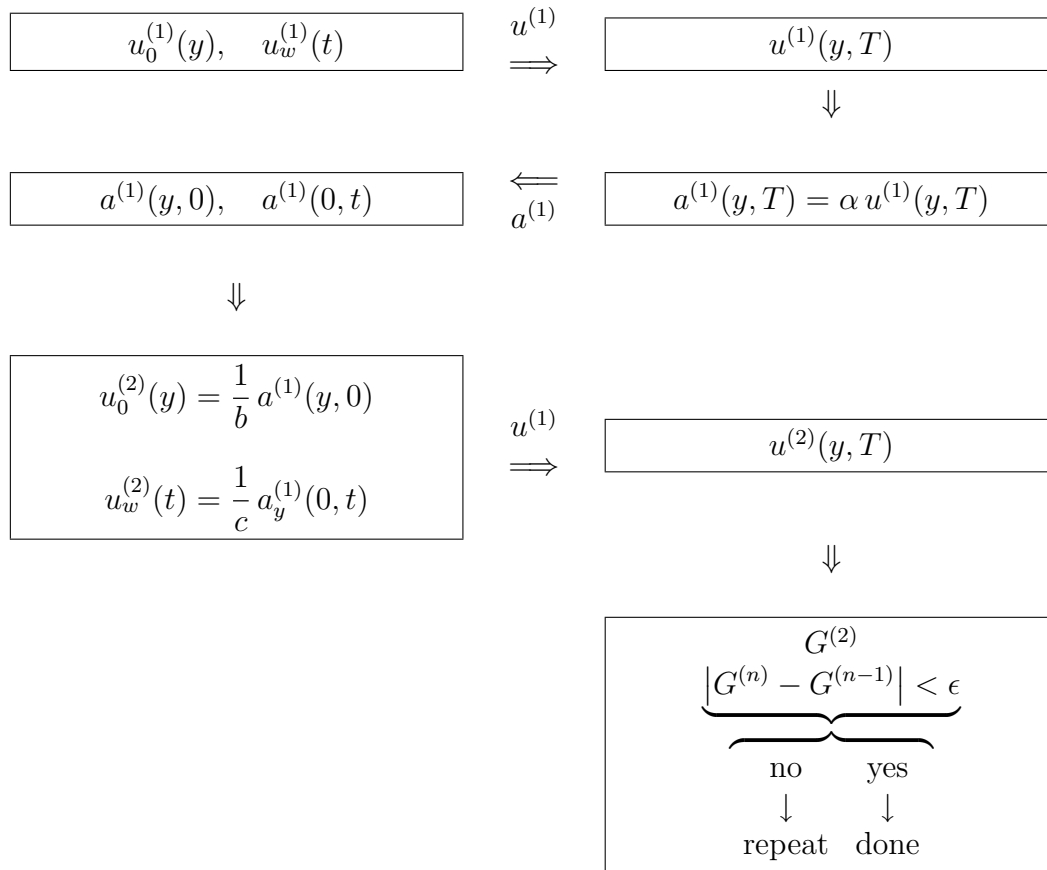
The two unknown Lagrange multipliers are found scaling u_0 or u_w in order them to satisfy the energy constraints. The equation in system (C.13) is a non homogeneous linear partial differential equation in the unknown a . It is parabolic in time, but the natural developing direction is backward due to the sign “+” in the term a_{yy} . This is the reason why the adjoint formulation of the direct problem (C.12) requires one “initial” condition at $t = T$ a part from the two usual boundary conditions at $y = 0$ and $y \rightarrow \infty$.

The procedure in order to get the solution to the optimization problem is therefore the following. We start from a guess initial condition $u_0^{(1)}(y)$ and $u_w^{(1)}(t)$ for the direct problem, finding the final profile $u^{(1)}(y, T)$ which allows us to compute the “initial condition” $a^{(1)}(y, T)$ for the adjoint problem. Marching backward, the solution $a^{(1)}(y, 0)$ obtained at $t = 0$ and $y = 0$ gives the new initial and boundary condition at the wall for the direct problem. The two constants b and c are found imposing the satisfaction of the two energy constraints. Then a new direct computation is performed and the procedure stops when the difference between the gain G computed for two successive iterations is lower than a certain threshold.

The optimization problem applied to the simple Burger’s equation can be used in order to find the optimal initial condition or the optimal boundary condition at the wall which renders stationary the gain G defined in (C.5). In the first case the unknown is u_0 and $\alpha = 1$, $\beta = c = 0$ because usually we are interested in maximising the energy at the final station for a given initial energy and for given boundary conditions. In the case of control, on the contrary, the initial condition is given ($b = 0$) as well as the controlling

energy, while the gain to be minimized can be the final energy ($\alpha = 1; \beta = 0$) or the integral of the energy over all the domain ($\alpha = 0; \beta = 1$). In this case the unknown is the boundary condition u_w .

The following scheme should help in order to get a “visual” idea of such a procedure.



Appendix D

Discretization of the non linear direct problem

The solution of the direct problem is expanded in Fourier modes along the spanwise direction:

$$\begin{aligned} u(x, y, z) &= \sum_{n=-\infty}^{\infty} U_n(x, y) e^{in\beta z}; & v(x, y, z) &= \sum_{n=-\infty}^{\infty} V_n(x, y) e^{in\beta z}; \\ w(x, y, z) &= \sum_{n=-\infty}^{\infty} W_n(x, y) e^{in\beta z}; & p(x, y, z) &= \sum_{n=-\infty}^{\infty} P_n(x, y) e^{in\beta z}; \end{aligned} \quad (\text{D.1})$$

so that the nonlinear terms in equations (3.2.1) produce a double summation similar to a convolution. Introducing expressions (D.1) in the equations (3.2.1) yields:

$$\begin{aligned} \sum_{n=-\infty}^{\infty} [(U_n)_x + (V_n)_y + in\beta W_n] e^{in\beta z} &= 0 \\ \sum_{n=-\infty}^{\infty} [(C_n^{UU})_x + (C_n^{UV})_y + in\beta C_n^{UW} - (U_n)_{yy} + n^2\beta^2 U_n] e^{in\beta z} &= 0 \\ \sum_{n=-\infty}^{\infty} [(C_n^{UV})_x + (C_n^{VV})_y + in\beta C_n^{VW} - (V_n)_{yy} + n^2\beta^2 V_n + (P_n)_y] e^{in\beta z} &= 0 \\ \sum_{n=-\infty}^{\infty} [(C_n^{UW})_x + (C_n^{VW})_y + in\beta C_n^{WW} - (W_n)_{yy} + n^2\beta^2 W_n + in\beta P_n] e^{in\beta z} &= 0 \end{aligned} \quad (\text{D.2})$$

Since each equation is satisfied if each term in the summation is zero, the following system is obtained:

$$\begin{aligned} (U_n)_x + (V_n)_y + in\beta W_n &= 0 \\ (C_n^{UU})_x + (C_n^{UV})_y + in\beta C_n^{UW} - (U_n)_{yy} + n^2\beta^2 U_n &= 0 \\ (C_n^{UV})_x + (C_n^{VV})_y + in\beta C_n^{VW} - (V_n)_y + n^2\beta^2 V_n + (P_n)_y &= 0 \\ (C_n^{UW})_x + (C_n^{VW})_y + in\beta C_n^{WW} - (W_n)_{yy} + n^2\beta^2 W_n + in\beta P_n &= 0 \end{aligned} \quad (\text{D.3})$$

System (D.3) is discretized using second-order finite differences in x and y , but after that it is yet nonlinear and couples the general unknown $F_n(x, y)$ with $G_k(x, y)$ because of the coefficient $C_n^{FG}(x, y)$. In order to linearize (D.3), we separate the mode F_n and G_k in two contributions

$$F_n = \bar{F}_n + f_n;$$

where \bar{F}_n is considered known and f_n is small in such a way that, neglecting terms like $f_k(x, y)g_{n-k}(x, y)$ in the coefficient $C_n^{FG}(x, y)$, which was the origin of the nonlinearity in the system, one gets:

$$C_n^{FG}(x, y) = \sum_{k=a}^b F_k(x, y)G_{n-k}(x, y) = \sum_{k=a}^b (\bar{F}_k\bar{G}_{n-k} + \bar{F}_kg_{n-k} + f_k\bar{G}_{n-k})$$

Since \bar{F}_n and \bar{G}_{n-k} are known, the unknowns reduce to f_n and g_{n-k} . In the previous expression, the coefficient $C_n^{FG}(x, y)$ is linear in the unknowns g_{n-k} and f_k , but it still couples the unknowns corresponding to different modes.

Since our aim is to decouple different modes so that a small linear system can be solved for each mode n , in the summations

$$\sum_{k=a}^b \bar{F}_kg_{n-k} \quad \text{and} \quad \sum_{k=a}^b f_k\bar{G}_{n-k}$$

we retain only the terms \bar{F}_0g_n and $f_n\bar{G}_0$. This reduces C_n^{FG} to

$$C_n^{FG}(x, y) = \sum_{k=a}^b \bar{F}_k\bar{G}_{n-k} + \bar{F}_0g_n + f_n\bar{G}_0 = C_n^{\bar{F}\bar{G}} + \bar{F}_0g_n + f_n\bar{G}_0$$

where obviously $C_n^{\bar{F}\bar{G}} = \sum_{k=a}^b \bar{F}_k\bar{G}_{n-k}$.

Under these assumptions, the original nonlinear coupling coefficient $C_n^{FG}(x, y)$ has been simplified in a linear form and couples only mode n and mode zero, so that the system of equations reads:

$$\begin{aligned} (u_n)_x + (v_n)_y + in\beta w_n &= - [(\bar{U}_n)_x + (\bar{V}_n)_y + in\beta\bar{W}_n] \\ (\bar{U}_0u_n + u_n\bar{U}_0)_x + (\bar{V}_0u_n)_y + in\beta\bar{W}_0u_n - (u_n)_{yy} + n^2\beta^2u_n + (\bar{U}_0v_n)_y + in\beta\bar{U}_0w_n &= \\ &\quad - [(C_n^{\bar{U}\bar{U}})_x + (C_n^{\bar{U}\bar{V}})_y + in\beta C_n^{\bar{U}\bar{W}} - (\bar{U}_n)_{yy} + n^2\beta^2\bar{U}_n] \\ (\bar{U}_0v_n + u_n\bar{V}_0)_x + (2\bar{V}_0v_n)_y + in\beta\bar{W}_0v_n - (v_n)_y + n^2\beta^2v_n + in\beta\bar{V}_0w_n + (p_n)_y &= \\ &\quad - [(C_n^{\bar{U}\bar{V}})_x + (C_n^{\bar{V}\bar{V}})_y + in\beta C_n^{\bar{V}\bar{W}} - (\bar{V}_n)_{yy} + n^2\beta^2\bar{V}_n + (\bar{P}_n)_y] \\ (\bar{U}_0w_n + u_n\bar{W}_0)_x + (\bar{W}_0v_n)_y + (\bar{V}_0w_n)_y + 2in\beta\bar{W}_0w_n - (w_n)_{yy} + n^2\beta^2w_n + in\beta p_n &= \\ &\quad - [(C_n^{\bar{U}\bar{W}})_x + (C_n^{\bar{V}\bar{W}})_y + in\beta C_n^{\bar{W}\bar{W}} - (\bar{W}_n)_y + n^2\beta^2\bar{W}_n + in\beta\bar{P}_n] \end{aligned}$$

in a more compact form:

$$(\mathbf{A}_0 \mathbf{f}_n)_x + \mathbf{B}_n \mathbf{f}_n = -\mathbf{r}_n \quad (\text{D.4})$$

where

$$\mathbf{A}_0 = \begin{pmatrix} 1 & 0 & 0 & 0 \\ 2\bar{U}_0 & 0 & 0 & 0 \\ \bar{V}_0 & \bar{U}_0 & 0 & 0 \\ \bar{W}_0 & 0 & \bar{U}_0 & 0 \end{pmatrix}$$

$$\mathbf{B}_n = \begin{pmatrix} 0 & (\cdot)_y & in\beta & 0 \\ B_{21} & (\bar{U}_0 \cdot)_y & in\beta \bar{U}_0 & 0 \\ 0 & B_{32} & in\beta \bar{V}_0 & (\cdot)_y \\ 0 & (\bar{W}_0 \cdot)_y & B_{43} & in\beta \end{pmatrix}$$

with

$$\begin{aligned} B_{21} &= (\bar{V}_0 \cdot)_y + in\beta \bar{W}_0 - (\cdot)_{yy} + n^2 \beta^2 \\ B_{32} &= (2\bar{V}_0 \cdot)_y + in\beta \bar{W}_0 - (\cdot)_{yy} + n^2 \beta^2 \\ B_{43} &= (\bar{V}_0 \cdot)_y + 2in\beta \bar{W}_0 - (\cdot)_{yy} + n^2 \beta^2 \end{aligned}$$

$$\mathbf{r}_n = \begin{pmatrix} (\bar{U}_n)_x + (\bar{V}_n)_y + in\beta \bar{W}_n \\ (C_n^{\bar{U}\bar{U}})_x + (C_n^{\bar{U}\bar{V}})_y + in\beta C_n^{\bar{U}\bar{W}} - (\bar{U}_n)_{yy} + n^2 \beta^2 \bar{U}_n \\ (C_n^{\bar{U}\bar{V}})_x + (C_n^{\bar{V}\bar{V}})_y + in\beta C_n^{\bar{V}\bar{W}} - (\bar{V}_n)_{yy} + n^2 \beta^2 \bar{V}_n + (\bar{P}_n)_y \\ (C_n^{\bar{U}\bar{W}})_x + (C_n^{\bar{V}\bar{W}})_y + in\beta C_n^{\bar{W}\bar{W}} - (\bar{W}_n)_{yy} + n^2 \beta^2 \bar{W}_n + in\beta \bar{P}_n \end{pmatrix} \quad (\text{D.5})$$

The known term $-\mathbf{r}_n$ can be re-written as

$$\mathbf{r}_n = (\mathbf{r}_{xn})_x + \mathbf{r}_{0n}$$

where \mathbf{r}_{xn} contains the x -derivative and \mathbf{r}_{0n} contains the other terms:

$$\mathbf{r}_{xn} = \begin{pmatrix} \bar{U}_n \\ C_n^{\bar{U}\bar{U}} \\ C_n^{\bar{U}\bar{V}} \\ C_n^{\bar{U}\bar{W}} \end{pmatrix}$$

$$\mathbf{r}_{0n} = \begin{pmatrix} (\bar{V}_n)_y + in\beta\bar{W}_n \\ (C_n^{\bar{U}\bar{V}})_y + in\beta C_n^{\bar{U}\bar{W}} - (\bar{U}_n)_{yy} + n^2\beta^2\bar{U}_n \\ (C_n^{\bar{V}\bar{V}})_y + in\beta C_n^{\bar{V}\bar{W}} - (\bar{V}_n)_{yy} + n^2\beta^2\bar{V}_n + (\bar{P}_n)_y \\ (C_n^{\bar{V}\bar{W}})_y + in\beta C_n^{\bar{W}\bar{W}} - (\bar{W}_n)_{yy} + n^2\beta^2\bar{W}_n + in\beta\bar{P}_n \end{pmatrix}$$

The final system therefore is:

$$\mathbf{T}_n^i \mathbf{f}_n^i = \mathbf{y}_n^i \quad (\text{D.6})$$

where the index \cdot_n denotes the n -th mode, the apex \cdot^i denotes the i -th station in x , the vector \mathbf{f}_n^i is the vector of unknowns

$$\mathbf{f}_n^i = \begin{pmatrix} u_n^i \\ v_n^i \\ w_n^i \\ p_n^i \end{pmatrix} \quad (\text{D.7})$$

and the matrix \mathbf{T}_n^i depends on n and is defined as

$$\mathbf{T}_n^i = C_0 \mathbf{A}_0^i + \mathbf{B}_n^i$$

Matrix \mathbf{A}_0^i contains only the mode zero of the solution and both \mathbf{A}_0^i and \mathbf{B}_n^i account for the y -discretization of the derivatives. The vector \mathbf{y}_n^i is due to all known terms:

$$\mathbf{y}_n^i = -C_1 \mathbf{A}_0^{i-1} \mathbf{f}_n^{i-1} - C_2 \mathbf{A}_0^{i-2} \mathbf{f}_n^{i-2} - C_0 \mathbf{r}_x^i - C_1 \mathbf{r}_x^{i-1} - C_2 \mathbf{r}_x^{i-2} - \mathbf{r}_0^i$$

The numerical solution of the direct problem is obtained marching in x -direction, from $x = 0$ to $x = X$.

Bibliography

- [1] ACKERBERG, R. C., AND PHILIPS, J. H. The unsteady laminar boundary layer on a seminfinite flat plate due to small fluctuations in magnitude of the free-stream velocity. *J. Fluid Mech.* 51 (1972), 137–157.
- [2] AIRIAU, C. Non-parallel acoustic receptivity of a Blasius boundary layer using an adjoint approach. *Flow, Turbul. Combust.*. Submitted.
- [3] ANDERSSON, P. *Modelling of Boundary Layer Stability*. Doctoral thesis, Royal Institute of Technology – Department of Mechanics – Stockholm, 1999.
- [4] ANDERSSON, P., BERGGREN, M., AND HENNINGSON, D. S. Optimal disturbances and bypass transition in boundary layers. *Phys. Fluids* 11 (1999), 134–150.
- [5] ANDERSSON, P., BRANDT, L., BOTTARO, A., AND HENNINGSON, D. S. On the breakdown of boundary layer streaks. *J. Fluid Mech* 428 (2001), 29–60.
- [6] ASAI, M., AIBA, K., AND NISHIOKA, M. A nonlinearity-coupled receptivity process generating a Tollmien–Schlichting wave behind a backward-facing step. *Fluid Dyn. Res.* 17 (1996), 225–236.
- [7] ASHPIS, A. E., AND RESHOTKO, E. The vibrating ribbon problem revisited. *J. Fluid Mech.* 213 (1990), 531–547.
- [8] BAYLY, B. J., AND ORSZAG, S. A. Instability mechanisms in shear-flow transition. *Annu. Rev. Fluid Mech.* 20 (1988), 359–391.
- [9] BENDER, C. M., AND ORSZAG, S. A. *Advanced Mathematical Methods for Scientists and Engineers*. McGraw–Hill, New York, 1978.
- [10] BERTOLOTTI, F. P., HERBERT, T., AND SPALART, P. R. Linear and non linear stability of the Blasius boundary layer. *J. Fluid Mech.* 242 (1992), 441–474.
- [11] BESSIERE, E. *Analyse asymptotique et numérique de la réceptivité de la couche limite bidimensionnelle sur plaque plane*. Ph.d. dissertation, Université Paul Sabatier — Institut de Mécanique des Fluides de Toulouse, Mar. 1999.
- [12] BEWLEY, T., TERMAM, R., AND ZIANE, M. A general framework for robust control in fluid mechanics. *Physica D* 138 (2000), 360–392.

- [13] BEWLEY, T. R., AND LIU, S. Optimal and robust control and estimation of linear paths to transition. *J. Fluid Mech* 365 (1998), 305–349.
- [14] BOBERG, L., AND BROSA, U. Onset of turbulence in a pipe. *Z. Naturforschung* 43a (1988), 697–726.
- [15] BODONYI, R. J., WELCH, W. J. C., DUCK, P. W., AND TADJFAR, M. A numerical study of the interaction between unsteady free-stream disturbances and localized variations in surface geometry. *J. Fluid Mech.* 209 (1989), 285–308.
- [16] BUTER, T. A., AND REED, H. L. Boundary layer receptivity to free-stream vorticity. *Phys. Fluids* 6, 10 (1994), 3368–3379.
- [17] BUTLER, K. M., AND FARRELL, B. Three-dimensional optimal perturbations in viscous shear flow. *Phys. Fluids A* 4 (1992), 1637–1650.
- [18] CASALIS, G., GOUTTENOIRE, C., AND TROFF, B. Etude de réceptivité de bord d’attaque et de réceptivité localisée par simulation numérique directe. First AFOSR International Conference on DNS and LES, Ruston, LA (USA), August 4–8 1997.
- [19] CASALIS, G., GOUTTENOIRE, C., AND TROFF, B. Réceptivité localisée de la coche limite. C. R. Acad. Sci. Paris, t. 325 Série II b, 1997.
- [20] CATHALIFAUD, P., AND LUCHINI, P. Algebraic growth in boundary layers: optimal control by blowing and suction at the wall. *Eur. J. Mech. B – Fluids* 19 (2000), 469–490.
- [21] CEBECI, T., AND COUSTEIX, J. *Modeling and Computation of Boundary-Layer Flows*. Horizon Publishing and Springer, Long Beach, California, 1999.
- [22] CEBECI, T., AND SMITH, A. M. O. *Analysis of Turbulent Boundary Layers*. Academic Press, New York, 1974.
- [23] CHANDRASEKHAR, S. *Hydrodynamic and Hydromagnetic Stability*. Clarendon Press, Oxford, 1961.
- [24] CHIU, W. K., AND NORTON, M. P. The receptivity of laminar boundary layer to leading edge vibration. *Journal of Sound and Vibration* 141 (1990), 143–173.
- [25] CHIU, W. K., SORIA, J., AND NORTON, M. P. Laminar boundary layer receptivity to transverse structural vibration. *Journal of Sound and Vibration* 186, 3 (1995), 463–493.
- [26] CHOUDHARI, M. Distributed acoustic receptivity in laminar flow control configurations. *Phys. Fluids* 6, 2 (1994), 489–506.
- [27] CHOUDHARI, M., AND KERSCHEN, E. Boundary layer receptivity due to three dimensional convected gust. In *Instability and Transition Workshop, ICASE/NASA LaRC*. Springer-Verlag, Berlin, 1990.

- [28] CHOUDHARI, M., AND KERSCHEN, E. Instability wave patterns generated by interaction of sound waves with three-dimensional wall suction or roughness. AIAA Paper (90-0119), 1990.
- [29] CHOUDHARI, M., AND STREETT, C. L. A finite Reynolds-number approach for the prediction of boundary-layer receptivity in localized regions. *Phys. Fluids A* 4, 11 (1992), 2495–2514.
- [30] CORBETT, P. *Non-modal growth in boundary layers and its optimal control*. Ph.d. dissertation, École Polytechnique Fédéral de Lausanne, 2000.
- [31] CORBETT, P., AND BOTTARO, A. Optimal linear growth in swept boundary layers. *J. Fluid Mech* 435 (2001), 1–23.
- [32] CORBETT, P., AND BOTTARO, A. Optimal perturbations for boundary layers subject to stream-wise pressure gradient. *Phys. Fluids* 12, 1 (2009), 120–130.
- [33] CROUCH, J. D. Localized receptivity of boundary layers. *Phys. Fluids A* 4, 7 (1992), 1408–1414.
- [34] CROUCH, J. D. Non-localized receptivity of boundary layers. *J. Fluid Mech.* 244 (1992), 567–581.
- [35] CROUCH, J. D. Receptivity and the evolution of boundary-layer instabilities over short-scale waviness. *Phys. Fluids A* 5, 3 (1993), 561–567.
- [36] CROUCH, J. D. Distributed excitation of Tollmien–Schlichting waves by vortical free-stream disturbances. *Phys. Fluids* 6, 1 (1994), 217–223.
- [37] CROUCH, J. D., AND SPALART, P. R. A study of non-parallel and nonlinear effects on the localized receptivity of the boundary layers. *J. Fluid* 290 (1995), 29–37.
- [38] DE MATTEIS, P., DONELLI, R. S., AND LUCHINI, P. Application of the ray-tracing theory to the stability analysis of three-dimensional incompressible boundary layers. 1–10. Atti del XIII Congresso Nazionale AIDAA, Roma, 11-15 sett.
- [39] DIETS, A. J. Local boundary-layer receptivity to a convected free-stream disturbances. *J. Fluid Mech.* 378 (1999), 291–317.
- [40] DRAZIN, P. G., AND REID, W. H. *Hydrodynamic Stability*. Cambridge University Press, Cambridge, 1981.
- [41] DUCK, P. W., RUBAN, A. I., AND ZHIKHAREV, C. N. Laminar flow over unsteady humps: the formation of waves. *J. Fluid Mech.* 160 (1985), 465–498.
- [42] DUCK, P. W., RUBAN, A. I., AND ZHIKHAREV, C. N. The generation of Tollmien–Schlichting waves by free-stream turbulence. *J. Fluid Mech.* 312 (1996), 341–371.

- [43] ELLINGSEN, T., AND PALM, E. Stability of linear flow. *Phys. Fluids* 18 (1975), 487–488.
- [44] FARRELL, B. Optimal excitation of perturbations in viscous shear flow. *Phys. Fluids* 31, 8 (1988), 2093–2102.
- [45] FLORYAN, J. M., AND SARIC, W. S. Stability of Görtler vortices in boundary layer with suction, AIAA 12–th Fluid and Plasma Dynamics Conf., Williamsburg. AIAA Paper (79–1479), 1979.
- [46] GAD–EL–HAK, M. *Flow Control: Passive, Active, and Reactive Flow Management*. Cambridge University Press, London, 2000.
- [47] GAD–EL–HAK, M. Flow control: the future. *Journal of Aircraft* 38, 3 (2001), 402–418.
- [48] GAD–EL–HAK, M., POLLARD, A., AND BONNET, J.-P. *Flow Control: Fundamentals and Practices*. Springer–Verlag, Berlin, 1998.
- [49] GASTER, M. On the generation of spatially growing waves in a boundary layer. *J. Fluid Mech.* 22 (1965), 433–441.
- [50] GASTER, M., AND SENGUPTA, T. K. The generation of disturbance in a boundary layer by wall perturbations: The vibrating ribbon revisited once more. In *Instability and Turbulence in Engineering Flows*. Springer–Verlag, Berlin, 1993, pp. 31–49.
- [51] GOLDSTEIN, M. E. The evolution of Tollmien–Schlichting waves near a leading edge. *J. Fluid Mech.* 127 (1983), 59–81.
- [52] GOLDSTEIN, M. E. Scattering of acoustic wave into Tollmien–Schlichting waves by small streamwise variation in surface geometry. *J. Fluid Mech.* 154 (1985), 509–529.
- [53] GOLDSTEIN, M. E., AND HULTGREN, L. S. A note on the generation of Tollmien–Schlichting waves by sudden surface curvature change. *J. Fluid Mech.* 181 (1987), 519–525.
- [54] GOLDSTEIN, M. E., AND HULTGREN, L. S. Boundary–layer receptivity to long–wave free–stream disturbances. *Ann. Rev. Fluid Mech.* 21 (1989), 137–166.
- [55] GOLDSTEIN, M. E., LEIB, S. J., AND COWEL, S. J. Generation of Tollmien–Schlichting waves on interactive marginally separated flows. *J. Fluid Mech.* 181 (1987), 485–517.
- [56] GOLDSTEIN, M. E., SOCKOL, P. M., AND SANZ, J. The evolution of Tollmien–Schlichting waves near a leading edge. part 2. numerical determination of amplitudes. *J. Fluid Mech.* 129 (1983), 443–453.

- [57] HAMMERTON, P. W., AND KERSCHEN, E. J. Boundary-layer receptivity for a parabolic leading edge. *J. Fluid Mech.* 310 (1996), 243–267.
- [58] HEINRICH, R. A. E., CHOUDHARI, M., AND KERSCHEN, E. J. A comparison of boundary layer receptivity mechanisms. AIAA Paper AIAA–88–3758, 1988.
- [59] HENNINGSON, D. S., AND ALFREDSSON, P. H. Stability and transition of boundary layer flows. In *Turbulence and Transition Modelling*, M. Hallböck, D. S. Henningson, A. V. Johansson, and P. H. Alfredsson, Eds. Kluwer Academic Publishers, 1995, pp. 13–80.
- [60] HENNINGSON, D. S., LUNDBLADH, A., AND JOHANSSON, A. V. A mechanism for bypass transition from localized disturbances in wall-bounded shear flows. *J. Fluid Mech.* 250 (1993), 169–207.
- [61] HERBERT, T. Secondary instability of boundary layers. *Annu. Rev. Fluid Mech.* 20 (1988), 487–526.
- [62] HERBERT, T. Parabolized stability equations. *Annu. Rev. Fluid Mech.* 29 (1997), 245–283.
- [63] HILL, D. C. Adjoint systems and their role in the receptivity problem for boundary layers. *J. Fluid Mech.* 292 (1995), 183–204.
- [64] HUERRE, P., AND MONKEWITS, P. A. Local and global instabilities in spatially developing flows. *Annu. Rev. Fluid Mech.* 22 (1990), 473–537.
- [65] HULTGREN, L. S., AND GUSTAVSSON, L. H. Algebraic growth of disturbances in a laminar boundary layer. *Phys. Fluids* 24, 6 (1981), 1000–1004.
- [66] HUNT, J. C. R., AND DURBIN, P. A. Perturbed vortical layers and shear sheltering. *Fluid Dyn. Res.* 24 (1999), 375–404.
- [67] KACHANOV, Y. S. Physical mechanisms of laminar–boundary–layer transition. *Annu. Rev. Fluid Mech.* 26 (1994), 411–482.
- [68] KACHANOV, Y. S. Three-dimensional receptivity of boundary layers. *Eur. J. Mech., B – Fluids* 19 (2000), 723–744.
- [69] KACHANOV, Y. S., KOZLOV, V. V., AND LEVCHENKO, V. Y. Occurrence of Tollmien–Schlichting waves in the boundary layer under the effect of external perturbations. *Fluid Dyn.* 13 (1979), 704.
- [70] KERSCHEN, E. Boundary layer receptivity. A.I.A.A. Paper (90–1109), 1989.
- [71] KERSCHEN, E. Linear and nonlinear receptivity to vortical free stream disturbances. A.S.M.E. FED 114: 43, 1991.
- [72] KLEBANOFF, P. S., TIDSTROM, K. D., AND SARGENT, L. M. The three-dimensional nature of boundary layer instability. *J. Fluid Mech.* 12 (1962), 1–34.

- [73] KOBAYASHI, R., FUKUNISHI, Y., NISHIKAWA, T., AND KATO, T. The receptivity of flat plate boundary layers with two-dimensional roughness elements to free-stream sound and its control. In *IUTAM Symposium*. Sendai, Japan, 1994.
- [74] LANDAHL, M. T. A note on an algebraic instability of inviscid parallel shear flow. *J. Fluid Mech.* 98 (1980), 243–251.
- [75] LEEHEY, P., AND SHAPIRO, P. J. Leading-edge effect in laminar boundary-layer excitation by sound. In *Proceeding of the IUTAM Symposium on Laminar-Turbulent Transition*. Springer-Verlag, Berlin, 1980, pp. 321–331.
- [76] LIN, C. C. *The Theory of Hydrodynamic Stability*. Cambridge University Press, Cambridge, 1967.
- [77] LIU, Z., XIONG, G., AND LIU, C. Instability wave patterns generated by interaction of sound waves with three-dimensional wall suction or roughness. AIAA Paper (90-0119), 1990.
- [78] LUCHINI, P. Reynolds-number-independent instability of the boundary layer over a flat surface. *J. Fluid Mech.* 327 (1996), 101–115.
- [79] LUCHINI, P. Reynolds-number-independent instability of the boundary layer over a flat surface: optimal perturbations. *J. Fluid Mech.* 404 (2000), 289–309.
- [80] LUCHINI, P., AND BOTTARO, A. Görtler vortices: a backward-in-time approach to the receptivity problem. *J. Fluid Mech.* 363 (1998), 1–23.
- [81] MATSUBARA, M., AND ALFREDSSON, P. H. Disturbance growth in boundary layer subject to free-stream turbulence. *J. Fluid Mech.* 430 (2001), 149–168.
- [82] MICHALKE, A. Receptivity of axisymmetric boundary layers due to excitation by a Dirac point source at the wall. *Eur. J. Mech., B - Fluids* 14, 4 (1995), 373–393.
- [83] MICHALKE, A. Excitation of a 3D-wavetrain by dirac point source at the wall and its growth in a decelating laminar boundary layer. *Eur. J. Mech., B - Fluids* 16, 6 (1997), 779–795.
- [84] MICHALKE, A., AND NEEMANN, K. Excitation of instability waves in wall boundary layers with adverse pressure gradients by various types of Dirac sources. *Acta Mech.* 122 (1997), 33–48.
- [85] MILLING, R. W. Tollmien-Schlichting wave cancellation. *Phys. Fluids* 24, 5 (1981), 979–981.
- [86] MORKONVIN, M. V. Bypass transition to turbulence and research desiderata in *Transition in Turbines*. Nasa conf. pub. 2386, 1984.
- [87] MORKOVIN, M. V. Critical evaluation of transition from laminar to turbulent shear layers with emphasis on hypersonically traveling bodies. Tech. Rep. 68-149, AFFDL, 1969.

- [88] MORKOVIN, M. V., AND RESHOTKO, E. Dialogue on progress and issues in stability and transition research. In *Laminar–Turbulent Transition*, D. Arnal and R. Michel, Eds. Springer, 1990, pp. 3–29.
- [89] MURDOK, M. V. The generation of Tollmien–Schlichting waves by a sound wave. *Proc. Roy. Soc. Lond. A* 372 (1980), 517–534.
- [90] MYOSE, R. Y., AND BLACKWELDER, R. F. Control the spacing of streamwise vortices on concave walls. *AIAA J.* 29, 11 (1991), 1901–1905.
- [91] MYOSE, R. Y., AND BLACKWELDER, R. F. Control of streamwise vortices using selective suction. *AIAA J.* 33 (1995), 1073–1080.
- [92] NAYFEH, A. H., AND ASHOUR, O. N. Acoustic receptivity of a boundary layer to Tollmien–Schlichting waves resulting from a finite–height hump at finite Reynolds numbers. *Phys. Fluids* 6, 11 (1994), 3705–3716.
- [93] PANTON, R. L. *Incompressible flow*. Wiley – Interscience, New York, 1984.
- [94] PRALITS, J. O., HANIFI, A., AND HENNINGSON, D. H. Adjoint–based optimization of steady suction for disturbance control. Part 1. Incompressible flows. *J. Fluid Mech.* Submitted.
- [95] REED, H. L., AND SARIC, W. S. Stability of three–dimensional boundary layers. *Ann. Rev. Fluid Mech.* 21 (1989), 235–284.
- [96] REED, H. L., SARIC, W. S., AND ARNALD, D. Linear stability theory applied to boundary layers. *Ann. Rev. Fluid Mech.* 28 (1996), 389–428.
- [97] RESHOTKO, E. Boundary–layer stability and transition. *Ann. Rev. Fluid Mech.* 8 (1976), 311–349.
- [98] RUBAN, A. I. On generation of Tollmien–Schlichting waves by sound. *Fluid Dyn.* 19 (1985), 709–716.
- [99] SARIC, W. S. Görtler vortices. *Ann. Rev. Fluid Mech.* 26 (1994), 379.
- [100] SARIC, W. S., HOOS, J., AND RADEZTSKY, R. Boundary–layer receptivity of sound with roughness. In *Boundary Layer Stability and Transition to Turbulence*, D. C. Reda, H. L. Reed, and R. Kobayshi, Eds. American Society of Mechanical Engineers, New York, 1991.
- [101] SARIC, W. S., AND NAYFEH, A. H. Nonparallel stability of boundary–layer flows. *Phys. Fluids* 18, 8 (1975), 945–950.
- [102] SCHLICHTING, H. *Boundary–Layer Theory – Seventh Edition*. McGraw–Hill, New York, 1979.
- [103] SCHUBAUER, G. B., AND SKRAMSTAD, H. K. Laminar–boundary–layer oscillations and transition on a flat plate. Tech. rep., 1948. NACA TR-909.

- [104] SENGUPTA, T. K., BALLAV, M., AND HIJHAWAN, S. Generation of Tollmien–Schlichting waves by harmonic excitation. *Phys. Fluids* 6, 3 (1994), 1213–1222.
- [105] TADJFAR, M., AND BODONYI, R. J. Receptivity of a laminar boundary layer to the interaction of a three–dimensional roughness element with time harmonic free-stream disturbances. *J. Fluid Mech.* 242 (1992), 701–720.
- [106] TAM, C. K. W. The excitation of Tollmien–Schlichting waves in low subsonic boundary layers by free–stream sound waves. *J. Fluid Mech.* 109 (1981), 483–501.
- [107] TREFETHEN, L. N., TREFETHEN, A. E., REDDY, S. C., AND DRISCOLL, T. A. Hydrodynamic stability without eigenvalues. *Science* 261 (1993), 578–584.
- [108] WHITE, F. M. *Viscous Fluid Flow – Second Edition*. McGraw–Hill, New York, 1991.
- [109] WHITHAM, G. B. *Linear and Nonlinear Waves*. John Wiley and Sons, New York, 1999.
- [110] WILKINSON, J. H. *The Algebraic Eigenvalue Problem*. Clarendon Press, Oxford, 1965.
- [111] WU, X. Generation of Tollmien–Schlichting waves by convecting gusts interacting with sound. *J. Fluid Mech.* 397 (1999), 285–316.